UNIVERSITY
of
GLASGOW

Scintillation analysis of solar wind dynamics

by

Noelle M. Daly B.Sc.

Thesis
submitted to the
University of Glasgow
for the degree of
Ph.D.

Astronomy and Astrophysics Group
Department of Physics and Astronomy,
University of Glasgow,
Glasgow G12 8QQ

January 2000

ProQuest LLC.
789 East Eisenhower Parkway
P.O. Box 1346
Ann Arbor, MI 48106 – 1346

Acknowledgements

Though the Sun is rarely seen in Glasgow, I'm very glad that I came here to study it. My task was made easier by the wonderful folk who've helped me out along the way, and the warm, friendly atmosphere in the A&A group. First of all, I must thank all of those brave Glasgow astronomers that put their lives at risk in the effort to move my piano, twice!

More seriously, it must be said that this thesis would have been much the poorer without the input of my supervisor, Graham. He almost never turned me away when I tapped at his door and asked, "Have you got a minute?". It never took shorter than 60 seconds! Thank you Graham for your enthusiasm, patience and your generosity with your vast pool of knowledge.

Guillian has been a great office mate, ever ready to help out even in the silliest of my difficulties, and always willing to lend an ear to my rantings and ravings. Thanks for putting up with me. Gail, you've been a great running buddy, thanks for dragging me out into the great Glasgow outdoors, and then there was the Loch Katrine experience.... As I'm on the subject of the variable Scottish weather, Martin might well remember that gale force cycling trip around Hoy, just a tad nippier than the jungles of Mexico!

Many thanks to the computing genii of Graeme, Norman, Paul, Scott and Shashi who have all gotten me out of sticky (and often elementary!) computer mishaps. Huge gratitude to Paul and Gail for getting this volumnious volume printed and bound.

In no particular order (well, how about reverse chronological?), I'd like to thank, for their friendship and any other little thing that they might have done along the way, Hugh (the mechanical wizard, both two wheels, and four!), Helen (Little Miss Sociable), Paul A. (Mr. Scrabble), Stewart (he's up, up and awaaaay), Neal (Mr. Bouncy), Darren (he of the sarcastic wit), Chris (with his green fingers and flourescent lights), Suzanne (our lovely, bubbly Wigan lass), Andrew (another wit, with a particular partiality for Irish jokes),

Richard (the wise old sage who knows everything), Ute (wife of the wise old sage), Aidan (Mr. Smiley), Iain (the penguin-hater) and Paul Mac. (another poor soul who's been dragged on my cyclying expeditions). And who could ever forget Daphne, the lynchpin of the group, and Eve, who makes all the magic (in the planetarium) happen.

To my non-astro friends who've helped me to keep sane - Margit, Mary, Hugh, Judith, Adrian, Laszlo, Emma, Jane and all the others who know who they are - Go raibh MÍLE maith agaibh go léir!

Thanks to Mam and Dad, who never put an obstacle in my way. And to my brother, Eoin, and the rest of my family at home, thanks for always welcoming me back.

And thanks to Victor, who's been so patient in listening to the minutiae of my struggles, and always encouraging in his own wonderful little way.

Goodbye and thanks to Glasgow. I'm off to check out the weather down south!

Summary

Interplanetary scintillation (IPS) is a phenomenon that has been known of and used as a measuring technique for nearly four decades. The aim of this thesis is to explore the practical capacity of IPS as a tool for probing the solar wind.

The radio waves from distant sources (radio galaxies, quasars, etc.) must pass through the turbulent interplanetary medium (IPM) before being detected on Earth. Plasma density variations in the IPS cause scintillation of these radio waves. By careful analysis of the signal, the scintillating component can be extracted, and the amount of scintillation quantified. This relates to variations in the density of the plasma through which the radio waves have passed. The velocity of the solar wind can also be determined from IPS.

By observing thousands of scintillating sources across the whole sky, an all-sky image of the solar wind can be created. Of course, scintillation can occur at any point along the line of sight to the source. Careful modeling can calculate where the dominant contribution to scintillation takes place, enabling a 3-dimensional image of plasma density to be inferred. In this thesis, a large IPS data set has been examined and evaluated, to reveal large scale structure in the inner heliosphere over a 5-year period.

Chapter 1 introduces the history and theory of IPS, and the different applications to which it can be applied. The theory is first presented as a simplified approximation, and then developed to a more complex form, closer to reality. The solar wind itself is also discussed, as well as the different phenomena on the Sun that affect the properties of the solar wind. The areas of solar-terrestrial relationships and geomagnetic storms are explored.

Chapter 2 focuses on the gathering of IPS information for the Cambridge 1990-94 IPS survey. The 3.6 hectare Cambridge IPS array is described, along with the observing procedure for the survey. The new computer software that processed the raw data is

described and the algorithms discussed.

Chapter 3 begins the task of quantifying the scintillation of each source. It examines the algorithm written to fit a template over the scintillating flux recorded for each source for every day of the survey. The density and velocity parameters computed for the whole survey are then thoroughly checked and analyzed. Finally, all sky maps are made to display the computed parameters for one day at a time.

The verification of the Cambridge data set by comparison with other experimental data is the main theme of chapter 4. Measurements of plasma density and velocity taken by in-situ spacecraft are available on the Internet. Data from the IMP-8, SAMPEX and GOES satellites, from the Ulysses spacecraft and from ground-based facilities are correlated with the Cambridge data set. Though it is difficult to make direct comparisons of two different observing systems, some satisfying correlation is found.

After verification of the data set, chapter 5 begins to apply this data to a number of different situations. Initially, the issue of 3-dimensional interpretation of the 2-dimensional maps is explored and modelled carefully. The trends observable over the solar cycle are then investigated, particularly those trends that depend on heliographic latitude. The ability of IPS to track large-scale structure in the IPM, and therefore to predict geomagnetic storms is also investigated in chapter 5, with some specific examples being researched. Lastly, IPS data is used to help verify the existence of a pulsar planet.

Chapter 6 draws some conclusions about the research that has taken place, and the successes achieved, before giving some suggestions for improvements and future work.

Contents

Chapter 1

An introduction to IPS and the solar wind

"O wild West Wind, thou breath of Autumn's being,
Thou, from whose unseen presence the leaves dead
Are driven, like ghosts from an enchanter fleeing..."

P. B. Shelley - Ode to the West Wind

1.1 Introduction

Emanating continuously from the Sun, the dynamic solar wind has a huge influence on conditions in the interplanetary medium. Interplanetary scintillation (IPS) can be used as a diagnostic tool for studying structures in the solar wind. This project involves the analysis of the data set from the five-year Cambridge IPS survey, 1990-94. From this data set, it is hoped that new understanding will be gained into how IPS information can be exploited, in conjunction with other data sources, to investigate the solar wind.

In this chapter, the history, applications and theory of IPS will be explored. Then, the solar wind will be studied, the influence the Sun has on its composition, and the enormous effects that it can have on Earth and the near Earth space environment.

1.2 The history of IPS

IPS has been studied at Cambridge since the 1960s. It began with a series of radio observations carried out in June 1962 and July 1963 at a frequency of 178 MHz, to determine accurate positions for a number of sources [17]. It was noticed by Clarke that that certain radio sources appeared to scintillate, i.e., the measured intensity was observed to fluctuate in a random manner [37], see `Figure 1.1`. Further investigations revealed that this phenomenon only occurred for radio sources of very small angular size, less than $1''$.

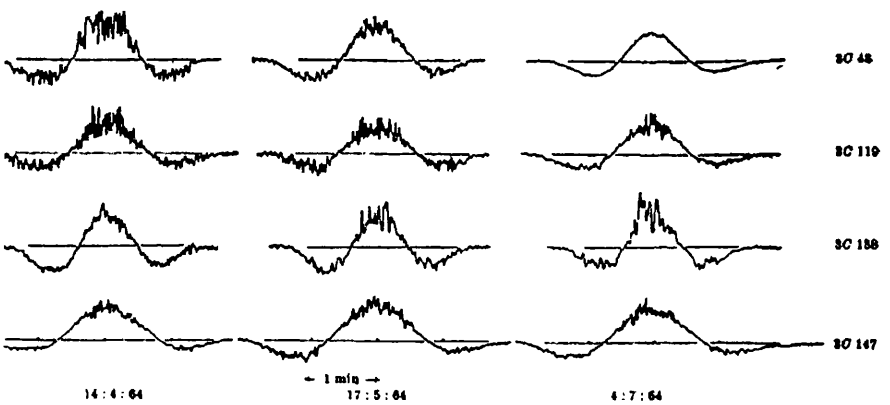

Figure 1.1: Early IPS recordings made at Cambridge by Hewish *et al.* [37].

This scintillation is due to refractive index variations in the interplanetary medium (IPM), along the line of sight to the radio source, which themselves are caused by density inhomogeneities in the solar wind. A source having an angular extent greater than $1''$ acts as a number of point sources all creating similar but displaced and overlapping diffraction patterns on the ground. Therefore, the fluctuations are smeared out, and sufficiently extended sources exhibit practically no interplanetary scintillation at all. This is analogous to the optical case, where a star (point source) will twinkle due to distortion in the Earth's atmosphere, while a planet (extended source) will not.

The degree to which a source exhibits IPS is dependent on its angular structure, hence, IPS measurements can be used to measure the angular extent of distant radio sources, in the range $0.1''$ to $1''$. Early results of radio source structure using IPS at 178 MHz were published by Little and Hewish [52], [53], as well as a detailed description of the scintillation dependency on source structure. To further these efforts, the Cambridge IPS array was purpose-built, completed in 1967, and operating at the lower frequency of

81.5 MHz. The first survey is described by Hewish and Burnell [36], with initial results published in 1972 by Burnell [8], who found 163 scintillating sources. In 1974, Readhead and Hewish [66] reported that 60% of the $\sim$ 1500 4C sources (fourth Cambridge radio survey) between declinations of $-12°$ and $+90°$ were observed to scintillate, and thus, structural information was calculable.

After further analysis of data from the IPS array, some cosmological implications were drawn about the angular size of extragalactic radio sources by Readhead and Longair [69] in 1975, and by Readhead and Hewish [67] in 1976. Since then, the role of IPS in radio source structural studies has been largely superseded by long baseline interferometry, although only recently (with the low-frequency modifications to the VLBA) has VLBI matched its resolution at metre wavelengths.

The scintillation (in the interplanetary medium) of radio sources has been extensively used to probe the IPM itself. Tappin [89] has studied the relationship between scintillation and the density of the material causing that scintillation. After careful analysis, he arrived at a direct relationship, detailed in `Section 3.1`, allowing the determination of the density of the solar wind over the whole sky by observing the scintillation of a large number of radio sources.

The all-sky view afforded by IPS has a huge advantage over the limited information available from in-situ spacecraft taking measurements of their immediate environment. IPS allows the whole sky to be imaged, from a ground based radio telescope. Thus it is possible to see the first appearance of a large scale structure in the solar wind, then to track its movement, and help predict whether it will arrive at and affect the near-Earth environment.

Tappin *et al.* [90] have modelled a disturbance in the IPM, and the IPS variations caused by it. This has been matched with some success to real observations. Gapper *et al.* [25] presented density maps (g-maps) made using the Cambridge IPS array in 1978, and interpreted some of the features as interplanetary disturbances. The origin of transients in the solar wind has been a controversial issue for a long time.

Hewish and Bravo [35] were able to contribute to this discussion with their analysis of ninety-six disturbances mapped during August 1978 to September 1979 using the Cambridge IPS array. By back-projection to the Sun, they concluded that the sources of all the disturbances were associated with coronal holes. Sometimes, there was also flaring

and other activity near the source, which could have been related to the interplanetary disturbance as a peripheral event, but often there was no such activity. CMEs of the "curved-front" variety were often located above coronal holes, suggesting that they too can be related to the same activity which results in interplanetary disturbances and shocks.

Multi-station IPS can be used to determine the velocity of the solar wind. The basic idea is to measure the scintillation pattern simultaneously at a number of spaced receivers, and then to estimate the time delays between the observations at the different locations. Then, taking into account the orientation of the baseline, and the direction of the wind, the time delay is used to calculate the solar wind velocity. This method was first applied to the solar wind by Dennison and Hewish [22].

1.2.1 IPS around the world

Both single-station and multi-station IPS observations have been made by groups all over the world. Coles [19] has reviewed different radio propagation methods for revealing solar wind structure, including IPS observations at UCSD and Nagoya. `Figure 1.2` shows an example of simultaneous recordings made at the three different observing stations, at a frequency of 103 MHz, by the P.N. Lebedev Radioastronomical Institute, at Puschino and other sites in Russia [94].

A three-antenna system operating at 73.8 MHz was established at UCSD (University of California at San Diego) in 1969. Though now suspended, this system was used for multi-station IPS observation, and discovered a lot about the large scale velocity structure of the solar wind. Rickett and Coles [72] describe sixteen years of these observations, and the solar cycle trends that they found.

Operated by the University of Nagoya, Japan, three antennae operating at 327 MHz are dedicated to multi-station IPS observation [45]. See `Section 4.2.3` for more details.

The Ooty radio telescope in India (327 MHz) [6] has been used for a novel single-station IPS method of measuring the velocity of the solar wind, using spectral methods. See `Section 3.2.5` for a description of this work. Using this method, Manoharan [55] has found excellent agreement with the velocity data recorded by the multi-station use of the Nagoya telescope. `Figure 1.3` shows some of his results, the solar wind velocity is plotted as a function of heliographic latitude, for two different periods near solar minimum and solar maximum. Gothoskar and Khobragade [27] have employed the technique of neural

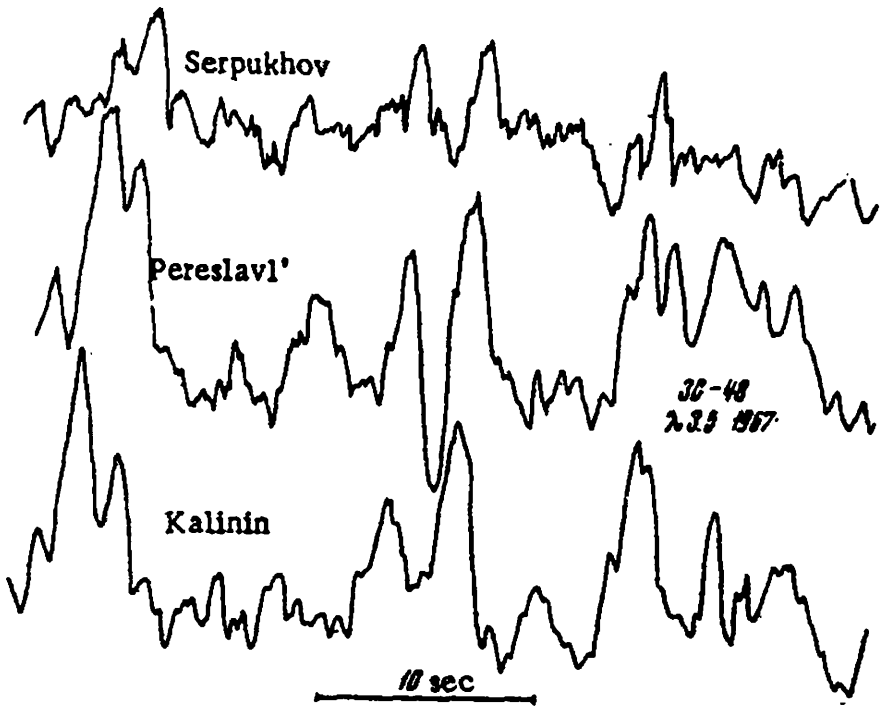

Figure 1.2: Simultaneous recordings made at three different stations at Puschino by Vitkevich and Vlasov [94].

networks to analyse the scattering power spectra obtained at Ooty to identify normal, disturbed and strong IPS spectra.

The EISCAT (European Incoherent SCATter) telescopes (933 MHz) have been regularly used for IPS observations [13], in the multi-station mode, to obtain solar wind velocity measurements. Some results of such observations are discussed by Breen *et al.* [14].

Although the Cambridge IPS array is currently out of commission, these other telescopes around the world are continuing to make IPS observations. There is much analysis to be done on the 1990-94 data set from the Cambridge array. The purpose of this thesis is to exploit this data set, and thereby prove to a further extent the usefulness of this kind of IPS observation.

1.3 Scintillation theory

Radio waves from a distant source must pass through the IPM before they are detected on Earth. The dynamic density variations in the IPM cause refractive index fluctuations which serve to diffract the radio waves as they pass through. To describe this diffraction,

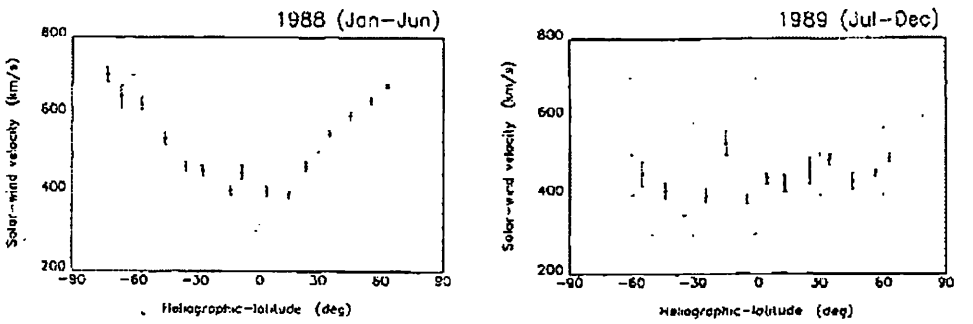

Figure 1.3: The solar wind velocity determined by single-station IPS methods at Ooty, plotted against heliographic latitude. The left hand graph represents solar minimum, where the velocity has a marked dependency on latitude, while the right hand graph is for a period near solar maximum and the same dependency is not at all clear.

we shall first develop the theory for a general, infinitely-distant, incoherent, point source illuminating a thin sinusoidal phase screen, as has been explained by Hewish [32]. Subsequently, this theory will be extended to include extended sources illuminating a random phase screen, as summarised neatly by Codona [18].

By the time they arrive in the solar system, the radio waves from a distant point source can be considered to be plane waves. Of course, an extended source will be emitting plane waves over a spread of angles, θ, but initially, we shall only consider plane waves coming from one angular direction, i.e., from a point source. The plasma in the IPM acts as a phase-changing screen, i.e., by passing through, the phase of the plane wave is changed in the plane perpendicular to the propagation direction due to the refractive index variations.

1.3.1 Weak scattering of the waves from a point source by a thin, sinusoidal, phase-changing screen

Consider the plane wave incident on the screen in the xy-plane,

$$A(x,t) = e^{i(kz-\omega t)}, \tag{1.1}$$

where k is the wavenumber of the incident radiation, and z is the spatial distance in the direction of travel of the wave, see `Figure 1.4`. After passing through the phase-changing screen, the phase of the incident wave front is modulated by up to $\Delta\phi$. We assume that the screen varies sinusoidally, with a wavenumber κ, giving an emerging wave of complex

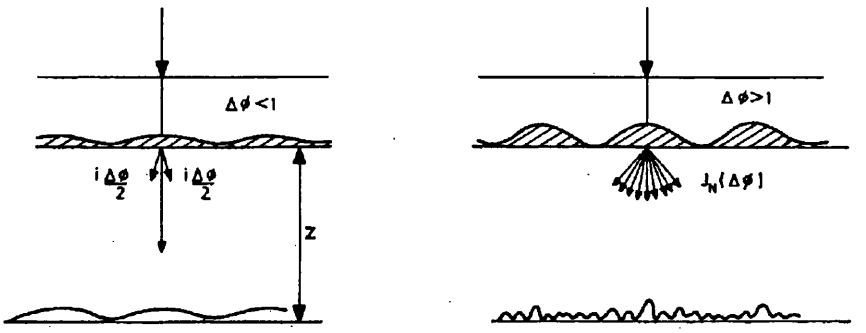

Figure 1.4: Scintillation by a sinusoidal phase-changing screen. On the left, the phase change is small, $\Delta\phi < 1$ radian, causing "weak scattering". The theory for this type of scattering is developed in this section. On the right, $\Delta\phi > 1$ radian. This is strong scattering and it will not be described in detail.

amplitude

$$A(x,t) = e^{i\Delta\phi \sin\kappa x} e^{-i\omega t}, \tag{1.2}$$

in the plane $z = 0$. As $\Delta\phi < 1$ radian, we can simplify this to

$$A(x,t) \simeq (1 + i\Delta\phi \sin\kappa x) e^{-i\omega t}. \tag{1.3}$$

Hewish [32] shows that the effect of a thin, sinusoidal phase-changing screen is to introduce a pair of additional waves of complex amplitude $i\frac{\Delta\phi}{2}$ where $\Delta\phi < 1$ radian, and inclined at $\pm\sin^{-1}\frac{\kappa}{k}$ to the z-axis. These extra waves are shown in Figure 1.4. This follows because two, unit amplitude, plane waves travelling at angles of θ and $-\theta$ to the z-axis have a resultant

$$2\sin(kx\sin\theta)\cos(kz\cos\theta - \omega t), \tag{1.4}$$

where $\theta = \pm\sin^{-1}\frac{\kappa}{k}$. Assuming the spatial scale of the screen is much greater than a wavelength, i.e. $\kappa \ll k$, we can say that $\theta = \frac{\kappa}{k}$.

The case of strong scattering, $\Delta\phi > 1$ radian, applies to our IPS observations (at 81.5 MHz) only when the elongation of the source is less than 30° from the Sun (due to the increased plasma density there). The mathematical treatment is more involved, and will not be developed here.

As the three emergent waves propagate out from the screen, they will interfere with each other. At a certain distance from the screen, called the Fresnel distance, they will first be in phase and the diffraction pattern becomes fully developed.

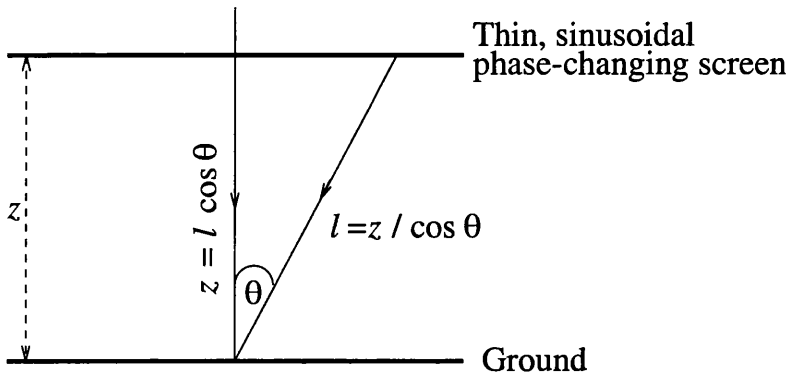

Figure 1.5: From the phase-changing screen, the main wave emerges, with one beam on either side, separated by θ.

The phase difference between the scattered and unscattered waves varies with distance from the screen. The unscattered wave travels a distance z, while the scattered wave travels a distance $l = z/\cos\theta$, as can be seen in `Figure 1.5`. The unscattered wave can be written as e^{ikz}, and the scattered as $\frac{i\Delta\phi}{2}e^{\frac{ikz}{\cos\theta}}$. Thus, the path difference, ΔL between the two waves can be written as

$$\Delta L = kz - \left(\frac{kz}{\cos\theta} - \frac{\pi}{2}\right). \tag{1.5}$$

The extra $\frac{\pi}{2}$ is a result of the extra i in the expression for the scattered wave.

$$\begin{aligned}
\Delta L &= kz - \frac{kz}{1-\frac{\theta^2}{2}} + \frac{\pi}{2} && (1.6)\\
&\simeq kz - kz\left(1+\frac{\theta^2}{2}\right) + \frac{\pi}{2} && (1.7)\\
&= -kz\frac{\theta^2}{2} + \frac{\pi}{2} && (1.8)
\end{aligned}$$

Now substitute for $\theta = \frac{\kappa}{k}$,

$$\begin{aligned}
\Delta L &= -kz\frac{\kappa^2}{2k^2} + \frac{\pi}{2} && (1.9)\\
&= -\frac{\kappa^2 z}{2k} + \frac{\pi}{2} && (1.10)
\end{aligned}$$

So we can say that the component in phase with the unscattered waves has amplitude

$$\begin{aligned}
\Delta A &= \Delta\phi\cos\left(\frac{\kappa^2 z}{2k} + \frac{\pi}{2}\right)\sin(\kappa x) && (1.11)\\
&= \Delta\phi\sin\left(\frac{\kappa^2 z}{2k}\right)\sin(\kappa x), && (1.12)
\end{aligned}$$

where $\Delta\phi$ is the amplitude of the phase modulation, and $\sin(\kappa x)$ accounts for the interference caused by the sinusoidal phase screen of wavenumber κ. The term $\sin\left(\frac{\kappa^2 z}{2k}\right)$ is known as the "Fresnel filter". This is very important, as it determines where along z that the diffraction pattern will be strongest. It too varies sinusoidally, with increasing z. The characteristic distance, $z = \frac{\pi k}{\kappa^2}$, is called the Fresnel distance, and it denotes where the intensity modulation in the Fresnel diffraction pattern first becomes fully developed.

As well as being dependant on z and k, the Fresnel filter is proportional to κ^2, which has the effect of reducing the influence of long wavelength perturbations in refractive index, i.e., large scale variations in refractive index are not as important as smaller ones. The Fresnel filter appears again in the next section where IPS theory is extended to cover the real, rather than the simplified situation.

1.3.2 Weak scattering of the waves from an extended source by a thin, random, phase-changing screen

Hewish assumed a sinusoidal phase-changing screen which would in turn produce a sinusoidal intensity pattern on the ground. As can be seen from `equation 1.12`, it is a characteristic of weak scattering that the spatial scale of the phase fluctuations in the scattering screen is the same as the spatial scale of the diffraction pattern on the ground.

In reality, the screen is made up of many different sizes and shapes of plasma structures. Because of this random and unpredictable nature of the plasma fluctuations, the diffraction pattern will have rather a random shape. Also, as the plasma is moving (at the speed of the solar wind), then on the ground we observe a drifting pattern.

If the source is extended, then instead of just one plane wave passing through the screen and producing three emergent beams, we get many waves passing from the different parts of the source, and creating many more emergent beams. The combination of all these waves of different phase makes the intensity pattern on the ground even more complex.

To quantify the IPS phenomenon under these conditions, it is instructive to think in terms of correlation. We will describe the intensity of the diffraction pattern on the ground in terms of the scintillating flux density, as measured by the Cambridge IPS array. The random flux density pattern will be described by $S(x)$, where x is a positive vector in the observation plane. The two-point intensity correlation can be written as

$$C_S(a) = \langle S(x)S(x+a)\rangle\,, \tag{1.13}$$

where angle brackets denote ensemble averaging over the fluctuations in the IPM. $S(x)$ will be very similar to $S(x+a)$ when a is very small compared to the typical distance over which the intensity pattern changes. If the intensity pattern is quite smooth, then $C_S(a)$ will be large for all values of a, so we can say that the pattern is highly correlated. But when the intensity pattern varies rapidly, the correlation falls.

To describe the pattern contrast, the "scintillation index", m, is defined as the fluctuation in the rms flux density, normalized by the mean flux density

$$m^2 = \frac{(\Delta S)^2}{\langle S \rangle^2} = \frac{\langle (S - \langle S \rangle)^2 \rangle}{\langle S \rangle^2} = \frac{C_S(0) - C_S(\infty)}{C_S(\infty)} . \tag{1.14}$$

m will be large when there is a big difference between the correlation at no separation and the correlation at a separation of infinity, i.e., if the flux density pattern is heavily modulated. If the scintillation is low, then the intensity pattern will not be varying as much, and the scintillation index will be correspondingly lower. Note that m is always less than 1.

We also define two other important quantities similar to m.

$$A = \frac{(\Delta S)^2}{\langle (\Delta S)^2 \rangle} . \tag{1.15}$$

A describes the scintillating flux density squared, normalized by the mean scintillating flux density squared for that source over a long period of time ($\geq$ 1 year). In the Cambridge IPS data set, a value of A can usually be found for every source, for every observation. This is done by measuring the squared fluctuation in flux density for the source on any particular day, and then dividing this by the square of the five-year average value of fluctuation, $\langle \Delta S \rangle$.

We can also define

$$g = \frac{\Delta S}{E(\Delta S)} . \tag{1.16}$$

g is the fluctuation of the flux density, this time normalized by the *expected* value of ΔS, $E(\Delta S)$ for the observing geometry. The expected value of ΔS will change for a particular source during the course of the year, because the source will be at different elongations from the Sun during the year. This means that the line of sight will be passing through dense plasma close to the Sun at one time, and then through plasma of lower density far away from the Sun at another time. We characterize this behaviour by averaging over 3° elongation bins for each source, over the course of the five-year survey, and assembling

graphs showing scintillation as a function of elongation. `Chapter 3` discusses this process in more detail.

Scintillation is caused by small fluctuations in plasma refractive index, η. In interplanetary conditions, η can be expressed as

$$\eta^2 = 1 - \frac{\nu_p^2}{\nu^2}, \tag{1.17}$$

where ν is the frequency of the radiation and ν_p is the plasma frequency. The plasma frequency is the frequency below which waves cannot propagate in a plasma, and which is up to a few tens of KHz in the IPM. It is expressed as

$$\nu_p^2 = \frac{1}{4\pi^2}\frac{n_e e^2}{\epsilon_0 m_e}, \tag{1.18}$$

where n_e is the electron density, e is the charge on an electron, ϵ_0 is the permittivity of free space, and m_e is the mass of an electron.

Now we can write the refractive index as

$$\eta = \sqrt{1 - \frac{\nu_p^2}{\nu^2}} \tag{1.19}$$

$$\simeq 1 - \frac{1}{2}\frac{\nu_p^2}{\nu^2}, \tag{1.20}$$

because $\nu \gg \nu_p$. Now, filling in for ν_p

$$\eta = 1 - \frac{1}{2\nu^2}\frac{1}{4\pi^2}\frac{n_e e^2}{\epsilon_0 m_e} \tag{1.21}$$

$$= 1 - \frac{1}{8\pi^2}\frac{n_e e^2}{\epsilon_0 m_e \nu^2}. \tag{1.22}$$

The fluctuations in η can be expressed as

$$\mu(\mathbf{r}) \equiv \eta(\mathbf{r}) - \langle\eta\rangle, \tag{1.23}$$

where $\eta(\mathbf{r})$ is the refractive index at a position r in space, and $\langle\eta\rangle$ is the mean of η. We can relate $\mu(\mathbf{r})$ directly to density at a particular point, $n_e(\mathbf{r})$ and to the mean density, $\langle n_e\rangle$.

$$\mu(\mathbf{r}) = \left(1 - \frac{1}{8\pi^2}\frac{n_e(\mathbf{r})e^2}{\epsilon_0 m_e \nu^2}\right) - \left(1 - \frac{1}{8\pi^2}\frac{\langle n_e\rangle e^2}{\epsilon_0 m_e \nu^2}\right) \tag{1.24}$$

$$= \frac{1}{8\pi^2}\frac{e^2}{\epsilon_0 m_e}\frac{\langle n_e\rangle - n_e(\mathbf{r})}{\nu^2}. \tag{1.25}$$

So if we have a technique for measuring $\mu(\mathbf{r})$, then we can determine the deviation in density at a particular point. IPS is such a technique, as will be explained in this section.

The fluctuations in the random phase-changing screen can be described by a power spectrum. It can be calculated by taking the Fourier transform of the autocorrelation of the index of refraction fluctuations, as given by the Wiener-Khinchin theory (see chapter 12 of Numerical Recipes [64]).

$$\phi_\mu(\kappa) = \frac{1}{(2\pi)^3} \int_{-\infty}^{\infty} \langle \mu(\mathbf{r}_0)\mu(\mathbf{r}_0 + \mathbf{r}) \rangle e^{-i\boldsymbol{\kappa}\cdot\mathbf{r}} d^3r \,, \tag{1.26}$$

where $\boldsymbol{\kappa}$ is a three-dimensional wave vector, $\langle \mu(\mathbf{r}_0)\mu(\mathbf{r}_0 + \mathbf{r}) \rangle$ is the autocorrelation of the refractive index fluctuations and $\frac{1}{(2\pi)^3}$ is a normalization factor.

We will assume that the turbulence spectrum can be described by a Kolmogorov turbulence spectrum

$$\phi_\mu(\kappa) \propto C_n^2 \kappa^{-11/3} \,, \tag{1.27}$$

where C_n^2 is the turbulence structure constant, determining the overall "power" in the spectrum.

Because it is an extended source, we must add up the individual flux density patterns, $S_{pw}(x)$, caused by each plane wave to get the total flux density pattern, giving

$$S(x) = \int_{-\infty}^{\infty} B(\theta) S_{pw}(x + z\theta) d^2\theta \,, \tag{1.28}$$

where $B(\theta)$ is the brightness distribution of the source. Because of the extra $z\theta$ factor, the resulting flux density pattern on the ground is smudged somewhat. If θ is too large (in our case, $\theta > 1''$), then the flux density pattern will be too smeared out to detect.

We write the correlation of the flux density pattern of two points on the ground, separated by a, assuming a plane wave illumination of the screen, as

$$C_{pw}(a) = \langle S_{pw}(x) S_{pw}(x + a) \rangle \,. \tag{1.29}$$

We can now sum over all values of θ to take into account that it is an extended source to give

$$C_S(a) = \int \int_{-\infty}^{\infty} B(\theta_1) B(\theta_2) C_{pw}(a - z(\theta_1 - \theta_2)) d^2\theta_1 d^2\theta_2 \,. \tag{1.30}$$

The power spectrum of the flux density can be found by again using the Wiener-Khinchin theorem [64], i.e., by finding the Fourier transform of the correlation, $C_S(a)$

$$\phi_S(\boldsymbol{\kappa}) = \frac{1}{(2\pi)^2} \int_{-\infty}^{\infty} C_S(a) e^{-i\boldsymbol{\kappa}\cdot\mathbf{a}} d^2a \,, \tag{1.31}$$

where $\boldsymbol{\kappa}$ is the two-dimensional "spatial frequency". We can expand this out by taking the Fourier transform of $C_S(a)$, leading to

$$\phi_S(\boldsymbol{\kappa}) = (2\pi)^4 |\tilde{B}(z\boldsymbol{\kappa})|^2 \phi_{pw}(\boldsymbol{\kappa}) , \tag{1.32}$$

where $\tilde{B}(z\boldsymbol{\kappa})$ is the Fourier transform of the brightness distribution with respect to θ, and $\phi_{pw}(\boldsymbol{\kappa})$ is the transform of $C_{pw}(a)$.

$\phi_{pw}(\boldsymbol{\kappa})$ is the flux density spectrum for a plane wave incident on a weakly scattering thin phase screen as derived earlier, and it is well known [32]

$$\phi_{pw}(\boldsymbol{\kappa}) = \delta(\boldsymbol{\kappa}) + 8\pi k^2 l \sin^2\left(\frac{z\kappa^2}{2k}\right) \phi_\mu(\boldsymbol{\kappa}) , \tag{1.33}$$

where l is the thickness of the screen, $k = 2\pi/\lambda$ and λ is the wavelength of the radiation. The factor $\sin^2\left(\frac{z\kappa^2}{2k}\right)$ is the square of the "Fresnel filter", as described in `equation 1.12` (it is squared because `equation 1.12` was calculated for amplitudes, while here we are dealing with intensity).

To find the flux density spectrum for an extended source, we substitute `equation 1.33` into `equation 1.32`, and using $S_{\text{tot}} = (2\pi)^2 \tilde{B}(0)$, we obtain

$$\phi_S(\boldsymbol{\kappa}) = S_{\text{tot}}^2 \delta(\boldsymbol{\kappa}) + (2\pi)^4 8\pi k^2 l |\tilde{B}(z\boldsymbol{\kappa})|^2 \sin^2\left(\frac{z\kappa^2}{2k}\right) \phi_\mu(\boldsymbol{\kappa}) . \tag{1.34}$$

The second term here is the flux density spectrum. Taking the inverse Fourier transform, we get the flux density spatial correlation function. Noting that the total flux density is equal to the mean flux density, `equation 1.34` can be used in `equation 1.14` to give the scintillation index,

$$m^2 = 8\pi k^2 l \int_{-\infty}^{\infty} \frac{|\tilde{B}(z\boldsymbol{\kappa})|^2}{|\tilde{B}(0)|^2} \sin^2\left(\frac{z\kappa^2}{2k}\right) \phi_\mu(\boldsymbol{\kappa}) d^2\kappa . \tag{1.35}$$

In this expression, the $8\pi k^2 l$ term is for normalization and the "Fresnel filter" is as before. $|\tilde{B}(z\boldsymbol{\kappa})|^2/|\tilde{B}(0)|^2$ is the factor that accounts for the blurring of an extended source. $\phi_\mu(\boldsymbol{\kappa})$ is the power spectrum of refractive index variations, as previously defined in `equation 1.27`.

What we have found is the thin screen expression. It can be extended to a thick screen by summing the contributions to m^2 from all the screens along the line of sight.

Utilizing `equation 1.35`, it should be possible to predict the scintillation index produced by any particular spectrum of refractive index variations. m itself is measured using the first part of `equation 1.14`. m depends on the power spectrum of refractive index variations, which themselves depend on the electron number density variations in the

plasma (see `equation 1.25`). Therefore, m will give a measure of the density fluctuations of the plasma in the IPM. In this project, the parameter A is measured, which is related to m.

We have seen that the refractive index is frequency dependent (`equation 1.25`). This means that the phase modulation is proportional to the wavelength. So at smaller wavelengths, there will be less scintillation caused by the same screen. Therefore, the changeover from weak to strong scattering takes place much closer to the Sun for shorter wavelengths. Thus, at higher frequencies, IPS can probe closer to the Sun. For example, the EISCAT facility observes at a frequency of 931.5 MHz, and so it can observe as close as 18 solar radii, whereas the Cambridge IPS array at 81.5 MHz can only observe as close as 120 solar radii.

1.4 The solar wind

The solar wind is a continuous, rapid expansion of the solar corona into interplanetary space, and it is a natural consequence of the high coronal temperature. The photosphere (the visible surface of the Sun) is at a mere 6000 K, while the temperature of the corona (the atmosphere) has been measured to be $\sim 10^6$ K from coronal emission lines [9]. At such high temperatures, the ionization of hydrogen in the corona is almost complete, so the corona is composed of a proton-electron gas, with small proportions of ions of other elements. The electrons in this mixture scatter the photospheric light so that the "white light" corona is visible in coronographs or during eclipses.

The presence of the solar wind is evident in a variety of phenomenon. The ionic tail of a comet always points away from the Sun, because it is "blown" back by the solar wind. The Aurora (or Northern Lights) is caused by plasma carried from the Sun as the solar wind, and entering the Earth's atmosphere at the poles.

At 1 AU, the average speed of the wind is $\sim$400 km s^{-1}, and the typical number density is about 10 cm^{-3}. It is thought that at about 100 AU, the solar wind has thinned out to become indistinguishable from interplanetary space. The mass loss from the Sun due to the solar wind is only about 5×10^{16} kg per year, only 2.5×10^{-14} of the solar mass itself [62].

In the early days, before the solar wind was recognised, Biermann (1953) tried to

explain why parts of a comet's tail would occasionally show accelerations along the tail's length. He proposed that it was due to a continuous outflow of ions from the Sun. In 1954, Chapman [16] put forward his idea of coronal extension into interplanetary space, by assuming that the solar atmosphere was in a state of hydrostatic equilibrium, i.e., that the gas pressure was balanced by gravity. Unfortunately, this model leads to plasma densities at the Earth that are far too large, and there are more difficulties at large heliospheric distances, in blending into the interstellar background.

Recognizing these problems, Parker concluded that "probably it is not possible for the solar corona, or, indeed, perhaps the atmosphere of any star, to be in complete hydrostatic equilibrium out to large distances" [58]. He then considered a new possibility, that the Sun's gravitation could not hold back the pressure force of the extremely hot coronal gas, leaving the corona free to steadily expand. So, instead of hydro*static* equilibrium, the Sun would be in a state of hydro*dynamic* equilibrium. An important factor was that he assumed a constant temperature in the corona.

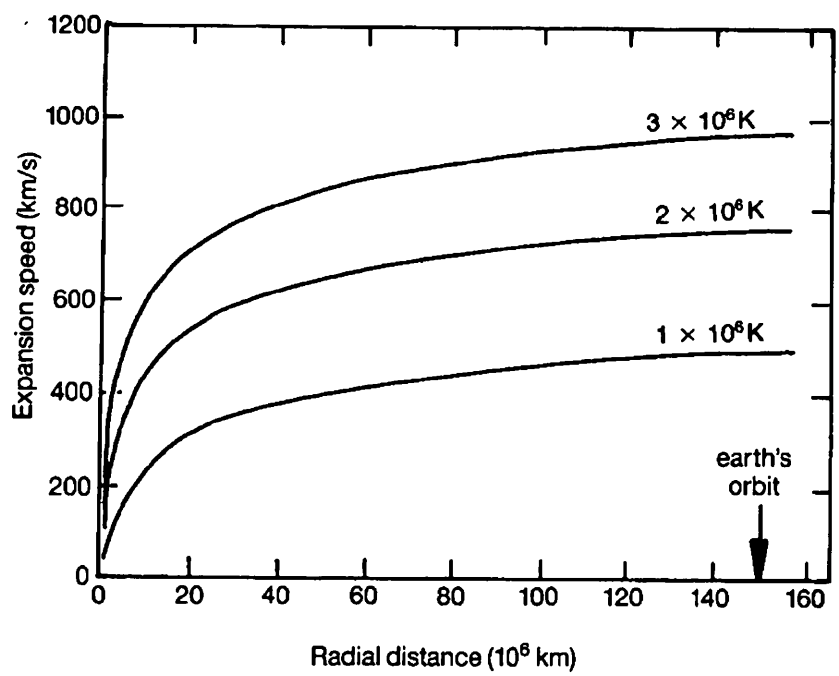

Figure 1.6: Velocity of the solar wind as a function of distance, for different temperatures.

Figure 1.6 shows Parker's predicted velocity of the solar wind at varying distances from the Sun, for different isothermal coronal temperatures. Taking, for example, the

curve for a temperature of 2×10^6 K, the wind speed at 1 AU will be $\sim$700 km s^{-1}, which is far above the sound speed for this temperature (about 150 km s^{-1}), so the flow is definitely supersonic. Finally, direct spacecraft measurements became possible in the early 1960s and clearly confirmed Parker's supersonic expansion model.

An important aspect of the solar wind influence is that it carries out with it the magnetic field of the corona. This is because the magnetic field lines are "frozen into" the plasma of the corona, so, when it expands, the field lines are drawn out into interplanetary space. Because the Sun rotates, the field lines emerge as spirals. Though the plasma expands radially (to an observer at Earth), the field lines are wound up in an Archimedean spiral, with their footpoints back on the Sun, see `Figure 1.7`.

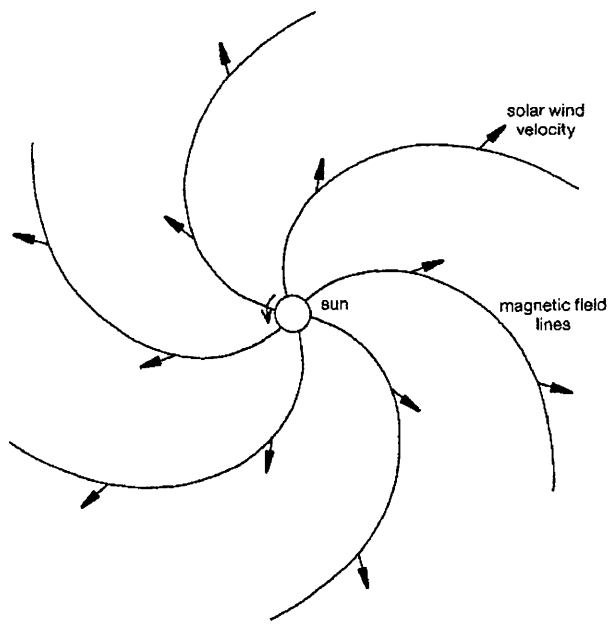

Figure 1.7: The solar wind velocity is always directed radially out from the Sun, as shown by the short arrows. Because the Sun rotates, the magnetic field lines emerge as spirals.

1.4.1 Coronal holes

The velocity of the solar wind depends, to a large extent, on the part of the corona that it emerged from. The magnetic field lines at a coronal hole are open, so the plasma from these areas is not so bound to the Sun, and can flow out more freely, and faster. `Section 4.2.4` discusses coronal holes again in more detail. `Figure 4.7` shows an image of a

coronal hole. A long lived coronal hole can cause a co-rotating high speed stream, which describes a spiral out from the Sun. Due to solar rotation, this fast moving stream can be observed with a period of about 27 days at the Earth.

Two recurrent high speed streams evident in 1974 were seen by the Vela and IMP near-Earth spacecraft, shown in Figure 1.8. 1974 was the declining phase of the solar cycle, when coronal holes tend to be larger and longer-lasting. Bame *et al.* [5] suggest that this is due to the greater number of transients during solar maximum, which disrupt long-living streams from forming. During solar minimum, the Sun is quieter, so long-lived streams have more of a chance to develop.

A long lived high speed stream will inevitably catch up with the slower wind in front, creating an interacting region, where plasma compression may lead to the formation of shock waves both upstream and downstream of the interface. (A shock wave is characterized by a very steep density gradient over a short distance, called the shock front.) These interplanetary shocks form the boundary of a corotating interaction region (CIR).

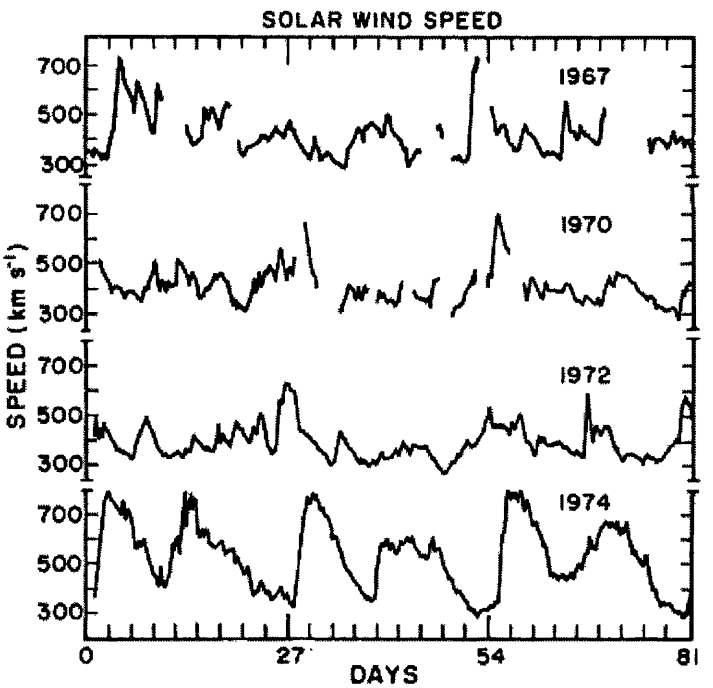

Figure 1.8: Some solar wind velocities measured by Vela and IMP spacecraft between 1967 and 1974, in 63 day intervals. Two well-defined, high speed streams are very obvious in 1974, probably related to two coronal holes seen by the Skylab mission.

1.4.2 Transient events affecting the solar wind

If the Sun was a constant, never-changing star, then the solar wind would also be homogenous and invariable. But, as we have already seen with coronal holes, this isn't the case. Because of the 11 year sunspot cycle, the Sun goes through its active phase at cycle maximum, when many transient events occur, and then it experiences the lull of solar minimum, when activity is very low. The solar wind can have a very different character, depending on the stage of the solar cycle. Some of the different types of transient event that happen at the Sun include solar flares, prominences and coronal mass ejections (CMEs).

Coronal mass ejections

A CME occurs when the corona releases a huge amount of mass, up to 10^{12} kg, and this travels out into interplanetary space at speeds that can be anything between 20 and 2000 $\mathrm{km\,s^{-1}}$ [30]. They are usually associated with erupting prominences on the Sun (where a filament at the limb is seen to erupt upward, with a large release of energy), see `Figure 1.9`. They can have a huge influence on the solar wind, creating shocks as they may be travelling faster than the material in front. On average over the solar cycle, one CME will happen every day, but there is a tendency for more CMEs at solar maximum, and fewer at minimum [38].

CMEs were first observed in 1973 [92] by the Orbiting Solar Observatory - 7 (OSO-7), and they have been closely observed by many instruments since, for example, see `Figure 1.9`. Initially, the Navy Research Laboratory's Solwind [81] and the High Altitude Observatory's coronagraph/polarimeter (C/P) on SMM (Solar Maximum Mission) [54] made many observations in the 1980s, as reported by Howard *et al.* [40]. Currently, the LASCO coronograph on SoHO (SOlar Heliospheric Observatory) [23] is recording CMEs in fine detail as the next solar activity maximum approaches in 2000/2001.

Because they are so faint compared to the disk of the Sun, CMEs emerging from the Sun can only be viewed by using coronagraphs, which block out the disk of the Sun. Therefore, it is usually only the CMEs ejected from near the limb of the Sun that are observed, so, even though a CME is emitted about once per day, that doesn't mean that it is possible to observe one every day. Occasionally, a CME that is emitted off-limb is large enough, and dense enough to be still visible once it has travelled beyond the obscuring disk of the

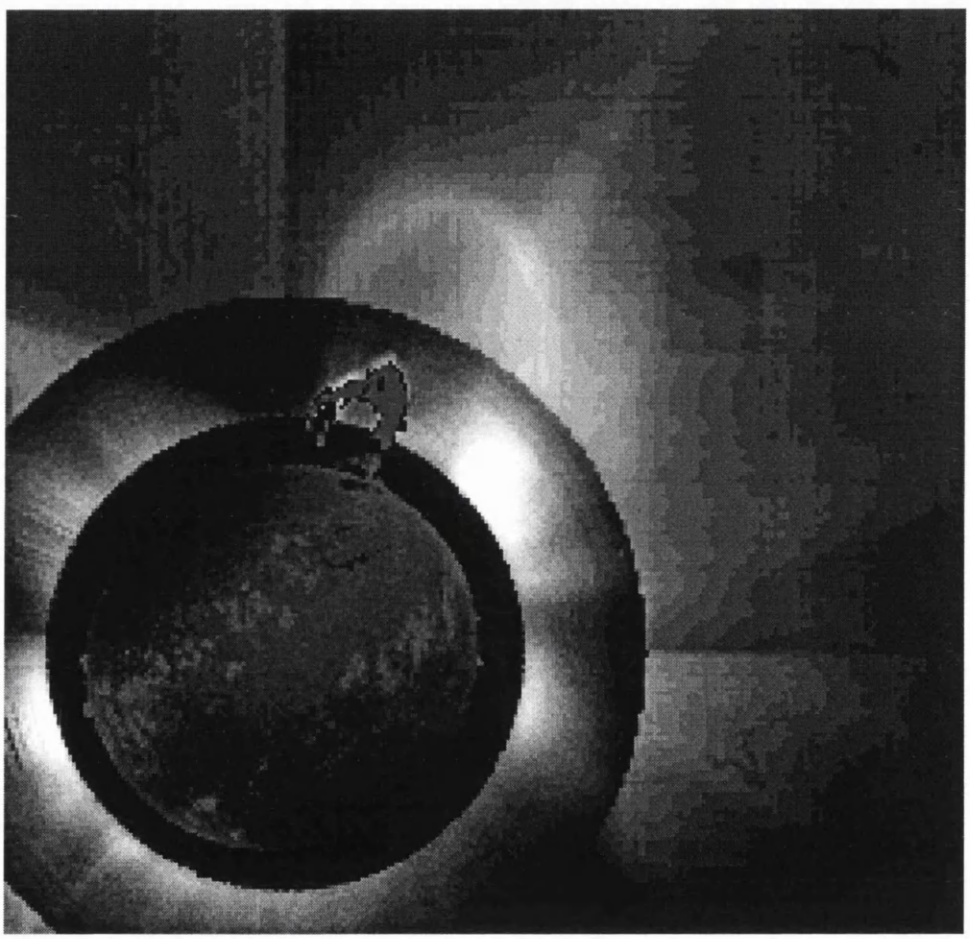

Figure 1.9: A composite image of a CME recorded on 5 October 1989. The disk of the Sun is a H-α picture, the inner corona is imaged in white light by the Mauna Loa MK-III coronagraph, and the outer corona is a white light image taken by the Solar Maximum Mission (SMM). The CME is emerging from the corona at the top right of this image. Behind it, a huge eruptive prominence extends far out into the corona. This prominence was captured by the Mauna Loa H-α prominence monitor.

coronagraph (as viewed from Earth). If this kind of CME is observed to be encircling the Sun, then it is called a halo CME, and it is most likely heading in the direction of the Earth, and there causing geomagnetic effects. Schwenn *et al.* [78] discuss one such CME observed by Solwind in November 1979.

Unfortunately, there was no orbiting coronograph during the course of our IPS survey, so no direct comparisons can be made between IPS observations of proposed CMEs and transients seen in an orbiting coronagraph. The Mauna Loa coronagraph was indeed operating at this time, but it does not give continuous coverage due to rotation of the Earth, and adverse weather conditions.

CMEs happen very quickly, so it is not always possible to detect them on IPS g-maps. For a CME emitted at the limb, by the time it is beyond 30° elongation, the CME itself is often too tenuous to cause an appreciable increase in scintillation. But it might be possible to view the high density, fast moving shock front that builds up in front of it. `Chapter 5` discusses specific examples in more detail.

A thorough review of the physics of CMEs was given in 1987 by Kahler [42] and references therein. More recently, Vilmer [93] has examined the current understanding of CMEs and other solar activity that can affect the solar-terrestrial environment. When a CME is detected in interplanetary space, away from the Sun, Vilmer has described them as ICMEs (Interplanetary CMEs) to distinguish them from what we see in a coronograph.

Solar flares

A solar flare has been classified, by Svestka, as "a rapid, temporary heating of a restricted part of the solar corona and chromosphere" [86]. From the highly-stressed magnetic fields of the solar atmosphere, a flare releases up to 10^{25} J of energy, over a wide range of electromagnetic radiation, in some tens of minutes. Energetic particles are also produced by the acceleration of protons and electrons. Normally, the amount of flare activity follows the sunspot cycle. The search continues for a theory covering all aspects of flaring behaviour, though important strides have been made [87]. In the context of this report, we wish to know whether or not they affect appreciably the solar wind.

It is possibly through the acceleration of energetic particles that flares can mostly affect the IPM, and sometimes the terrestrial environment. In 1973, OSO-7 first detected

nuclear γ-radiation coming from flares, and since then, the Compton Gamma Ray Obsetvatory (CGRO) has been finding events with 50-100 MeV γ-ray production lasting for several hours [44]. These particles are carried along by the solar wind, following the spiral magnetic field lines, and sometimes arriving at Earth.

Solar activity: Connection between CMEs and flares?

All forms of solar activity have one thing in common, they are all related to magnetic fields. A CME is thought to be the result of a large-scale departure from equilibrium, when the magnetic and gravitational forces no longer counter the coronal gas expansion, and thus the CME lifts off with constant speed, either slow or fast. Solar flares are caused by magnetic reconnection.

It is therefore reasonable to ask if there is a connection between the two events. Does one precede, and cause the other? Harrison and Sime [30] presented a number of cases where preconceived ideas had damaged the interpretation of coronal mass onsets. Taking these into account, Harrison [29] later investigated both phenomena and attempted to draw conclusions from a few large data sets. He pointed out the obvious bias in observational techniques for the two different phenomena: CMEs are usually detected at the solar limb, whereas flare investigations stay away from the limb to avoid the effects of foreshortening. There are so many free parameters (velocity, expansion, acceleration, etc.) that a CME could be back-projected to almost any active region desired, or if there is no convenient flare site, then perhaps it happened to be beyond the limb.

Harrison concluded that CMEs generally precede the flare onset, but a flare does not always follow a CME. `Figure 1.10` shows his theory relating the lift-off of a CME to X-ray flaring activity, with this associated flaring commonly lying to one side of the CME span.

In 1992, Kahler [43] made it clear that a flare (H-α or X-ray) is not a necessary condition for a CME to occur. The two different types of event often occur around the same time, but not necessarily. This lack of definite association is important when interpreting IPS studies of transient events in chapter 5.

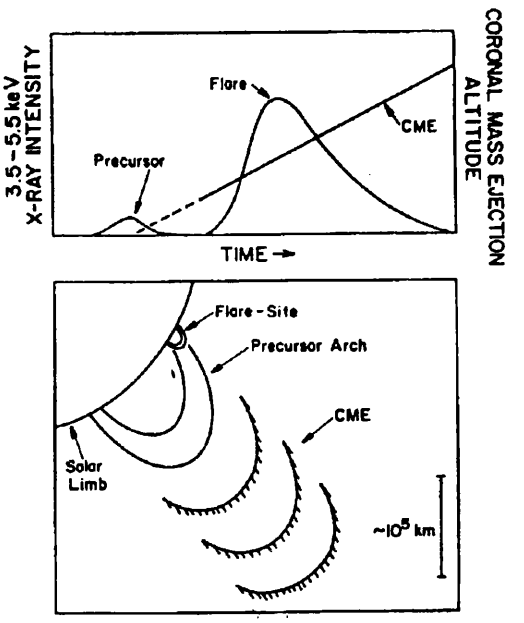

Figure 1.10: The graph on top shows the X-ray intensity from a precursor, and then from a flare, while also displaying the lift-off of a CME. Note that the CME is launched well before the flare (some tens of minutes). Underneath, we see how the flare appears at the foot of the arch.

Shocks and energetic particles

As we have seen, a fast moving CME can create a transient interplanetary shock by stacking up the slower moving material in front of it. Between 1979 and 1982, Sheeley *et al.* [80] investigated the CMEs observed by the Solwind spacecraft and the in-situ plasma measurements made by the Helios-1 spacecraft. They found 80 interplanetary shocks in the Helios data, out of which 50% could be definitely associated with a big, bright CME seen by Solwind. 24% were possible associations, and with 25% of the shocks, there wasn't enough data coverage to ascertain whether or not a respectable and suitably-timed CME might have occurred. This is strong evidence that most CMEs can produce a shock front that is measurable at 1 AU.

For many years it was believed that all solar energetic particles (SEPs) were accelerated by solar flares, part of Gosling's "solar flare myth" [26]. But since the discovery of CMEs, it is believed that most major proton energetic events result from particle acceleration occurring in the outer corona and in interplanetary space at shocks driven by fast CMEs [70]. These types of events show a gradual rise, perhaps over a day, and typically persist at high intensity levels for several days or more.

In contrast, there is a different kind of energetic particle event that shows a sharp, impulsive rise in its time profile, as measured by orbiting spacecraft at the Earth. These events are usually associated with solar flaring on the west side of the Sun, from where magnetic connection with the Earth is best. These impulsive events are usually of far less intensity and duration (only a few hours) than the gradual events. It can be said, therefore, that major particle events are most often of the gradual type which are associated with CMEs and shocks. Gosling [26] concludes that "all of the available observational evidence indicates that gradual events are the product of the shock acceleration of coronal and solar wind particles in interplanetary space".

An alternative theory of shock formation has been put forward by Bravo and Perez-Enriquez [12]. They re-examined the 49 CMEs that were confidently linked to interplanetary shocks by Sheeley *et al.* In doing so, they found that in most of those cases, a coronal hole was present within 30° of longitude of the limb where the CME was observed, and many were a lot closer than this.

From this evidence, they suggest that a shock is formed when a coronal hole undergoes rapid changes linked with solar activity, perhaps the ejection of a CME. Intermittent changes in the coronal hole's structure may lead to rapid changes in the characteristics of the solar wind emerging from the hole, including a sudden, large increase in velocity, as explained by Bravo [11]. This huge jump in speed could lead to the formation of an interplanetary shock, and the acceleration of particles to relativistic energies.

This theory is employed in chapter 5 when examining IPS maps during times of interplanetary disturbances.

1.5 Solar-terrestrial interactions

In the previous section I have attempted to describe some of the more important factors which influence the solar wind. Now, we shall investigate how these phenomena can affect the near Earth environment. This topic has become known as "space weather".

The Earth is protected from the worst affects of the solar wind by its dipolar magnetic field. This is distorted in shape because the solar wind pushes it on the sunward side (creating the magnetopause), and stretches it out on the other side (forming the magnetotail), to make the tear-drop-shaped magnetosphere, see `Figure 1.11` [73]. As the

solar wind flows at supersonic speeds, a shock wave, the bow shock, forms in front of the magnetosphere.

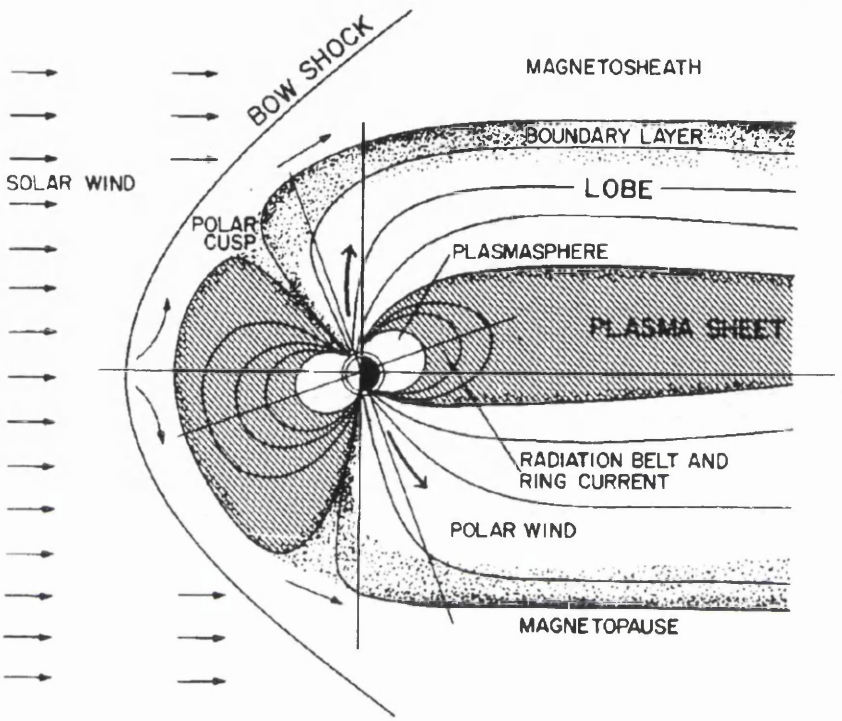

Figure 1.11: The structure of the magnetosphere, in a noon-midnight meridian cross-section.

With this arrangement, 99.9% of the incident ionized particles are deflected from entering the Earth's atmosphere. Most of those that enter do so at the poles, causing auroral displays and geomagnetic activity.

The aurorae (aurora borealis at the north pole, and the aurora australis at the south pole) are luminous phenomena in the upper atmosphere of the Earth, between 100 km and 1000 km, caused by solar charged particles that excite the atoms of the air. The colour of the curtain-like streamers can be green, red and blue, corresponding to emission lines from oxygen and nitrogen.

Some solar wind particles are trapped in radiation belts around the Earth, the Van Allen belts. These are doughnut shaped rings around the Earth, one about 4000 km above the Earth's surface, the other at 16000 km. Further up again, at 60000 km, a ring-current of electrons circles the Earth. All of these particles cause problems for orbiting satellites and spacecraft, but the conditions in the belts are well known and don't normally fluctuate

very much. Therefore, measures can be taken to withstand the dangers posed here. It is the intermittent nature of intense geomagnetic storms which poses the greatest threat.

We have seen that events at the Sun can cause temporary enhancements in the solar wind density, velocity and its population of energetic particles. When the changes in the solar wind are dramatic enough, this can lead to a geomagnetic storm, defined as a large decrease in the horizontal component of the Earth's magnetic field. The Ap index increases dramatically during a geomagnetic storm. Averaged over a planetary scale, Ap measures the fluctuations of the magnetic field about its normal diurnal drifts. **Figure 1.12** shows a huge increase in Ap on 23 March 1991, due to a severe geomagnetic storm caused by a strong interplanetary shock.

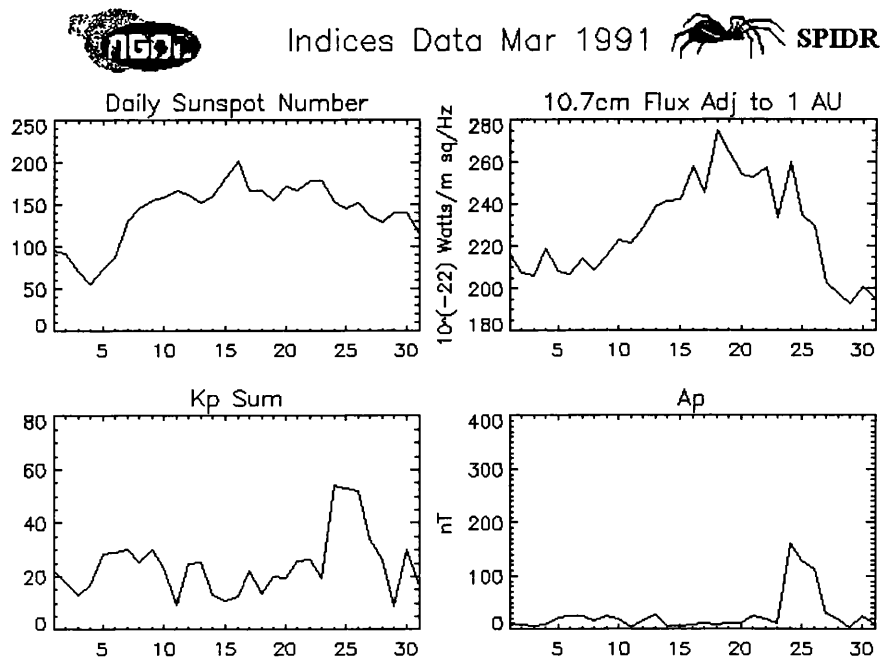

Figure 1.12: Provided by NGDC, these data for March 1991 include the daily sunspot number, the 10.7 cm flux, the Kp sum index and the Ap index. Note the huge jump in Ap on 23 March.

During a geomagnetic storm, high fluxes of energetic particles can severely damage satellites, by upsetting the electronics in an SEU (single event upset), as explained by Baker [3]. In a microelectronics circuit, an SEU is caused by an individual charged particle, usually a heavy ion, when it deposits enough charge at a sensitive portion of the circuit to change the state of that circuit, see **Figure 1.13**. The smaller a circuit, the more likely an SEU will occur. The trend for making integrated circuits smaller and faster is also

opening up the possibility for more SEU failures.

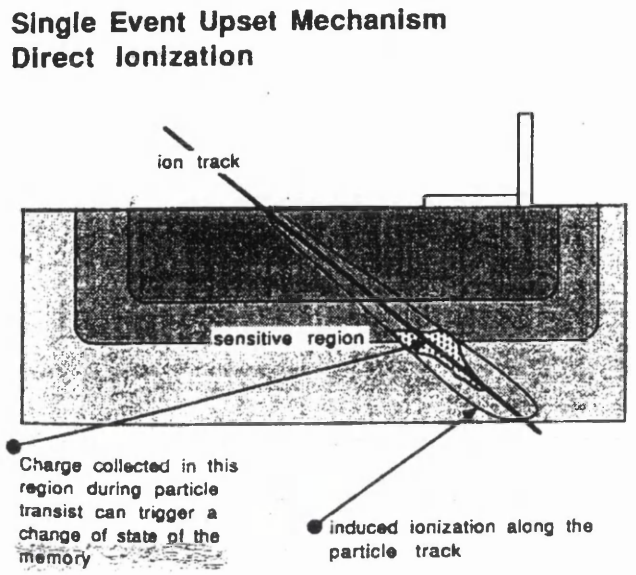

Figure 1.13: The mechanism of a single event upset in a microelectronics device. Often, the depletion region is the most sensitive to SEUs. In a flip-flop circuit, an SEU can cause a change of state, possibly leading to spurious commands in the satellite.

These anomalies can lead to spurious commands on satellite onboard computers, and possibly the disruption of communications with Earth. The worst case scenario would end with the complete loss of the satellite. Miniaturization of electronics and the smaller overall size of satellites means that modern satellites are increasingly vulnerable, especially as more and more satellites are sent into orbit.

In January 1994, the ANIK E-1 and E-1 communications satellites had major problems with attitude control, causing a huge, and very costly interruption in its communications services, see `Figure 1.14`. This failure has been attributed to greatly elevated populations of high energy electrons, as measured by the SAMPEX and GOES spacecraft. The solar wind speed measured by IMP-8 rose to $750\,\mathrm{km\,s^{-1}}$ during this time.

In January 1997, AT&T lost contact with its Telstar 401 satellite, again leading to expensive losses. During the March 1991 storm (`Figure 1.12`), the magnetopause was compressed by the shock wave from its nominal 10 Earth radii position to inside the 6.6 Earth radii geosynchronous orbit [49]. This led to huge increases in particle flux, and many spacecraft experienced difficulties. Thirty seven SEUs were reported for six geostationary satellites.

Figure 1.14: Some newspaper headlines after the failure of the ANIK E-1 and E-1 communications satellites, due to the elevated intensity of high energy electrons in the Earth's outer magnotosphere.

Geomagnetic storms can severely disrupt radio communications on Earth, due to disturbances in the ionosphere. Also, electrical power grids can be affected by GICs, geomagnetically induced currents [1]. In 1989, a severe geomagnetic storm left six million people without electrical power in Quebec, Canada [7]. The economic consequences of such a blackout are highly significant, and have prompted electric utilities to invest in research for developing means for protecting electric power systems against the effects of these storms.

Another danger from geomagnetic storms is for humans either working in space, or travelling in polar-crossing aircraft. Having adequate warning of dangerously high radiation levels is absolutely essential for their safety.

Often, days of high geomagnetic activity (Ap$\geq$30) will recur after $\sim$ 27 days, i.e., there is a 27 day periodicity in the occurrence of enhanced geomagnetic activity. As 27 days is approximately the rotation period of the Sun at low latitudes, this has been linked to coronal holes. The fast flowing plasma from these holes travels out into the IPM along a streamline, possibly forming a shock at the leading edge. This streamline rotates around to meet the Earth every 27 days. Here, the shock front can cause the increased geomagnetic activity. The link between coronal holes and geomagnetic storms has been

firmly established by Hewish [31].

The August 1972 events were investigated by Houminer and Hewish [39]. This period of intense geomagnetic activity and energetic proton events had been associated with solar flares. Using Cambridge IPS data, in-situ plasma recordings and Nagoya multi-station IPS velocity measurements, Houminer and Hewish put forward a convincing argument that the root cause of all the activity at the Earth was actually a coronal hole undergoing an eruption and producing a shock wave driven by high velocity coronal plasma.

Hapgood has investigated the 27 day recurrence of geomagnetic activity [28], and has concluded that the recurrence is very apparent during the declining phase of the solar cycle, and it is strongest for the even numbered cycles, i.e., there is a double solar cycle in the 27 day pattern of activity.

A southward-pointing field in the solar wind is known to favour magnetic reconnection processes on the Earth's frontside magnetosphere which leads to increased geomagnetic activity [77]. Therefore, it is usually only when there is a southward IMF (interplanetary magnetic field) that the strongest geomagnetic storms can occur.

For ground-based systems, orbiting spacecraft and for people in high-risk locations (in a spacecraft, on an EVA (extra-vehicular activity), or in a polar crossing flight), it is of extreme importance to be able to predict the arrival of shocks, large populations of energetic particles and the onset of geomagnetic storms. There is increasing technological ability to gather information for the science of space weather forecasting, with more satellites observing the Sun and taking measurements in the IPM and geospace. IPS too can play its part in this field, by providing all-sky maps of density and velocity in the inner heliosphere.

If geomagnetic storms are successfully predicted, then satellites in danger can take precautionary measures by carrying out evasive manoeuvres or by going into "sleep" mode. Another, more robust approach, is to better understand the kinds of disturbances that occur in near-Earth space, and then to build satellites that are shielded enough to withstand these effects.

1.6 Conclusions

This chapter has reviewed the topics needed to fully understand the aims and achievements of this project. The history of IPS has been explored, along with a short survey of some IPS facilities around the world. An insight into the theory of IPS revealed how it can be used to probe the solar wind. This data can be seen in context when the solar wind itself and its causes and effects are appreciated.

Chapter 2

The data set

" When I was young, I used to scintillate,
Now I only sin till ten past three."

Ogden Nash

2.1 Introduction

The project is centred around a large data set, so it is essential to understand how and where the data were collected, and how they were subsequently processed. This chapter describes in detail the Cambridge IPS array, the structure of the data produced by it, and how these data were reduced to the analysis stage.

2.2 The 3.6 hectare Cambridge IPS array

All the data for this survey were taken by the Cambridge IPS array between April 1990 and November 1994. On a research visit to Cambridge in May 1997, Dr Woan and I examined the telescope in detail. Though presently out of commission, it was still possible to make many important measurements, characterizing the shape and orientation of the array. This is very important for knowing in what direction the telescope was "looking".

There are many published descriptions of the IPS array, from its original format, through the many modifications [36], [65].

The array operates as a radio interferometer. The basic unit is a full-wave dipole

antenna, of length 3.68 m, therefore it is in resonance at 81.5 MHz,

$$\nu = \frac{c}{\lambda} = \frac{3 \times 10^8 \,\mathrm{ms}^{-1}}{3.68\,\mathrm{m}} = 81.5\,\mathrm{MHz}\,. \tag{2.1}$$

The antenna turns the incident radiation into a corresponding electric signal. It is an effective absorber of radiation polarized parallel to the dipole, over an area defined roughly by the length of the dipole and a width of $\lambda/2$ centred on it. Each dipole has an impedance of 2500 Ω. Groups of eight dipoles are arranged along a resonant open-wire feeder, giving a resultant impedance of

$$\frac{2500\,\Omega}{8} \simeq 300\,\Omega\,. \tag{2.2}$$

The array can be "steered" in declination to respond to radiation from a particular direction by introducing the appropriate phase delays between dipole rows before their outputs are combined.

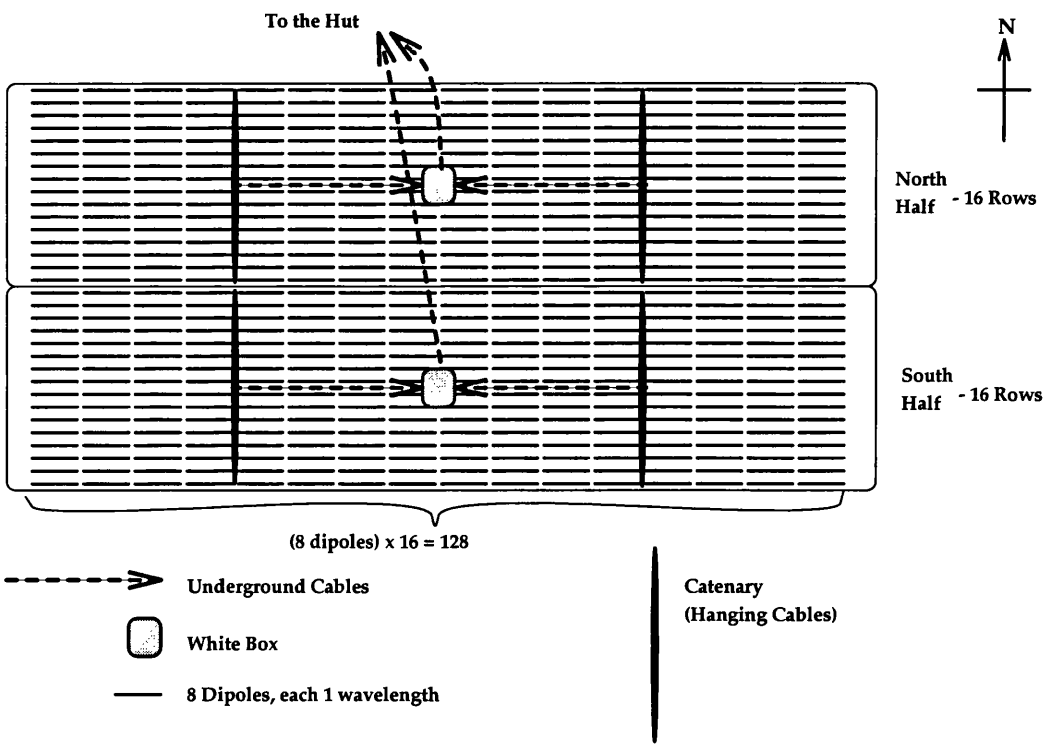

Figure 2.1: Layout of the Cambridge IPS Array, at Lord's Bridge, Cambridge.

Altogether, the array consists of 4096 full-wave dipoles. As can be seen in Figure 2.1, these dipoles are arranged in 32 rows of 128 dipoles per row. The array is split up into

a northern half of 16 rows, and a southern half (16 rows), to make a north-south phase-switching interferometer. To collect together the signals from each dipole in the correct manner involves precise wiring to ensure that the phase is properly recorded.

With a spacing of 0.65λ between the rows, there is a total geometric collecting area of 36,055 m^2. This is about half the area of the Arecibo radio telescope in Puerto Rico, the largest radio telescope in the world in terms of collecting area.

There are 128 dipoles along each row, separated from electrical contact by insulators. The dipoles are attached to wooden posts, and in each row, there is one wooden post for every eight dipoles. The dipoles are also supported from above by a cable which runs the whole length of the row. From each dipole runs an open-wire feeder, linking together sixteen dipoles into a pre-amplifier. There are therefore eight amplifiers along each row.

Cables carry the amplified signal from each amplifier to a catenary, see `Figure 2.1`. There is one catenary for each quarter of the array. From the middle of each catenary, a bundle of cables runs underground to one of the two white boxes on the N/S centre line of the array. The white boxes therefore collect all of the signals coming from the 16 rows in their half of the array.

From there, the 2×16 cables are sent to the wooden hut at the side of the array, where they are fed into Butler matrices [15]. The Butler matrices perform an action which is basically the analogue equivalent of a fast Fourier transform. For each half of the array, 16 rows are phase shifted in 16 different ways to get 16 beams on the sky. This is done by using selected cable lengths, which are all multiples of $\lambda/16$, and are chosen so as to insert a constant phase difference of $2\pi n/16$ between adjacent rows.

Now we have 16 beams on the sky, at different pre-set declinations, covering the sky from approximately $-10°$ to $80°$. The array observes at meridian transit, hence taking one sidereal day to survey the whole sky. The declination of peak response for each beam is given by

$$\delta_0(N) = 52.16° + \arcsin\left(\frac{N-10}{10.4}\right), \tag{2.3}$$

where the beam number, N, goes from 1 to 16. $52.16°$ is the latitude of the Cambridge array [83].

Inserting a phase gradient in the north-south direction across the array has the effect of shifting the whole pattern by half a beamwidth. This means that intermediate declination beams can be observed. For the purposes of this survey, it was not done, but it was

employed at other stages, e.g. in the 1978-81 survey which produced the list of sources that is used in the current project [65].

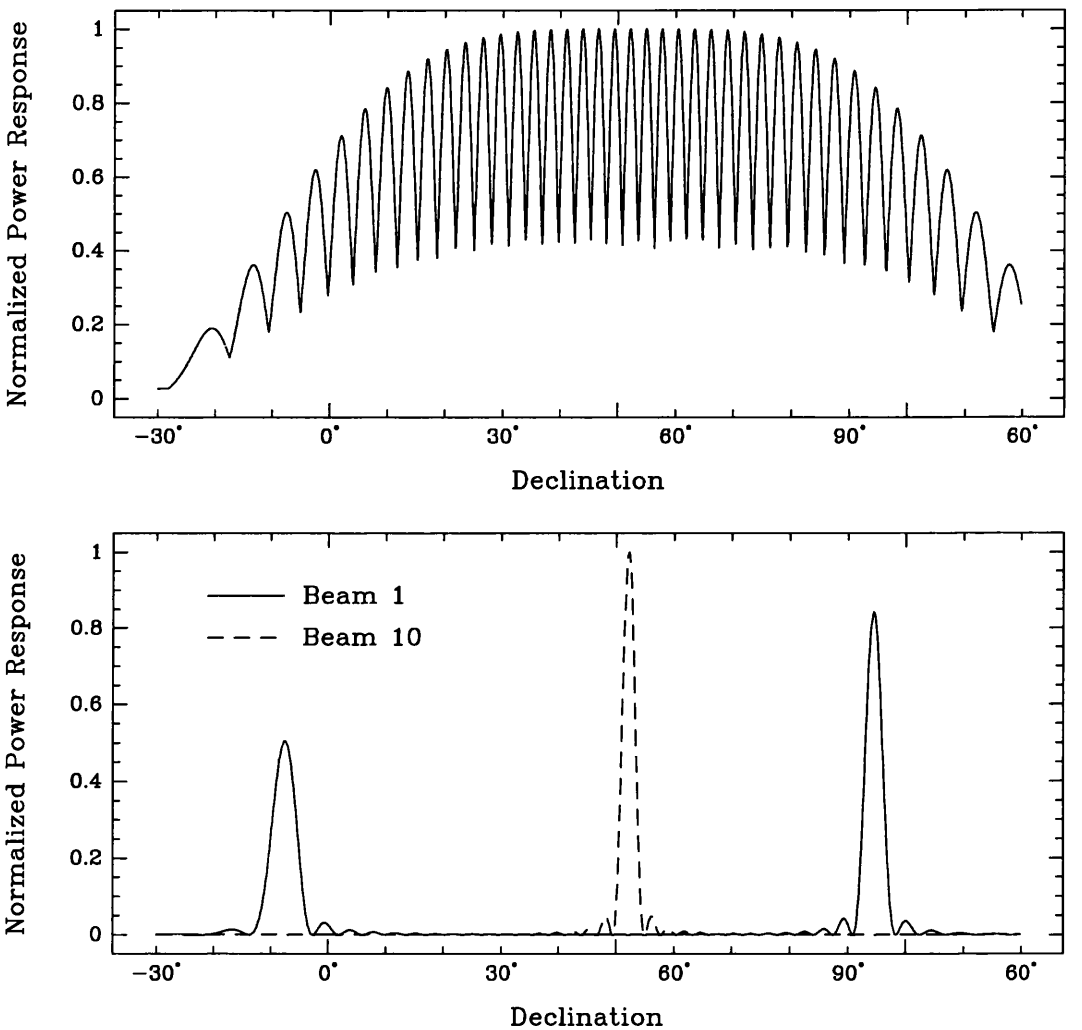

Figure 2.2: The power response of the Cambridge IPS array as a function of declination. In the second graph, we can see that the main response of beam 1 is at −8°, but that it also has a secondary response 102° away at +94°.

Figure 2.2 shows the response pattern for each beam, including the secondary responses of some of the beams [82]. Also, the intermediate beams are included.

There is a horizontal reflecting screen $\lambda/4$ under the dipole array. It has been shown [88] that the declination power response, D, of the antenna follows that expected for an array of dipoles at $\lambda/4$ above a flat, horizontal reflecting screen, i.e.

$$D = \left(4D_0 \sin^2\left[(\pi/2)\cos\phi\right] \frac{\sin^2(16\psi)}{\sin^2\psi}\right)^2, \tag{2.4}$$

where

$$\psi = \frac{\pi d \sin\phi}{\lambda} + \frac{(N-10)\pi}{16}\,, \tag{2.5}$$

$$\phi = 52.16 - \delta\,, \tag{2.6}$$

d is the spacing between the rows and D_0 is the peak response. It is this function that is plotted out in `Figure 2.2`.

The time taken by each source to transit is dependent on its declination, δ. The half power transit time, $T_{\rm tr}$, in seconds is

$$T_{\rm tr} = \frac{107}{\cos\delta}\,, \tag{2.7}$$

so sources at higher declinations will take longer to transit.

At the next stage, each signal is mixed with a local oscillator signal of frequency 92.2 MHz. This shifts the frequency of the beam signals down to an intermediate frequency of 10.7 MHz. The 2 × 16 I.F. signals are then sent by underground cable to the laboratory.

At the laboratory, the beams from the north half of the array are interfered with those from the south, using phase-switching receivers, giving sine and cosine output signals in phase quadrature. These outputs are combined in a "total-power scintillometer" [24], which includes a high-pass filter that only allows through the scintillating signal (and receiver noise). These signals are squared, added and then integrated in software with a time constant of 10 s. The output is now proportional to the mean square scintillating flux density, multiplied by the square of the antenna power response. This output is recorded by computer on $5\frac{1}{4}''$ disks.

2.3 The original data format

The survey was carried out over 1687 days, from 4 April 1990, to 16 November 1994. A day's worth of data (24 hours) fitted conveniently onto one disk, so there is one disk per day, each containing 8 files of 3 hours duration. The name of each file is of the format:

`a_j49576.499`

where:

49567 is the Mean Julian Day Number (MJDN)

.499 is the fraction of the day, i.e. 0.499 refers to just before 12pm.

Before any detailed analysis could be done, the data set had to be prepared from its primitive state into a readily-usable format. The first task was to transfer all of the data from the $5\frac{1}{4}''$ disks onto the hard drive of a Sparc workstation.

This was done using a personal computer, by FTP (File Transfer Protocol). It involved inserting every individual disk into the PC and then transferring the information across to the Unix cluster. Each disk took about 5 minutes to process, taking care that all had gone smoothly, and noting any missing or corrupted data. The task of going through all the disks took about a month to complete.

Some processing software already existed, written in Pascal for the PC, but it was decided to use the C programming language here, due to its greater power and portability, and my own previous experience. Nevertheless, some of the old Pascal programs were used extensively to devise the structure of the new C programs.

All the a_j files begin with a 256 byte header containing important information which describes the data in the file. This header is split up as follows:

- Selsis header - 128 bytes, containing technical detail, as defined in the Selsis handbook [51], but not relevant to how the data are organized (SEL is the Space Environment Laboratory in Boulder, now the Space environment center (SEC), where some of the old IPS software was written).

- IPS Header - 128 bytes altogether, described in `Table 2.1`.

Interpreting the header was essential to understanding the structure of the data set as a whole. It provides parameters about the data contained later in the file, such as the starting and finishing times, and the structural layout of the data. A program was written which could extract the header information from the file. If the information was organized as it should be (according to `Table 2.1`), then it was a good indication that the file was not corrupted.

As soon became apparent, the method of storing numbers is different for the two machines. The PC uses a low-byte high-byte combination to store 4 byte numbers, while the workstation uses high-byte low-byte. This conflict was solved by reading in the numbers byte-by-byte, then recombining them in the correct format.

Type	Name	Comment
LongInt	MJDN	Mean Julian Day Number
LongInt	RT_Start	Initial time index, in jiffies [Note: 18.2 jiffies = 1 second]
LongInt	RT_Finish	Final time index
Word	TicksPerSample	Sample every 10secs, so TicksPerSample = $10 \times 18.2 = 182$
Word	Scan_Length	18 channels, 4 bytes per channel, plus time tag of 4 bytes Scan_Length = $(18 \times 4) + 4 = 76$
Word	Num_Scans	Number of scans in a 3 hour file $= 6 \times 60 \times 3 = 1080$
Word	Num_Channels	Number of channels = 18
Integer Array	Channel_List	Code describing the channels
Boolean	DIO_Present	False
Byte	Pack	Pack to end with Zeros
Word Array	PackInt	Pack to end with Zeros

Table 2.1: The IPS Header

2.4 The new format

Once it was certain that the original files were not corrupted, and that the format of the headers, number storage etc. was fully understood, the next task was to rewrite the whole data set in a new format, appropriate for a Unix environment, and more easily accessible for further processing.

The new files were produced by the program `days_head.c`. This takes a list containing the names of all the a_j files as input, and concatenates up to 8 (or possibly more) files per day, to make a binary output file for each day, called `d4****.raw`. The `4****` part represents the five digit Mean Julian Day Number (MJDN) of the observations.

This output file contains a header (64 bytes), which is composed of:

- MJDN (long, 4 bytes)
- Number of Scans for the day (long, 4 bytes)
- Channel code, which indicates the type of channel list in which the data were recorded (long, 4 bytes)
- The rest of the header is filled with zeros.

The channel list explains the way in which the information was fed out through the different channels to the recording computer, and records times in the data set when gain changes can be expected, due to the reconfiguration of the data requisition hardware.

The data are stored in scans of 76 bytes in size. Each scan contains the time-tag (fraction of the day, in hours, represented as a 4-byte number) and the outputs of the 18 beams (each a 4-byte number). Only 16 actual beams are recorded by the telescope. The last two "beams" recorded are actually containing diagnostic information that is not strictly relevant to the current analysis.

$$(1 + 18) \times 4 = 76\,\text{bytes}\,. \tag{2.8}$$

A "scan" is generated every 10 seconds, so a typical day will have $6 \times 60 \times 24 = 8640$ scans, thus making the total size of the average d.raw file $64 + (76 \times 8640) = 656704$ bytes. In practice, most days have a few extra or fewer scans due to variations in timing, and sometimes the data can be corrupted.

When the program had completed all the d.raw files, some of these new files were checked with a hexadecimal editor. They were exactly as expected, so only the new d.raw files were used in subsequent analysis.

2.5 Identification of sources

To relate the telescope output to particular sources in the sky, and later to make precise maps, it is essential to know where exactly the telescope is pointing at any time. The precision in declination is limited to the size of each beam in the sky, but if a source appears in two adjacent beams, it is possible to calculate better its declination from the relative strength of the signal in each beam. This method was employed in an algorithm used by Purvis *et al.* in their IPS survey [65]. The size of each beam has previously been discussed `Section 2.2`.

The accuracy in Right Ascension (RA) is dependent on the array geometry, and comes from `Equation 2.7`. At the equator, the transit time for beam 2 is 107 s. Therefore, the width of the beam in RA is

$$107\,\mathrm{s} \times \frac{360^\circ}{24 \times 60 \times 60\,\mathrm{s}} = 0.45^\circ = 27'. \tag{2.9}$$

The issue here is to know exactly where the telescope is looking, i.e. is the line of beams on the sky that the telescope sees exactly co-incident with the local meridian? Unfortunately the telescope is slightly skewed, so corrections had to be made for this, as for other matters dealt with in the next section.

2.5.1 Correcting for precession and skewing of the array

The original list of sources used for previous surveys [65] was given with epoch 1950 co-ordinates, so it needed to be precessed to the epoch of the present data for comparison. Also, because our survey took place over 5 years, the sources had to be precessed over the course of this period. A precession-nutation function, called `sla_prenut`, was taken from the STARLINK software library, SLALIB, to do all this.

Another factor to be taken into account is that the array is not quite on the Greenwich Meridian. Therefore, everything will not transit at their sidereal time in RA, but earlier than this. As the telescope's site at Cambridge (Lord's Bridge) is $0^\circ 2' 26''$ East of Greenwich, the sources transit $2 + (26/60)) \times 4 = 9.73$ seconds early.

Also, as mentioned earlier, the array is not perfectly aligned east-west, or in the other 2 dimensions. The tiny deviations were carefully measured using a theodolite, a measuring tape, a compass and the reference point of the adjacent One Mile Telescope track as a perfect east-west line. `Figure 2.3` shows how the array should be, in perfect alignment with the cardinal points and the horizon. The reality is shown in `Figure 2.4`, with the telescope skewed about the three principle axes.

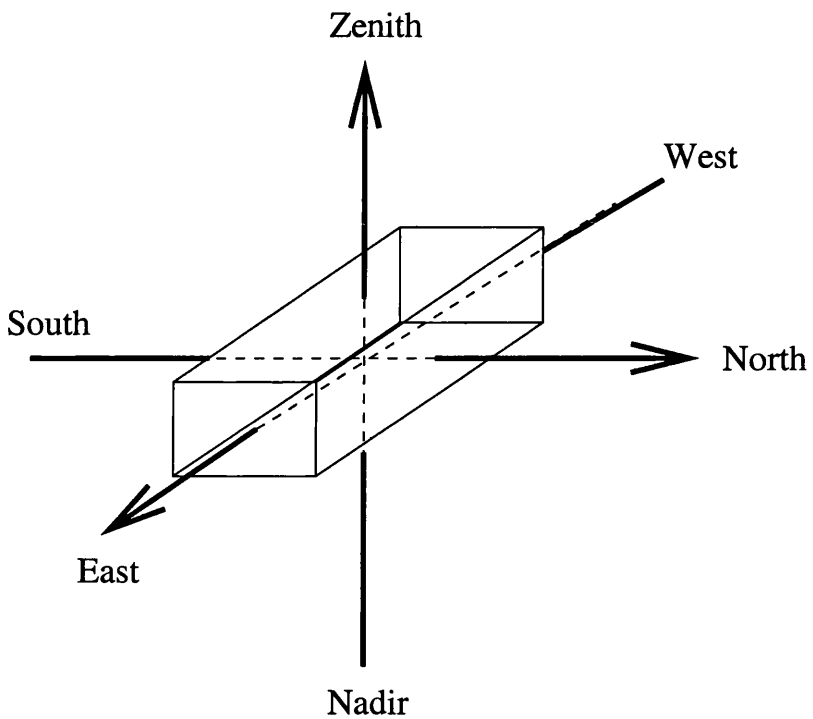

Figure 2.3: Geometry showing the array as it would be if it were perfectly aligned to the cardinal points and to the horizon.

These slight angular deviations were used to set up rotation matrices. The co-ordinates of all the sources were rotated using these matrices in a program `src_out.c` to make a new, corrected source list. This list predicts the exact time that a source will transit, so it is used when labelling any source. This program needed to be carefully tested and the final tests showed that the sources seen in the telescope output were consistent with existing low-frequency sky surveys.

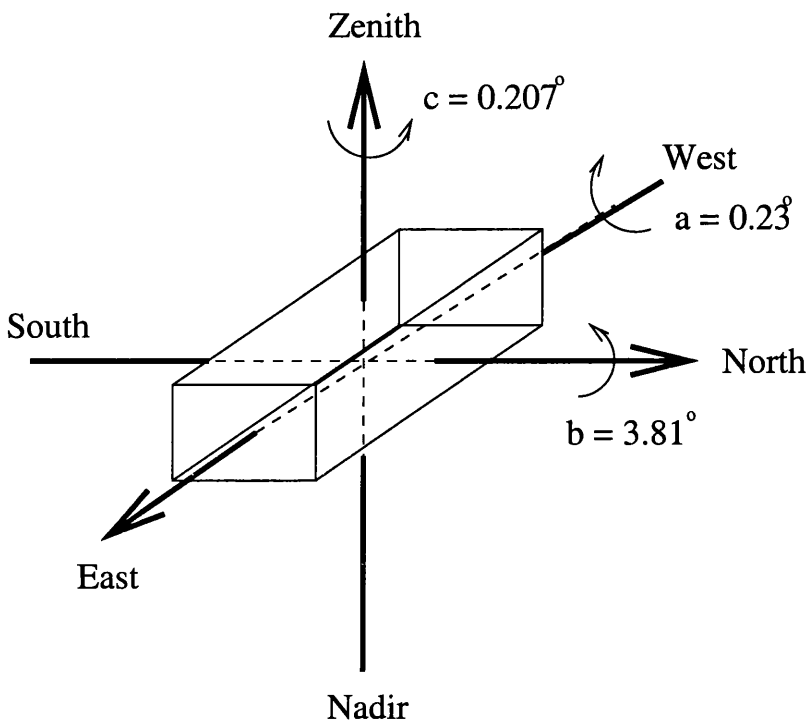

Figure 2.4: Geometry showing the array as it is, skewed from perfect alignment.

2.5.2 Plotting the data for a set time period

The most user-friendly way to present the raw binary data was in plots of beam output against sidereal time. Initially, these plots were done using "gnuplot", but soon I switched to "pgplot", as it is far more powerful, especially in terms of axis labeling. Also, it could be called from a C program, which is where most of the processing was done

The original version of pgplot uses routines written in Fortran, but recently a special version was made which is callable from C. The C-binding information, and the software itself was downloaded from the website at Caltech, noting the differences between the manner in which Fortran and C handle parameters and arrays for functions, and how the function itself is called.

Because the sidereal day is $\sim$ 4 minutes shorter than the civil day, the daily `d.raw` files start at different sidereal times as the year progresses. This increases the complexity of the programming. For the final resulting program, `plotall_pg.c`, the input parameters are the MJDN, the Beam Number, the Centre RA (in sidereal time), and the width in RA that we want to plot. The output is then a PostScript (PS) file of the graph of beam output for the time required. An example is in `Figure 2.5`. The sources are labelled

with their name, and their ΔS (mean scintillating flux density, in janskys, at 90° solar elongation).

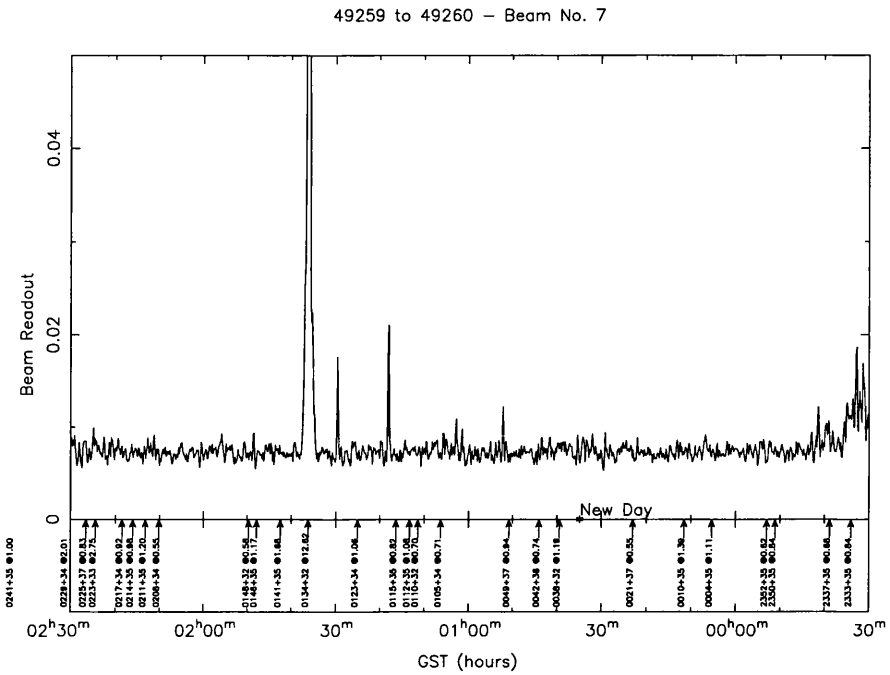

Figure 2.5: A typical plot produced by `plotall_pg.c`, running over two hours from one day to the next, through 'midnight' in RA. The strong source (labelled 0134+32), 3C48 can easily be seen. The two smaller adjacent peaks are sharp interference peaks. Most of the other sources in the plot are below the noise level, thus indistinguishable.

`plotall_pg.c` can look into the day before or after the day with the central RA, but no more days than this. The maximum width is 3 hrs, but this can be extended by enlarging the storage arrays. This program can handle the situation when the time goes from 23^h, through 0^h, and onwards into the next day. It also converts from the fraction of a day to sidereal time, which is important for finding the correct source at its transit time, i.e., when it crosses the meridian. It labels the output graphs at the bottom with the source names, taken from one of the lists of corrected co-ordinates, `source_4****.txt`. There is a different source list for every 200 days, to deal with precession over the course of the survey.

2.6 Gray scale plots over many days

2.6.1 Gray-scaling the beam outputs

A grey scale map of the beam outputs over a number of days is a useful diagnostic for locating sources. Pgplot has a grey scaling function that was used in the program `grey2.c` to produce informative diagnostic plots such as `Figure 2.6`. Each day is shown as a horizontal strip running from 0^h to 24^h in GST (Greenwich Sidereal Time). In this strip, there are 8640 sections for each of the 10 s data outputs. Each section is given a grey scale value corresponding to this output, where light grey means the output is at the background level, and black is a very strongly scintillating source.

When the Sun is on or near the meridian, it is such a strong radio source that it appears in all of the beams. Therefore, the Sun can be seen on the grey scale plot for any beam. Throughout the year, the Sun's sidereal time of transit will change, so that it appears almost as a perfect diagonal trace on our grey scale plots. It appears in `Figure 2.6` at a GST of 2^h at the beginning of the plot, and it then moves westwards in GST and 365 days later, it is again seen at 2^h.

As these plots use sidereal time, any scintillating radio source will appear at the same position every day, to form a dark vertical line on the plot. Of course, the intensity of this line will change from day to day, depending on the amount of scintillation measured for that source, and over the course of the year, according to its elongation from the Sun.

At $\sim$ 6^h25^m in `Figure 2.6`, a strongly scintillating source, `0624-04`, is seen. It is noticeably darker when near to the Sun, and it is less intense when far from the Sun. This behaviour is well understood [25], and is referred to as the $A(\epsilon)$ curve, where A is a measure of the scintillation for the source relative to its mean level, and ϵ is the elongation of the source from the Sun. This is further discussed in `section 3.2.7`.

For beam 1, `Equation 2.3` shows that the declination of peak response is at $-7.767°$. The transit time (`Equation 2.7`) is therefore 107.99 s. So on the grey scale plot, the width of the trace for any source in this beam should be under two minutes. This is consistent with the width of `0624-04` in `Figure 2.6`.

Spurious spikes of interference are apparent, many of them followed by an undershoot showing up in white. Interference is particularly apparent at the middle of the day, i.e. near to the Sun, because this time corresponds to a maximum in human activity, e.g. the

switching on of electrical equipment and the passage of cars. The horizontal white strips correspond to missing data.

There are two very strong sources that are also seen in all the beams. Cassiopeia A is seen at approximately 23^h30^m. It is the brightest radio source in the sky at 81.5 MHz, other than the Sun. Cygnus A (of comparable brightness) is at 20^h. Both are too strong to be useful for day-to-day IPS studies as they usually saturate the receivers. Their traces are very wide on the grey scale plots, with sidelobes. At certain times, e.g. from approximately 48081 to 48088, they both appear to disappear from the plot. In fact, at these times, they're probably overloading the IPS receivers.

Every 6 hours, the beams are decorrelated for about three minutes, so that the telescope isn't looking in any particular direction. The signal received at this time is a measure of the system noise, and is useful for later analysis. There are no scintillating sources to be seen at these times, and it appear as a bland, whitish section, with well defined dark sides, e.g., just after 18^h in `Figure 2.6`. The dark sides are because of a spike before and just after the decorrelation occurs. There are other decorrelation events after 0^h, 6^h and 12^h.

At 14^h10^m there is a strong, broad source. Because it takes so long to transit, it must be a high latitude source. For example, a source in beam 15 takes over 11 minutes to transit (`Equation 2.7`). This source is actually in the secondary response of beam 1, so, its true declination is not $-7.767°$, but 102° away from that, at 86° in declination, at the other side of the pole, as seen in `Figure 2.2`.

There is a strong source at this position, `0221+80` or 4C77.03, which has a mean scintillating flux density at 90° solar elongation of 3.62 Jy, according to the survey of Purvis *et al.* Note that the $A(\epsilon)$ curve is opposite to what would be expected for a source in Beam 1. If the trace for it were slid from 14^h10^m back to 12 hours before that (where it actually is), at 02^h10^m, then the $A(\epsilon)$ curve would indeed show stronger scintillation nearer the Sun, and weaker scintillation away from the Sun.

`Figure 2.7` plots out beam 14 for the same time period. The Sun appears in exactly the same position. The sources take about 6 minutes to transit. This makes it appear that there are more sources, and that they are stronger. This is not necessarily the case. In fact, at such a high declination, 75°, the area in the sky covered by this beam is much smaller than for a lower declination beam.

Grey scale maps such as these have been generated for all the beams, for the whole

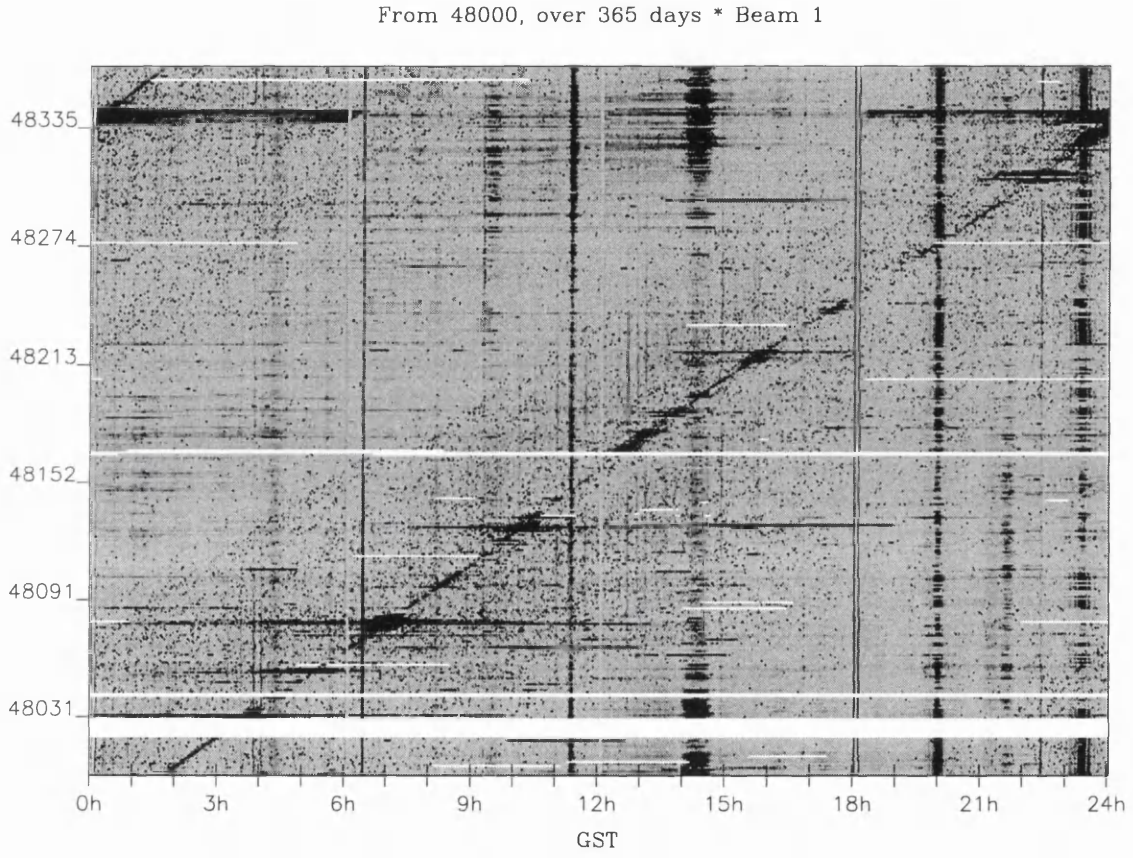

Figure 2.6: Made with the program `grey2.c`, this plot reveals many scintillating radio sources over a period of one year, for beam 1. The date is represented on the vertical axis, in MJDN (Mean Julian Day Number). The date runs from 48000 at the bottom (19 April 1990) to 48365 at the top (19 April 1991). The time of day is shown on the horizontal axis, in GST (Greenwich Sidereal Time), going from 0^h to 24^h. In the grey scale plot itself, black represents a strongly scintillating source at that GST, on that day, and light grey represents the background. The sources are the uneven darkened lines running vertically up. The Sun's trace is the diagonal line, as it moves westwards in GST as the year progresses. There is a slight wobble in this diagonal trace, which is explained by taking the Equation of Time into account.

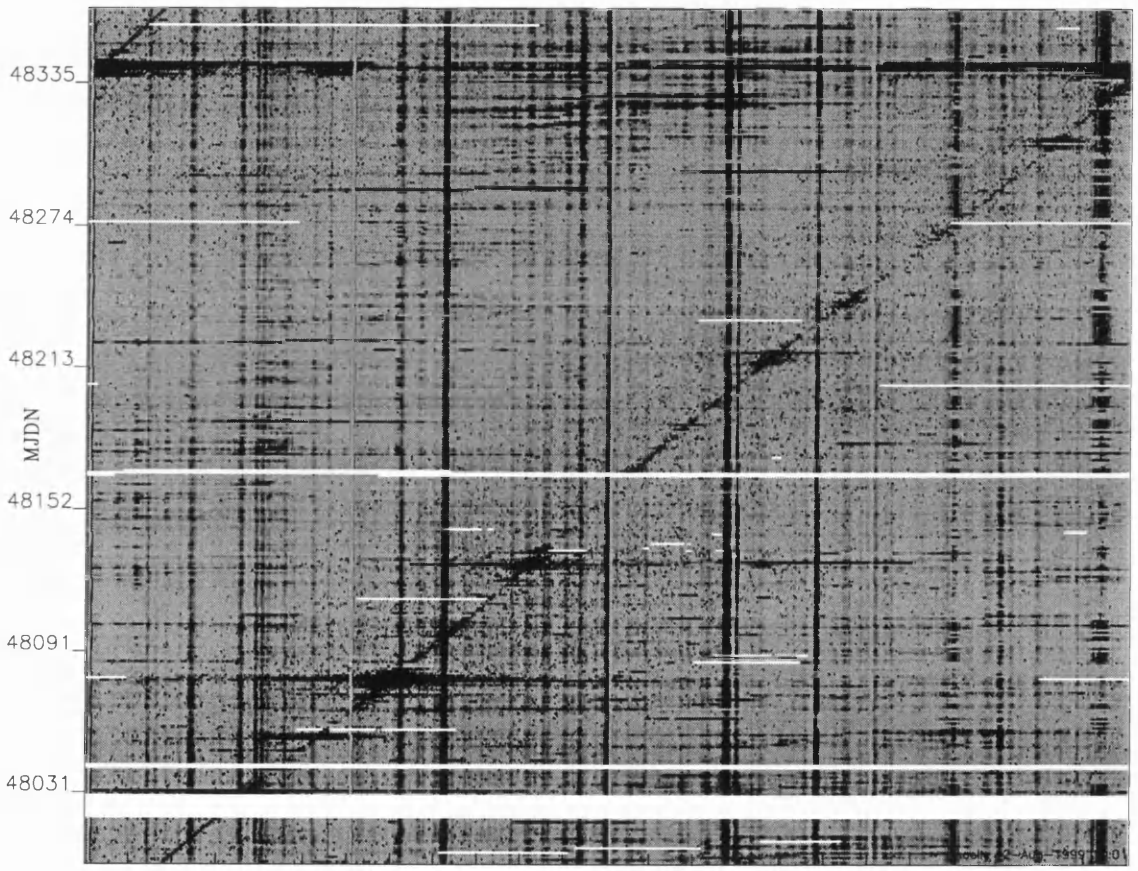

Figure 2.7: For the same time period as `Figure 2.6`, this plot shows beam 14. The higher latitude sources take much longer to transit.

course of the survey. They have been an extremely helpful diagnostic during many stages of the analysis. For example, to check when there were gaps in the data, to determine roughly the elongation of a source on a particular day and to see how badly the data were affected by interference and/or any changes in the gain of the system. From November 1993 to June 1994, the second Cambridge pulsar search [82] was carried out with the IPS array. This necessitated the loss of many days for IPS studies, as can be seen by the many gaps in the grey scale plots for this period.

They have also revealed a slow deterioration of the array's performance, and of the radio environment. A significant degradation is clearly seen towards the end of the survey.

2.7 Concluding remarks

The origin of the data for this survey has been well studied and understood. The data set itself has been processed in preparation for the subsequent analysis, and this processing has been checked and verified by the extremely useful grey scale plots.

Chapter 3

Mapping the IPM

"Do I dare
Disturb the universe?
In a minute there is time
For decisions and revisions which a minute will reverse."

T.S. Eliot - The love song of J. Alfred Prufrock

3.1 Introduction

The production of density enhancement maps (g-maps) and velocity maps is one of the most fundamental parts of this project. The IPS technique is intrinsically noisy, so it is important to extract as much information from the scintillation data as possible. Unless all the major factors that affect the measurements are taken into account, the resulting analysis will not be useful.

The disturbance factor, g, for any particular source on a chosen day, describes the amount of scintillation being experienced by the radio waves from that source, as they travel through the IPM. g would be:

~ 1 for a source whose radio waves are experiencing normal, average scintillation

< 1 for waves undergoing decreased scintillation

> 1 for waves experiencing enhanced scintillation.

When many sources across the sky are observed during a day, a map can be plotted using each individual g at each source's position. After some interpolation and smoothing,

this map can reveal areas of sky showing similar scintillation. As shown by Tappin [89], g is related to the electron number density, n,

$$g \simeq \left(\frac{n}{9}\right)^{0.52}, \tag{3.1}$$

where the units of n are cm^{-3}. We can thus infer the large-scale density structure of the solar wind.

Of course, these maps can only show a 2-D projection of a 3-D structure. It is therefore important to know where along the line-of-sight to a source that most of the scintillation occurs. This problem has been well modelled by Woan [97], whose IPS weighting function shows the maximum contribution occurring in a shell around the earth, of radius 0.5 AU, as shown in `Figure 3.1`. It is the material in this shell that causes most of the scintillation. This problem is further discussed in `Section 5.2`.

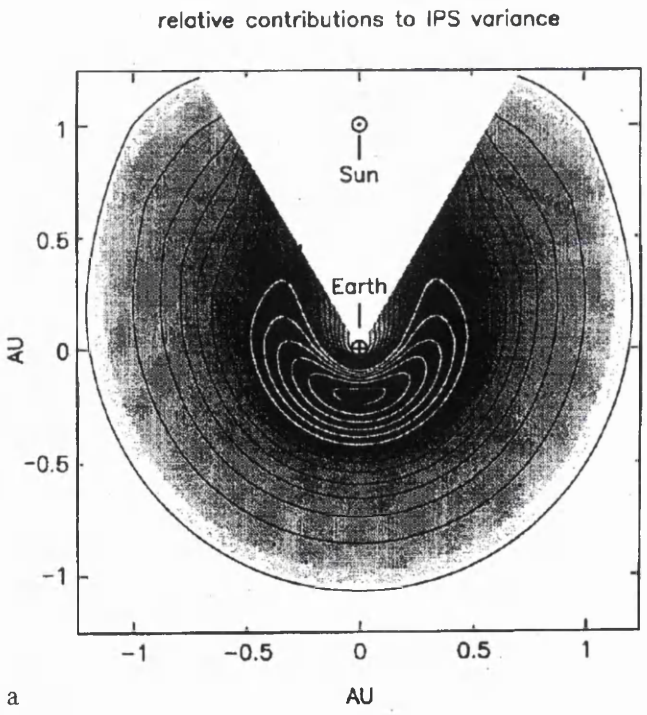

Figure 3.1: The IPS weighting function, $K(r, \epsilon)$ is plotted out for a point at a distance r from the Sun at solar elongation ϵ. As seen by an IPS instrument on Earth, most of the scintillating material along a line of sight to a source is concentrated in the darker areas. This can be taken to be a shell around the Earth of radius 0.5 AU. Any source that is within an elongation of 30° from the Sun is excluded, due to the strong scattering that happens there.

The velocity, v, is calculated from measuring the timescale, τ_s, over which the scintillation occurs. Knowing the typical scalelength, a, of the fluctuations, we can use the

timescale to get the velocity of the wind. This scalelength is estimated at ~200 km, so the velocity is indirectly proportional to the timescale,

$$v = \frac{a}{\tau_s}, \tag{3.2}$$

$$v \propto 1/\tau_s. \tag{3.3}$$

3.2 Steps involved

The scintillation enhancement factor, g, is expressed as the square root of the ratio of the observed, A, to the expected, A_E, rms scintillating flux density,

$$g = \sqrt{\frac{A}{A_E}}\ , \tag{3.4}$$

for each source on any particular day.

A number of stages are needed to extract daily g-maps from the raw data.

3.2.1 Averaging over the whole survey

The expected scintillation, A_E, is derived from two elements: the average scintillation of the source over the whole survey, and the manner in which the source behaves as its solar elongation, ϵ, changes during the course of the year.

Using the program `clean2.c`, a file was created which stores the average of each time slot along each beam over all the 5 years of the survey. This averaged file, called `THE.avg`, was subsequently used to extract the expected scintillating power, as a function of ϵ, for each source.

`THE.avg` was made as follows. The IPS array outputs one data point per beam every 10s. Therefore, the day is divided up into 8640 bins for each beam, each 10s wide.

$$6 \times 60 \times 24 = 8640. \tag{3.5}$$

When a data point is dropped into the appropriate bin, it is added to the total there. `clean2.c` employs a certain degree of interference rejection before allowing any particular data point to be used in calculating the average. Before being accepted into a time slot bin, each point of raw data is passed through a simple interference filter which gets rid of sporadic spikes of interference which have nothing to do with the scintillating signal.

This filter depends on the square-gradient of the time series,

$$[f'(x_t)]^2 = \left[\frac{f(x_t) - f(x_{t-1})}{x_t - x_{t-1}}\right]^2 , \tag{3.6}$$

where $f(x_t)$ is the value of the time series at time x_t. The data point is rejected if

$$[f'(x_t)]^2 > (f')^2_{\max} , \tag{3.7}$$

where $(f')^2_{\max}$ is an empirically set specified threshold. Once all the days have been processed, the collecting bin for each time slot is normalized by the number of observations it contains. The more data points within a particular time slot, the better the resulting averaged profile.

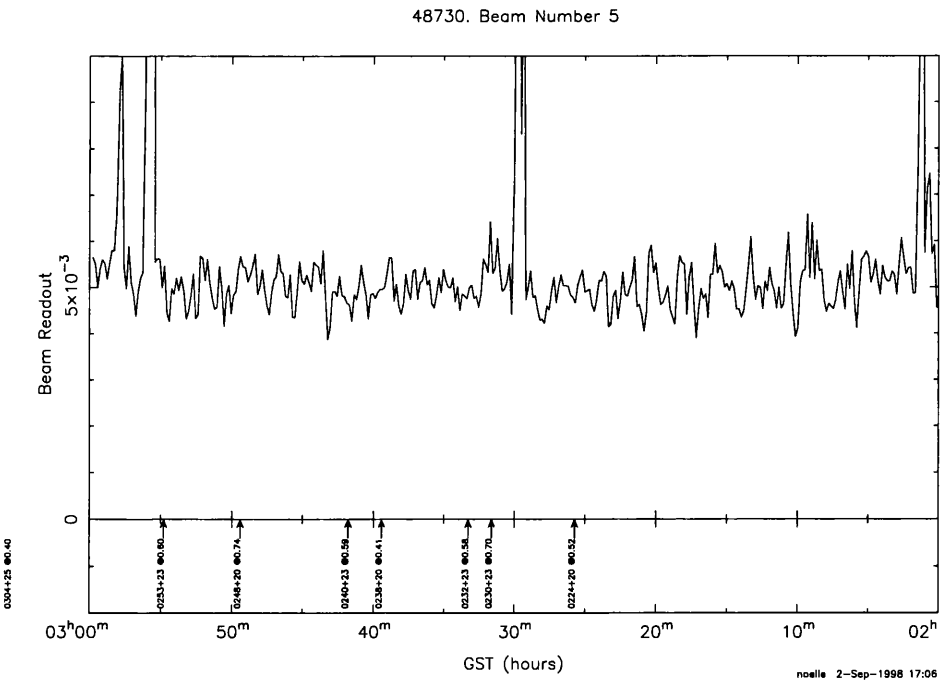

Figure 3.2: A one hour section of raw data from a typical day for Beam 5.

Figure 3.2 shows the output for one hour from beam five on a typical day. The individual sources are named from the original survey of Purvis *et al.* [65]. Interference, noise and the intrinsic scintillation make it difficult to determine the type of signal being received from each of the sources, i.e. whether there is enhanced or decreased scintillation.

Looking at Figure 3.3, we see the same hour for 7 beams taken from the averaged file. The interference has been removed, and most of the noise and day-to-day variation of

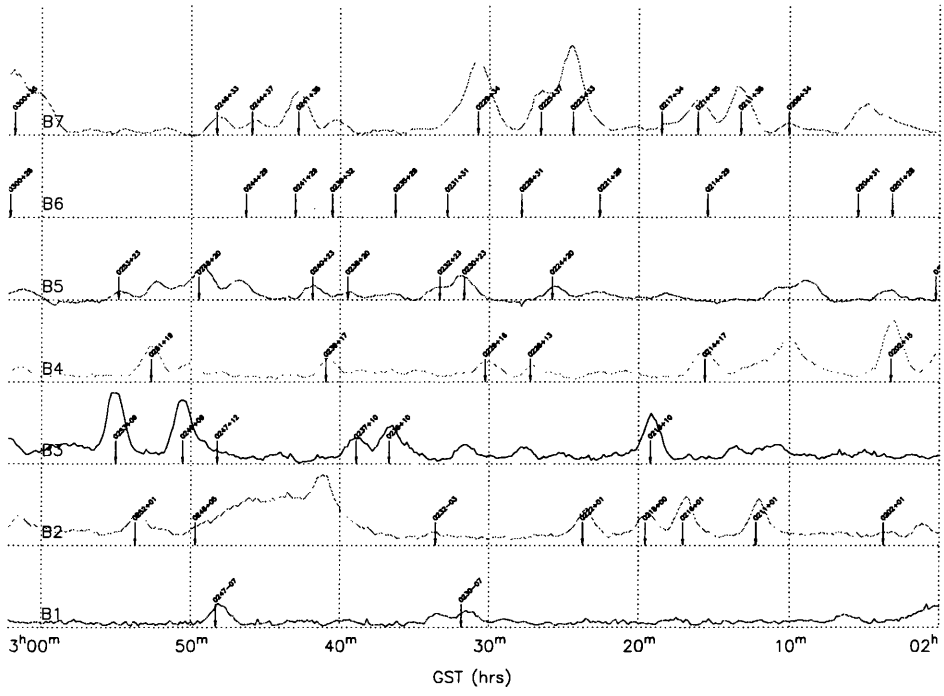

Figure 3.3: Taken from THE.avg, this figure shows one hour of Right Ascension, averaged over the whole 1631 days of the survey, for seven of the telescope's beams.

scintillation has been smoothed out by averaging over such a large data set. What remains is an average scintillation template for each of the sources.

3.2.2 Defining each source's profile

When the radio waves from a compact source enter one of the telescope's beams, the output of that beam, the scintillating flux (ΔS), will increase and show a maximum at the transit of the source across the meridian. To determine how much scintillation those waves are experiencing, a profile of that source is fitted to the raw data.

Previous efforts to find how much scintillation is occurring have taken the simple average of the observed ΔS for the time that the source is in the beam [89]. This does not take into account that scintillation is intrinsically varying, and thus it is not an accurate model. A large spike caused by scintillation might cause the interpretation of those data to be far higher than it should be.

But with the novel method of template-fitting that's used here, mistakes such as above would not be so easy to make. This is because this method looks at *all* the data for a source together, and fits the template in the best manner by taking all the data points

into account.

The starting and finishing points of the profile need to be defined from the averaged file, `THE.avg`. This will then be the "window" around the source. The program `window.c` automatically selected the starting, finishing, and maximum points for each of the 1749 sources. The extreme edges were chosen to be where the data dropped below the noise level, or where there was a minimum between two sources close together. These profiles were also checked by eye, as `window.c` was not always able to select the best window.

When the declination of a source places it between two adjacent beams, it will appear in both beams. The profile of this source is best chosen from the beam where it appears strongest. The text file, `src2.txt` contains a list of sources with their profile boundaries extracted from the entire `THE.avg` file.

Having calculated the average profile for each source, the next task is to determine how to fit a source profile to the raw data on any particular day, and then use this method to characterise the behaviour of each source as its solar elongation changes.

3.2.3 Fitting the profile to the beam data

An algorithm was written which can fit a source profile to any corresponding section of data. This fitting process yields A, the factor by which the profile is multiplied to fit the beam data. For each source, A is therefore proportional to the mean square scintillating power. This fitting procedure is carried out over all the days of the survey, to give an A value for every source, for every day. Thus, an $A(\epsilon)$ curve can be drawn for each source. This curve usually peaks at $\epsilon \sim 30°$ (`Figure 3.12`). This feature will be discussed later in `Section 3.2.7`.

For each source, the A values from the whole survey are binned into 60 different solar elongation bins. Each bin is 3° wide ($3° \times 60 = 180°$). When these bins are normalized, we have the average or expected degree of scintillation for that source for any elongation from the Sun.

The program `maxL.c` fits a profile of a source, derived from the average file, to the raw data for that source, on a particular day. It then returns three parameters, A, τ_s and s.

- A is the multiplicative factor for fitting the profile onto the data. When $A = 1$, the source is undergoing the expected amount of scintillation. Otherwise, it is experiencing enhanced, or decreased scintillation, see `Figure 3.4`.

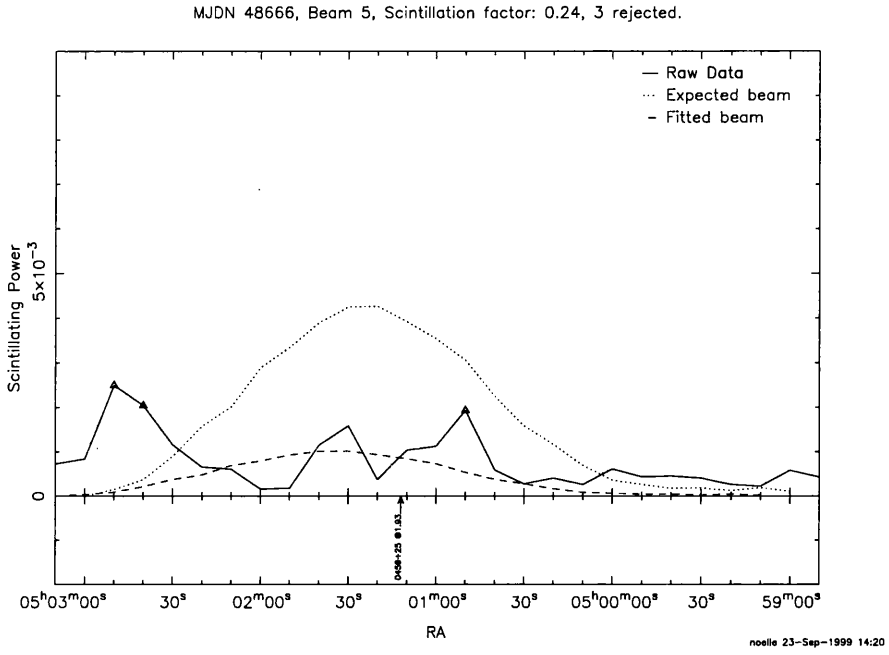

Figure 3.4: The subroutine `iterate` has fitted the beam profile to the raw data for this source, which is undergoing reduced scintillation. Its A value has been calculated as a quarter the usual. Three spurious data points have been rejected, and marked with a triangle. The best-fit was found to shift the profile to the left. No τ_s could be calculated, as the scintillation is too low.

- τ_s is the characteristic scintillation timescale. For IPS at a frequency of 81.5 MHz, this should be approximately 0.5 s. If there is ionospheric scintillation, then τ_s will be greater, as the pattern for ionospheric scintillation moves slower than that for IPS, as explained by Hewish [32].

- s is the shift of the profile, in time, for best fit. The profile sometimes fits better if displaced slightly to one side, in increments of 10 s. This is because distortions in the Earth's ionosphere cause the positions of the sources to appear to move about. These distortions are called TIDs (Travelling Ionospheric Disturbances) [91]. s can be either 1 for the centre position, 0 for a -10 s displacement, or 2 for a +10 s displacement.

The data points, b_i, for the average profile of a particular source, are taken out of the averaged file `THE.avg`, using the boundaries stored in `src2.txt`. The section of raw data corresponding to that source, D_i, is retrieved from the dayfile for a particular day. The fitting procedure uses the subroutine `iterate` to get the best fit of the profile onto the data, and hence determine a value for A. A flowchart showing the structure of the main

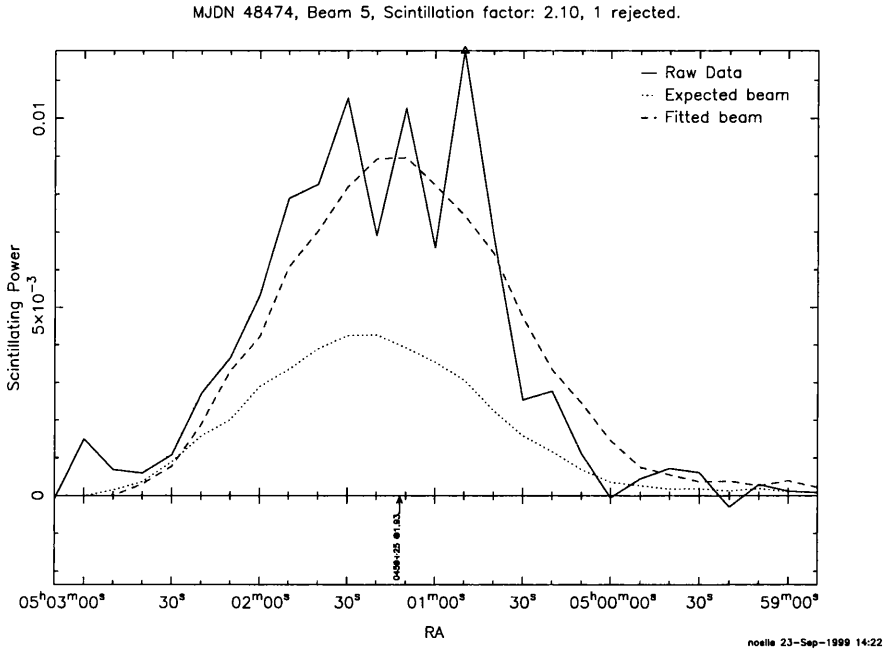

Figure 3.5: A different day for the same source as in **Figure 3.4**. Here, it's scintillating a lot more strongly, more than twice the normal. The τ_s was calculated as 0.536 s.

fitting algorithm is seen in **Figure 3.6**

The fitting algorithm works as follows. According to Woan [96], the scintillation datum, D_i, has χ^2 distribution, with $2n$ degrees of freedom, i.e.,

$$p(D_i) = \frac{(2\sigma^2)^{-n}}{(n-1)!} D_i^{n-1} \exp\left(-\frac{D_i}{2\sigma^2}\right) . \tag{3.8}$$

The σ^2 term has two components, one from the system noise, σ_N^2, and one from the scintillating signal, σ_S^2. The system noise is related to the constant offset, y_0, by

$$2n\sigma_N^2 = y_0 \tag{3.9}$$

and the scintillating component can be expressed as

$$2n\sigma_S^2 = Ab_i , \tag{3.10}$$

where b_i is the expected value from the profile, for the ith data point.

After substituting these values into **equation(3.8)**, and taking the natural log of both sides, the result is

$$\ln p = L = -\ln A + \sum_i^n (n-1)\ln D_i - \sum_i^n n\ln(Ab_i + y_0) - \sum_i^n \frac{nD_i}{Ab_i + y_0} . \tag{3.11}$$

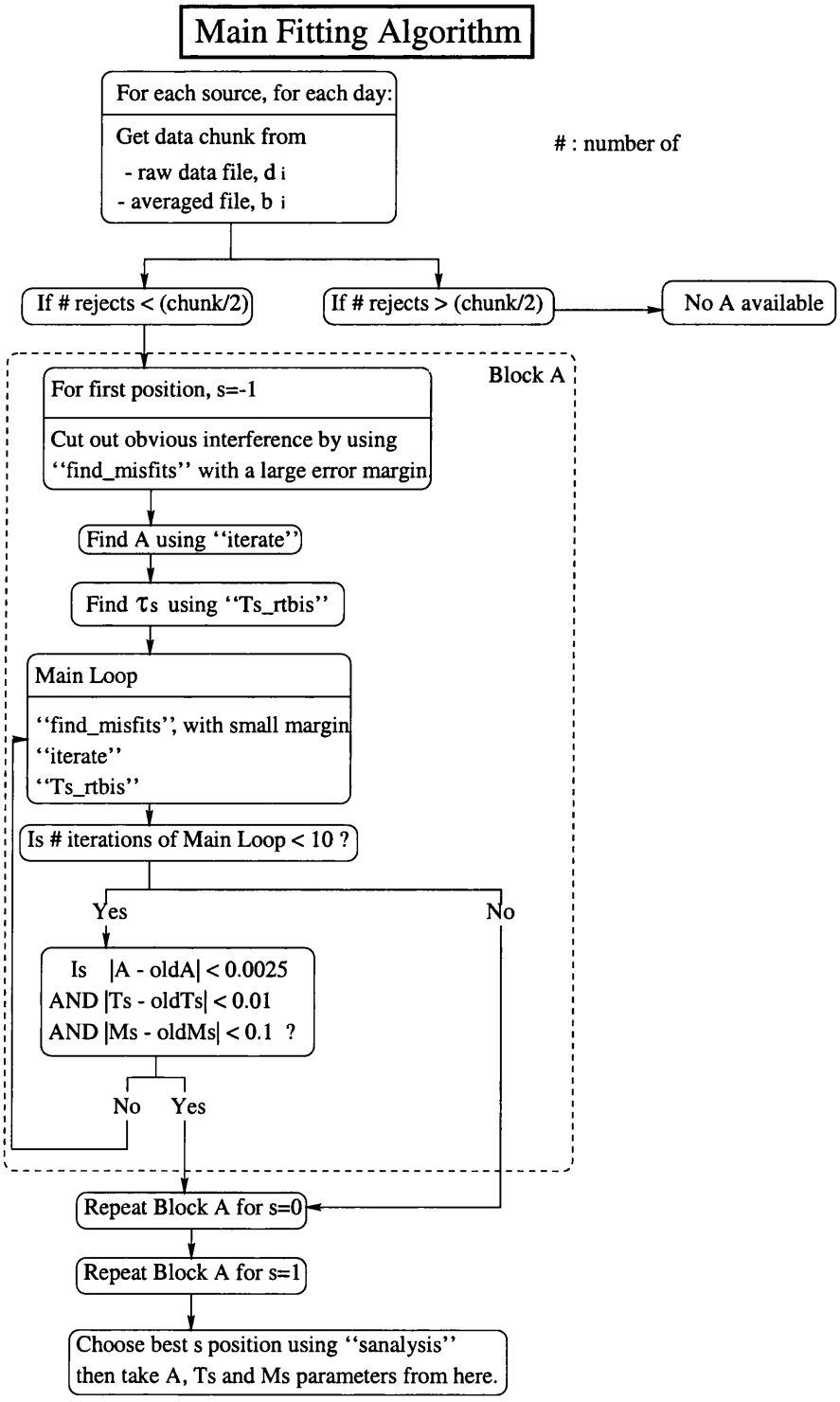

Figure 3.6: Flowchart describing the main fitting algorithm.

L, the log-likelihood, is used as the estimator for A. To get the best-fitting A, L is maximized. This maximization is done using Hessian Matrix theory (see `chapter 10` in Numerical Recipes [64]). Any function, $F(L)$, can be expressed as a Taylor series around A_0:

$$F(L) = F(A_0) + (\Delta A)F'|_{A_0} + \frac{(\Delta A)^2}{2}F''|_{A_0} + .. \tag{3.12}$$

Take the derivative with respect to ΔA

$$\frac{dF}{d\Delta A} \simeq F'|_{A_0} + (\Delta A)F''|_{A_0} \tag{3.13}$$

At a maximum, `equation(3.13)` equals zero. Therefore

$$\Delta A = -\frac{F'|_{A_0}}{F''|_{A_0}} \tag{3.14}$$

To run the subroutine `iterate`, an initial A_0 value of 1 (i.e. average scintillation) is fed into the algorithm. It then produces a ΔA value, which is added to the original A_0. This process is continued until the percentage change in A is less than 0.1%. If there's no convergence after 25 iterations, then the subroutine stops. This non-convergence could be caused by a small number of outliers which are corrupting the data. `Figure 3.7` shows a flowchart of how `iterate` works.

3.2.4 Rejecting the least-likely data points

If a good value of A can't be found, then the problem might be caused by interference spikes. To get rid of such outliers, the residual minimization subroutine, `find_misfits` finds the least-likely data point, and rejects it. If the ith datum is a perfect fit, then

$$Ab_i + y_0 = D_i \tag{3.15}$$

and L_i would be a maximum, $L_{i(\max)}$. For corrupt data, the difference between L_i and its corresponding $L_{i(\max)}$ would be greatest for the least-likely data point. This point can then be rejected, and A evaluated again.

If `find_misfits` rejects more than half the data points, then the data are considered too badly corrupted to get a meaningful value for A, so no information is then available for that source, for that day. See `Figure 3.8` for a flowchart of the subroutine.

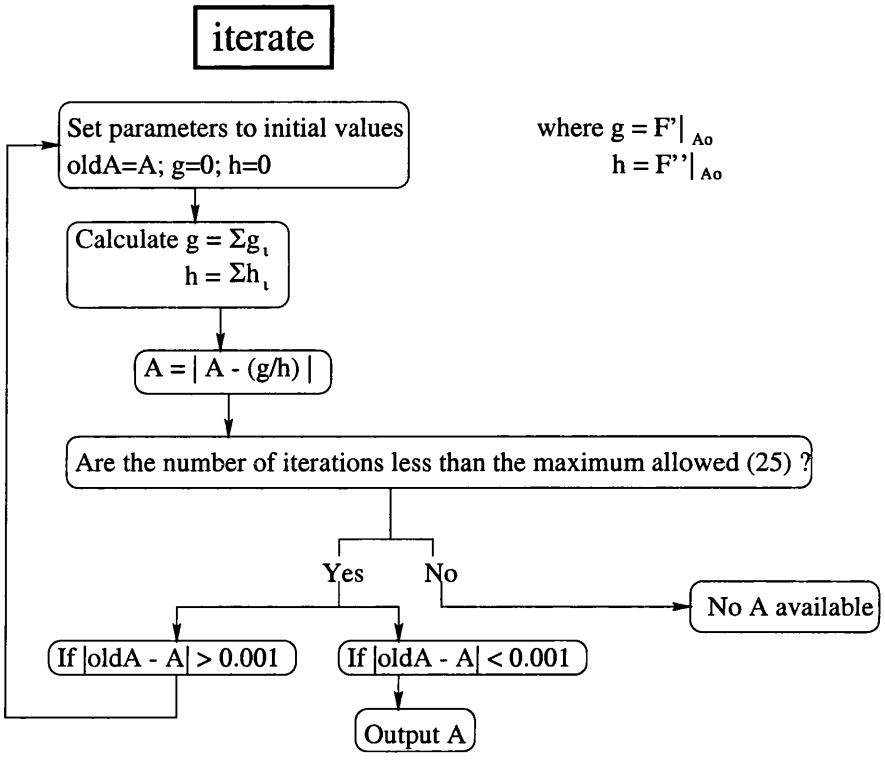

Figure 3.7: Flowchart describing the operation of the subroutine `iterate`.

3.2.5 Determining the scintillation timescale

The characteristic timescale of IPS is ~ 0.5 s, and our integration time is 10 s. Therefore, there are, on average, only 20 scintillations per integration. With a typical transit time of only two minutes, this makes it very difficult to get a reliable estimate of τ_s.

In order to estimate the characteristic timescale of the scintillation observed, the data are assumed to consist of two separate parts: the system noise and the scintillating signal. Each of these has an associated own coherence time, τ_N and τ_s respectively. τ_N is taken as being 0.1 s, which is the best estimate derived from the instrument parameters during the survey.

To take both of these into account, we use the Gaussian limit of `equation 3.11`, by assuming the integration time, T is much longer than both τ_N and τ_s, as explained by Woan [96]. A Gaussian probability density function can be written

$$f(x) = \frac{1}{\sigma\sqrt{2\pi}} \exp\left(-\frac{(x-\mu)^2}{2\sigma^2}\right), \tag{3.16}$$

where μ is the mean and σ is the standard deviation of the distribution. `Equation 3.11`

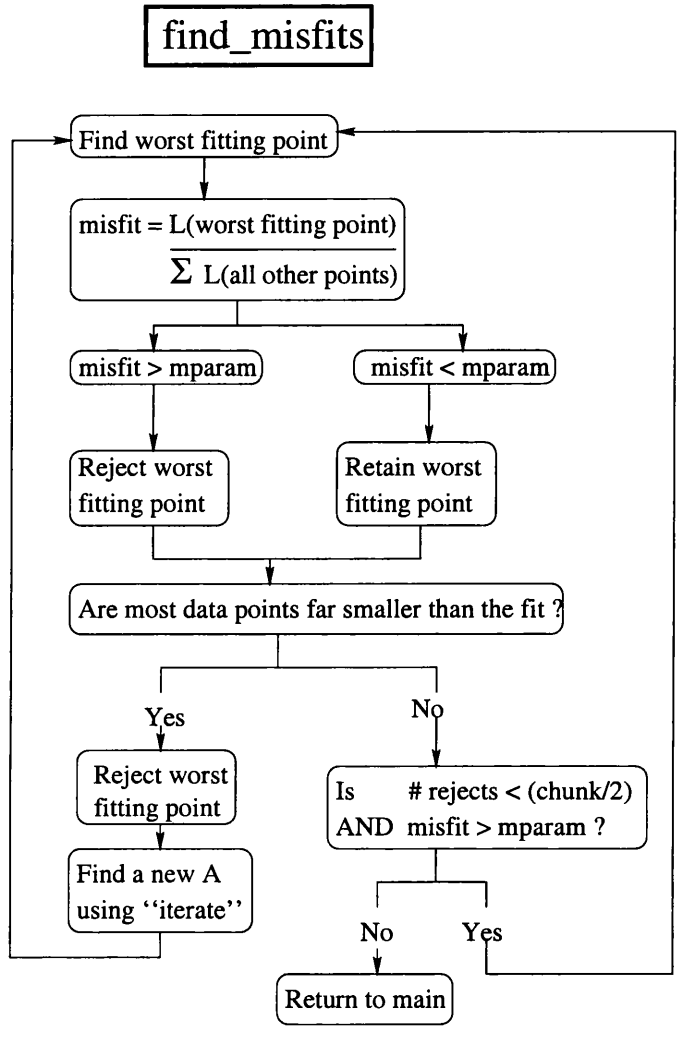

Figure 3.8: Flowchart describing the operation of the subroutine `find_misfits`.

therefore becomes

$$p(D_i|A) = \frac{1}{\sqrt{2\pi\Lambda_i^2(A,\tau_s)}} \exp\left(-\frac{(D_i - Ab_i - y_0)^2}{2\Lambda_i^2(A,\tau_s)}\right), \tag{3.17}$$

where $\Lambda_i^2(A,\tau_s)$ is the data variance, which is dependent on A and the two noise coherence times.

$\Lambda_i^2(A,\tau_s)$ can be found by modelling the noise spectra as Lorentzian, with e-folding times of τ_N and τ_s respectively. The e-folding time of τ_s is simply the time over which the autocorrelation of the scintillating flux drops by a factor of e. We assume that the autocorrelation of the scintillating flux is of the form

$$f(t) = e^{-\frac{t}{\tau_s}}. \tag{3.18}$$

Taking the Fourier transform, we get the power spectrum

$$f(\omega) = \frac{\frac{2}{\tau_s}}{\frac{1}{\tau_s^2} + \omega^2}, \tag{3.19}$$

with a half width at half power of $\frac{1}{\tau_s}$. Figure 3.9 shows a diagram of this power spectrum.

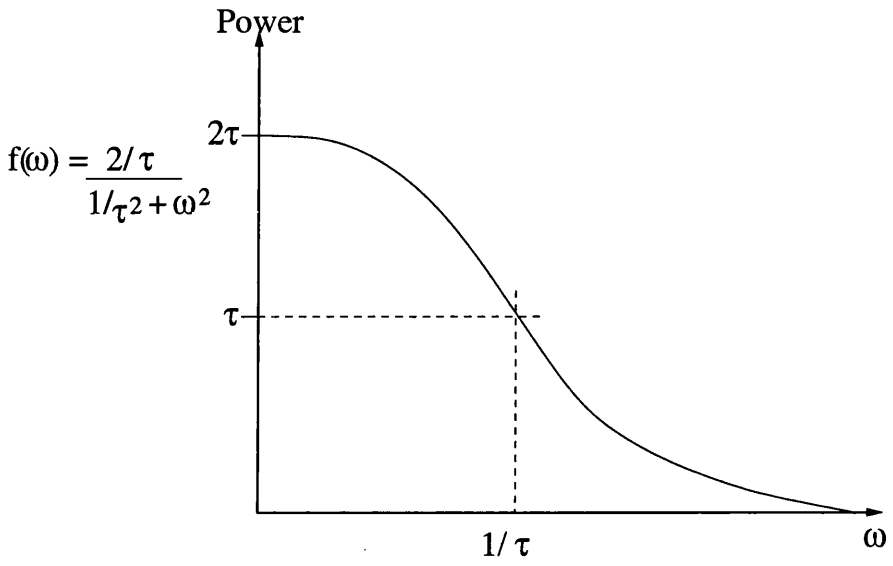

Figure 3.9: The scintillation power spectrum. The half width at half power is $\frac{1}{\tau_s}$.

The data variance has been calculated by Woan [96] as

$$\Lambda_i^2(A, \tau_s) = \frac{2}{T}\left(y_0^2\tau_N + A^2 b_i^2 \tau_s + 4y_0 A b_i \frac{\tau_N \tau_s}{\tau_N + \tau_s}\right). \tag{3.20}$$

To determine the most likely value of τ_s, we take the natural log of equation 3.17, giving

$$L = -\sum_i^n \ln \Lambda_i^2(A, \tau_s) - \sum_i^n \frac{(D_i - Ab_i - y_0)^2}{\Lambda_i^2(A, \tau_s)}. \tag{3.21}$$

In reality, the second term in equation(3.21) dominates, so the first term can be ignored.

L, therefore, has a "chi-squared" form, and its most probable value is equal to the number of data points, n. To find τ_s, the bisection method (see chapter 9 in Numerical Recipes [64]) is used to solve

$$L - n = 0. \tag{3.22}$$

The bisection method works as follows. It is assumed that a function changes sign within a certain interval, therefore, it must pass through zero at least once. The function is evaluated at the interval's midpoint, and its sign examined. The midpoint then replaces

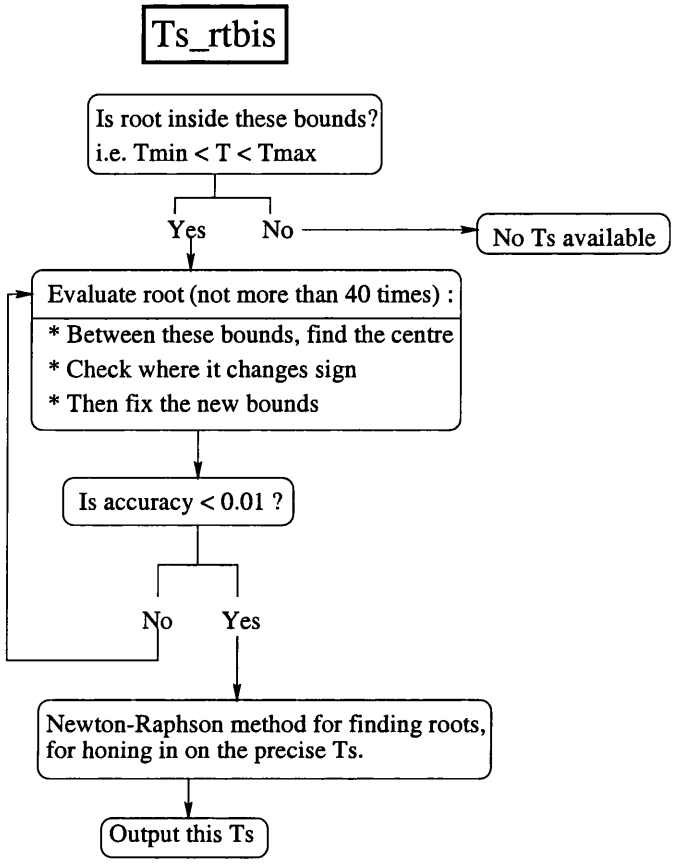

Figure 3.10: Flowchart describing the operation of the subroutine `Ts_rtbis`.

whichever limit has the same sign. This is continued until the the root is contained within a sufficiently small interval.

This method is implemented in the subroutine `Ts_rtbis`, illustrated by the flowchart in `Figure 3.10`. This subroutine keeps iterating to find τ_s until the accuracy to which τ_s is known is less than 0.01 s. If this does not converge after 40 iterations, the attempt is abandoned.

Later, when doing statistical studies of the computed parameters, it became apparent that this method resulted in the τ_s values being quantized, with a period of 0.00732 s. This period is exactly the size of the smallest bounded interval that the bisection method worked with. So, to home in on the exact answer, within these bounds, the Newton-Raphson method was put to use (see `chapter 9` in Numerical Recipes [64]) :

$$x_{n+1} = x_n - \frac{F(x_n)}{F'(x_n)}, \tag{3.23}$$

where x_n, the first guess, leads to x_{n+1}, the next best guess. Only one iteration was needed to get the accuracy desired.

Now that it is known how to evaluate τ_s, the velocity of the solar wind can be calculated. If we assume that the typical scalelength, a, of refractive index fluctuations in the IPM is constant, then the velocity is simply

$$v = \frac{a}{\tau_{rms}}. \tag{3.24}$$

An alternative single site IPS velocity determination

Though the technique described in the last section is novel, there have been other attempts to determine solar wind velocity using single-site IPS facilities, by relying on spectral analysis. Scott *et al.* [79] made an extensive series of observations near the Sun from September to October 1974 with single antennae at Nancay, France at 1420 MHz and at Owens Valley, California at 8085 MHz. By model-fitting to the observed spectrum, solar wind velocities were obtained, and they compared well with velocity data from spaced receiver observations made at Goldstone, California at a frequency of 2295 MHz.

Manoharan and Ananthakrishnan [56] have also employed the method of spectral fitting on single-station IPS measurements made by the Ooty telescope in southern India, at 327 MHz. Their data correlated well with the multi-station velocity data obtained by the Nagoya telescope during the same period, from 1986 to 1988.

As previously discussed in `section 1.3.1`, the spectrum of scintillation is dependent on the Fresnel filter. The Fresnel filter can be written as

$$\sin\left(\frac{z\kappa^2}{2k}\right), \tag{3.25}$$

where z is the spatial distance from the phase changing screen to the observer, κ is the wavenumber of the turbulence spectrum of the screen and k is the wavenumber of the incident radiation. The diffraction pattern is well formed when the Fresnel filter is close to 1, i.e., when

$$\frac{z\kappa^2}{2k} \simeq \frac{\pi}{2}. \tag{3.26}$$

At the Fresnel distance from the screen, the first diffraction pattern forms. It can be expressed, using the previous equation, as

$$z = \frac{2k\pi}{2\kappa^2} = \frac{\pi k}{\kappa^2}. \tag{3.27}$$

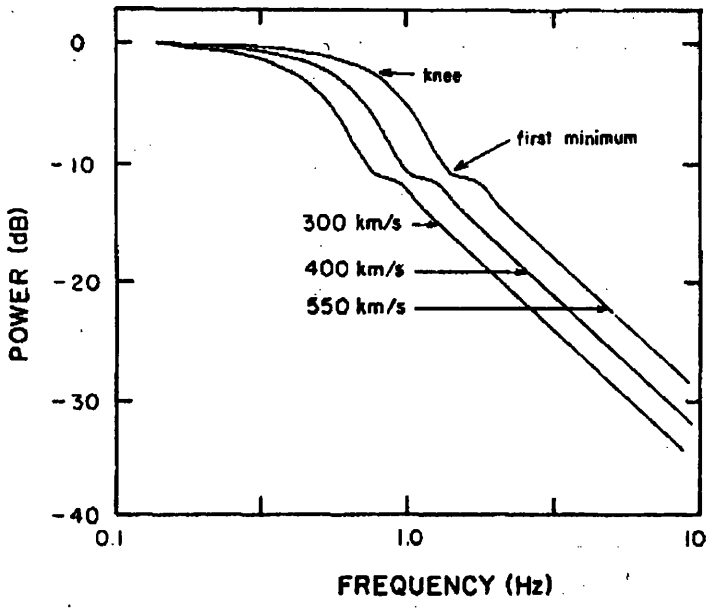

Figure 3.11: The spectra modelled for three different solar wind velocities, by Manoharan and Ananthakrishnan [56]. The spectrum expands for a higher velocity, and contracts for a lower velocity.

z depends strongly on κ. The cutoff value of κ, below which all wavenumbers are blocked, is

$$\kappa = \sqrt{\frac{2\pi^2}{\lambda z}}. \tag{3.28}$$

This filter has the effect of cutting out very large scale modulations in the refractive index, i.e., only the modulations of a small wavelength have an effect on the scintillation spectrum observed at the Earth. Wavenumbers (in the thin screen's turbulence spectrum) below a certain value determined by the Fresnel filter (`equation 3.28`) will be blocked out. This causes a "Fresnel knee" in the typical temporal spectrum of a compact source. This spectrum will have a flat portion at low frequency (low wavenumbers are not blocked), followed by an asymptotic fall above the Fresnel knee.

The temporal frequency of the Fresnel knee is dependent on the velocity of the medium, because the frequency, f, and the wavenumber, κ of the spectrum are related to the velocity, V as

$$V = \frac{2\pi f}{\kappa}. \tag{3.29}$$

A change in velocity affects the Fresnel knee, and therefore the shape of the spectrum changes. The whole spectrum expands or contracts, depending on whether the velocity

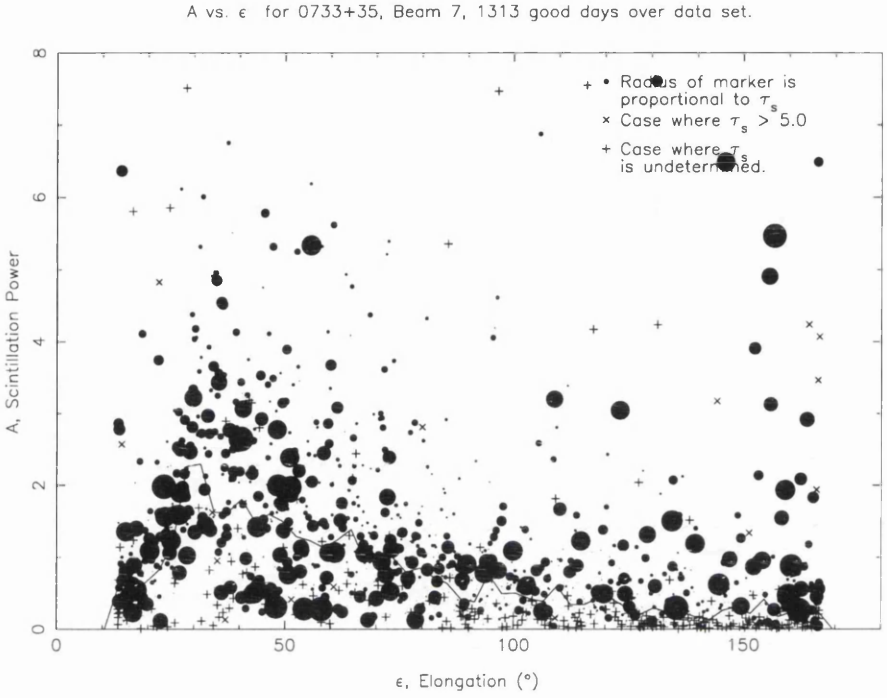

Figure 3.12: For a typical source, the $A(\epsilon)$ curve is the solid line, showing a maximum around 30°. For $0 < \tau_s < 5$, the A value is plotted as a circle whose radius is proportional to the associated τ_s. There are only a few cases where the associated τ_s is greater than 5 s or is undetermined. The plot shows that a lot of the high A values, especially at large elongations, are associated with long scintillation times, perhaps suggesting the slower ionospheric scintillation.

increases or decreases. `Figure 3.11` shows three different model spectra for three different solar wind velocities [56].

This method is comparable to the single-site velocity determination used in this survey. Our method approximates the temporal scintillation spectrum by a Lorentzian, and $\frac{1}{\tau_s}$ is taken as the half width at half maximum of this power spectrum, similar to `Figure 3.9`.

3.2.6 Displacing the beam

In some cases, the profile fits better if it is displaced to one side by one time slot of 10 s each. This sliding about of sources could be caused by TIDs (Travelling Ionospheric Disturbances). Therefore, the parameters A and τ_s are found for the centre position, and also for the cases where the profile is slid one slot to either side. The best of these three is chosen, and the shift, s, is saved with the other parameters.

3.2.7 Making $A(\epsilon)$ curves

The amount of scintillation a source's radio waves exhibit depends on the turbulence of the heliosphere. If the electron density here was dropping off smoothly with distance from the Sun, then the expected scintillation picture would show A decreasing smoothly with elongation, ϵ, from the Sun. However, at solar elongations less than 30°, the electron density is sufficient for strong scattering to dominate. At the observing frequency of 81.5 MHz, the bandwidth of this scintillation is very narrow. Unless the receiver has an extremely small bandwidth, the scintillation will be smeared out and unobservable.

The observing bandwidth used by the Cambridge array is far too wide, and all the detail is smeared out, as explained by Gapper *et al.* [25]. Therefore the A values peak at $\sim 30°$, and then drop off at elongations less and greater than this.

During the year, different sources cover different elongation ranges. Therefore, when the A values for a particular source are plotted against elongation, ϵ, the typical $A(\epsilon)$ curve results, showing a peak at $\sim 30°$.

The program `AvE4.c` fits a profile to each source for every day of the survey. A file is created for each source, containing all these A values, such as `Sa0729+44.ave`. The $A(\epsilon)$ curve can be plotted by `plotAvE.c` for each source from its file, as shown in `Figure 3.12`.

The expected scintillation of a source, $E(A)$, for a particular elongation bin (chosen to be 3° wide) is calculated as the geometric mean of all the A values falling within this bin over the course of the survey.

3.3 Testing the algorithms: Monte Carlo Simulations

To test out the accuracy of the beam-fitting algorithms, a series of Monte Carlo simulations were carried out. The scintillating behaviour of a source is simulated, with known parameters of A and τ_s. Then the algorithms are used on the resulting test beam data. The accuracy with which the algorithms can reproduce the original parameters is a good indicator of how useful the algorithms are, and how much faith can be put in their results. It also gives a good estimation of errors for the g-maps and τ_s-maps.

The data are modelled using the expression for data variance from `equation 3.20`

$$\Lambda_i^2(A, \tau_s) = \frac{1}{T}\left(y_0^2\tau_N + A^2 b_i^2 \tau_s + 4y_0 A b_i \frac{\tau_N \tau_s}{\tau_N + \tau_s}\right). \tag{3.30}$$

For a particular data point in a source,

$$D_i = Ab_i + y_0\,, \tag{3.31}$$

we add to it a random number, Q, multiplied by the square root of the variance

$$D_i = Ab_i + y_0 + (Q\sqrt{\Lambda_i^2(A,\tau_s)})\,. \tag{3.32}$$

to give simulated data with a known A and τ_s.

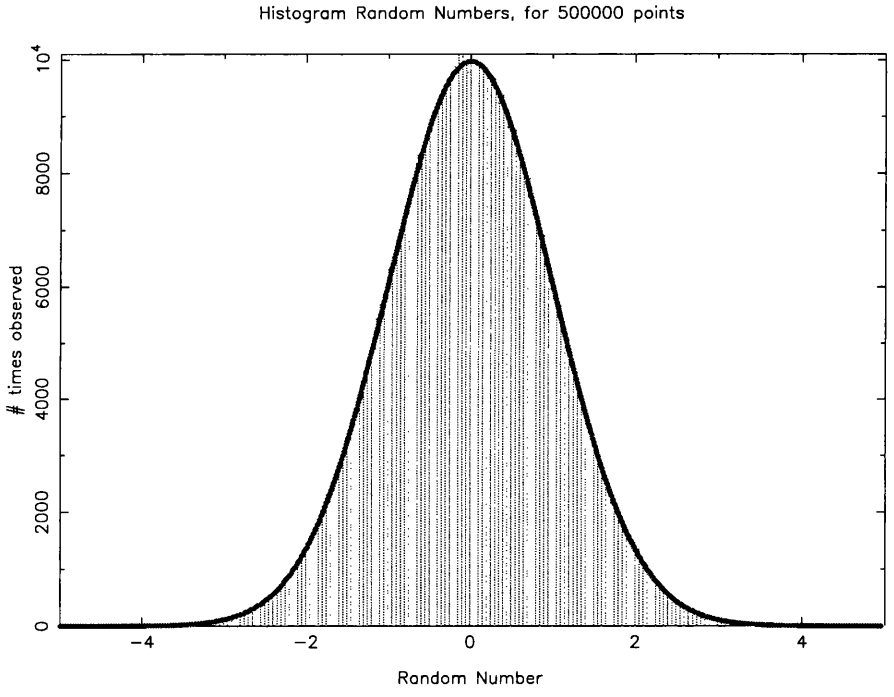

Figure 3.13: The histogram created by the random number generator, `ran1`. A Gaussian curve is plotted over the histogram, and it fits perfectly.

The random number generator used, `ran1`, was taken from `chapter 7` in Numerical Recipes [64], and it creates a Gaussian distribution, as shown in `Figure 3.13`. The curve plotted is the corresponding Gaussian, $H(x)$,

$$H(x) = \frac{N}{\sqrt{2\pi}} e^{-x^2/2}, \tag{3.33}$$

where N is the number of random numbers used to generate the histogram.

In a similar manner, large interference spikes can be introduced to test the rejection procedure.

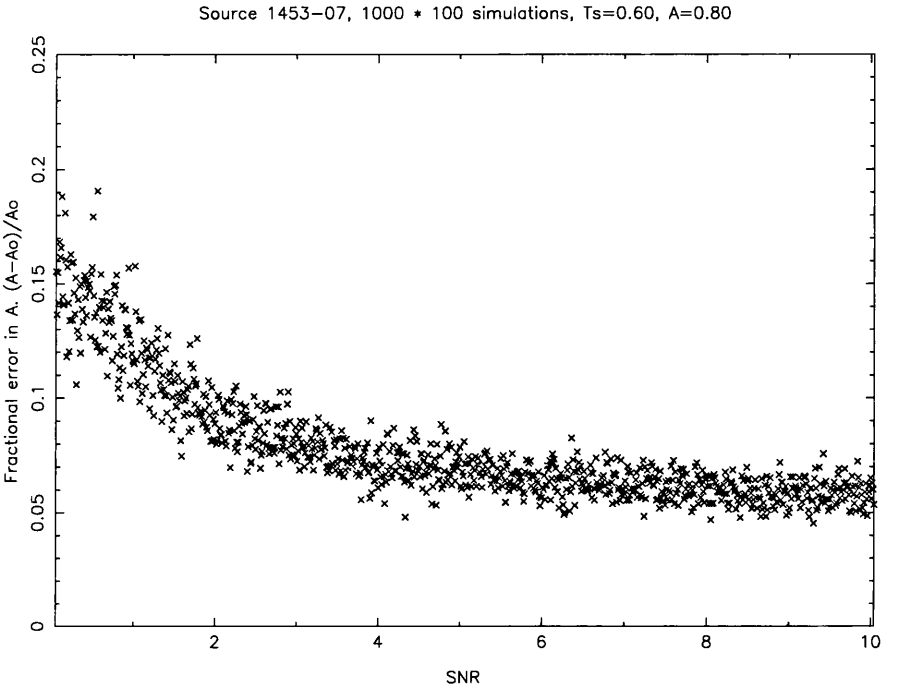

Figure 3.14: The set A is kept at 0.8. Each point is the average of 100 simulations at the same SNR. As the SNR is increased, the fractional error in A decreases.

3.3.1 Evaluating the A parameter

The program `monte3.c` implements the simulations, and, after some small adjustments, the algorithms gave statistically consistent results.

In `Figure 3.14`, we can see the effect of varying the SNR of the simulated data. The fractional error in A tends to level out after SNR $\sim$ 5, after which, the error is approximately 7%. There is a lower error for higher SNR because the signal is easier to distinguish from the noise, and the fitting algorithm therefore works better, producing lower errors. This is because, with a stronger signal, there is less margin for error in working out A. The underlying template is more apparent if the signal is far above the noise.

If all the A values are used to make the subsequent g-maps, then the error in A is at most, only 15%. If the A values with an SNR$<$ 2 are discarded, then the resulting map would be accurate to at least 10%. In practice, dropping the A values with an SNR$<$ 2 means losing a lot of data, causing many gaps in the g-maps. So all the A's are taken, and the error is estimated as 15%.

This fitting can be even more accurate if a higher latitude source is used, as in

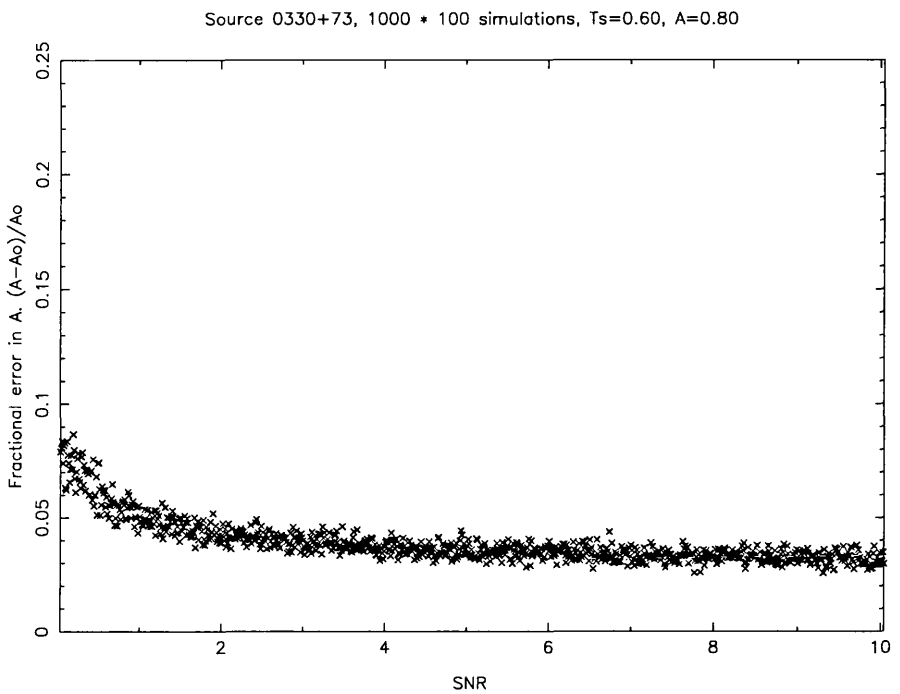

Figure 3.15: For a higher latitude source, the fractional error in A is lower still, and with less spread.

Figure 3.15. This is because a higher latitude source takes longer to transit, so it is observed for a longer period, and thus more information is gathered.

Next, simulations were carried out using a wide spread of input A values, to see how the algorithm performed. The resulting A's are plotted on a histogram, see Figure 3.16. This simulation tests the statistical performance of the beam-fitting algorithm over a large number of input cases.

In Figure 3.16, the SNR is set to 0.5. A is increased in steps of 0.025 from 0.1 to 2.6, and the beam is simulated 200 times for each A. All of these simulations are tested with the beam-fitting algorithm, and the resultant A values are plotted on the histogram below. At higher values of set A, the algorithm performs somewhat worse.

When the profile from a higher latitude source is used, as in Figure 3.17, this tailing off at high A values is not as significant. This again, is because the source is in the telescope beam for longer, and more data produce more trustworthy analysis.

If the input A is set to just one value for all of the simulations, then what is the resulting spread of computed A's? In Figure 3.18, the set A is kept at 0.8, and it can be seen that after 20000 simulations, the computed A values are spread around the centre value

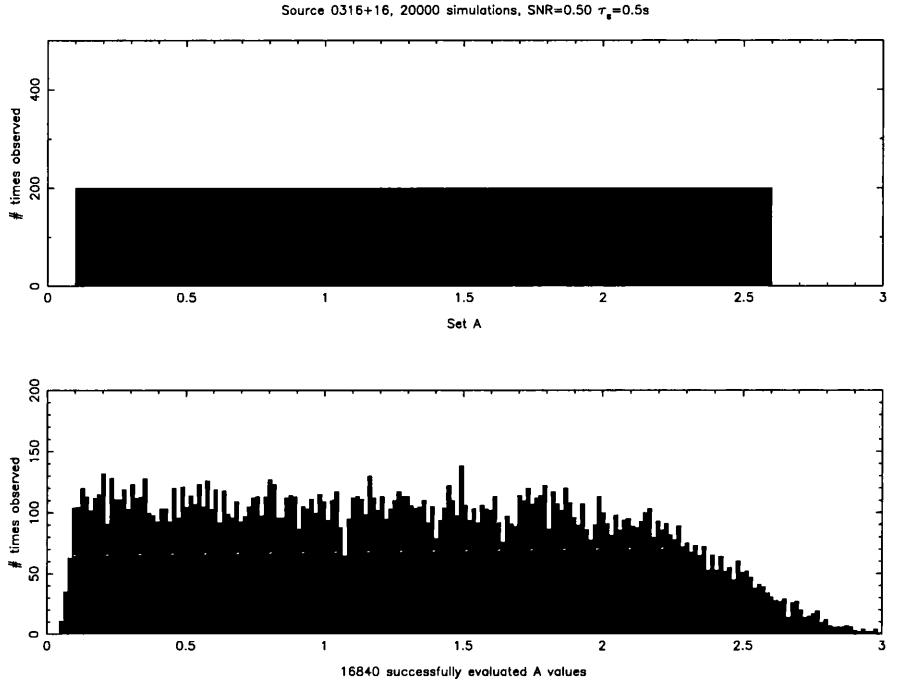

Figure 3.16: Using the profile of a low latitude source, and an SNR of 0.5,

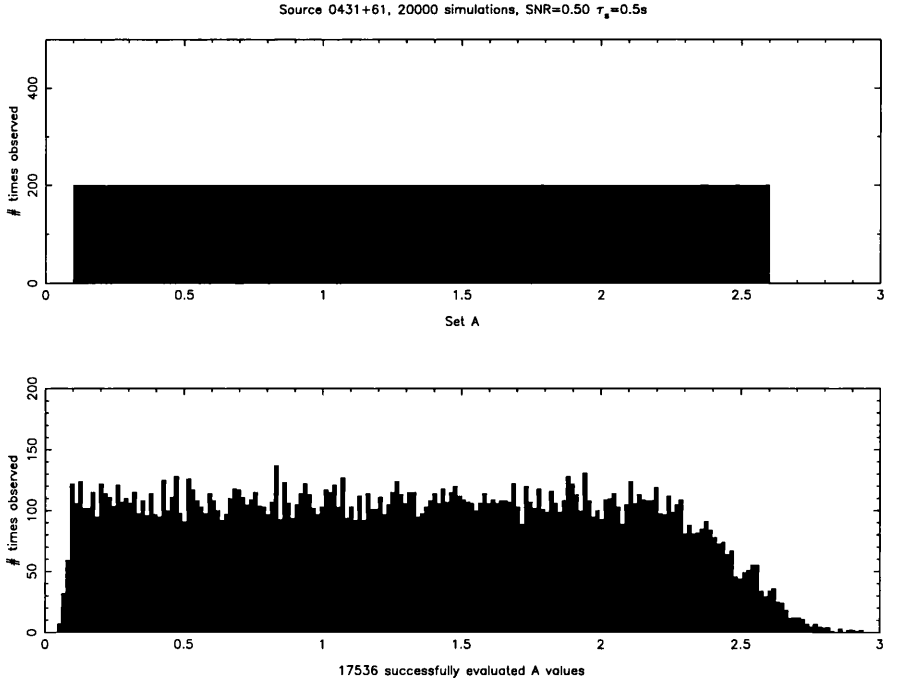

Figure 3.17: A higher latitude source profile is used, and the resultant A's are more similar to the input A's.

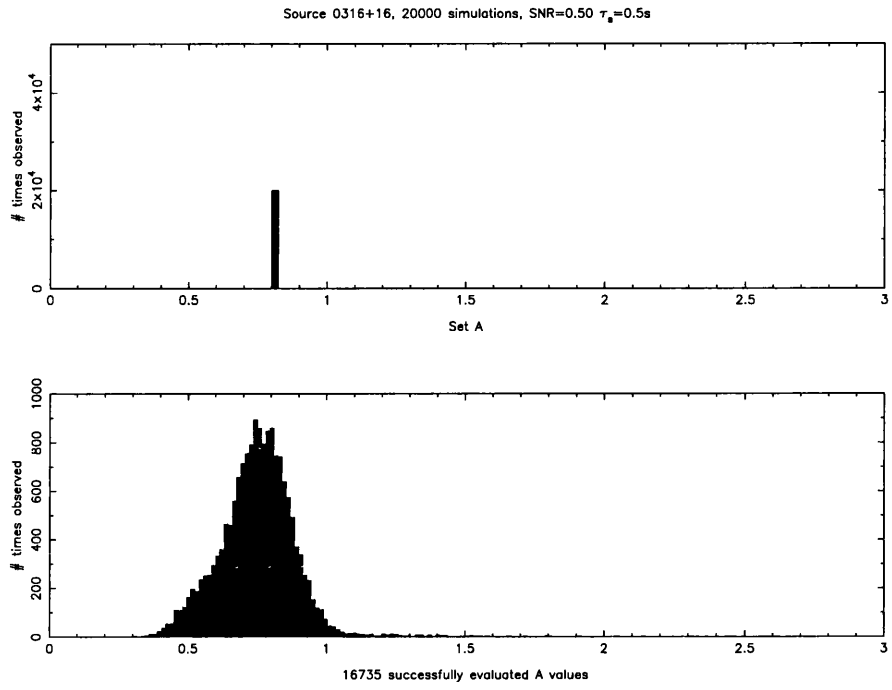

Figure 3.18: A low latitude source profile, and an SNR of almost zero, gives quite a wide spread in computed A's.

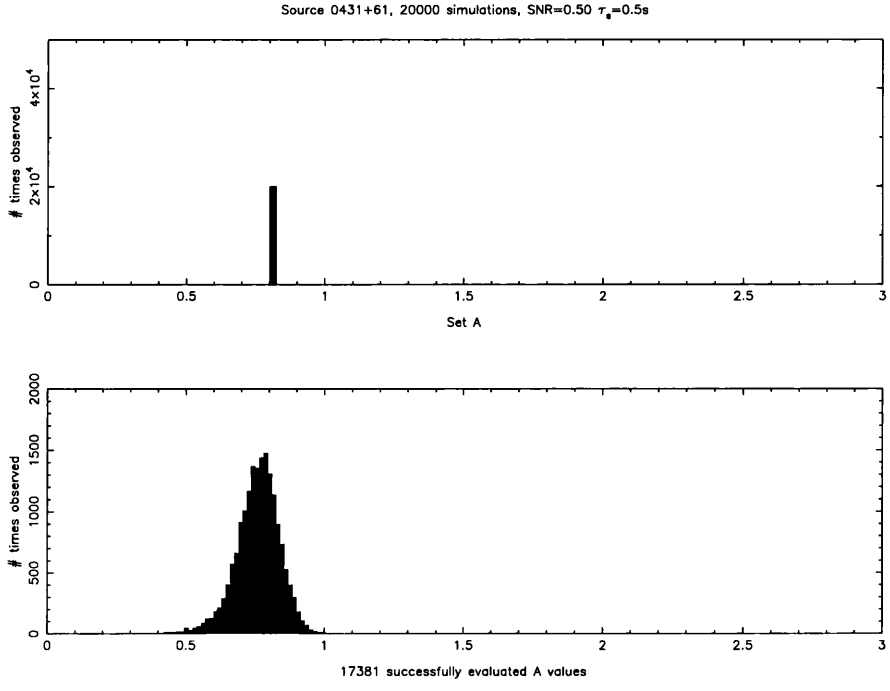

Figure 3.19: Using a high latitude source profile decreases the spread in computed A's, and increases significantly the number of successful evaluations.

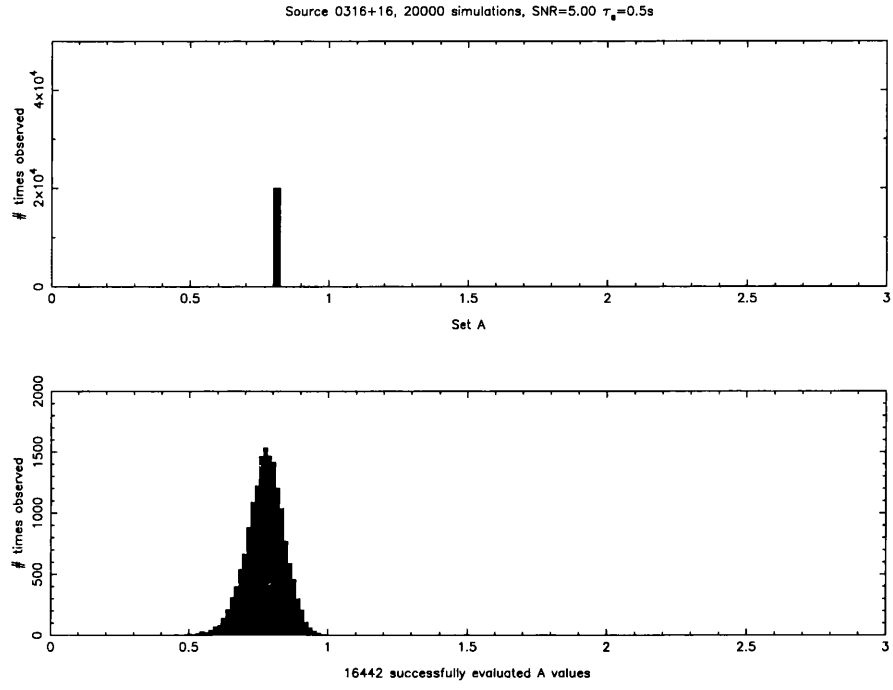

Figure 3.20: With a high SNR, and a low latitude source profile, the computed A spread is small.

of 0.8, and the FWHM (full width at half maximum) is ~0.24. We can say that A has been evaluated as 0.8 ± 0.12, therefore, the error in A is $0.12/0.8 \equiv 15\%$, exactly as what is predicted in `Figure 3.14` for a low latitude source with a very low SNR.

Performing the same simulation with a high latitude source, as in `Figure 3.19`, we see that the spread of computed A's is less, with an FWHM of ~0.17. With more data to work with, the fitting algorithm can more easily home in on the set A.

Then, using a low latitude source with a higher SNR, see `Figure 3.20`, the spread is also quite tight around the centre, with an FWHM of ~0.15.

In summary, the beam fitting algorithm performs better with a higher SNR, as expected. Limiting the SNR cuts out too many data points, so it will not be a deciding factor in rejecting A values. Here, and in the previous simulations, it was shown that the maximum error in A is $\sim 15\%$, which is quite acceptable.

Overall, these simulations were very helpful in finding bugs in the algorithms, and making them more reliable and efficient.

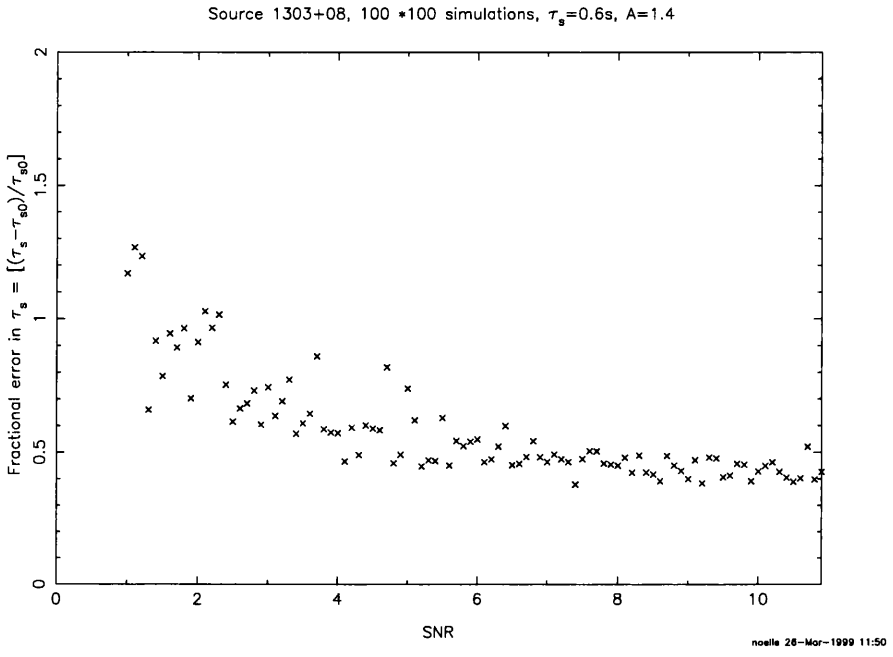

Figure 3.21: 10000 simulations, with an increasing SNR. The fractional error levels off to about 50% as the SNR is greater than 5.

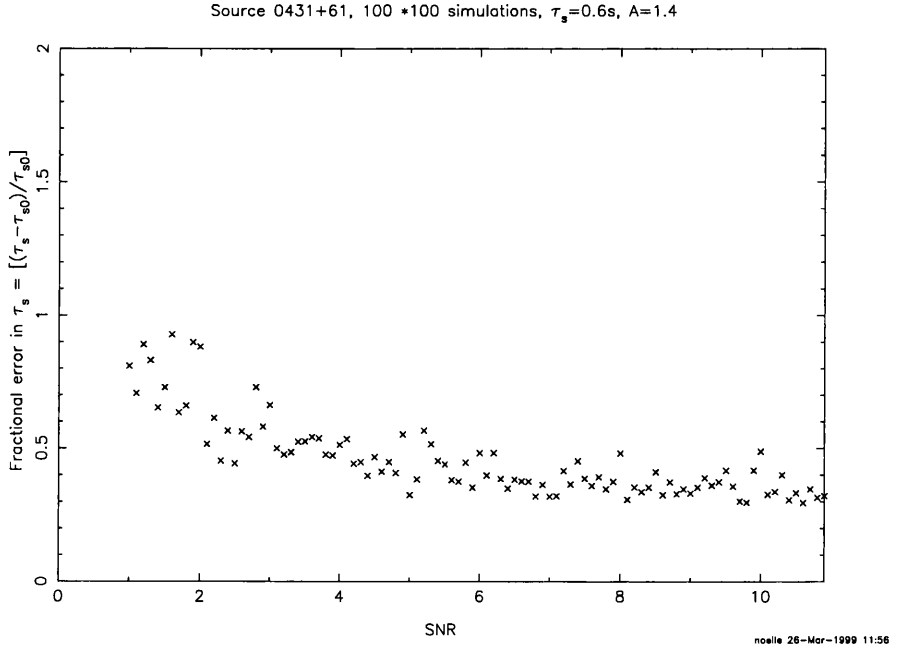

Figure 3.22: Now, with a high latitude source, the fractional error in τ_s has reduced to $\sim$ 40% after an SNR of 5.

3.3.2 Evaluating the τ_s parameter

It is much more difficult to measure the τ_s parameter. This is because of the small number of scintillations over which each source is measured. The characteristic timescale for IPS is ~ 0.5 s, and each data point has been integrated over 10 s. This means that there are only about 20 scintillations in each data point. A low latitude source might only be in the beam for 2 minutes, whereas a high latitude source can be observed for up to 10 minutes. This means that there will be a significant difference in the quality of the τ_s value taken from a high latitude source, to one taken from a low latitude source.

Looking at `Figure 3.21`, we see that the error in τ_s is quite high for a low SNR. It is only at a SNR higher than ~ 5 that the error levels off at $\sim 50\%$. Even with a high latitude source (`Figure 3.22`), the error in determining τ_s is still $\sim 40\%$ when the SNR is greater than 5.

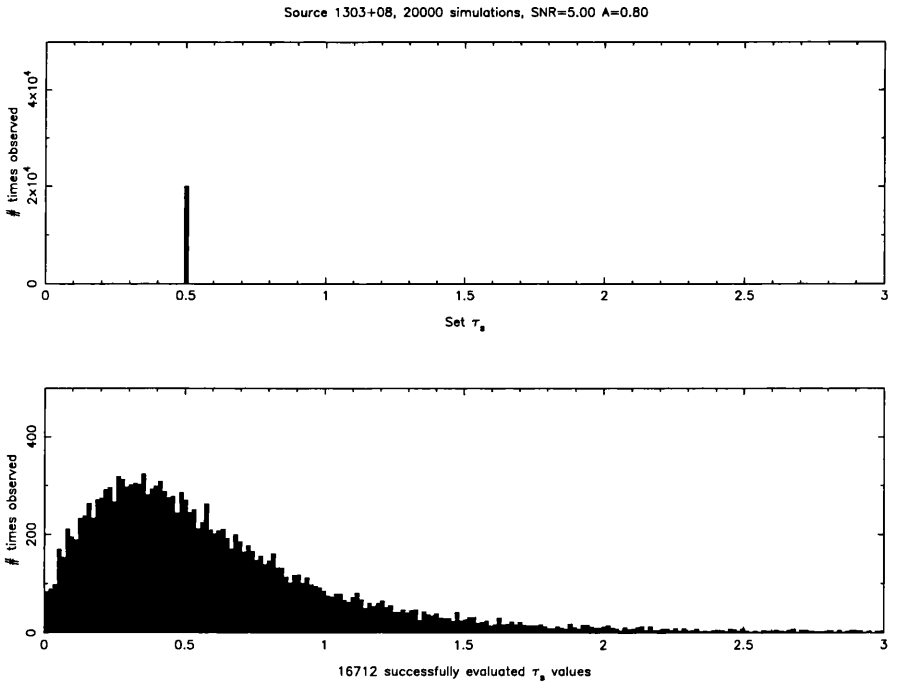

Figure 3.23: Using a low latitude source, and inputting just one value of τ_s, the spread in resulting τ_s values is quite wide, and the peak is lower than 0.5 s.

In `Figure 3.23`, 20000 cases have been simulated , all with a τ_s of 0.5 s, resulting in a spread of computed τ_s values. If a higher latitude source is used as a template, as in `Figure 3.24`, then the τ_s spread is tighter, as would be expected. Both of these simulations use a SNR of 5.

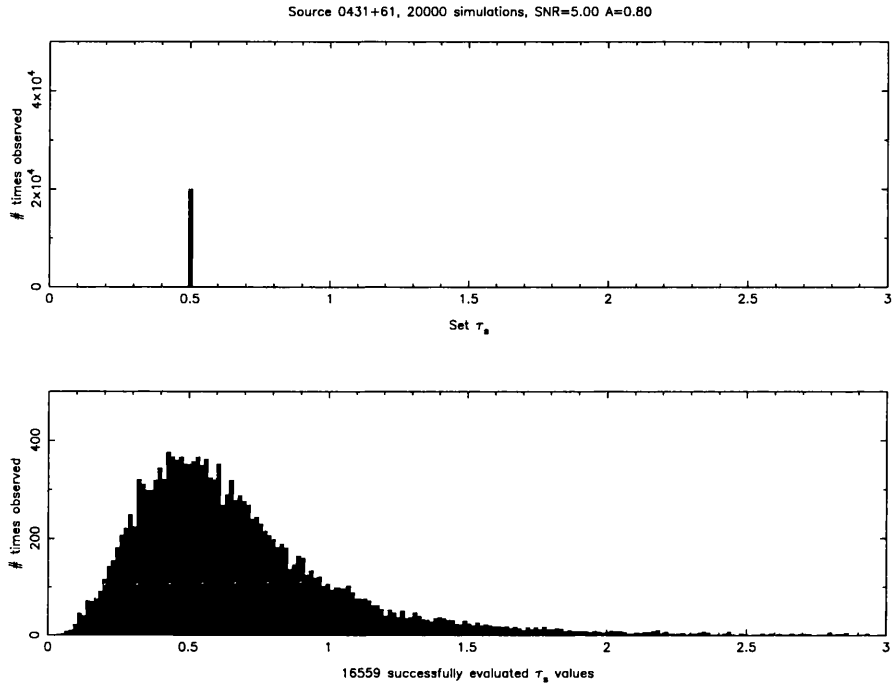

Figure 3.24: Now, using a higher latitude source, the resulting τ_s spread is more narrow, and centred around the target of 0.5 s..

In making τ_s-maps, it is therefore essential to discard τ_s values with an SNR less than 5. Unfortunately, this only leaves a handful of strong sources, giving only a limited number of data points over the all-sky map.

It is possible to group together two or three adjacent weak sources, and use the signals together to get a better estimate for τ_s. But, to understand the performance statistically, it is helpful to concentrate on individual strong sources. If the velocities gained from the strong sources are proved to be reliable, then it will validate this novel method of determining the velocity of the solar wind. The way to achieve this validation is to compare the resulting velocities with in-situ spacecraft, as in `chapter 5`.

3.4 Statistical analysis of the computed data

Accepting that the algorithms won't produce exact results, due to the noisy nature of the data, we need to examine the quality and reliability of the parameters computed. Thus, a statistical examination was carried out.

3.4.1 Analysis of the g values

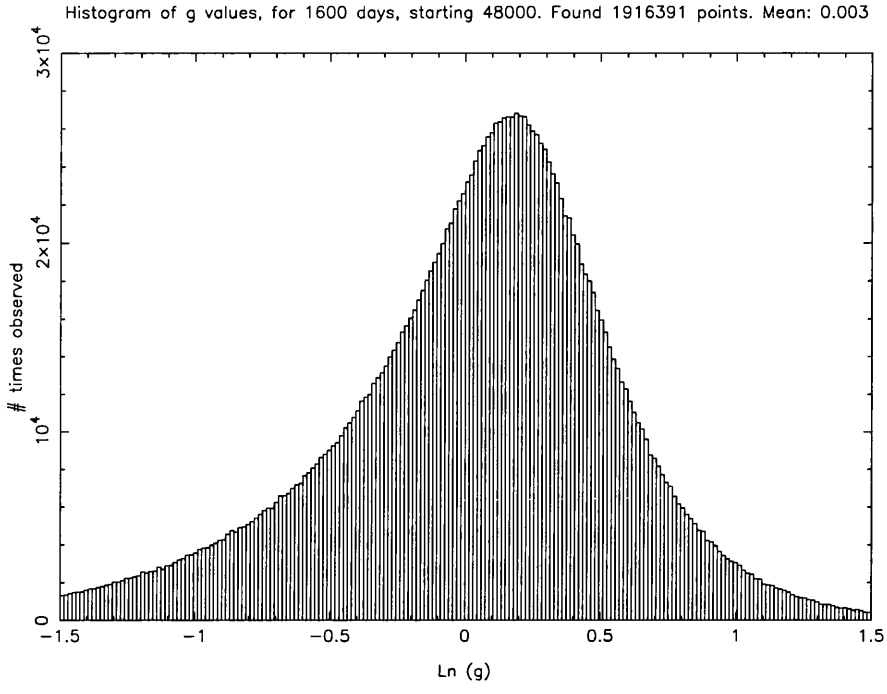

Figure 3.25: Covering most of the survey, this histogram shows that the mean value of all the g values is approximately 1 ($\ln(1) = 0$).

The g parameter has been normalized with respect to a five year average, and also with respect to the elongation of each source. Therefore, the geometric average value of g has to be approximately 1. To check this, a histogram of $\ln(g)$ for all the valid g values was plotted in `Figure 3.25`. The plot shows a skewed distribution with an off-centre peak. Even though the mean g is 1, the mode is slightly greater. This requires some explanation.

When the arithmetic mean of all the $\ln(g)$ values is worked out, it gives 0.003, i.e. practically 0. (The arithmetic mean of $\ln(g)$ is the same as the geometric mean of g.) So overall, the "average" g is 1. But the peak of the plot is 0.2, so the most probable g, the mode, is ~ 1.22 (because $\ln(1.22) = 0.2$).

This can be explained as follows. It is more probable that g is very small, than that g is very big. This explains why there are more values for the extreme left of `Figure 3.25` than for the extreme right. This could be because a limit was placed on extremely high g values, and for low g values, the error increased (because the SNR decreased). These factors combine to give the skewed distribution seen in the histogram.

Interestingly, if the survey is divided up into periods of 400 days each, the g histogram

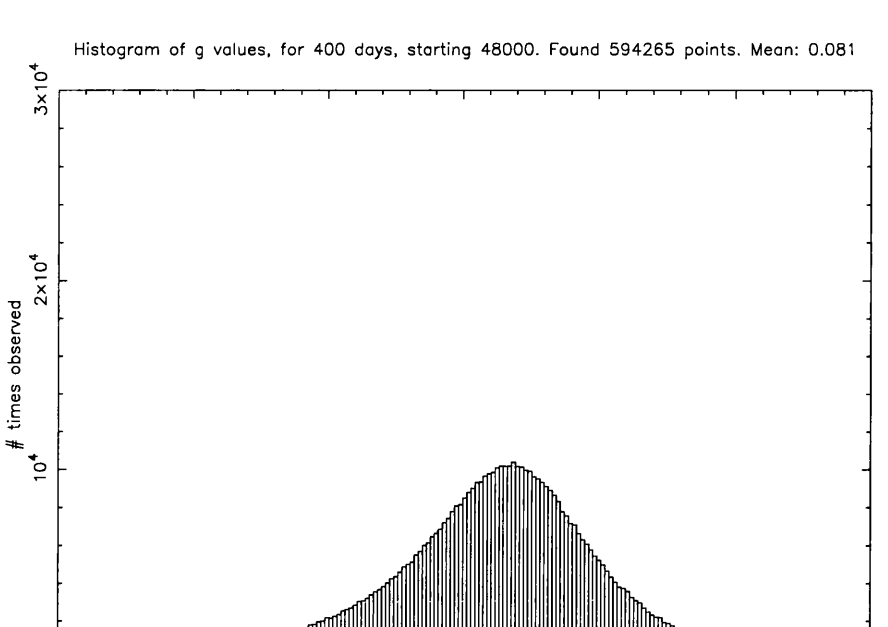

Figure 3.26: Covering the first 400 days of the survey, this histogram shows that the mean value of all those g values is approximately 0.081, and the mode is 0.2.

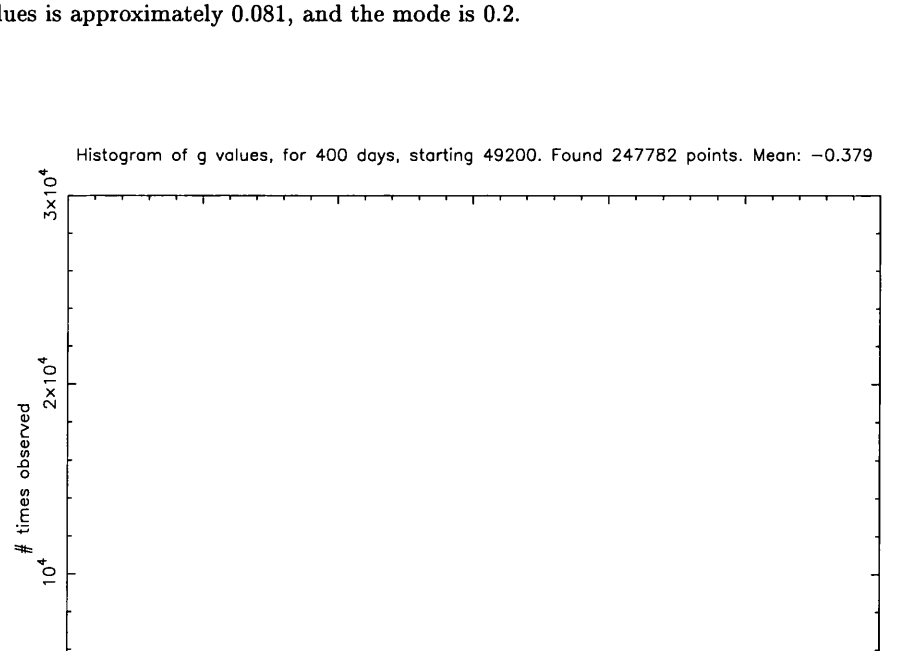

Figure 3.27: Covering the last 400 days of the survey, this histogram shows that the mean value of all those g values is approximately -0.379 and the mode is -0.25.

will look different for different periods, corresponding to the solar cycle. In the very first period (48000 to 48400), the mode is at ~ 0.2 while the mean is very nearly 0, see Figure 3.26, which is similar to the results for the second period.

In contrast, the last period (49200 to 49600) looks vastly different, see Figure 3.27. Although there are many fewer good g values, due mostly to interference and the telescope being off-line for weeks on end, both the mean and the mode are far below 0. So it seems that in the time of solar minimum, the typical g is much less than that at solar maximum.

In the histogram that incorporates all the survey, Figure 3.25, we see the effect of adding together the histograms for all of these different intervals. The mean is almost at zero, while the mode is slightly greater than this. When interpreting the g-maps, it must be taken into account that the most probable g is slightly greater than 1.

3.4.2 Analysis of the τ_s values

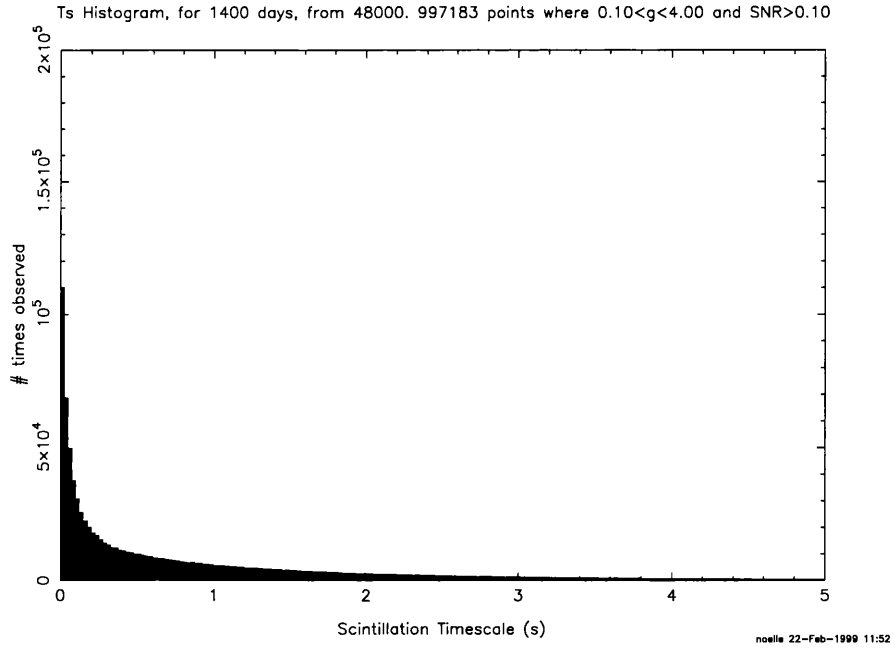

Figure 3.28: Histogram of τ_s values where no extra criteria have been applied to the selection of τ_s.

We know that the characteristic timescale of IPS is 0.5 s. Therefore, a histogram of thousands of computed τ_s values should peak at 0.5 s. Initially, this was not the case at all. Instead, the histogram showed a curve that rose exponentially as it approached zero, as in Figure 3.28. This is because all the τ_s values were included, no matter how reliable

the data they were taken from. As there is a limited amount of information contained in a brief scan of a source, then that scan must be under the best possible conditions, i.e. with a high SNR.

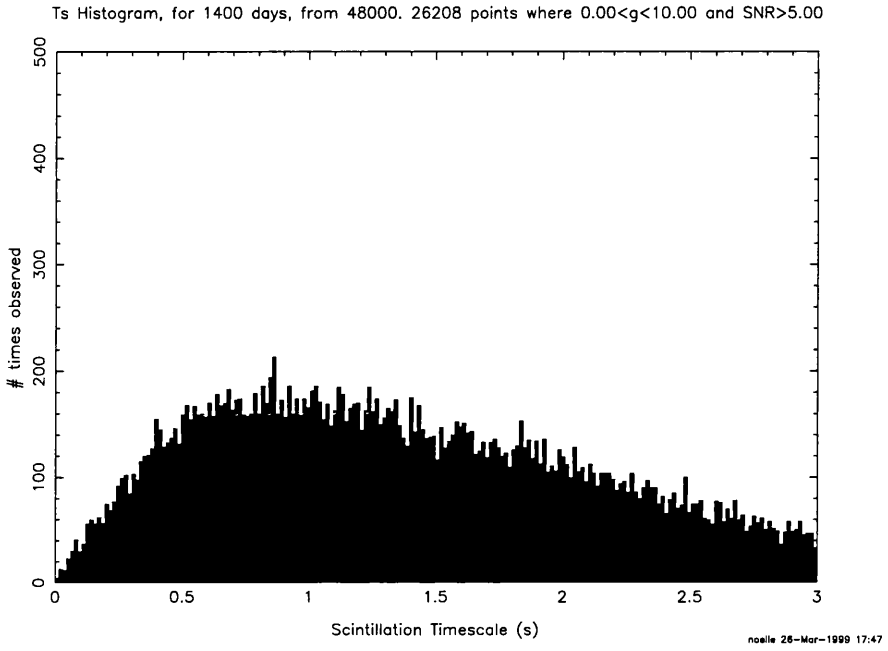

Figure 3.29: Histogram of τ_s values where stringent criteria have been applied to the selection of τ_s. But setting the SNR cutoff at 5 means that a lot of the high speed (and low density) wind is excluded, pushing the peak up from 0.5 s.

As shown in the last section, the τ_s value only begins to become reliable with an SNR greater than 5. By cutting out the τ_s values with an SNR less than 5, this preferentially excludes the lower g values. This is because a source undergoing depressed scintillation will have a weak scintillation flux signal, and a correspondingly low SNR. In effect, this approach is less sensitive to the high speed wind that is often associated with low density flow. This will result in the peak of the τ_s histogram being greater than 0.5 s, as in Figure 3.29.

For these evaluations, the SNR is defined as:

$$\mathrm{SNR} = \frac{\mathrm{signal}}{\mathrm{noise}} = A \times \frac{(\mathrm{beam}_{\mathrm{max}-1} + \mathrm{beam}_{\mathrm{max}} + \mathrm{beam}_{\mathrm{max}+1})/3}{y_0} \tag{3.34}$$

where the noise is equal to the average background level y_0. The signal is not simply taken as the beam output at the profile maximum as the source transits. Instead, it is the average of the three beam outputs around this maximum. This averaged signal is multiplied by the A value for the source on that day.

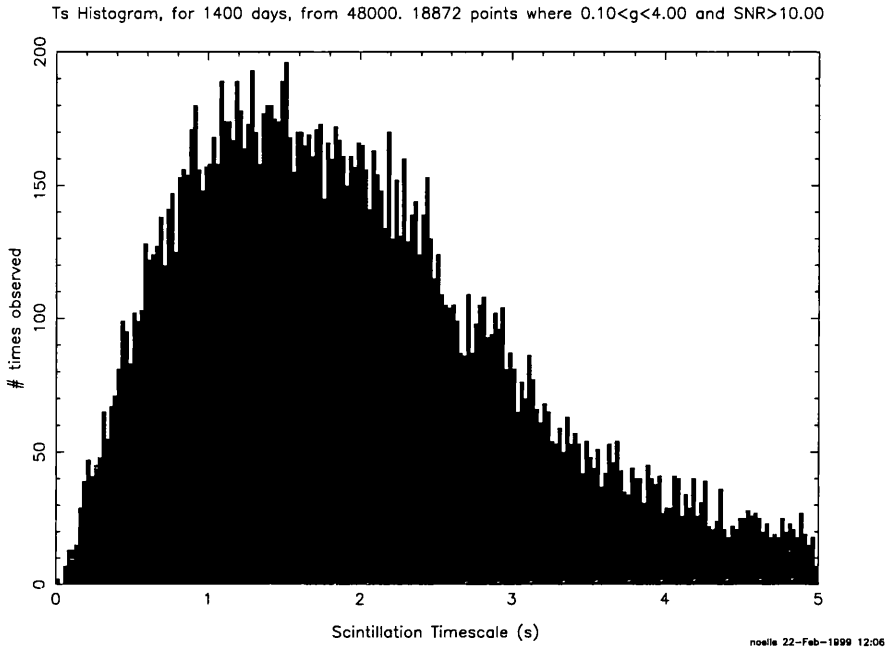

Figure 3.30: Histogram of τ_s values where the SNR cut-off is increased to 10. Note the peak has moved to ~ 1.3 s.

Interestingly, when the SNR cut-off is increased to 10, the histogram peak moves to even higher τ_s values, see **Figure 3.30**. This is further evidence that the higher the SNR cutoff, the slower will be the resulting flow, because the low density, high speed flow has been discarded. This trend would seem to validate the method of finding τ_s and hence the velocity of the solar wind.

Notice the similarity between **Figure 3.24** and **Figure 3.30**. The simulated data for a high latitude source in **Figure 3.24** show the same distribution curve as that for the real data at a high SNR cut-off in **Figure 3.30**. It would be instructive to study the differences between these two types of graphs, as they are caused by the spread in actual τ_s values that are in the real data. Both graphs incorporate system noise, but the simulated data don't include the intrinsic noise in the real wind. It might be possible to obtain the spectrum of τ_s values from a comparison such as this. This study is outside the scope of the present analysis.

IPS theory assumes that the measured scintillation comes mostly from the plasma in a sphere around the Earth, with a radius of about 0.5AU [97], see **Figure 3.1**. As the elongation, ϵ, of the line-of-sight to a source changes, we read a different projection of the velocity. The method of IPS measures the velocity tangential to the line-of-sight, which is

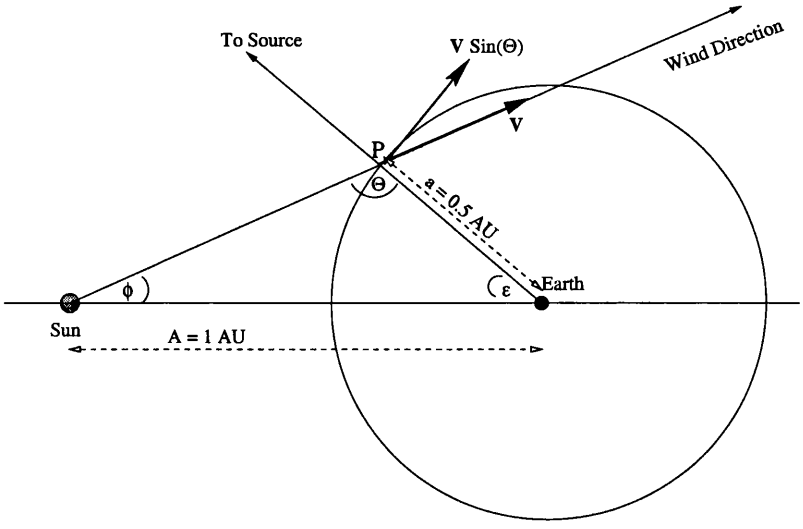

Figure 3.31: Most of the measured scintillation occurs in a sphere around the earth, of ~ 0.5 AU radius. The velocity calculated using IPS is tangential to this sphere, so the measured velocity is a projection of the true velocity, except when $\epsilon = 60°$. This figure shows the plane of the ecliptic, with ecliptic north up. Therefore ϕ corresponds to ecliptic latitude. This diagram would also be valid if the view was from the north downwards, because the maximum scintillation occurs in a 3-D sphere centred on the Earth.

reduced from the true velocity of the solar wind by a fraction, $\sin\theta$, where θ is the angle between the line-of-sight and the radially outwards flow of the solar wind from the Sun. This is seen in `Figure 3.31`, where the point of maximum scintillation is called the P point.

Apart from the case where $\theta = 90°$ (when $\epsilon = 60°$), the velocity reading will always be reduced from the true velocity. It is therefore essential to account for this when working out velocities from the τ_s values.

This weighting function is determined from the geometry of the diagram in `Figure 3.31`. The triangle composed of Sun-Earth-P point yields the Sine rule:

$$\frac{\sin(\phi)}{a} = \frac{\sin(\theta)}{A} \,. \tag{3.35}$$

Rearranging,

$$\sin(\theta) = \frac{A}{a}\sin(\phi) \tag{3.36}$$

$$= \frac{A}{a}\sin(\pi - (\epsilon + \theta)) \tag{3.37}$$

$$= \frac{A}{a}\sin(\epsilon + \theta)\,. \tag{3.38}$$

Now separate out the arguments to $\sin(\epsilon + \theta)$,

$$\sin(\theta) = \frac{A}{a}\left[\sin(\epsilon)\cos(\theta) + \cos(\epsilon)\sin(\theta)\right] . \tag{3.39}$$

Bring $\sin(\theta)$ terms to l.h.s.

$$\sin(\theta)\left[1 - \frac{A}{a}\cos(\epsilon)\right] = \frac{A}{a}\sin(\epsilon)\cos(\theta) . \tag{3.40}$$

Bring all θ terms to l.h.s.

$$\frac{\sin(\theta)}{\cos(\theta)} = \frac{\frac{A}{a}\cos(\epsilon)}{1 - \frac{A}{a}\cos(\epsilon)} . \tag{3.41}$$

Divide r.h.s. by $\frac{A}{a}$

$$\tan(\theta) = \frac{\sin(\epsilon)}{\frac{a}{A} - \cos(\epsilon)} . \tag{3.42}$$

Leading to:

$$\sin(\theta) = \sin\left\{\tan^{-1}\left[\frac{\sin(\epsilon)}{\frac{a}{A} - \cos(\epsilon)}\right]\right\} . \tag{3.43}$$

This function is plotted out in **Figure 3.32**. Note that $\sin(\theta) = 1$ at $\epsilon = 60°$, where the line-of-sight to the source is exactly perpendicular to the wind direction, and hence there is no distortion. Everywhere else, this factor has to be taken into account.

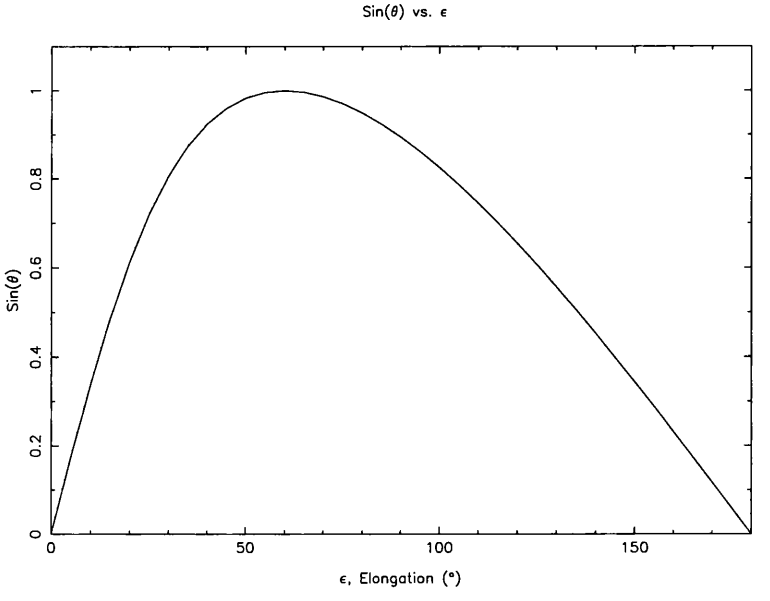

Figure 3.32: The weighting function, $\sin(\theta)$, as a function of elongation, ϵ.

Without using $\sin(\theta)$, a plot of τ_s values versus elongation looks like **Figure 3.33**, where the solid line represents the average of the valid τ_s values. Only elongations greater than

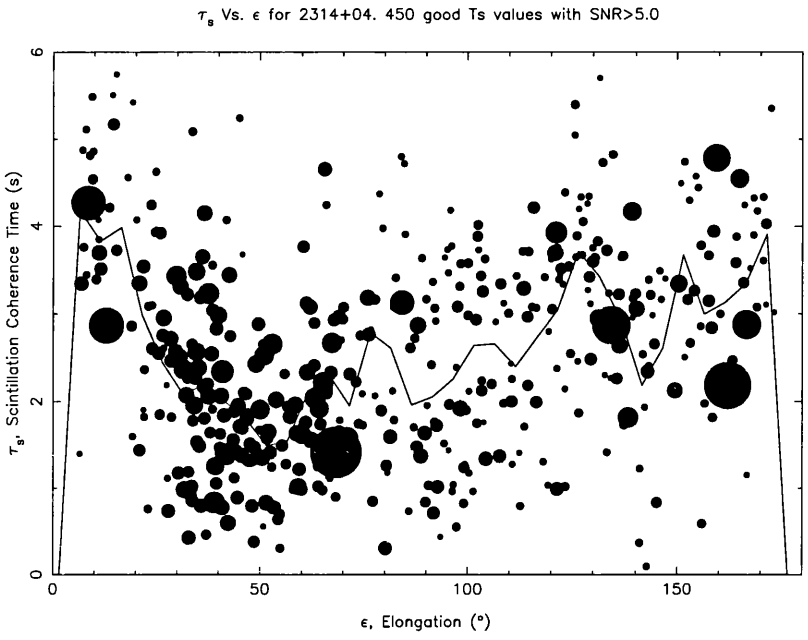

Figure 3.33: All the τ_s values for this typical source, plotted versus their elongation, with the SNR cutoff set at 5. The size of each marker is proportional to the value of the corresponding A. Also, the geometric average is drawn in. The weighting function is not being employed here, so we see that the timescale is greater at the two extremes of elongation i.e. no correction is being made for the different orientation of the wind direction and the perpendicular to the line of sight. Therefore, the velocity of the solar wind measured away from $\epsilon = 60°$ is too small.

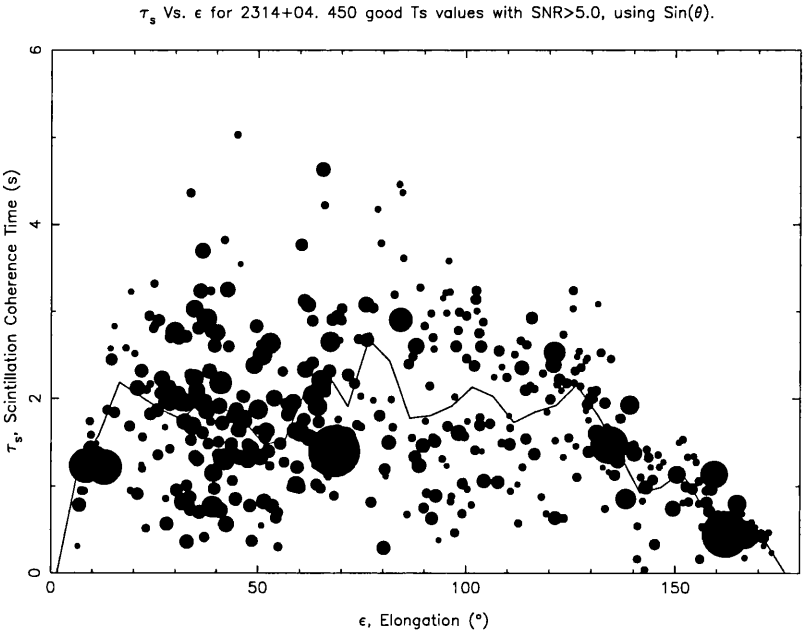

Figure 3.34: Similar to Figure 3.33, but now the weighting function is used, and the average τ_s remains approximately the same until $\sim 130°$, after which it falls off gradually with increasing elongation.

30° are important here, as inside 30° is the region of strong scattering, where the IPS signal gets smeared out and is useless for our purposes. The average line tends to dip down at mid elongations, then rises again at higher elongations. This can be interpreted as follows. As the weighting factor isn't being used, the speed of the wind is being underestimated i.e. the coherence time is too long. There is no need for adjustment at $\epsilon = 60°$, as previously explained, however, at other elongations, the error becomes significant.

With this weighting factor being used, the plot is shown in `Figure 3.34`. Here, the average τ_s line is relatively steady until after $\sim$ 130° where it gradually falls off . This implies that on average the solar wind speed doesn't change much in the near Earth environment. At large elongations, almost behind the Earth in relation to the Sun, the speed seems to increase according to this analysis. This is by no means certain, as θ is so small, and there is a larger margin of error in determining the solar wind speed from the small factor $\mathbf{V}\mathrm{Sin}(\theta)$.

This extra factor was of course taken into account in the previous statistical analysis. It is further discussed in `chapter 5`, along with a three dimensional interpretation of the measured IPS parameters.

3.5 Assembling daily maps

After the algorithms and their resulting parameters have been thoroughly tested and error estimates made, the next step is to use these parameters to make daily maps.

3.5.1 The g-maps

All the g values for a day need to be calculated from the source files and gathered into one file per day. This is done by `get_gday.c`, creating files such as `G48800.dat`. This file contains 1649 rows, one for each source. Each row has 4 figures: A, g, τ_s and s.

The Interactive Data Language (IDL) was chosen to plot the g-maps, because of its superior graphical ability, and the control one can have over the axes and other parameters. Instead of simply plotting g, we plot $\ln(g)$ because the process of scintillation enhancement, or reduction, is a multiplicative one, and therefore better described using a logarithmic display rather than a linear one.

As seen in Figure 3.35, these g-maps show the whole sky, from $-10°$ to $80°$ in declination, in Hammer-Aitoff projection. The Sun is always positioned at the centre of the map. Two curves are drawn around the Sun at elongations of $30°$ and $90°$. Lines of constant right ascension are drawn, at $60°$ intervals, while the lines of declination are drawn $30°$ apart. The Sun travels on the ecliptic, which is offset from the celestial equator (declination = $0°$).

The sky is divided into 1296 pixels, each $5°$ square.

$$\frac{360}{5} \times \frac{90}{5} = 1296\,. \tag{3.44}$$

Initially the values of $\ln(g)$ from all good sources for the day are added to a bin for the appropriate pixel. Each bin is then averaged over the number of good sources that have been added to it. Each pixel across the map will contain one figure, which is represented as a particular colour, according to the colour table chosen for the map.

The sources are not spread evenly across the sky, and data for each source are not always determinable, so there will be gaps in the pixelated map. To fill in some of these gaps, empty pixels are evaluated by interpolating from the surrounding pixels. Only if an empty pixel is surrounded by at least 4 non-empty pixels, will it be filled in by the geometric mean of those nearest neighbours. Therefore, instead of many little dots with gaps between, the map can begin to show coherent structures.

Before final presentation, the g-map is smoothed. This helps to remove erratic data, and thus produce a clearer image of what's happening.

3.5.2 Extra criteria for the τ_s-maps

From the statistical analysis of all the τ_s values found, it seems that we need to have extra criteria for sorting valid τ_s values from all the invalid ones. This criterion comes from using the SNR for a source for that day. Only if the SNR is greater than 5 will it then be included in the τ_s-map. We know that the error in τ_s is still quite large. However, the validity of the technique will be determined in chapter 4, by comparing the IPS data with in-situ spacecraft measurements of solar wind speed. This cutoff in the SNR means that there are only a few sources per day that give reliable estimates of τ_s, and hence the τ_s-maps are more sparsely populated than the g-maps.

3.5.3 Making movies

Once g- and τ_s-maps can be made for a sequence of days, these images can be linked together to form a movie. Watching an animation lasting several days makes it much easier to see the overall dynamic situation, and particular structures such as shocks and co-rotating interaction regions as they move outwards from the Sun.

The IDL program `movies.pro` creates an interactive widget, providing the opportunity to make maps for certain days, and then combine them together into a sequence of several days. This sequence can then be stored, and played as an animation on the XInteranimate tool.

3.6 Conclusions

The work described in this chapter has brought the data set to life, by making the animations. To obtain the parameters that make up these maps, some complex, iterative algorithms were written and used in a computer program. Once these computed parameters were tested and proven to be valid, it was possible to incorporate them in 2-dimensional maps of the IPM, see `Figure 3.35`.

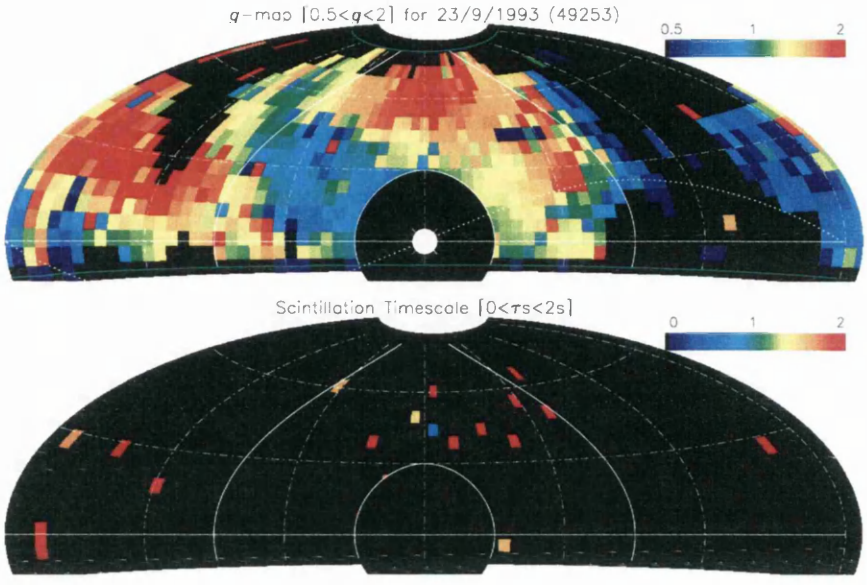

Figure 3.35: g-map and τ_s map for a typical day. The spread of g is from 0.5 to 2. The colour table at the top right explains that $g \leq 0.5$ is represented by dark blue, 1 is represented by green, and any $g \geq 2$ is represented by red. The red areas therefore show regions of enhanced scintillation, i.e., increased plasma density. No data have been put in the region less then 30° from the Sun, and other black areas indicate areas where there were no data determinable. In the τ_s map, there is very sparse data due to the difficulty in obtaining good τ_s values.

Chapter 4

Validating and interpreting the maps

4.1 Introduction

Before utilizing the Cambridge IPS maps to their full potential, it is imperative to prove that they are indeed giving a true measure of interplanetary plasma density and solar wind speed. The best way to achieve this is to compare the maps with corresponding data from other experiments, as other data sets have been tested in the past [71], [50], [59].

These data sets are available from internet databases, such as the World Data Centre. Data from the IMP, Yohkoh and Ulysses spacecraft and ground based observations from the Nagoya Radio Array were compared with the Cambridge IPS data. A brief description of each of these experiments, and the data sets they each provided, is included below.

Unfortunately, the period of the survey is one for which there are few concurrent data sources. The Solar Maximum Mission satellite (SMM) was responsible for many advances in solar physics [21], but it ceased operations in 1989, just before the start of the Cambridge IPS survey.

The Solar and Heliospheric Observatory (SOHO) has given many spectacular views of CMEs and other solar phenomena, but was launched in 1995, after the end of the Cambridge IPS survey. The Transition Region and Coronal Explorer (TRACE) was launched in 1998 and has produced extremely detailed images of the corona, though much too late to be used for any comparisons with the Cambridge IPS data.

A sound procedure for comparing the various data sets is to perform a detailed analysis

of a small number of events. Although a variety of different phenomena can be investigated through the IPS maps, it is instructive to start with the type of event that is most easily observed and interpreted.

The interpretation of long-lasting, co-rotating streams should be particularly straightforward. The stability of such structures over a long period of time means that it is easier to make comparisons with other experimental data. Even though the two data sets might not be observing the exact same part of the IPM, it is probable that the IPM conditions in adjacent areas of the sky are similar.

Also, for low density streams, the maps are less corrupted by ionospheric interference. If there were any such interference, it would show up as increased, but never reduced scintillation. In the case of one such stream, see `Section 4.4.1`, the data are examined from the many different sources, and a good correlation is found of the solar wind parameters. For example, there is evidence found on the Yohkoh images for a coronal hole being the source of a fast flowing stream.

Though the τ_s-maps don't offer the same amount of detail as the g-maps they can nevertheless be used effectively, especially for areas of high density flow by using sources that give a large scintillating flux.

Transient events can happen far too quickly to be detected with any great certainty by the IPS array. This is because the radio sources are each observed only once per day. However, impulsive events such as solar flares and CME's might create a disturbance which travels out with the solar wind, and might be detected in our maps.

4.2 Outside data sources

4.2.1 The Interplanetary Monitoring Platform

The Interplanetary Monitoring Platform (IMP-8), `Figure 4.1`, was one of a series of Earth-orbiting satellites, developed to measure the radiation environment in interplanetary space. The instrumentation is described in a paper by Lazarus [50]. It was launched in 1973, into a 12-day orbit of the Earth at $35R_E$, where it spends 7 to 8 days of each orbit in the solar wind. This, unfortunately, leads to gaps in the data when the spacecraft is within the Earth's magnetopause.

Among the measurements it provides are those of density and velocity of the solar wind.

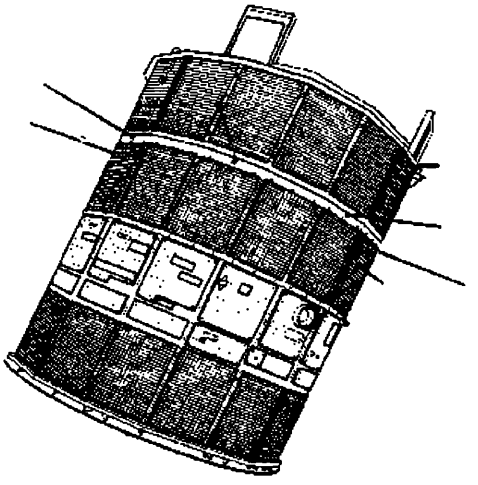

Figure 4.1: The Interplanetary Monitoring Platform (IMP-8).

These in-situ data can be compared with the Cambridge IPS data at 1AU, i.e. 90° from the Sun. `Figure 4.24` shows the daily-averaged density and velocity of the solar wind, as measured by IMP in April 1992.

4.2.2 The Ulysses spacecraft

The Ulysses spacecraft was launched in October 1990 as a joint ESA/NASA mission to study the properties of the Sun and solar wind as a function of solar latitude [84], [95]. Its path took it as far as 5 AU from the Sun. There, it used a Jupiter swingby in February 1992 to transfer to a heliospheric orbit with high heliocentric inclination. This orbit took it over the rotational south pole of the Sun in mid-1994 at 2 AU, and over the north pole in mid-1995. Ulysses will again visit the poles in 2000 and 2001 on its second solar orbit.

On board Ulysses are SWOOPS (Solar Wind Observations Over the Poles of the Sun) and SWICS (Solar Wind Ion Composition Spectrometer) which, among other things, measure the density and velocity of the solar wind at the spacecraft. As the position of Ulysses is continually changing, it is not always possible to make a direct comparison with IPS measurements, but there are some instances when this is successful, e.g. `Section 4.4.2`.

Also aboard is the URAP (Unified Radio And Plasma waves experiment) which can record radio waves from 1 kHz up to 1 MHz. Type III solar radio bursts are frequently detected, and these are often caused by solar flares or other solar activity.

All IMP and Ulysses data come from NSSDC, the National Space Science Data Centre.

4.2.3 The Nagoya UHF radio telescopes

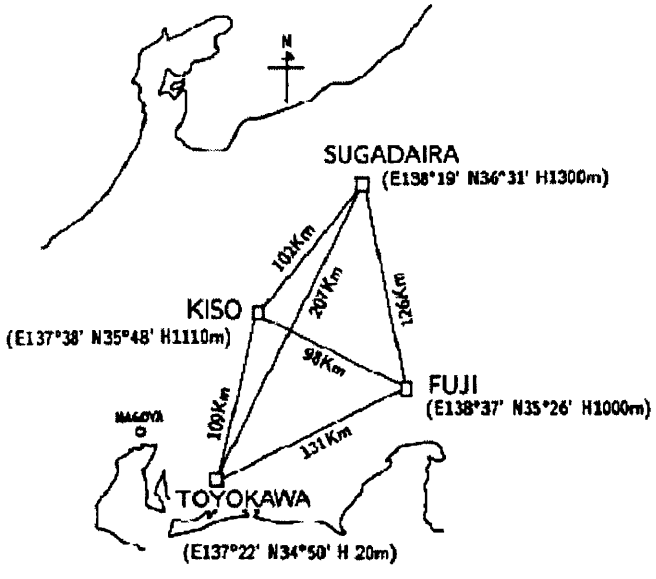

Figure 4.2: The locations of the four antennae of the Nagoya telescope.

The Solar-Terrestrial Environment Laboratory at Nagoya University, Japan operates the STE Laboratory UHF radio telescope. By using the four large cylindrical parabolic reflector antennae located as shown in `Figure 4.2`, multi-station IPS velocity measurements are carried out daily, at a frequency of 327 MHz. At this frequency, the Nagoya telescope can look much closer to the Sun than the Cambridge array, operating at 81.5 MHz.

The public database extends from 1973 up to the present day, so it covers the whole length of the Cambridge IPS survey. Unfortunately, the Nagoya telescope is not operated in the winter months, so there are gaps in the data from about November to February.

The IPS velocity technique involves recording the scintillation signal of a certain source at two different stations, separated by a baseline of a certain length. The time delay needed for maximum correlation is used to calculate the velocity of the scintillation pattern across the ground. Then, allowing for the orientation of the baseline in relation to the wind direction, the solar wind velocity is found at the point along the line-of-sight of the closest approach to the Sun. This method is well described by Kojima *et al.* [46].

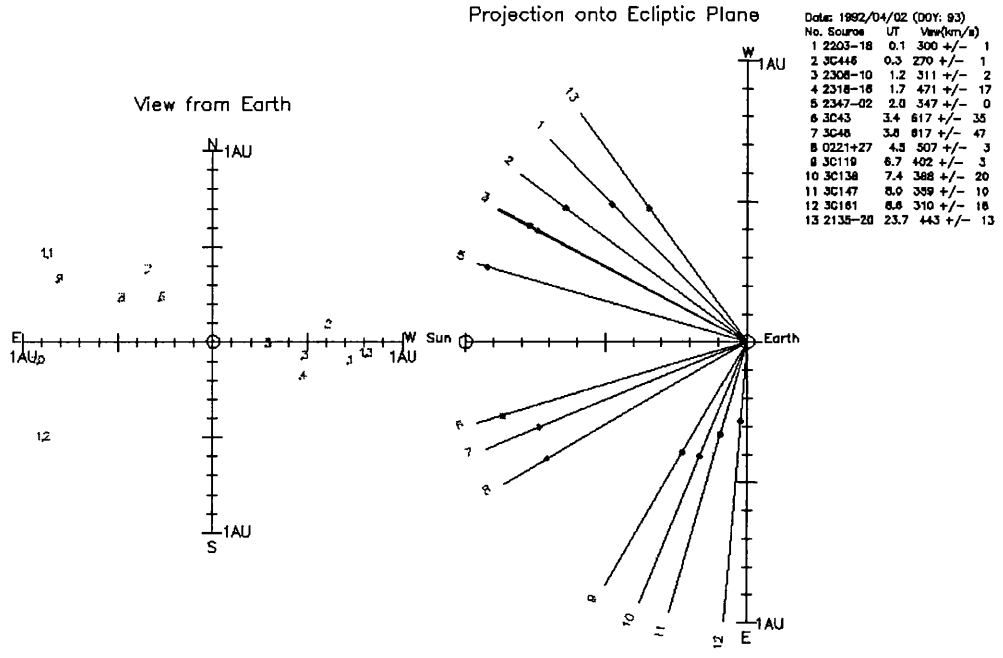

Figure 4.3: A T-map for 2 April 1992. Each number on the first diagram represents the position of a scintillating source, as viewed from Earth. The second diagram shows the view from above, looking down onto the plane of the ecliptic. The dots on the line-of-sight to each source are the 'P' points, which indicate the maximum point of the IPS weighting function, i.e. where most of the scintillation is taking place.

The Nagoya public database holds the velocity measurements made for different sources during each day. These are usually good, strong sources, which are observed for 10 or 15 minutes each. Most of the scintillation is assumed to occur at a particular 'P' point, which is found by using a weighting function along the line-of-sight to the source [46]. Then, the individual velocity data points can be plotted on a map, with the Sun at centre. This is called a T-map, as in **Figure 4.3**. As well as showing their positions in relation to the Sun, the T-map also displays their orientation as one looks down onto the ecliptic.

The wind speed measured from the scintillation of a particular source can be directly compared with velocity measurements made by the Cambridge IPS array.

It is possible to use the Nagoya data to make synoptic maps of the wind speed on the surface of the Sun over a number of rotations. This is done by taking an IPS velocity measurement, and then mapping it back onto the source surface along an Archimedean spiral, i.e., a stream line, but this does not consider the stream-stream interaction. Velocity data is built up over a number of rotations, then displayed as in **Figure 4.27**. Here, we can see that between $-30°$ and $+30°$ latitude, there is an average velocity of about $350\,\mathrm{km\,s^{-1}}$,

except for the small areas of fast wind which probably indicate the presence of coronal holes.

4.2.4 The Yohkoh satellite

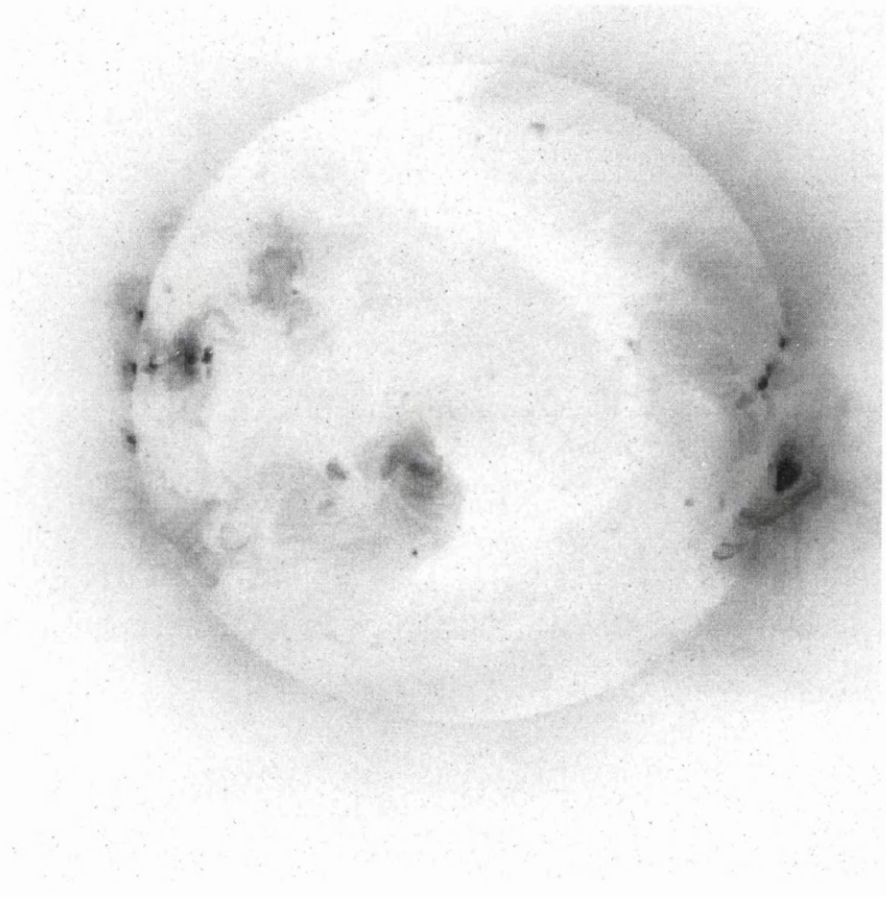

Figure 4.4: The Yohkoh SXT image for 7 July 1993. Note the coronal hole extending down from the North pole, and crossing the equator to join up with the southern coronal hole.

The Yohkoh satellite was launched in August 1991 from Japan, into a low Earth orbit with a period of 97 minutes. It carries a number of instruments, among them the soft X-ray telescope (SXT) which is sensitive to an energy band of 0.25 to 4 keV. The corona is at a temperature of several million degrees, emitting X-rays in this energy region, by a complex mixture of thermal bremstrahlung and line emission. Full-disk images of the corona taken daily by the SXT are available and from these, coronal holes can be studied.

In a coronal hole, the magnetic field is predominantly open, i.e. the region is threaded by magnetic field lines that have been drawn out into interplanetary space by the dynamical

forces of the coronal plasma. The electron density in a coronal hole is much lower than in a closed region of the corona.

In an isothermal plasma dominated by bremstrahlung, the coronal emission depends on the square of the electron density, as shown by Crannell [20]. The isothermal bremsstrahlung spectrum can be written as

$$I(\epsilon) = 1.3 \times 10^{-42}(n^2V)\epsilon^{-1.4}(k_BT)^{-0.1}e^{-\epsilon/k_BT} \quad \text{(photons/cm}^2\text{/s/keV)}, \tag{4.1}$$

Therefore, soft X-ray and EUV emission from open, low density coronal regions are very low compared to the dense closed corona that surrounds them. Coronal holes appear clearly on Yohkoh SXT images as white regions, see `Figure 4.4`. This image, and the others like it, comes YDAC, the Yohkoh Data Archive Centre, held at MSSL, Mullard Space Science Laboratory.

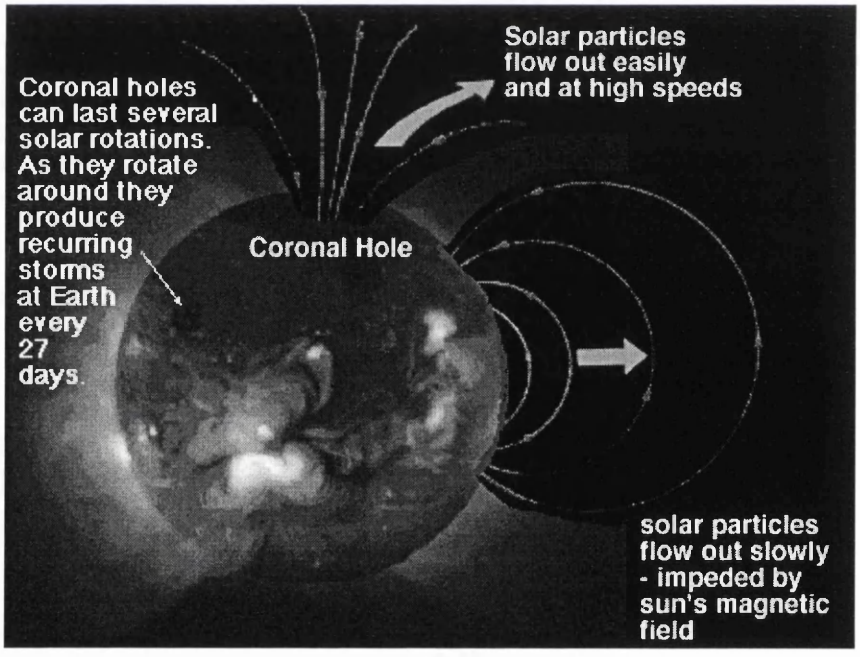

Figure 4.5: The magnetic field lines of the Sun, at a coronal hole, and elsewhere.

Coronal holes are believed to be the source of the fast solar wind [48], [100]. Because the holes are regions of open magnetic field lines, fast, free outflow of the solar wind is possible, see `Figure 4.5`. The long lived streams caused by stable coronal holes are

interesting to IPS observations, as explained later, and the Yohkoh STX images can help in the interpretation of the Cambridge IPS data.

4.2.5 The He 10830 Å Spectroheliogram

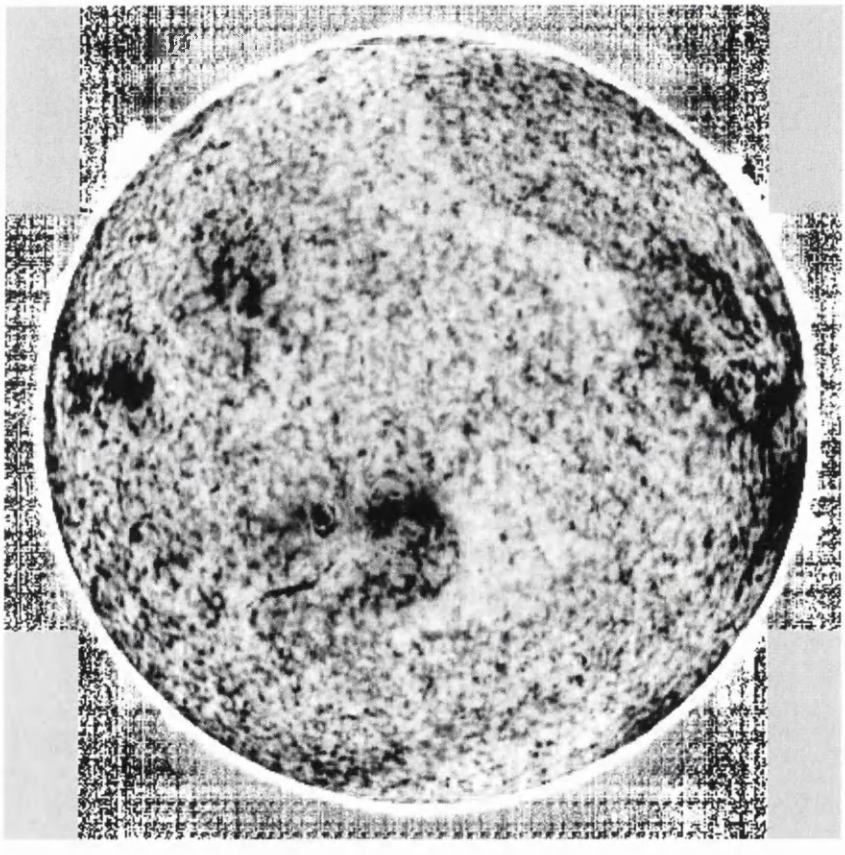

Figure 4.6: The He I spectroheliograph images of the full solar disk, taken on 7 July 1993, the same day as the SXT image in Figure 4.4. The position of the coronal hole in the SXT image can also be traced as the whiter area on this image.

Coronal holes are routinely monitored at the National Solar Observatory on Kitt Peak, by a spectroheliogram which takes a whole disk image of the Sun, in a Helium I line. This absorption line has a wavelength of 10830 Å, and is an excellent tracer of coronal holes.

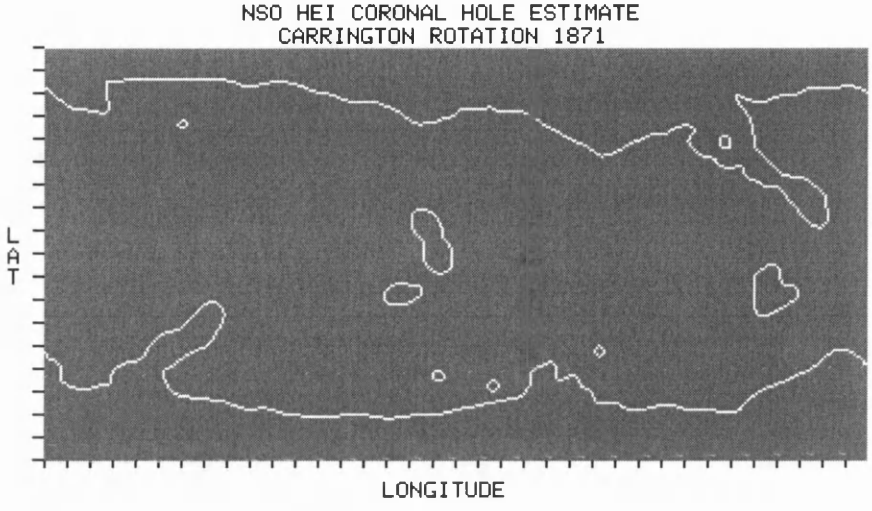

Figure 4.7: Synoptic He I map of Carrington rotation 1871, 3 - 30 July 1993. Heliographic longitude runs from 0° at the left to 360° at the right. The meridional strip at the centre of the Sun is recorded each day, and then stacked up together to form this plot. The meridional strip for the first day of the rotation (3 July) is at the extreme right, and the strip for the last day (30 July) is at the extreme left. The centre strip, at a longitude of 180° corresponds to the central meridian strip at the middle of the rotation (16 July). Heliographic latitude runs from −90° at the bottom (south pole) to +90° at the top (north pole). The coronal hole extending from the north pole at the beginning of the rotation (to the right of the map) is the same one seen in the previous whole disk images.

Because chromospheric helium is excited by the coronal soft X-ray emission, the spatial extent of coronal holes may be obtained from any monochromatic He picture. `Figure 4.6` shows a He I image for the same day as the SXT image in `Figure 4.4`. The same features can be observed in both images, especially the coronal hole. NSO/Kitt Peak data used here are produced cooperatively by NSF/NOAO, NASA/GSFC, and NOAA/SEL.

Also available are synoptic plots of coronal hole boundaries over a whole rotation. `Figure 4.7` shows a coronal hole reaching down from the North pole at the beginning of the rotation, and a southern hemisphere coronal hole near to it. These same two holes seem to be joined up in the corresponding SXT picture, `Figure 4.4`.

4.2.6 The GOES space environment monitor

NOAA (National Oceanic and Atmospheric Administration) operates a series of meteorology observing satellites called Geosynchronous Operational Environmental Satellites (GOES), orbiting the Earth at an altitude of 35000 km. GOES satellites carry onboard a space environment monitor subsystem, that measures X-rays, energetic particles and the magnetic fields at the spacecraft, as described by Joselyn *et al.* [41].

Solar Energetic Particles (SEPs) are often produced and then accelerated to very high velocities by the explosive release of energy associated with a solar flare, or the ejection of a CME. The travel times to Earth can be very short, depending on the location of the flare (or CME) on the face of the Sun presented to the Earth. The SEPs travel along the Sun's magnetic field lines [77], following an Archimedean spiral, due to the Sun's rotation. If the SEPs are ejected along a streamline that joins the Sun to the Earth (i.e. they are magnetically connected to the Earth), this enables the particles to arrive at the Earth promptly [26], perhaps within two hours, where they can be detected by GOES. If the location of the flare on the Sun is far from the streamline joined to the Earth, then the SEPs won't arrive at Earth until 2 hours after the Sun has rotated sufficiently for the flare location to be at the foot of the Earth-Sun streamline. This could be a matter of many days.

Also, energetic particles can be generated by particle acceleration at the front of an interplanetary shock wave [34]. The shock wave could be caused by high speed solar wind plasma emerging from a coronal hole. GOES should also be able to measure the energy and density of these particles.

Available online at NGDC (National Geophysics Data Centre) is a list of the solar proton events that have affected the Earth environment from 1976. This list is a starting point when searching for disturbances in the near-Earth environment, which led to enhanced geomagnetic activity.

4.2.7 The SAMPEX satellite

The Solar, Anomalous, and Magnetospheric Particle Explorer (SAMPEX) was launched by NASA in July 1992 into a near-polar, low Earth orbit, at an inclination of 82°. SAMPEX measures energetic electrons as well as ion composition of particle populations from ~0.4 MeV/nucleon to hundreds of MeV/nucleon. It can therefore record interplanetary fluxes of solar energetic particles (as well as galactic cosmic rays, which cause a known residual background rate) over the polar portions of its orbit. The intensities plotted in diagrams such as `Figure 5.13` are obtained by averaging over the two polar cap passes (i.e. above 70° invariant latitude) of each orbit. The spacecraft and its mission are described by Baker *et al.* [4].

Similar to GOES, SAMPEX data can be used to discover when the Earth is affected

by SEPs.

4.2.8 The Metsähovi Radio Observatory

The Metsähovi radio observatory is operated by the University of Helsinki in Finland. The 14m diameter radio telescope operates at frequencies of 5 - 120 GHz. About 25% of telescope time is spent on solar research [63]. From these observations, a solar flare catalogue has been compiled, detailing radio burst events caused by solar flares. The unit of radio emission from the Sun is the solar flux unit (sfu), where

$$1\,\mathrm{sfu} = 10^4\,\mathrm{Jy} = 10^{-22}\,\mathrm{W\,m^{-2}\,Hz^{-1}}\,. \tag{4.2}$$

During a radio burst, the measured flux can be as high as 500 sfu relative to the quiet Sun level. The solar flare catalogue is useful because it covers the entire period of the Cambridge IPS survey, and can indicate times of solar activity, which might lead to transients in the IPM.

4.3 Direct comparison of Cambridge data with other sources

The Cambridge IPS data can be compared with near-simultaneous observations made by other instruments. This comparison is a very good way of validating a new technique. Unfortunately, it is very difficult to make an exact match between the Cambridge data and any other data set, because no other instrument observed exactly the same part of the sky at the same time as the Cambridge IPS array.

The results of data set comparisons are instructive, and follow in the rest of the chapter.

4.3.1 Cambridge IPS density data versus IMP density data

Tappin [89] has compared IMP density values to IPS g values, and arrived at a relationship between g and the density, n (measured in particles per cm^3),

$$g \simeq \left(\frac{n}{9}\right)^{0.52}. \tag{4.3}$$

In doing so, Tappin was very careful to select days when both instruments were measuring approximately the same portion of solar wind material, i.e., since IMP is at a distance of 1 AU, its data can only be compared with IPS data corresponding to material at 1 AU.

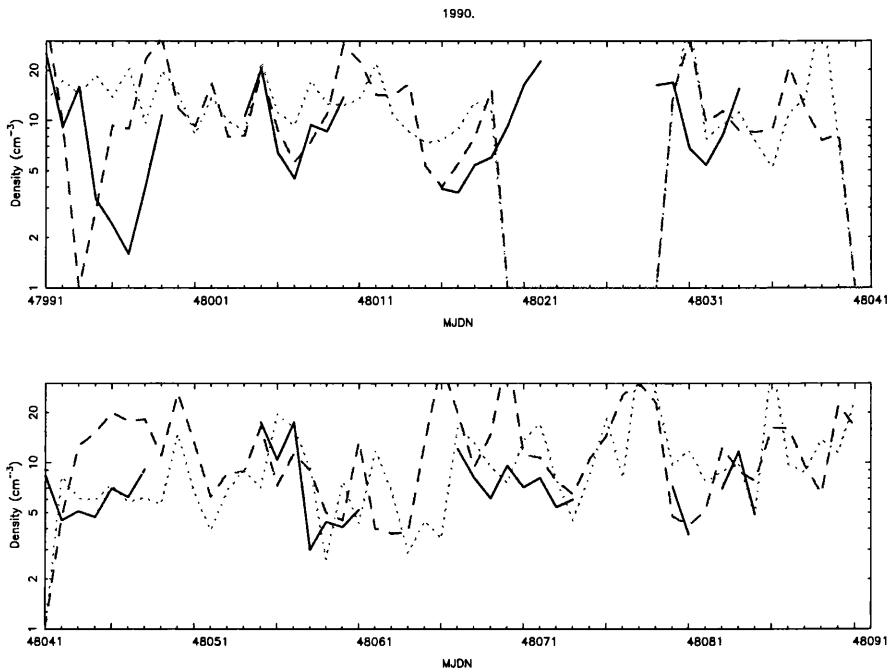

Figure 4.8: IMP density data plotted with the Cambridge IPS density (extracted from the g values using Tappin's relationship) for 100 days in 1990. The solid line represents the IMP density measurements. The dashed line shows the average density measured from sources east of the Sun by the IPS array, while the dotted line represents the Western IPS sources. When the IPS data drops to 1 (e.g. days 48019 to 48028), this means that there were no data taken on this day.

This same relationship is expected to come out of the present comparison of the 1990-94 data set, but it was difficult to emulate. This was due mainly to problems in determining where along a line-of-sight to a source the greater amount of the scintillation is occurring, and the possible disruption to the average g caused by a small amount of transient material.

Out of each 12-day orbit, the IMP spacecraft spends only 7 or 8 days actually in the solar wind, and the remainder within the Earth's magnetopause. This leads to regular gaps in the data set, and hence reduces the amount of possible correlations.

There is also a problem of where each instrument measures the density. IMP measures solar wind parameters at 1AU, at the position of the Earth. But the IPS array, when looking towards a source at an elongation of 90°, is observing the scintillation at 1AU from the Sun, but at 0.5AU from the Earth, as previously seen in `Figure 3.1`. It is therefore difficult to determine when both experiments are observing the same portion of the solar wind simultaneously.

`Figure 4.8` shows a straight comparison of the IMP density values and the IPS values, over 100 days. The IMP value is the average for that day of all the measurements, so by

taking this average, some transient activity could be missed.

The IPS density parameter is worked out by taking the average of all the g values from sources $\sim 90°$ elongation east and west of the Sun, for each day.

$$80° < \epsilon < 100° \tag{4.4}$$

and

$$\text{Declination} < 25°. \tag{4.5}$$

The density was inferred using Tappin's relationship, see `eqn. 4.3`. It can be seen that the IPS measurements generally follow the IMP measurements, especially the eastern sources. Because there is a time delay between the material arriving at the IPS observation point and the Earth (for IMP observation), there is some difficulty in correlating the IMP and IPS data points in time. Also, in this first comparison, no attempt was made to select only the days where the solar wind was uniform over the volume of IPM observed.

The best way to account for this time delay is to only take into account the days when the Earth is bathed in a long-lasting stream of material. Then, the material observed by IMP should be the same as that observed by the IPS array. Even though the solar wind travels radially out from the Sun, the rotation of the Sun means that we observe material to be moving out in an Archimedean spiral. It is therefore best to choose only the sources to the east of the Sun, as that is where the material appears first.

Taking these extra factors into account, the program `SCDcDi.c` was written. In the chosen area ($\sim 90°$ eastern elongation), all the valid g values from their respective sources are used to calculate the geometric average. Then, the gs are examined again, and any that show more than 50% deviation from the mean are discarded, and the geometric mean is recalculated. To ensure that it is the same material being observed by both instruments, the IMP density value is compared with the density on the preceding and following days. If these values are within a range showing $\sim 10\%$ deviation, then it may be considered to be a long lasting stream. Now it can be compared with the IPS density average for that day. Another condition applied was a maximum cutoff for the standard deviation of the g values.

Despite all these criteria, it proved to be very difficult to automatically choose the appropriate days for comparison. `Figure 4.9` shows the correlation for the first year, 1990, and a chi-squared straight line fit. Also shown is a dashed straight line plot of

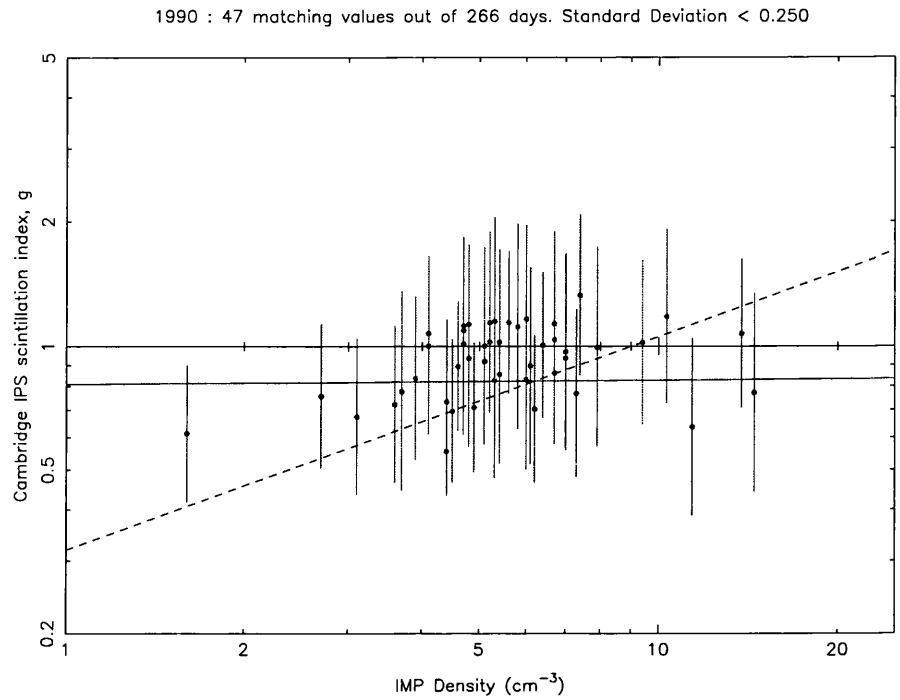

Figure 4.9: A scatter plot of IMP density data compared to the Cambridge IPS g values for 1990. The vertical error bars are the standard deviations from the sets of g values used. The solid line (not the g=1 axis) is a chi-squared fit to the data, and the dashed line is the relationship between density and g, as deduced by Tappin.

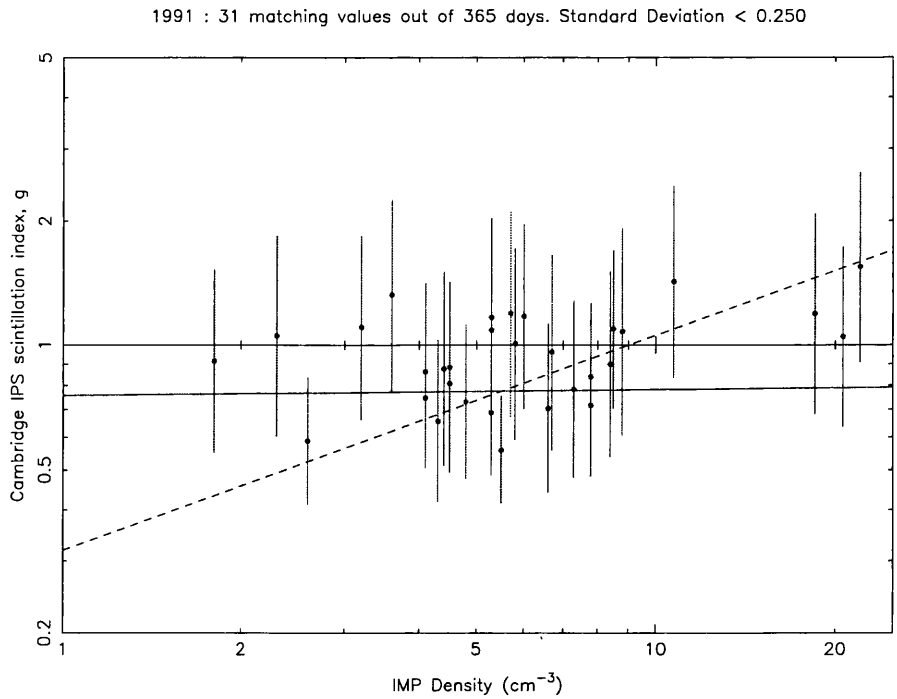

Figure 4.10: IMP density data compared to the Cambridge IPS g values for 1991.

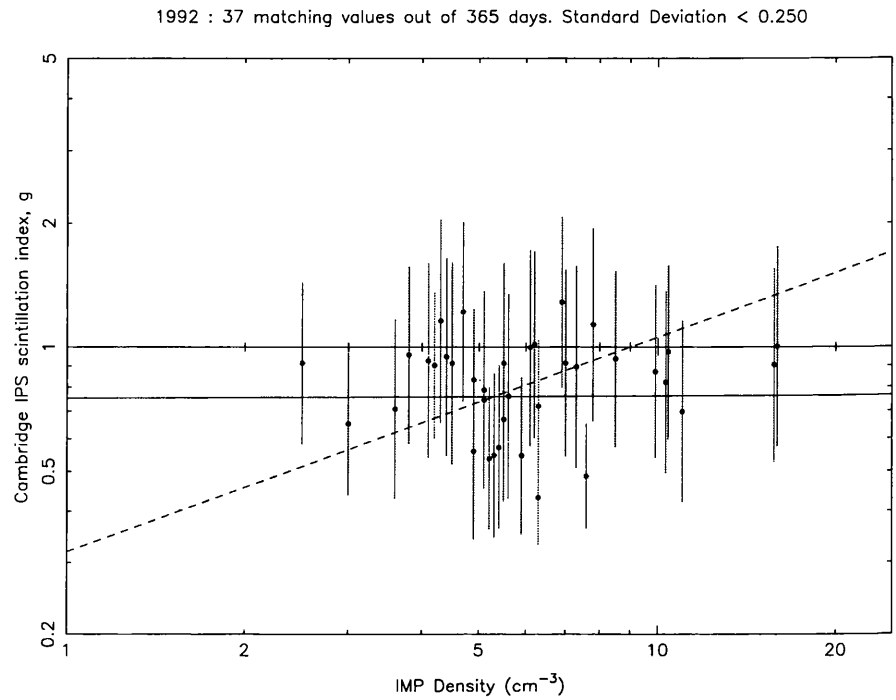

Figure 4.11: IMP density data compared to the Cambridge IPS g values for 1992.

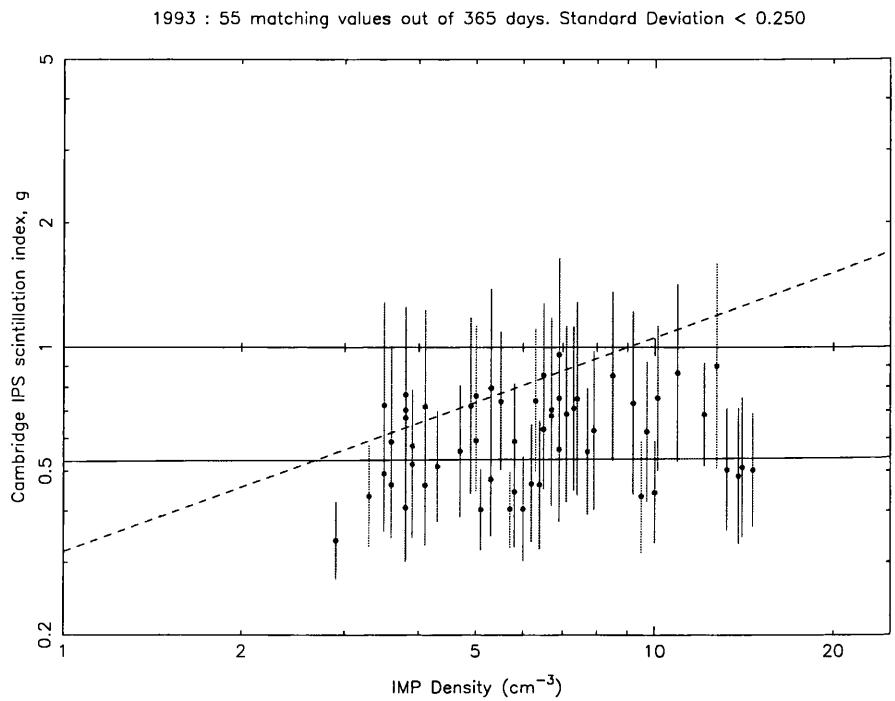

Figure 4.12: IMP density data compared to the Cambridge IPS g values for 1993.

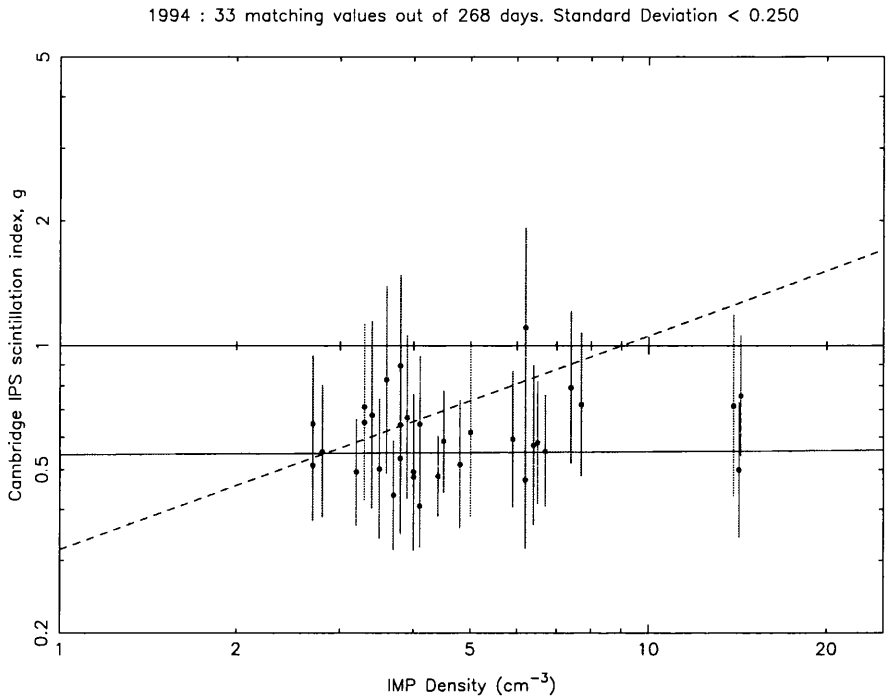

Figure 4.13: IMP density data compared to the Cambridge IPS g values for 1994.

Tappin's relationship between density and g. Then the following four figures show the plots for the next four years.

The chi-squared fit is quite diffferent from Tappin's relationship, but there is a definite trend in the data. It implies that Tappin's relationship can still be used on the current data set, with a certain degree of confidence. If each g value had been chosen separately on its individual merit, rather than by an automatic process, then the fit could be expected to be better.

4.3.2 Cambridge IPS density data versus Ulysses density data

In a similar manner, we can compare the Cambridge IPS density data with the data recorded by Ulysses. This is particularly the case when Ulysses was near to the Earth, e.g. in the two months after Ulysses was launched. `Figure 4.14` shows the direct comparison from the day that Ulysses began to take plasma measurements on 18 November 1990 until the end of 1990.

Soon after launch, on 18 November, Ulysses was only 1.15 AU from the Sun, and close to the Earth. Therefore, the plasma parameters recorded by Ulysses are very similar, in

spatial terms, to that measured by the IPS array.

There is a much greater probability that the plasma will retain the same properties in the short time between measurements. Indeed, the Ulysses density plot follows almost exactly the pattern of the east line for the first eight days. (As explained in the last section, the better correlation should be for the eastern sources rather than the western sources because the plasma coming out from the Sun is seen first to the east.)

After this, the Ulysses plot gradually falls behind the plot for the eastern sources, until there is a time lag of about three days at the end of the year. At this time, Ulysses has travelled to 1.51 AU. The average velocity measured over the last five days in December by Ulysses is about $339\,\mathrm{km\,s^{-1}}$, which corresponds to 0.196 AU per day.

The solar wind will travel approximately 3×0.196 AU=0.59 AU in three days. This is consistent with the previously deduced three day time lag between measurements at the Earth (1 AU) and at 1.51 AU from the Earth. The Ulysses data are therefore consistent with the densities measured by the Cambridge IPS array.

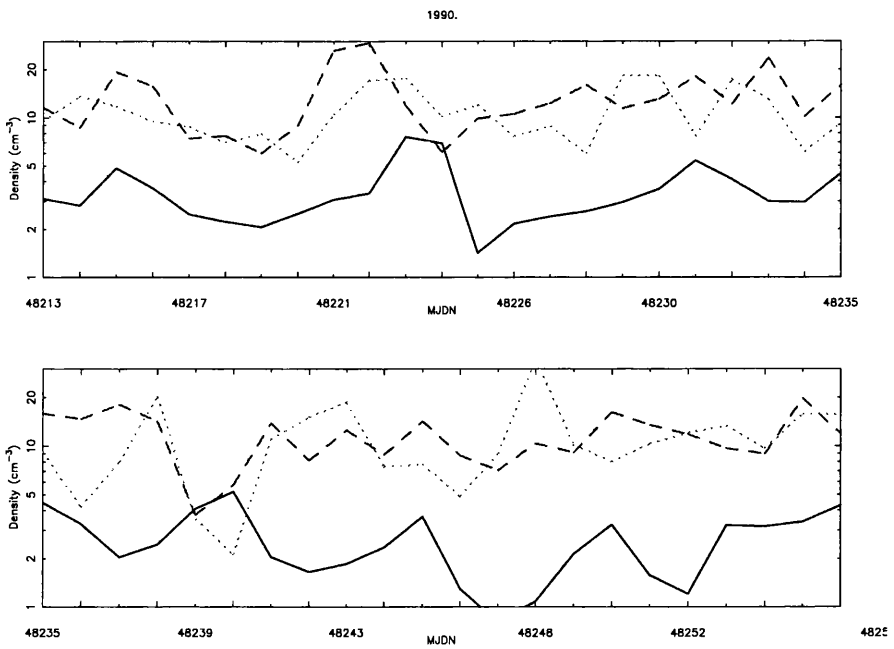

Figure 4.14: Ulysses density data are represented by the solid line. It is plotted against the average density measured by the Cambridge IPS array, from sources east (dashed line) and west (dotted line) of the Sun.

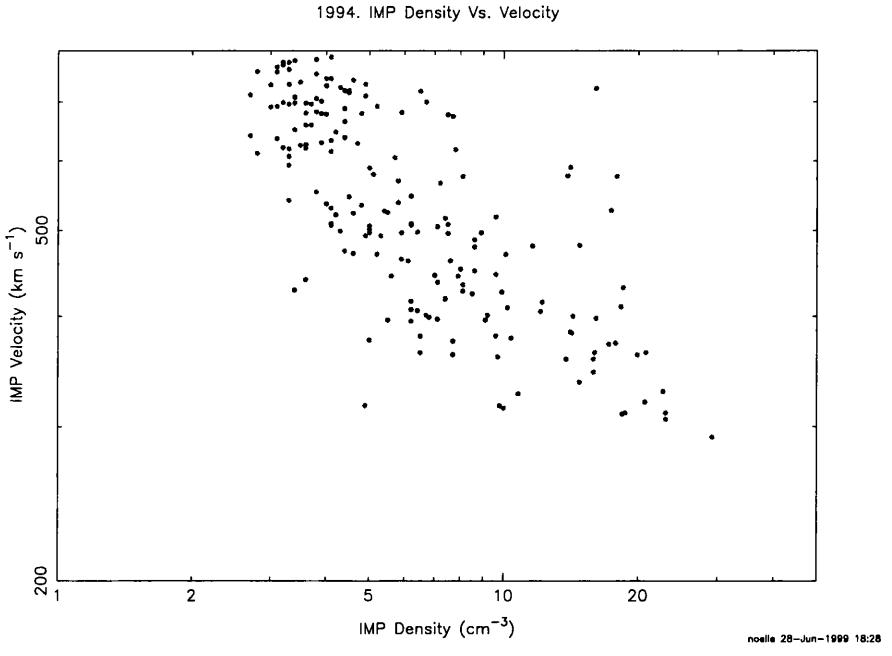

Figure 4.15: IMP density data plotted against the corresponding velocity measured by IMP on the same day, over 1994. The fastest wind is definitely the lowest density wind.

4.3.3 Density versus velocity

As a general trend, it is usually low density material that travels fastest. Therefore, a plot of density versus velocity will show the velocity decreasing as the density increases. `Figure 4.15` plots the density measured by IMP versus the velocity measured on the same day, over 1994. The decrease in velocity with increasing density is evident.

`Figure 4.16` plots the same parameters at solar maximum in 1990, and this trend isn't quite as obvious. This trend is not as strong at a peak of solar activity, where the interplanetary medium can get very complex and unpredictable. Fast wind can be as often high density as low density.

Now we look at the same relationship for the Cambridge data set, compared with the Nagoya velocity data. In this case, just one source is examined. Because both experiments are using IPS as their measuring tool, it might be thought that they are observing the same portion of the solar wind. However, the radio sources are observed at different times during the day, so the solar wind along the line-of-sight may have changed significantly during the period. This is because the Cambridge array is a meridian transit telescope, while the Nagoya telescope is steerable and can hence look at any part of the sky when

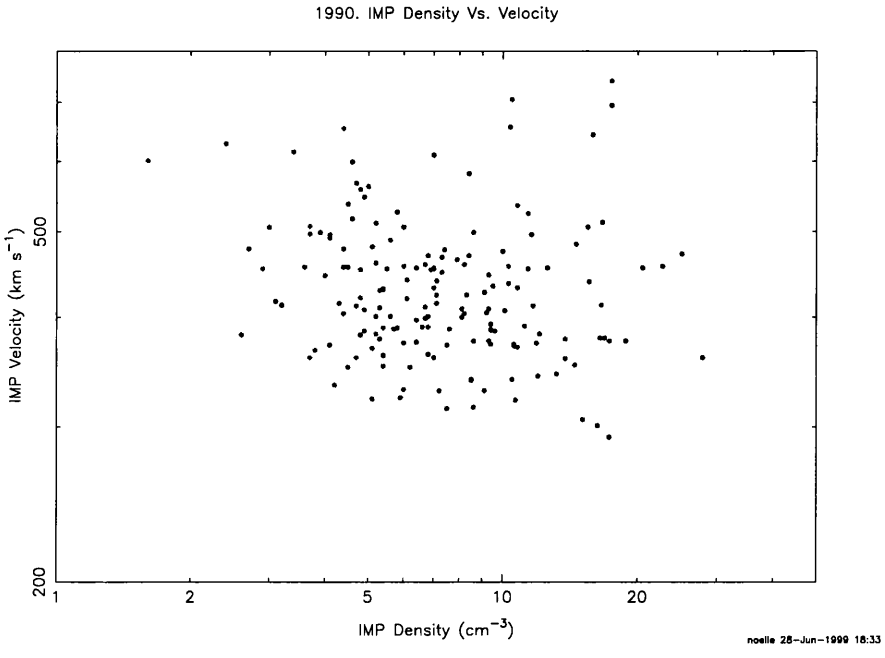

Figure 4.16: IMP density data plotted against the corresponding velocity measured by IMP on the same day, over 1990, the solar maximum. The relationship between velocity and density is not as clear-cut.

required.

In Figure 4.17, data are taken for the source 3C119, from the Cambridge and Nagoya data sets, in the year 1993. The density measured by Cambridge is plotted against the velocity as measured by Nagoya. The velocity/density trend is apparent, as would be expected during the relative quiet of solar minimum in 1993. The low density wind is seen to be moving faster.

But in Figure 4.18, the same parameters are plotted for 1990, the maximum in solar activity. This plot is more "confused", with no clear relationship between velocity and density, as would be expected.

So it has been shown that the Cambridge data set can be used in conjunction with Nagoya velocity data to display the same trends that are apparent in single-instrument IMP-8 studies.

4.3.4 Cambridge velocity versus Nagoya velocity data

As we discussed in the previous chapter, the errors in the Cambridge IPS timescale data are much larger than those in the density data. This is because the timescale algorithm needs a much longer integration time than is available with the Cambridge meridian transit

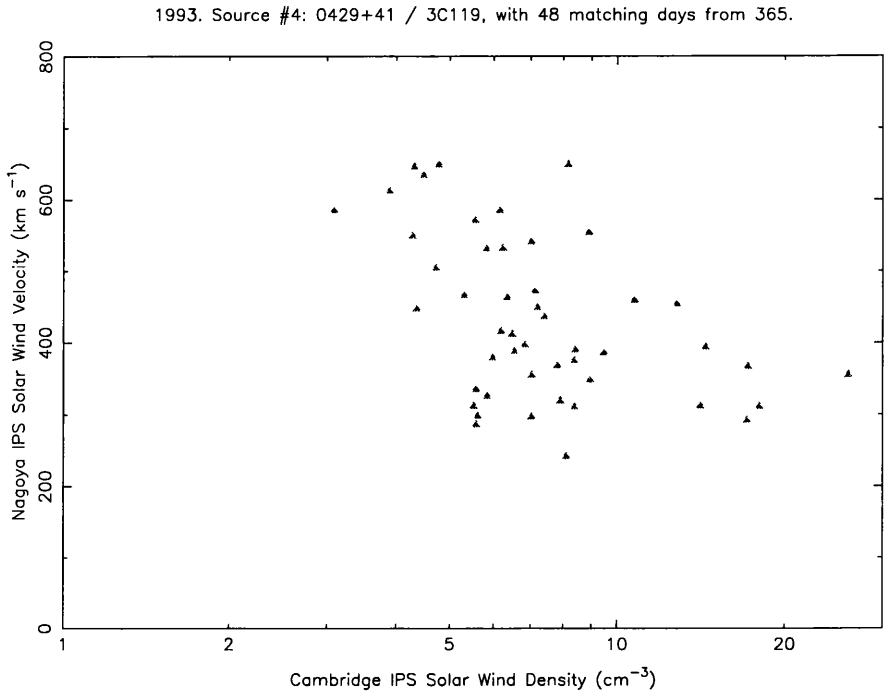

Figure 4.17: Cambridge IPS density data for one source plotted against the velocity from the same source measured by the Nagoya instrument on the same day, over 1993, after solar maximum. The velocity is certainly decreasing with increasing density.

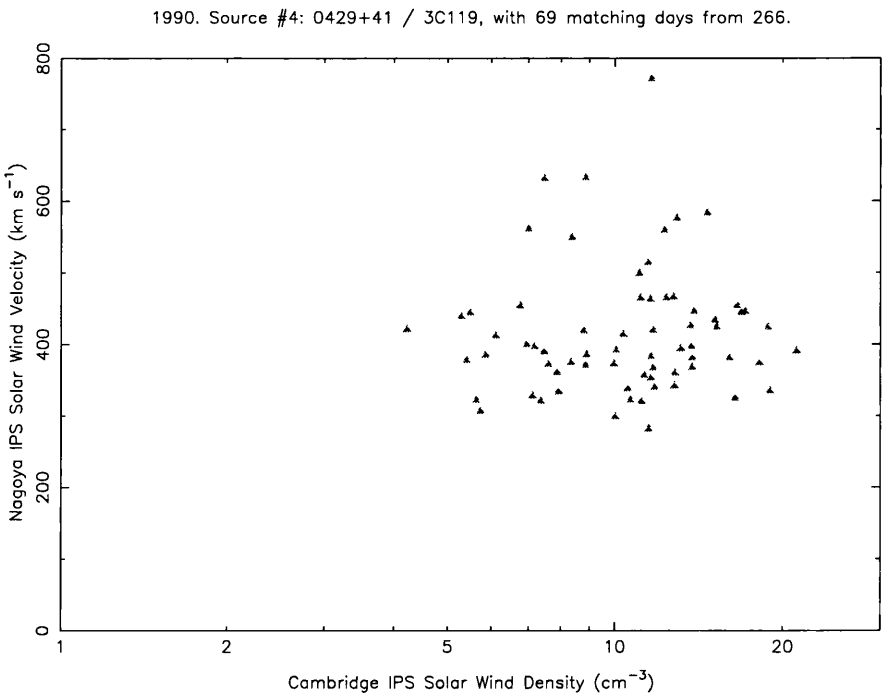

Figure 4.18: Cambridge IPS density data against Nagoya velocity, over 1990, the solar maximum. The velocity/density relationship is unclear, as would be expected for the complex solar wind during maximum solar activity.

telescope to obtain a respectable signal-to-noise ratio. But for high declination sources, the transit time is longer, so the algorithms have a lot more data to work with, and hence produce more accurate results.

There are about 22 strongly scintillating sources that regularly give reasonable timescale data, and which can be used to determine velocity information. Following Readhead *et al.* [68].

$$\text{velocity} = \frac{a}{\tau}, \tag{4.6}$$

where the scale length, $a(r)$, is the characteristic spatial coherence length over which the plasma density fluctuates, and r is the distance from the Sun. The expression for $a(r)$ has two forms, depending on r,

$$a = 175 r^{0.5}\,\text{km} \quad \text{for } (0.1\,\text{AU} < \text{r} < 0.6\,\text{AU}) \tag{4.7}$$

$$a = 250 r^{1.25}\,\text{km} \quad \text{for } (0.6\,\text{AU} < \text{r} < 1\,\text{AU}) \tag{4.8}$$

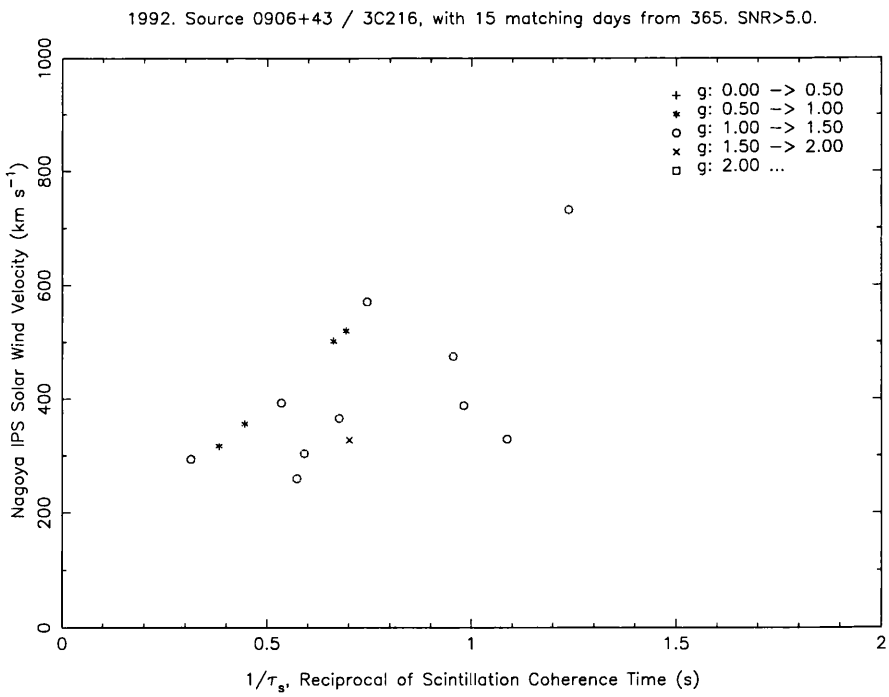

Figure 4.19: The reciprocal of Cambridge IPS timescale against Nagoya velocity, over 1992, for 3C216. The g value corresponding to each timescale measurement is represented by the type of symbol, as explained on the graph. The velocity is inversely proportional to the timescale, so we expect a straight line graph, as indeed observed here.

Figure 4.19 looks at the data for 3C216, a high declination source. The scintillation timescale has been worked out by the τ_s algorithm from data measured by the Cambridge

IPS array. Its reciprocal is plotted against the velocity measured by the multi-station Nagoya IPS telescope. There are only a limited number of days that both instruments observed the same source, and recorded reliable data with a good SNR.

As predicted, the timescale is inversely proportional to the velocity. The plot is expected to show reduced correlation because the source is usually observed at different times of the day by each telescope. This means that each telescope is sampling a slightly different portion of the solar wind.

Data recorded for this source, 3C216, were consistent with prediction. Unfortunately, there were practically no data that could be compared in the next two years for this source. This was because the few days that Nagoya observed the source didn't coincide with the days that the Cambridge observations were of high enough SNR for the τ_s algorithm to work properly. And other sources, most of lower declination, gave inconclusive results.

More work needs to be done to prove that this novel, single-station method provides sound information on scintillation timescale, and hence velocity. Using a steerable telescope would mean that sources can be observed for much longer, thus making the τ_s algorithm more effective in calculating the true velocity. But for the meantime, the values worked out by the τ_s algorithm will continue to be used, though always keeping in mind that there are errors involved. Only when a large number of sources are consistently providing similar output on a daily τ_s-map can we believe that we're seeing the true picture of conditions in the IPM.

4.4 Study of specific events

4.4.1 Observations of a long-lived solar wind stream

Before studying a particular event, it is essential to understand the geometry of how a co-rotating stream appears on a g-map. If the Sun were not rotating, the geometry of the IPM, and how the solar wind interacts with it would be much simpler. The corona would just expand out radially, as seen from Earth. But, because of the Sun's rotation, the streamline that follows material coming from the same section of the Sun is a Parker spiral, as seen in `Figure 4.20`. The speed of the wind determines just how tightly wound this spiral is. A slow wind would have a tightly wound spiral, while for a fast wind, the spiral would be looser.

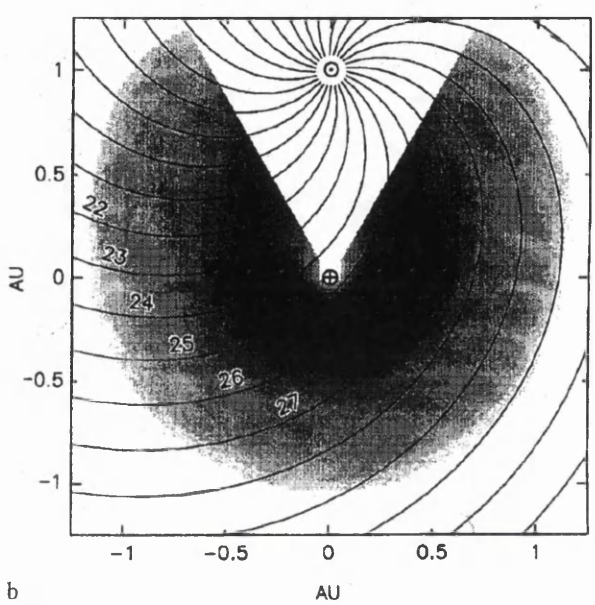

Figure 4.20: Parker ecliptic spirals for a solar wind at an average velocity of about 400 km s^{-1}, which corresponds to 0.25 AU day^{-1}. The numbers 22-27 show the approximate position of an enhancement front on consecutive days, when the thickness of this front is approximately the same as the distance between two adjacent spirals.

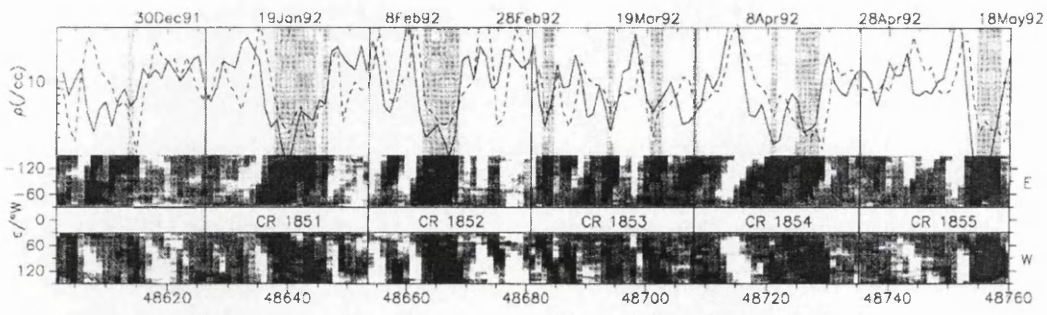

Figure 4.21: Synoptic plots covering Carrington rotations 1850 to 1855, when a long-lived stream was very prominent. It is seen as the recurrent, low-density section towards the middle of each rotation.

During a solar rotation, a long-lived, co-rotating stream will first appear to the east of the Sun and from there it will tend to spread out to greater eastern elongations. Then, as seen on day 25 in Figure 4.20, the stream will sweep across the Earth, and later appear to the west of the Sun. This is indeed what can be seen in the g-maps, as explained in the following example.

From Carrington rotation 1849 to 1856, a long-lived solar wind stream was observed by the Cambridge IPS array, as well as other experiments. This is very obvious in the synoptic plots made by Woan [97]. These plots divide the sky into 5° wide elongation strips. In each strip, the scintillation is averaged, and given a grey-scale value. This is then plotted for each strip, on a synoptic plot, for each day over a long time period. The co-rotating stream showed up as a low scintillation section, recurring every 27 days. It can be seen in Figure 4.21 to the middle of the Carrington rotation sequence.

During this interesting period, a large polar coronal hole was seen to extend to equatorial regions, sometimes even crossing the equator itself. On the He 10830 Å spectroheliogram maps, this extension of the polar coronal hole is located between heliographic longitudes of about 240° to 300°, as in Figure 4.22

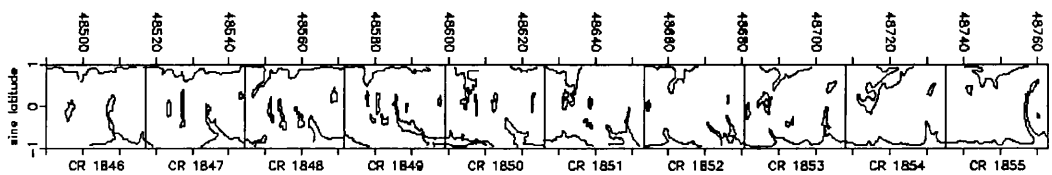

Figure 4.22: Coronal hole boundaries from the He 10830 Å spectroheliogram maps, for rotations 1846 to 1855. Carrington longitude runs from right to left.

This coronal hole can also be seen on the Yohkoh SXT image from April 3rd 1992, in Figure 4.23. The white areas are emitting fewer soft X-rays, and are therefore indicative of open magnetic field lines. Areas of high emission indicate closed field lines. As previously explained in section 4.2.4, a coronal hole is where the field lines are open, and material is streaming out into space. The white area extending from northern polar regions down to the equator in Figure 4.23 is the coronal hole that is contributing a great amount of fast moving, low-density material to the IPM. The material moves out quickly from the Sun to reach the Earth a few days later.

The high-speed, low density stream from the coronal hole is observed on the Cambridge

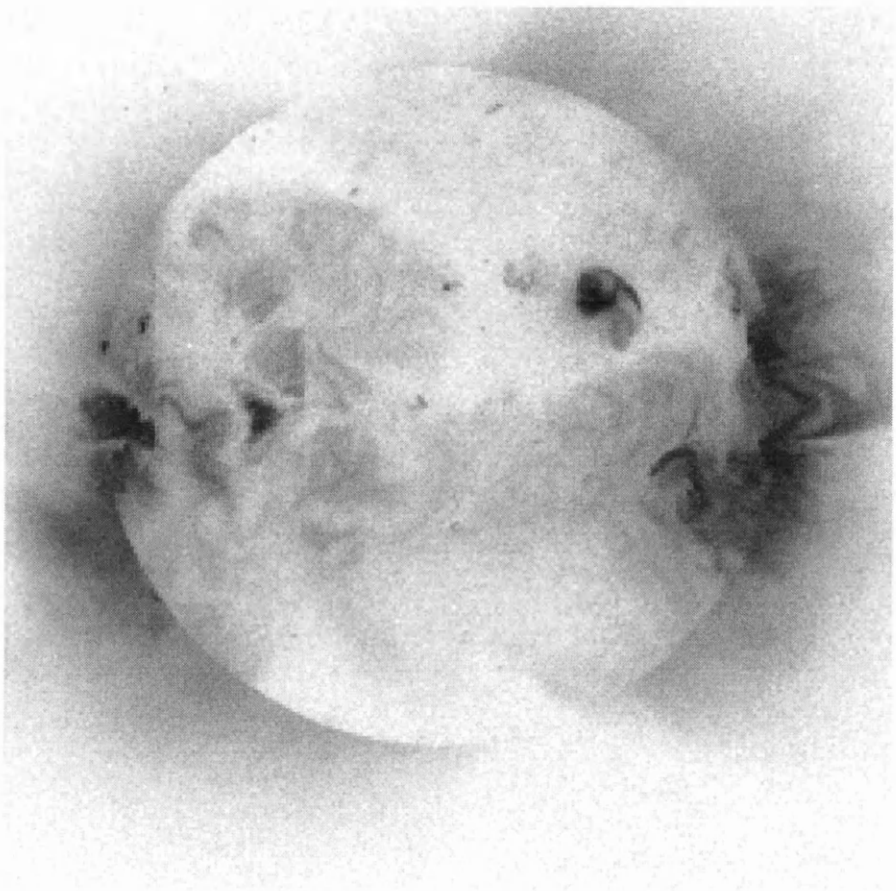

Figure 4.23: Yohkoh SXT image on 3 April 92. Intense soft X-ray emission shows up as the darker areas. The white, low emission areas represent coronal holes.

g-maps and τ_s-maps covering the period 1 to 9 April 1992. The low density plasma first appears to the east of the Sun (shown in `Figure 4.28` on 2 April 1992), and over the course of a few days, it moves outwards from the Sun to dominate the IPM to large elongations.

Clumped together in front of this high speed wind is a large expanse of high-density material - this is seen on 2 April 1992, in `Figure 4.28`, as the red area taking up most of the g-map. But also on this day we begin to see the low-density plasma flow. This is the low-g area directly to the east of the Sun, at an elongation of about 40° to 60° in `Figure 4.28`.

This same low-density flow is observed to travel outwards on the succeeding days. On the next day, 3 April, it has reached about 80°, as seen in `Figure 4.29`. By 4 April, `Figure 4.30`, it has progressed to an elongation of $> 90°$ and has therefore reached the

Earth. In Figure 4.31 we can see it on both sides of the Sun on 5 April. This low-density stream continues to dominate for some time.

Looking at the limited τ_s information that is also on these maps, it seems to agree generally with the high-speed stream hypothesis. The τ_s measurements which correspond to increased scintillation are more reliable because the scintillating flux is far above the noise level for many of the sources. In the case of low scintillation, there are very few sources whose scintillating flux is high enough above the noise level.

In Figure 4.28, there are a lot of sources with low τ_s readings, i.e., fast wind, at elongations of 90° to 120° to the east and at low latitude. This is the dense material that has been clumped up by the fast flow behind it, and now is moving rapidly itself. Similarly on 3 and 4 April, there are still many low τ_s measurements in this area. By 5 April, there are low g values in this particular area, leading to very few τ_s measurements, so no reliable wind speed values are available in that area.

If we now look to the west of the Sun, and concentrate on the areas where there is high scintillation, we see evidence again that the clumped-up material is moving rapidly. Even when the τ_s data are quite sparse on 5 April, almost all the measurements are low τ_s, indicating a fast wind.

Comparison with IMP data

Unfortunately, the IMP data for these dates are incomplete, but they can give us some indication of the conditions at 1 AU from the Sun. Figure 4.24 shows that on 2 April, the wind speed at IMP increases slightly, but then there are no further data until 7 April. By this time, the speed has reached over $600\,\mathrm{km\,s^{-1}}$, and falls gradually to $300\,\mathrm{km\,s^{-1}}$ by 11 April. Also, the density is very low on 7 April, and stays low for at least a further eight days. This is consistent with the interpretation of the IPS data above, and supports the idea of a long-lived, high-speed stream.

4.4.2 Observations of a transient event

This section describes a transient event observed by a number of instruments that took place in November 1990. The Cambridge IPS array observed a density enhancement with a g of at least twice the normal, moving outwards from the Sun and up out of the ecliptic plane. This enhancement front was very likely caused by a CME.

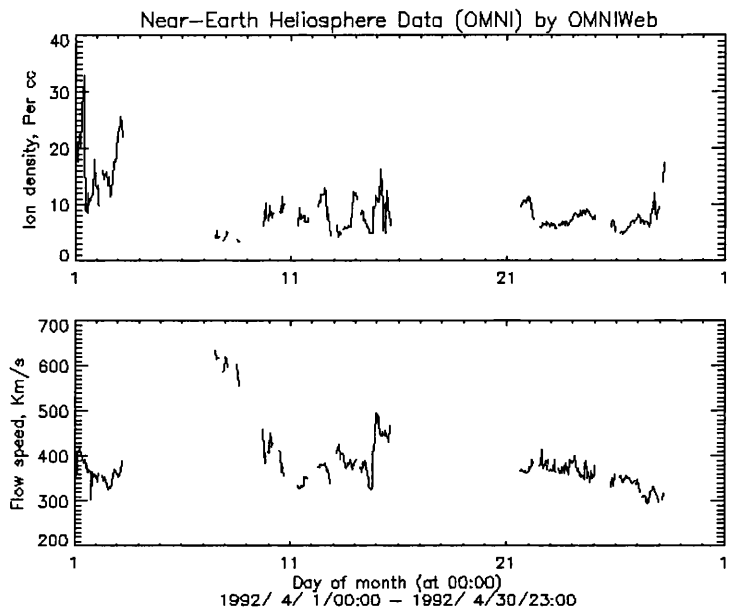

Figure 4.24: Density and velocity parameters as measured by IMP during April 1992. Though incomplete, the data here still match the conditions as found by the Cambridge IPS array.

On 19 November, there is some enhanced scintillation north of the Sun, but it is not very structured, as seen in **Figure 4.32**. Then, on 20 November a well-defined "arch" of high density material has formed, linking from the east to the west of the Sun, centred on approximately 60° solar elongation, as in **Figure 4.33**. In this arch, the g value is at least twice the normal, so the density is about four times the ambient. (Remember that $n \propto g^2$.)

This arched structure has travelled out to $\sim$ 90° from the Sun by 21 November (**Figure 4.34**), still retaining its arched shape. On 22 November, the structure seems to have moved on and left behind a void which can be seen as the reduced scintillation to the east of the Sun (**Figure 4.35**). The enhancement front itself has diffused a great deal to a degree that it is almost unobservable to the IPS array. Perhaps there is a faint trace of it in the slightly enhanced material at $\sim$ 90° west, and at $\sim$ 145° east.

If we now concentrate on the τ_s maps, there is much evidence that this enhancement front was moving fast. On 20 November, there are only sources with a short scintillation timescale in the area of the sky where the front is, while any other sources are showing a longer timescale. Then on 21 November, the only the sources showing short τ_s values are those at higher declinations (about 90° north of the Sun) where the front is observed. All

these short timescales would indeed suggest a fast moving enhancement front.

It is possible to do a crude calculation of the front velocity just from its position on successive days. Roughly, if we look along the north-south centre line, the elongation of the middle of the front is $\sim$ 60° on 20 November. On the following day, it has moved to $\sim$ 90°. That means a difference of 30° over one day, corresponding to $\frac{1}{3}$ AU per 24 hours.

$$\frac{\frac{1}{3} \times 1.496 \times 10^8 \text{ km}}{24 \times 60 \times 60 \text{ s}} = 577 \,\text{km}\,\text{s}^{-1}\,. \tag{4.9}$$

This is an approximated estimate of the velocity. If a different part of the structure were tracked, then a slightly different velocity would have ensued.

The movement of this structure leads us to believe that it was actually a transient, rather than a long-lived co-rotating stream. It appears in the sky at both eastern and western elongations at the same time. Then, instead of swinging westwards as a co-rotating stream would, this structure moves northwards, and retains its shape for two days at least. It is most likely to be a large, fast-moving CME, pushing together interplanetary material in front of it to form an enhancement front.

More evidence comes from other instruments. Unfortunately, the IMP spacecraft provides no information for the dates of this particular event, but Ulysses was in a favorable position, and was taking measurements.

Comparison with Ulysses plasma data

Figure 4.25 shows the plasma density and velocity as measured by the Ulysses spacecraft in November 1990. At that time, it was approximately 1 AU from the Sun, so it is appropriate to use these data as if they were taken in the IPM near to the Earth. The spacecraft was at 1.17 AU on 20 November. In fact, Ulysses only started to take plasma measurements on 18 November 1990, so that was just in time to observe the passage of this interplanetary transient.

There is an obvious increase in density on 20 November, from about 3 to 8 particles cm^{-3}. After two days, the density returns to normal. At the same time on 20 November, the measured velocity jumps from an average speed of about 425 $\text{km}\,\text{s}^{-1}$ to over 510 $\text{km}\,\text{s}^{-1}$. This is what would be expected for the passage of a CME. After two days, the velocity has returned to the ambient level, but continues to fall over the next five days, going as low as 300 $\text{km}\,\text{s}^{-1}$. This low velocity could be associated with the aftermath of the CME.

On 27 November, there is an even greater rise in density, and in velocity. This can be supported by features observed on the corresponding g maps. From 24 to 26 November, there is a high-density feature growing larger to the north-east of the Sun. On 27 November, most of the sky is showing enhanced scintillation, as this transient feature engulfs the Earth. Then it passes away northwards. Possibly this was another, larger CME.

This second transient was observed by IMP, as seen in **Figure 4.26**. There is a sizable increase in density on 27 November, from about 5 particles cm^{-3} to 30 particles cm^{-3}, and lasting just over one day. The velocity also jumps from approximately 330 $km\,s^{-1}$ to 575 $km\,s^{-1}$ on 27 November, and there are very sparse data in the following days.

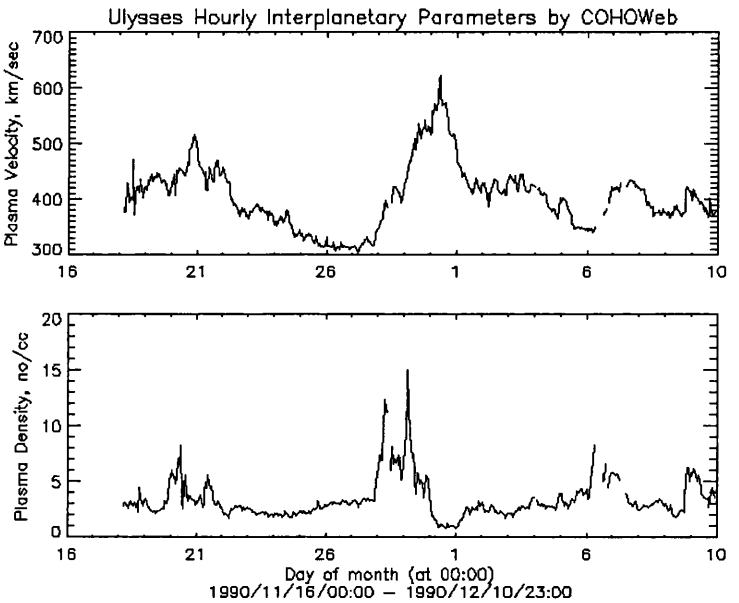

Figure 4.25: Ulysses plasma data from November to December 1990.

Ulysses & Metsähovi radio bursts

For most of 22 November, and from 10:20 to 16:00 on 23 November, Ulysses recorded a series of type III radio bursts. The maximum flux was 5.1 sfu (solar flux units). These type III bursts might be associated with solar flares or some other solar activity related to the CME.

Also, at 11:42, the Metsähovi radio telescope recorded a strong, 8-minute burst, with a flux of >20 sfu, supposedly related to a flare at latitude N15°, and longitude W28°.

Perhaps these radio bursts were associated with the same activity on the Sun as that

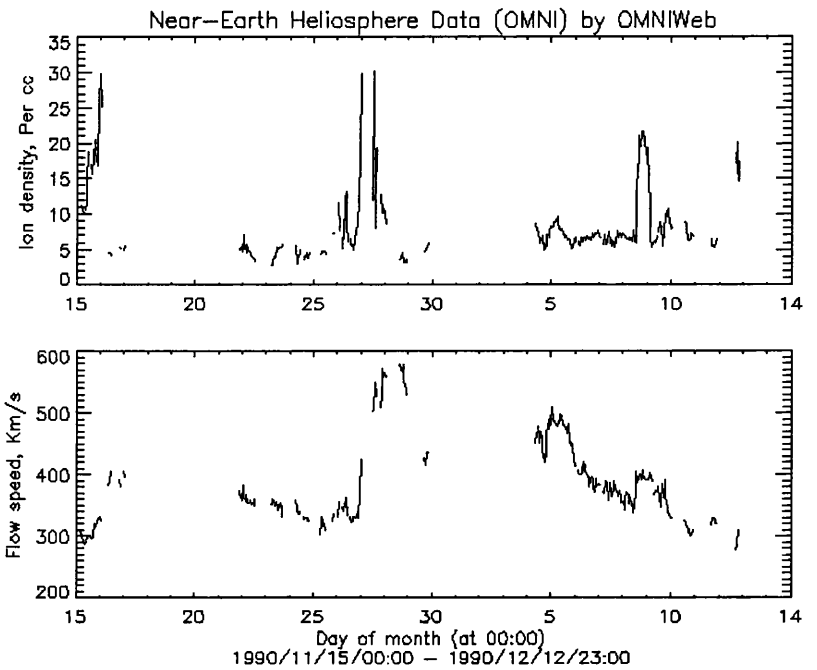

Figure 4.26: IMP plasma data from November to December 1990.

which caused the transients. It has been known for flares to be associated with the ejection of a CME, though it is certainly not always the case. It is very difficult ascertain this for certain, due to the small amount of evidence available.

4.5 Conclusions

It would not be feasible to have in-situ spacecraft all over the IPM to measure the solar wind parameters. Instead, the Cambridge IPS array is an ideal remote sensing device producing good quality, all-sky g-maps. The all-sky maps can be used to understand the physical processes in the IPM, as has been proved by comparisons with other data sources, when available.

The single-station method applied for calculating the velocity of the solar wind is not as accurate due to the very short observing time for each source. But if a large number of pixels across the sky are approximately the same colour, then many of the sources are correlated, so more confidence can be had in the velocity measurements.

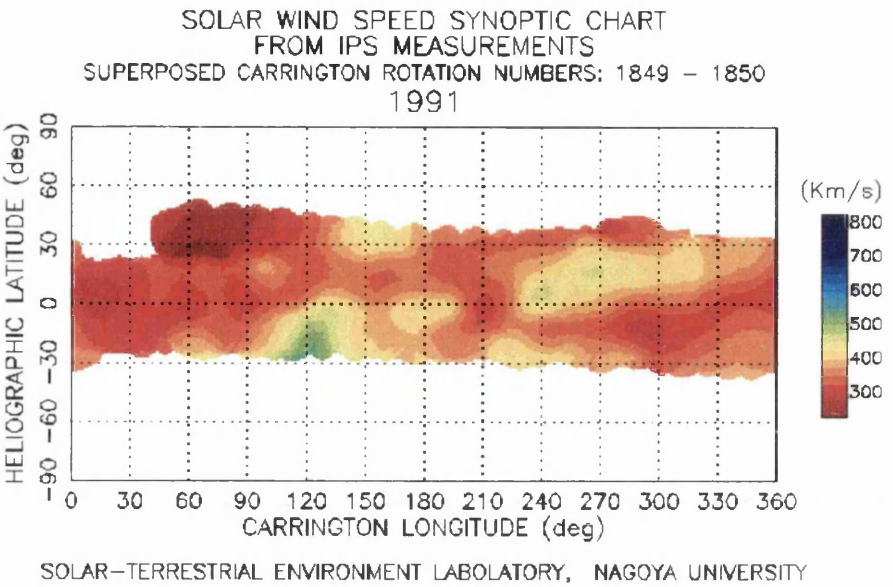

Figure 4.27: A synoptic velocity map, made over two rotations, using the Nagoya radio telescope. The faster wind located north of the equator, and between longitudes of 230° and 320°, is suggestive of a low latitude coronal hole.

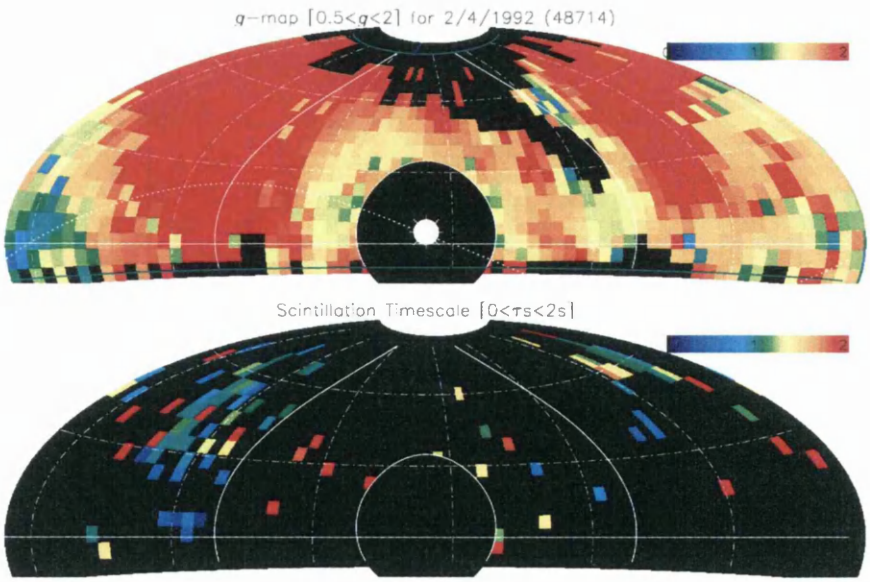

Figure 4.28: Cambridge IPS maps for 2 April 1992. On the g-map, the expansive red area to the East of the Sun indicates increased scintillation, i.e. high density material. In the τ_s-map, there are many green and blue pixels also to the East of the Sun. These indicate a short scintillation timescale, and hence fast moving wind.

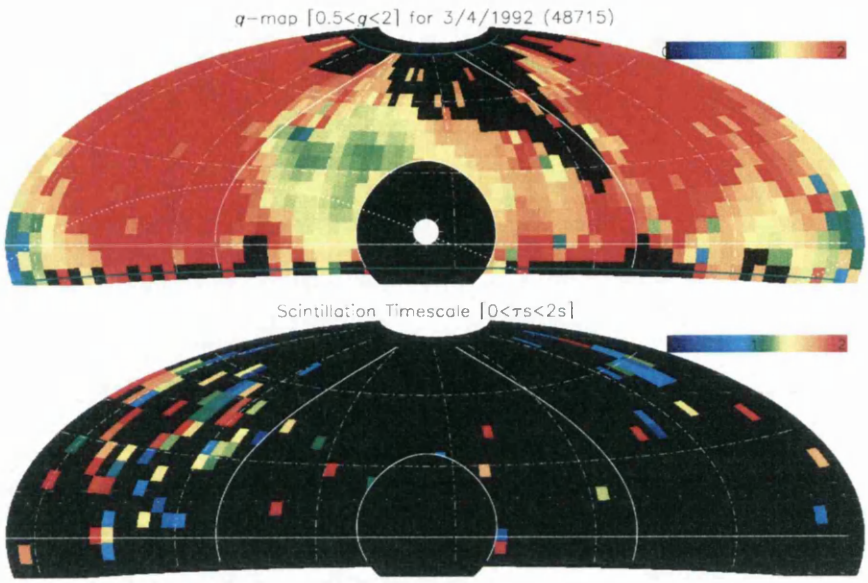

Figure 4.29: Cambridge IPS maps for 3 April 1992.

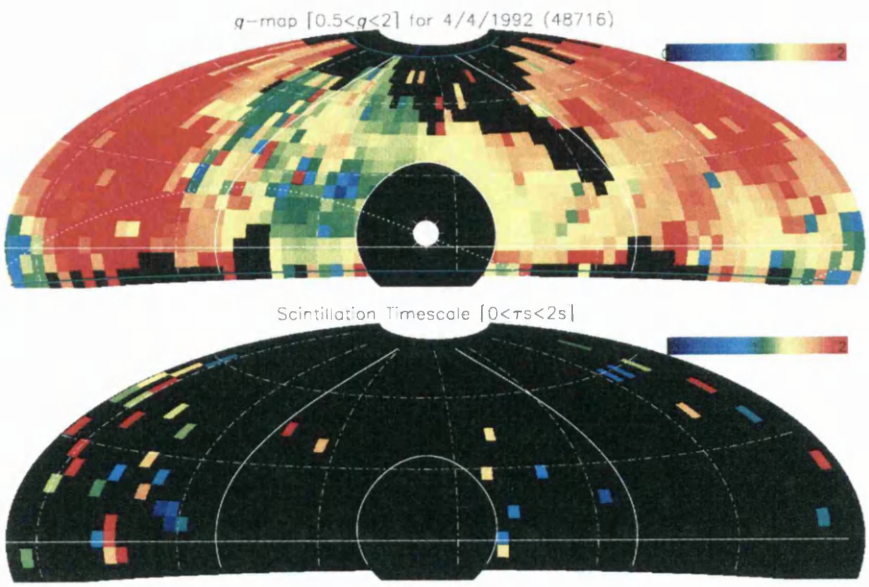

Figure 4.30: Cambridge IPS maps for 4 April 1992.

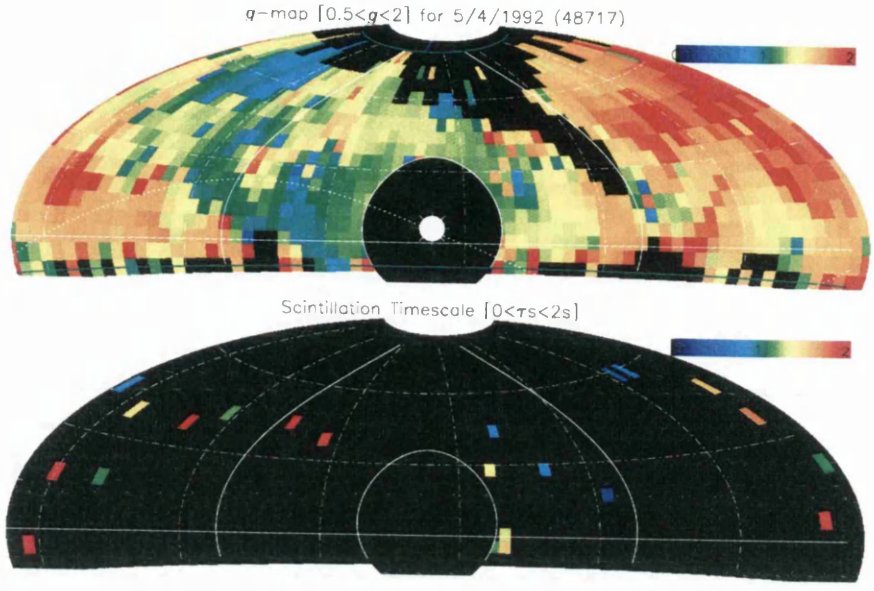

Figure 4.31: Cambridge IPS maps for 5 April 1992.

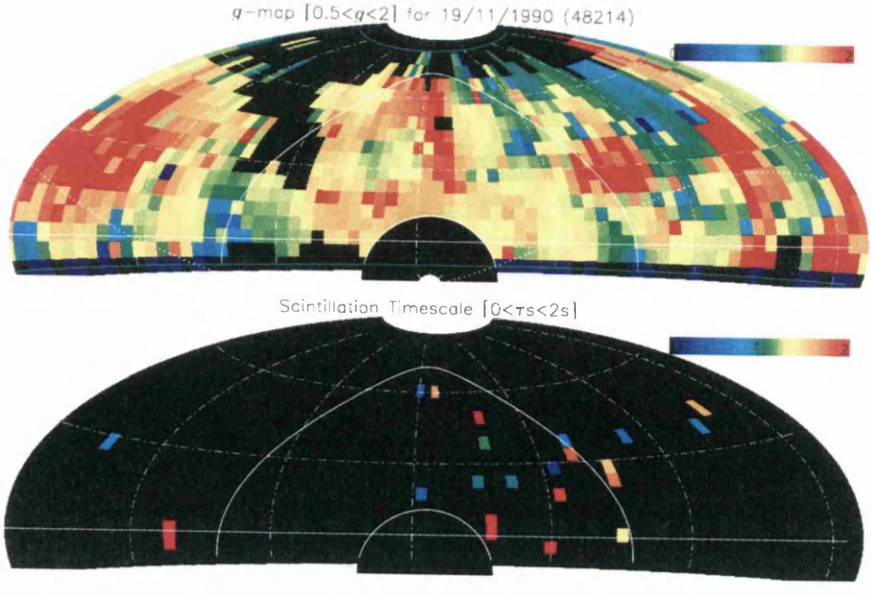

Figure 4.32: Cambridge IPS maps for 19 November 1990.

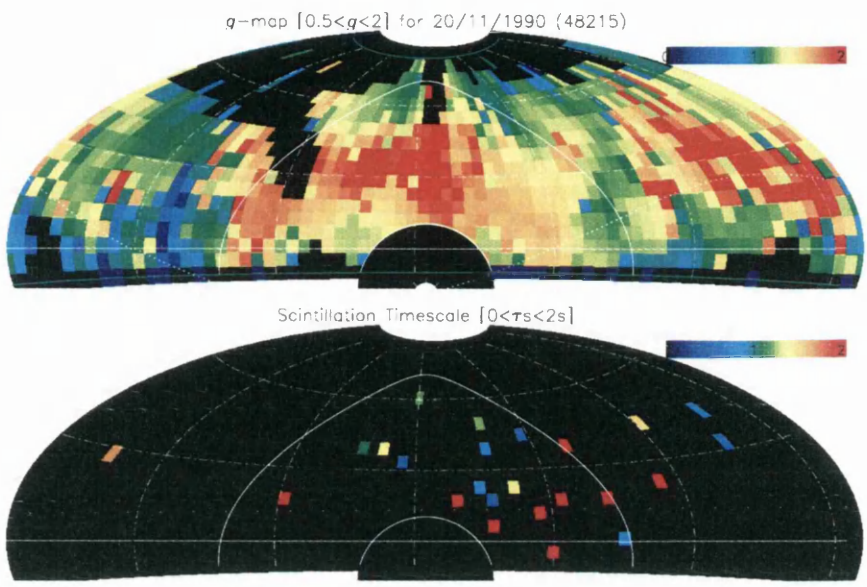

Figure 4.33: Cambridge IPS maps for 20 November 1990.

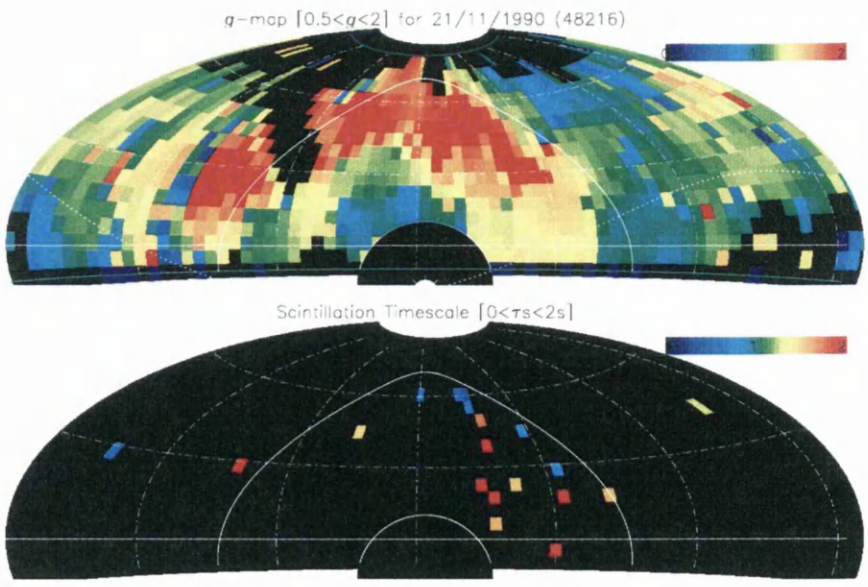

Figure 4.34: Cambridge IPS maps for 21 November 1990.

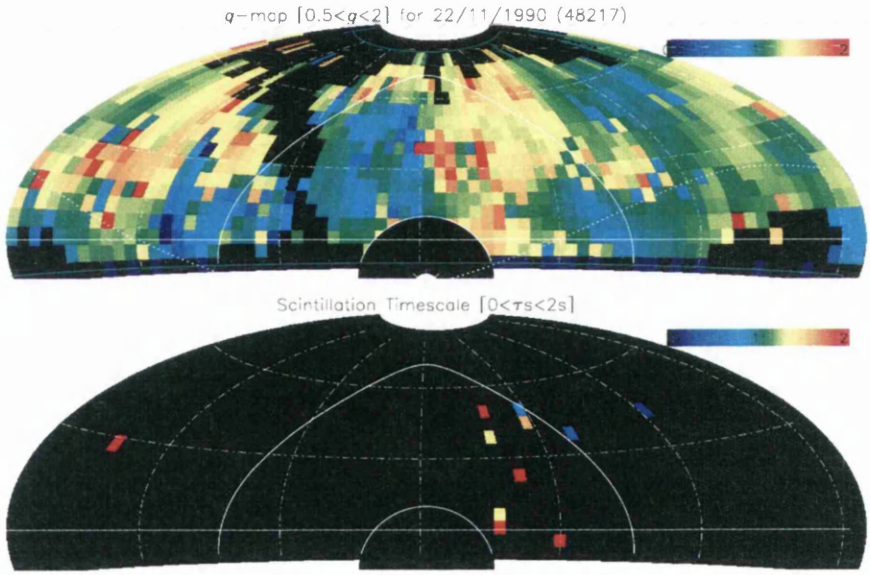

Figure 4.35: Cambridge IPS maps for 22 November 1990.

Chapter 5

Applications of the Cambridge IPS data set

"He is wise who knows how little he knows"

Socrates

5.1 Introduction

The Cambridge IPS data set has been developed and verified so that it is now ready to be applied in different ways, for various different purposes. But firstly, it is very important to understand how the 2-dimensional maps relate to 3-dimensional structures in the solar wind. Next, the average density and velocity of the solar wind, as measured by IPS, are examined as they change throughout the solar cycle. Then, the IPS maps are used to obtain an overall picture of conditions in the IPM during times of geomagnetic activity. Lastly, IPS data are used to provide more evidence for the existence of a pulsar planet.

5.2 Image interpretation: 3-dimensional structure from 2-dimensional imagery

To fully appreciate the structure of the interplantary medium, it is essential to interpret the 2-dimensional maps into three dimensions. This is always going to be difficult as it is never certain exactly where along the line-of-sight to a source the dominant scintillation

is taking place. As mentioned earlier in chapter 3, this problem has been modelled by Woan [97]. The IPS weighting function, $K(r, \epsilon)$ is plotted out in `Figure 3.1`, for a source size of 0.5". K depends on r, the distance from the Sun and ϵ, the solar elongation.

To a reasonable approximation, most of the scintillation takes place in a shell around the Earth, of radius 0.5 AU, as is obvious in `Figure 3.1`. The point along a line of sight to a source where most of the scintillation takes place is called the P point. Another school of thought places the P point along the line of sight at the point of closest approach to the Sun [72], i.e., the line joining the Sun to the P point is perpendicular to the line of sight, see P1 in `Figure 5.1`. From Woan's scintillation model [97], it is known that this scenario is valid only for a point source.

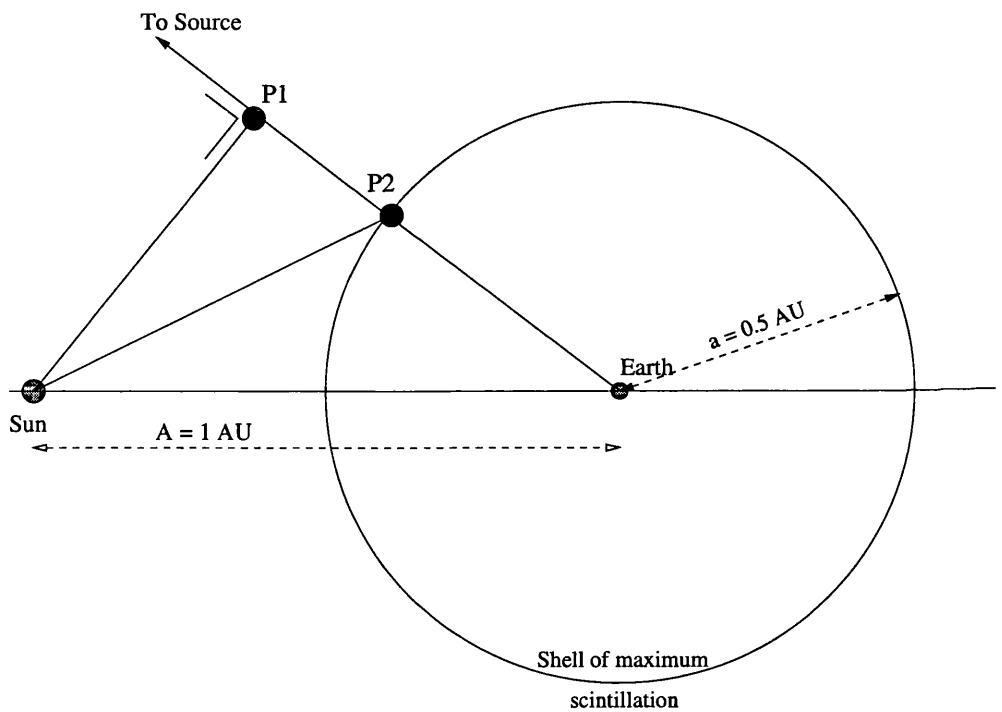

Figure 5.1: P1 is the P point given by `c190`, and P2 is that given by Woan's model. The discrepancy is not very significant for this analysis.

For a point source, $P1$ dominates the diffraction pattern observed at the Earth. But for a source of appreciable angular extent, the more distant contributions are blurred out and scintillation from material closer to the Earth dominates. This can be understood from the weak, thin screen approximation for scintillation, in which the spatial scale of the scintillation pattern seen on Earth equals that of the diffracting screen. A screen at a distance z from the Earth will give a pattern on Earth that is blurred by a length θz

(where θ is the angular size of the source) and will therefore have a reduced contribution to the scintillating signal. The greater the angular size of the scintillating source, the closer to Earth the P point will be. The weighting function in `Figure 3.1` shows where the P point will be for many lines of sight for a source of 0.5" angular extent.

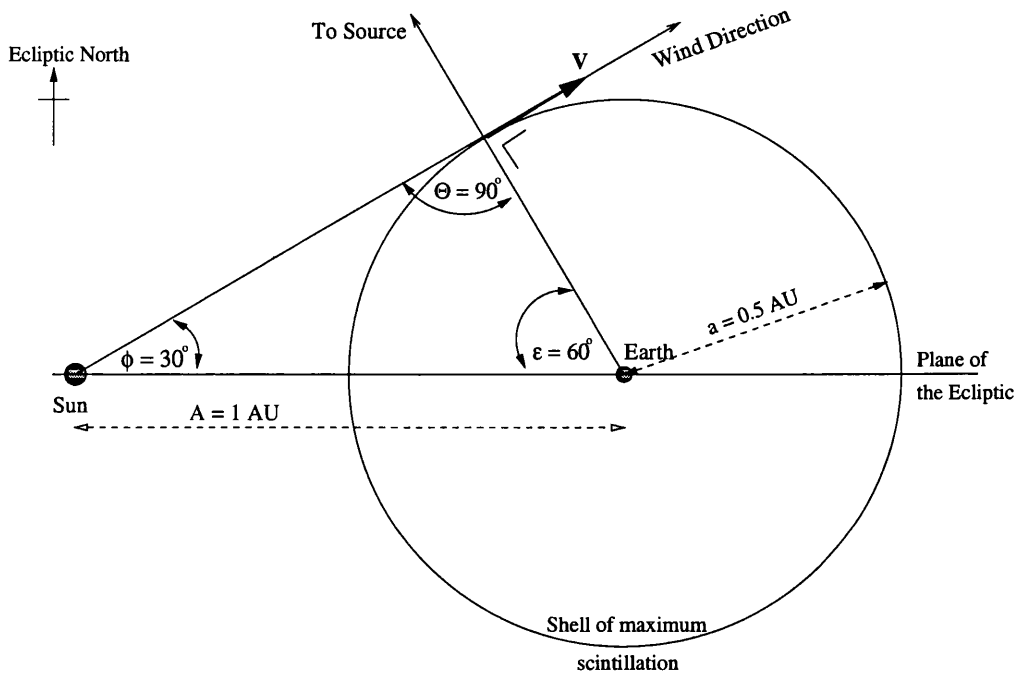

Figure 5.2: The geometry of the interplanetary medium, showing the shell where most scintillation takes place. This figure shows the limit of the wind direction from the Sun which still intersects the shell. This occurs at $\phi = 30°$ and $\epsilon = 60°$. In this figure, ecliptic north is up. Therefore, ϕ corresponds directly to ecliptic latitude.

When the geometry of this shell and the line of sight are considered, it is found to restrict the possible extent of observations of the solar wind by the Cambridge IPS array. `Figure 5.2` is a modification of `Figure 3.31`. The view is along the plane of the ecliptic, and ecliptic north is at the top of the page.

The figure shows the maximum ecliptic latitude from where the wind can emerge, and still intersect the shell of maximum scintillation around the Earth. Any wind emerging from latitudes higher than this will not intersect the shell, and will therefore be invisible in scintillation. The range of ecliptic latitude that can be "seen" is therefore limited to $< 60°$ from the ecliptic.

Ecliptic latitude does not correspond to heliographic latitude, as the north pole of the Sun is tilted by $7° 15'$ with respect to the ecliptic north, i.e. the inclination of the solar

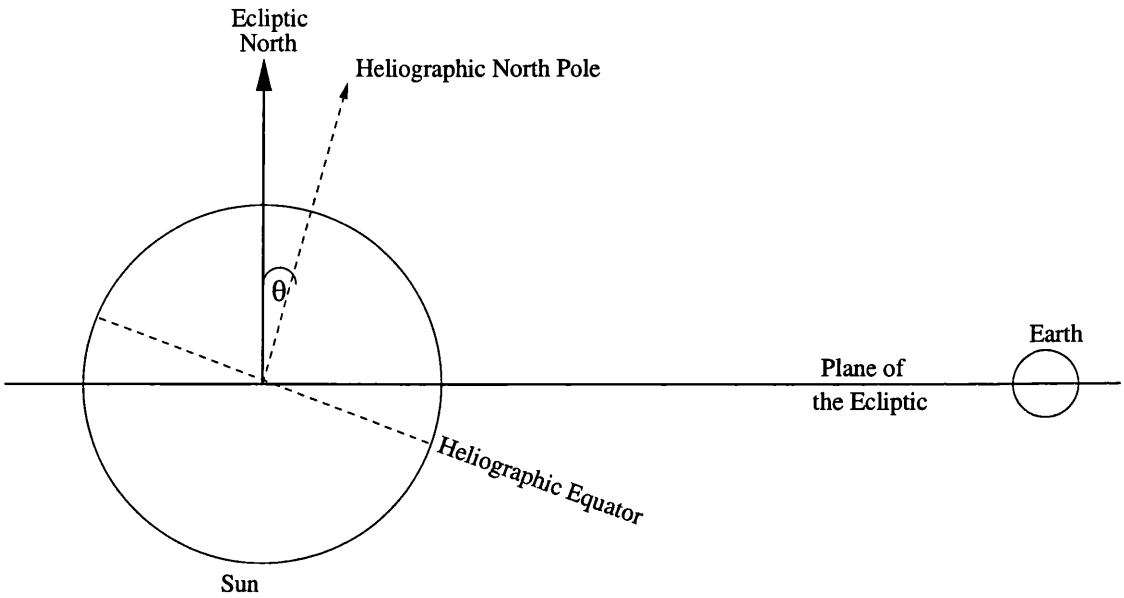

Figure 5.3: The geometry of the Sun's rotational axis in relation to the ecliptic, with ecliptic north up. $\theta = 7° 15'$. This orientation shows the heliographic north pole pointing towards the Earth, at least, as close as it gets to pointing towards the Earth. This only happens once per year, when the Sun is at an ecliptic longitude of 344°.

equator to the ecliptic is $7° 15'$ (see `Figure 5.3`). The ecliptic longitude of the ascending node is

$$\lambda_{an} = 74° 22' + 84'T \ , \tag{5.1}$$

where T is the epoch in centuries from 1900.0 [2]. A particular source will always be at the same heliographic latitude, but its heliographic longitude will change over the course of a solar rotation. To calculate heliographic longitude, the solar rotation period is taken as 25.38 days, which is the sidereal rotation period at the equator.

For the purposes of this analysis, we are interested in the heliographic latitude on the solar surface of the source of enhanced or reduced scintillation. The material that is contributing most to the total line of sight scintillation from a source is situated at the P point, as introduced earlier in this section. Even though the heliographic latitude of a source is constant, the heliographic latitude of its corresponding P point will change depending on the relative orientation of the Earth and the Sun.

To determine the heliographic latitude of the P point for a particular IPS observation of a source on a particular day, a Fortran subroutine was acquired from Dr A. Breen of the University of Aberystwyth, and this subroutine, called `c190`, was incorporated into

my C programs.

The `cl90` subroutine works out the P point as being the point along the line of sight at the closest approach to the Sun. This is different from Woan's shell model which is more realistic as it accounts for sources of appreciable angular extent (which includes most of the observed scintillating sources in our survey). There is only a slight discrepancy between the two methods, so the `cl90` subroutine can be used comfortably for the current analysis, as in the next section.

5.3 Trends from solar maximum to minimum

The Sun goes through huge changes from the peak to the trough of its activity cycle. At maximum, the Sun's magnetic field is "tangled-up" and complicated. There are many more sunspots, loops, flares and prominences than are seen during the quieter minimum. In the minimum stage of the cycle, the magnetic field is much simpler, and the polar coronal holes can extend down far enough to reach the equator. This leads to well-defined high speed flow from low heliographic latitudes.

Rickett and Coles [72] have explored the evolution of solar wind structure from 1972 (the declining phase of solar cycle number 20) to 1986 (the end of solar cycle 21), using the 73.8 MHz three antenna system at UCSD (University of California, San Diego). These multi-station IPS velocity measurements are plotted out as three-year averages, as a function of heliographic latitude. Their results show that during solar minimum, the velocities at the higher latitude ranges are far greater than the velocities at lower latitudes. And at solar maximum, slow speed wind is observed at all latitudes, as expected.

A review paper by Kojima and Kakinima [46] examines this solar cycle dependence for both the UCSD and Nagoya telescopes. The same conclusions are reached about the velocity-latitude profile over the solar cycle.

Nagoya synoptic maps on the internet make these differences obvious. `Figure 5.40` shows the synoptic map made from all the velocity measurements made over 1990. It covers the whole "surface" of the Sun, from $-90°$ to $+90°$ in heliographic latitude, and $0°$ to $360°$ in Carrington longitude. The speed of the wind is represented on a colour scale going from red ($300\,\mathrm{km\,s^{-1}}$) to blue ($800\,\mathrm{km\,s^{-1}}$). The map is mostly red, so it can be said that 1990 was dominated by slow wind at all heliographic latitudes.

The map for 1994, Figure 5.41, is decidedly different, as it's in the declining phase of the solar cycle. The slow wind is confined to a narrow band at the equator, at heliographic latitudes less than $\sim \pm 25°$. There is fast wind to be found much nearer the equator than before. At Carrington longitude 60°, there is a coronal hole as low as 35° N, where the wind is streaming out at $\sim 700\,\mathrm{km\,s^{-1}}$.

These changes are readily observable in the IPS data set, as will be demonstrated below.

5.3.1 Trends observed in the Cambridge IPS data set

The program THLat.c was written to plot out the average values of g and τ_s for all good sources, as a function of the heliographic latitude of their P points, eg. Figure 5.4. Over a certain time interval, the g and τ_s parameters were binned with respect to heliographic latitude, and then the geometric mean was taken. Only the τ_s values from observations with a SNR > 5 were taken into account. The heliographic latitude of the P point for each observation was worked out using the cl90 subroutine. At Cambridge, latitude 52.16°, the furthest south of the ecliptic that it is possible to observe with the radio array is about 10°. But, because of the motion of the Earth around the Sun, the range in heliographic latitude was quite large, from about $-60°$ to 65°.

The error bars on the average g and τ_s values represent the standard deviation of the mean, σ_m, and hence are dependent on the number of data points as well as the standard deviation of the parameters themselves. σ_m is calculated with the following formula [85]:

$$\sigma_m^2 = \frac{\Sigma x_i^2 - \frac{1}{N}(\Sigma x_i)^2}{N(N-1)}, \tag{5.2}$$

where x_i is any particular observation, and N is the number of observations.

It is clear that the error bars are greater at negative heliographic latitudes. This is because the Earth and Sun only spend a little time aligned so that the observed P points match with low heliographic latitudes, and therefore the data available are sparse. The error bars on the g points are much lower than those for the τ_s points because the τ_s points were only included in this analysis if their SNR was sufficiently large (SNR>5). This restriction is not necessary for the g data points, hence there are many more of them.

Figure 5.4 shows an example for the last 265 days in 1990. Concentrating mostly on positive heliographic latitude (as this is where most of the data points are to be found), the general trend is for an average g of approximately 1 at the equator, and a slightly higher

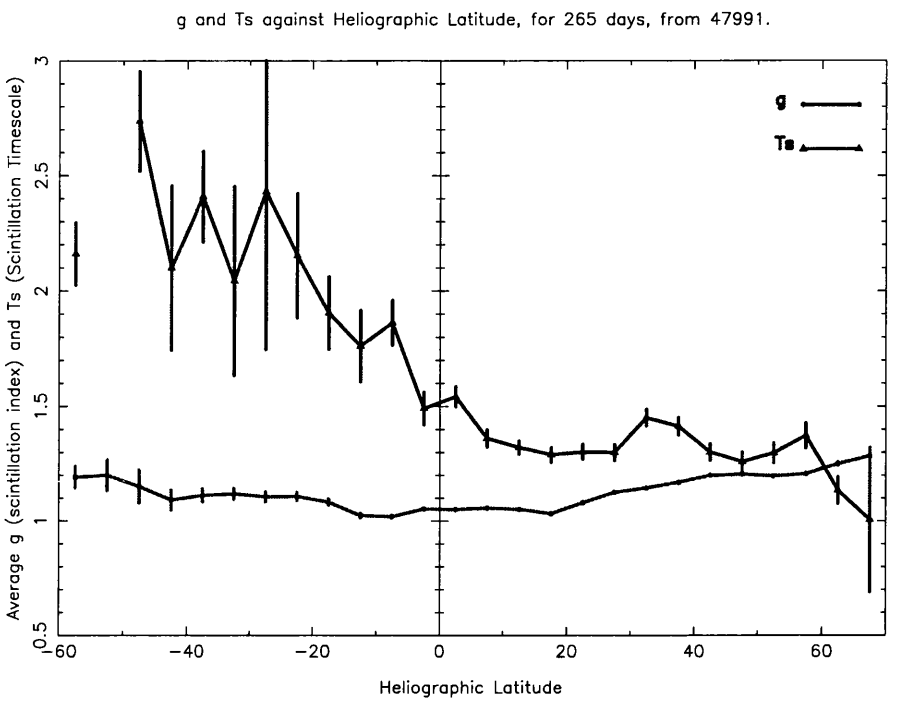

Figure 5.4: For an interval in 1990 (the last 265 days), the average g and τ_s values are plotted against the heliographic latitude of the corresponding P points. Only the observations in the range $30° < \epsilon < 100°$ were used. The g value is approximately 1 over the whole range in latitudes. The τ_s values at very low heliographic latitudes are not very reliable as only a few data points were found at these latitudes, as is can be seen from the large error bars.

average away from it. The τ_s average is not showing a definite trend, but it is slightly decreasing further away from the equator. The error bars are quite large south of the solar equator (negative heliographic latitudes), so even though I have included this part of the plot, it should not be taken as a significant trend that τ_s is greater to the south. In 1990, solar maximum, we do not expect to see organized structure with heliographic latitude, so this figure is consistent with that.

Figure 5.8 shows the same plot for 1994, when solar activity was declining. The τ_s average is certainly decreasing with heliographic latitude especially after 40°. The average velocity of the wind is therefore greater with increasing distance from the solar equator. This is what would be expected at solar minimum, as discussed earlier.

If we look at the intervening years, 1991 to 1993, we can see a gradual change from a disorganized τ_s profile in 1991 (Figure 5.5), to one that is decreasing with heliographic latitude in 1993 (Figure 5.7).

It is quite obvious that the g values in 1994 (Figure 5.8) are far lower than for 1990

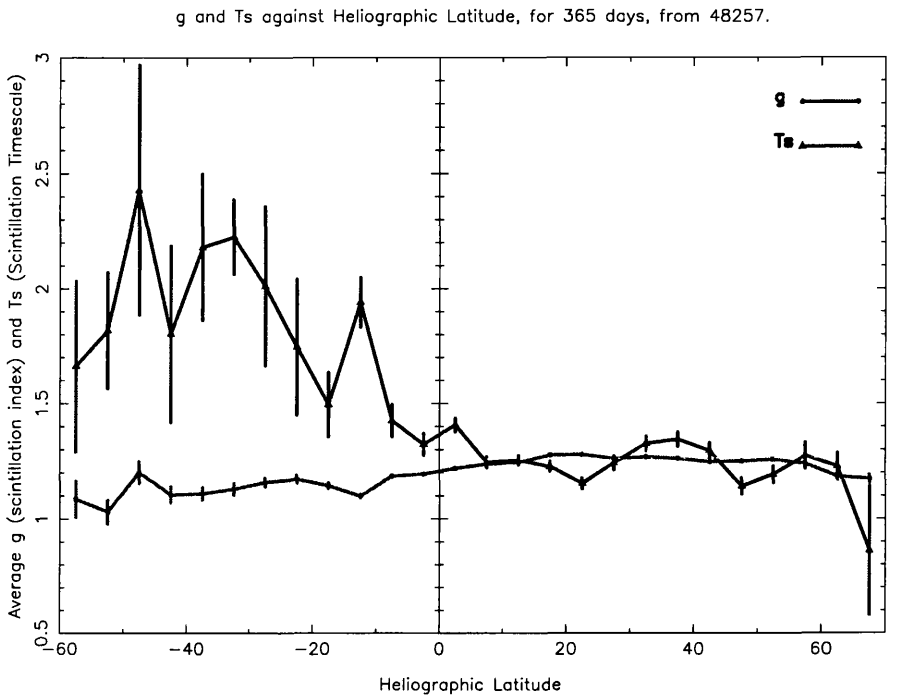

Figure 5.5: For 1991, the average g and τ_s values are plotted against the heliographic latitude of the corresponding P points.

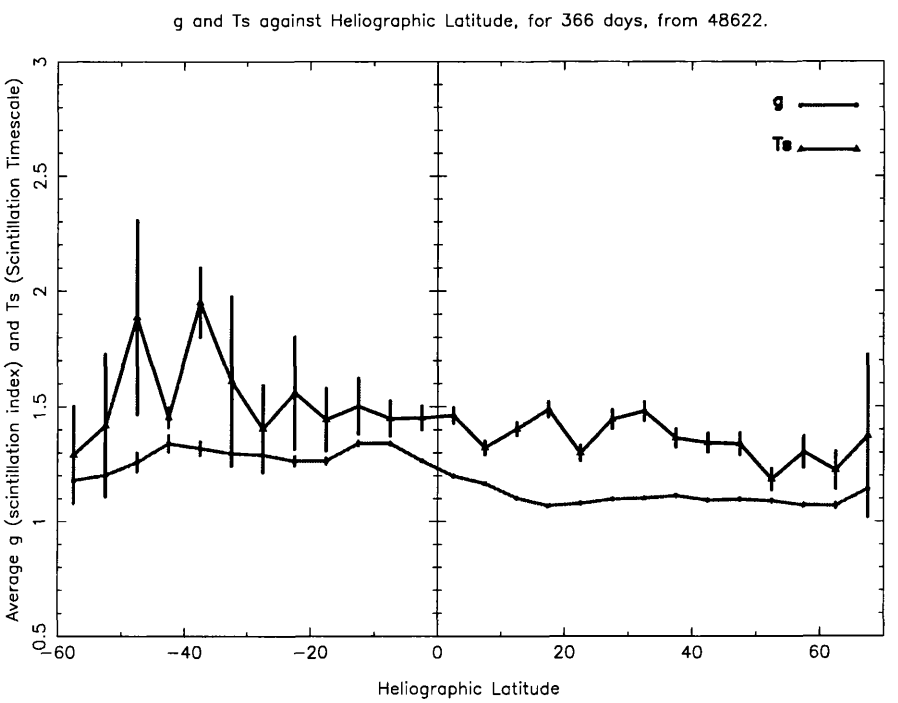

Figure 5.6: For 1992, the average g and τ_s values are plotted against the heliographic latitude of the corresponding P points.

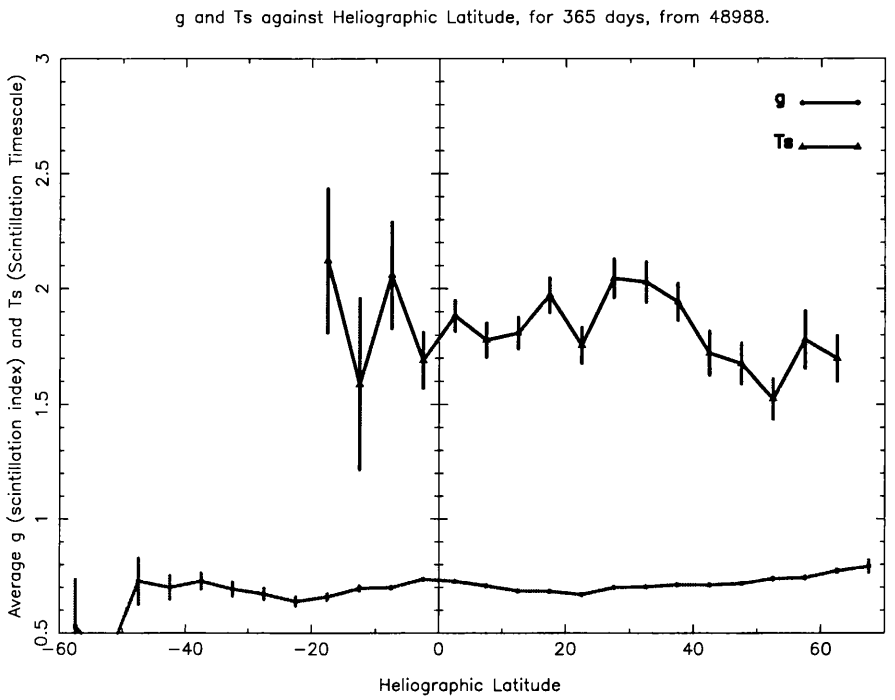

Figure 5.7: For 1993, the average g and τ_s values are plotted against the heliographic latitude of the corresponding P points.

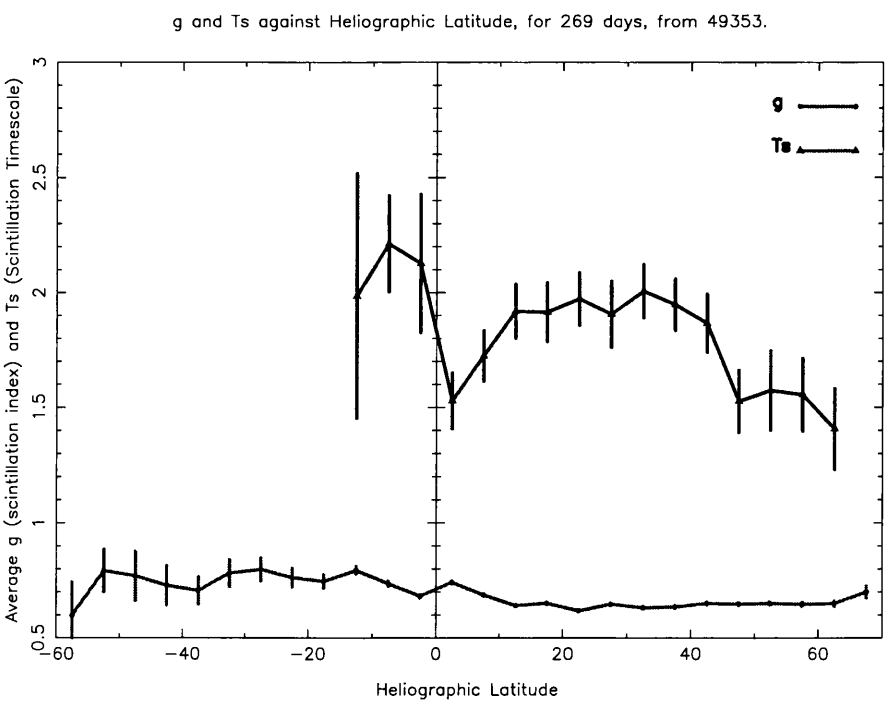

Figure 5.8: For an interval in 1994, the average g and τ_s values are plotted against the heliographic latitude of the corresponding P points.

(Figure 5.4). Therefore, it can be said that the typical density in 1994 was lower than in 1990. This is possibly because there were more coronal holes in 1994, with fast, low density streams flowing out. At solar maximum, in 1990, there are fewer, less-stable coronal holes, therefore the solar wind is, on average, slower and more dense.

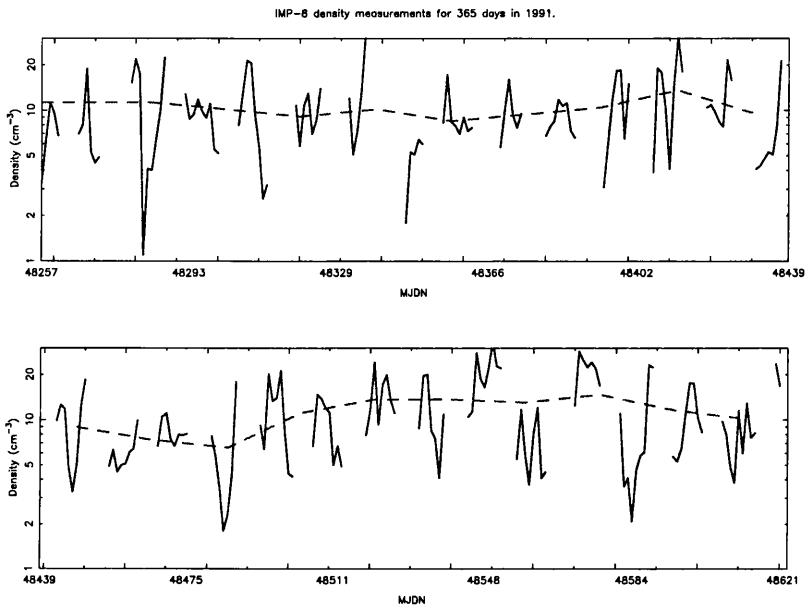

Figure 5.9: The IMP-8 density measurements for the whole of 1991, with a running 18-day average (broken line).

This trend can also be seen in IMP-8 density measurements. Figure 5.9 shows the density measured by IMP-8 over the whole of 1991, at solar maximum. The average density value is over $10\,\mathrm{cm}^{-3}$. But in 1994, seen in Figure 5.10, the average density is much lower, typically about $5\,\mathrm{cm}^{-3}$.

The Cambridge IPS results have agreed with the observations of Rickett and Coles [72] and with those made by the Nagoya telescope. The velocity of the wind shows a tendency to increase with heliographic latitude in the declining phase of the solar activity cycle. This is consistent with the theory that coronal holes dominate the IPM structure more at solar minimum than at maximum.

5.4 The link between IPS imaging and geomagnetic storms

In this section, specific events are investigated which caused a notable geomagnetic effect at the Earth. In conjunction with other experiments, the evidence provided by the IPS

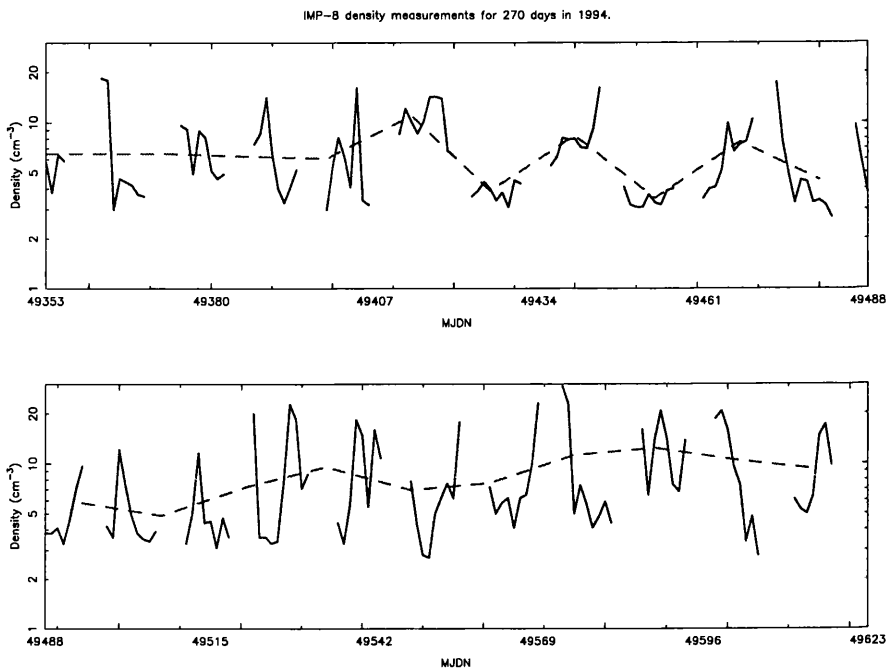

Figure 5.10: For an interval of 270 days in 1994, IMP-8 density measurements are plotted.

maps contribute to our understanding, but make it clear just how difficult it can be to piece together the precise chain of events that can cause geomagnetic disturbances.

5.4.1 The August 1992 events

The events of August 1992 did not lead to a major geomagnetic storm - the Ap index only rose to 40 - yet it is still an active, interesting period.

The Yohkoh satellite observed a large solar flare on 3 August, 1992 (Figure 5.11) near the eastern limb, and reaching a maximum soft X-ray intensity at a UT of 0706. On Figure 5.11, a coronal hole can be seen at the centre of the disk, extending from the north pole to the equator. This coronal hole is also evident in the He 10830 Å spectroheliogram map for this Carrington rotation (1858) shown in Figure 5.12. On 4 August, the SAMPEX satellite recorded a sharp increase in proton levels in the near-Earth IPM, especially in the high-energy protons (20-29 MeV), shown in Figure 5.13. The maximum was reached on 6 August.

GOES also noted the passage of this disturbance, as seen in Figure 5.14. The proton levels begin to rise on 3 August, and reach their peak on 6 August. This event is named as one affecting the Earth environment, in the GOES list. In this list, it is associated with

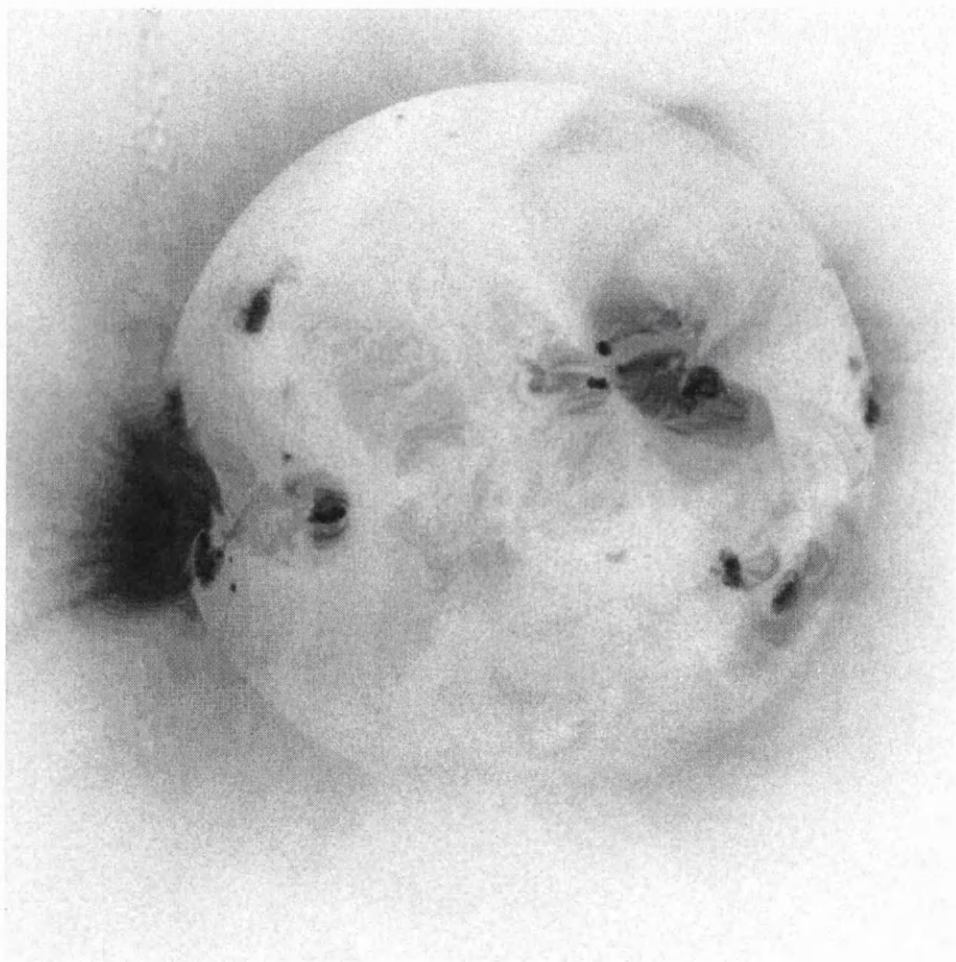

Figure 5.11: Yohkoh SXT image for 3 August 1992. Note the large active, flaring region near the eastern limb, just below the equator. Also apparent is a significant coronal hole towards the centre of the visible disk, reaching down to the equator.

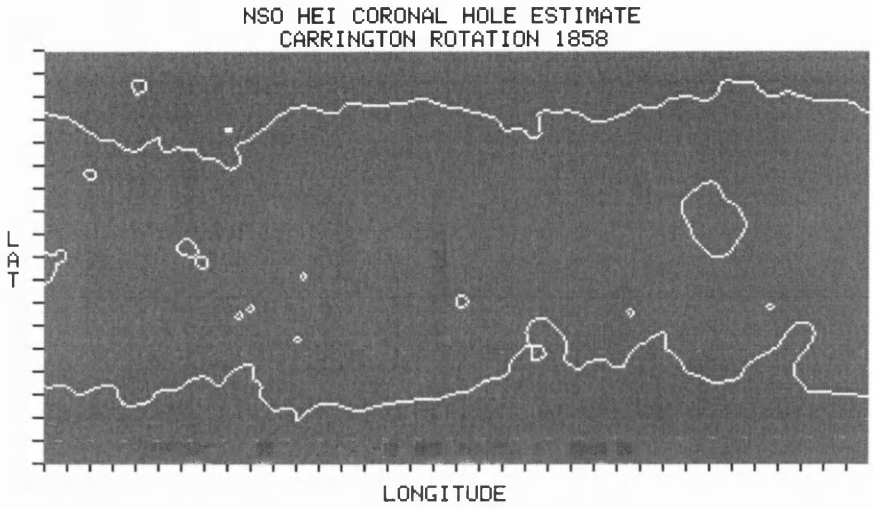

Figure 5.12: The Helium 10830 Å image for Carrington rotation 1858. Heliographic longitude runs from 0° at the left to 360° at the right. Heliographic latitude runs from −90° at the bottom (south pole) to +90° at the top (north pole). The coronal hole seen in the Yohkoh image is also apparent here at easterly longitudes, reaching down to a heliographic latitude of +30°.

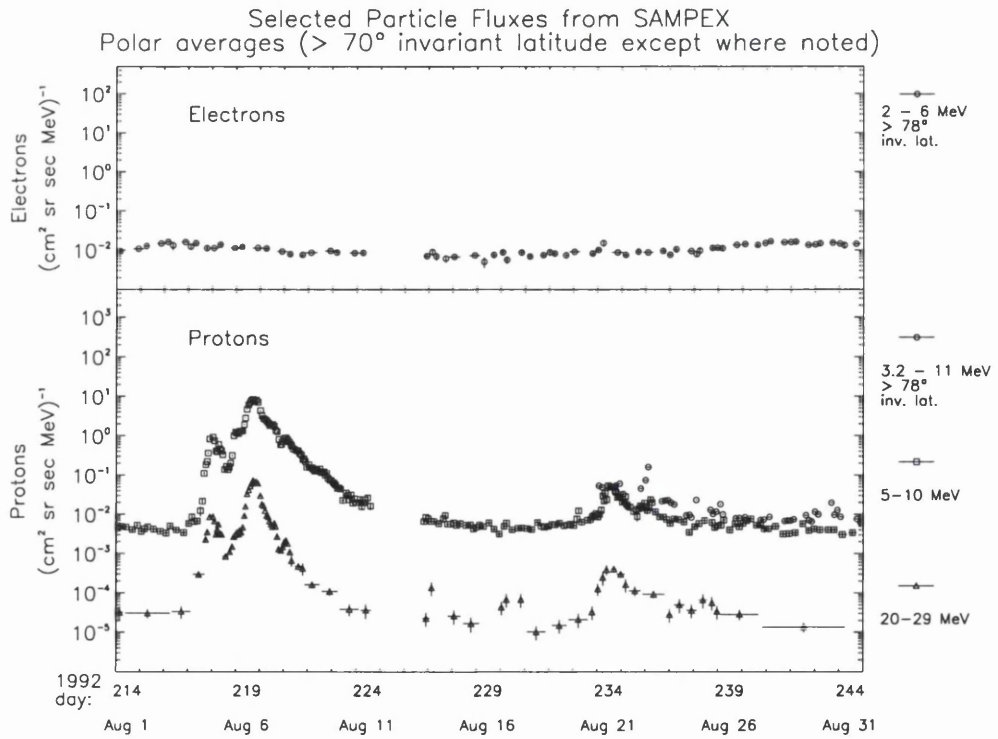

Figure 5.13: The SAMPEX Energetic Particle record for August 1992, measured in-situ at the geographic poles (averaged over the two polar cap passes, i.e., above 70° invariant latitude, of each orbit). Note the significant increases from 3 to 9 August.

a flare on the Sun at 9° south and 68° east, that was observed on 3 August, the same one observed by Yohkoh in Figure 5.11.

Both GOES and SAMPEX show a gradual build-up to the peak proton intensity. This is not consistent with the flare association. If SEPs (solar energetic particles) are emitted by a flare on the west side of the Sun, there would be an almost direct magnetic connection to the Earth, and the particles would have arrived almost all at once, causing a sharp discontinuity in the proton flux profile. If the source of the SEPs is a flare on the eastern side of the Sun, then the SEPs would not arrive for a few days, due to poor magnetic connection.

In this case, the flare was at the east, and the SEPs started to arrive on the day of the flare. Therefore the flare association for these energetic particles is less plausible. Of course, this is merely a general trend for a regular magnetic structure of the Sun. In reality, the magnetic lines can get very tangled and complicated, especially during solar maximum.

More indications of the interplanetary conditions in this period are observable on a series of IPS maps, which shows a disturbance travelling out from the Sun. Figure 5.42 to Figure 5.45 show the evolution of this disturbance, possibly a CME that was related to the same active region that produced the flare and the SEPs. But if it is a CME, then it was emitted far too early to be associated with the flare. On 2 August, it had already travelled to $\sim 60°$ According to Harrison [29], CMEs are ejected no more than one hour before a flare if the two are to be associated.

Another possibility is that this enhanced scintillation is caused by a shock front produced by a sudden increase in the speed of the outflow from the coronal hole seen in the Yohkoh image, Figure 5.11, and also in the He 10830 Å spectroheliograph, Figure 5.12. This would follow from the postulation of Bravo that shock fronts are caused by intermittent eruptions from coronal holes [11]. We shall explore this hypothesis in the following analysis.

In the IPS g maps from 28 July to 3 August, there is a low density region very apparent to the east of the Sun. This is probably the fast, low density plasma coming from the central coronal hole. It is moving out from the Sun. On 2 August, an enhanced scintillation region appears at about 60° elongation. This could be caused by changes in the coronal hole configuration leading to a rapid increase in flow from the hole. This high speed plasma

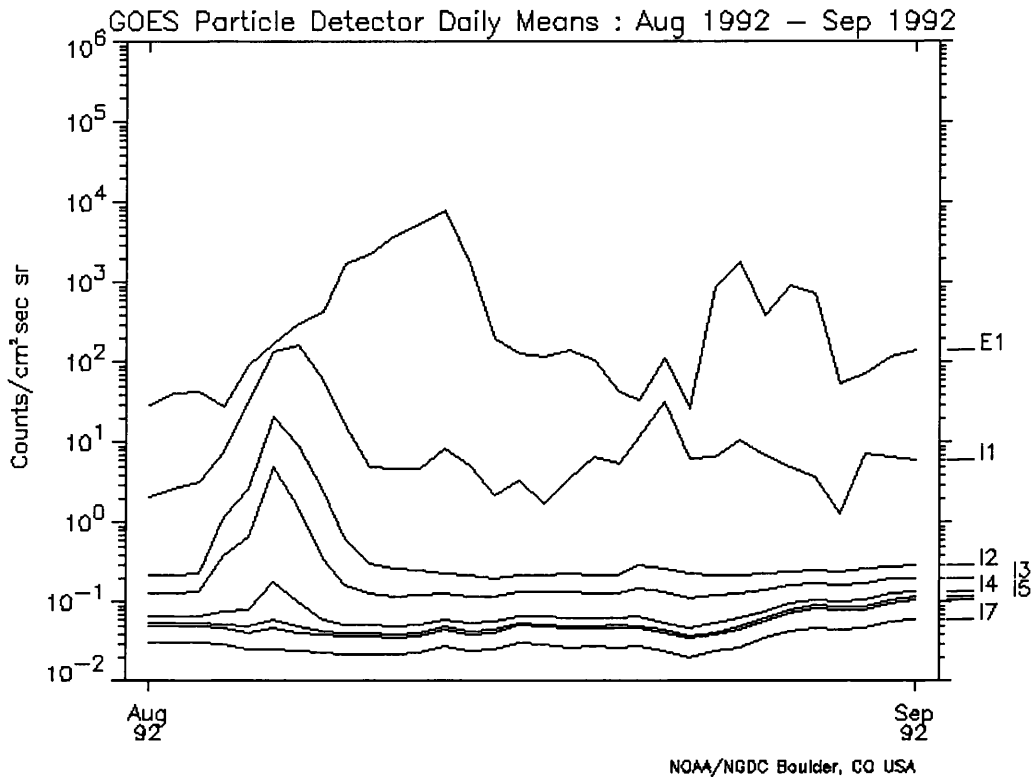

Figure 5.14: The GOES Energetic Particle record for August 1992, measured in-situ and displayed as daily averages. The top line, E1, represents electrons with energy >2 MeV. The next seven lines down the plot show protons of increasing energy, from I1>1 MeV to I7>100 MeV. There is a significant significant increase in proton levels from 3 to 9 August.

has created a shock front, and this is what we see in **Figure 5.42**.

By 3 August, this enhancement front has moved out further from the Sun, and is seen at about 80° east in **Figure 5.43**. On 4 August, the high density shock is totally dominating the near Earth environment, as in **Figure 5.44**. This dominance continues on 5 August, see **Figure 5.45**, suggesting that it is a very large disturbance. By 6 August, it has moved off to the west.

This high density material was observed by the IMP spacecraft. The first graph of **Figure 5.15** shows the plasma density rising on 4 August, reaching a dramatic peak at the middle of the day, the same day that the g maps show a large density enhancement near the Earth. The wind is also increasing in speed on 4 August, after decreasing from a high at the beginning of the month caused, perhaps, by the coronal hole. Again, the speed increases on 5 August. Then there is a gap in the solar wind data as IMP travels

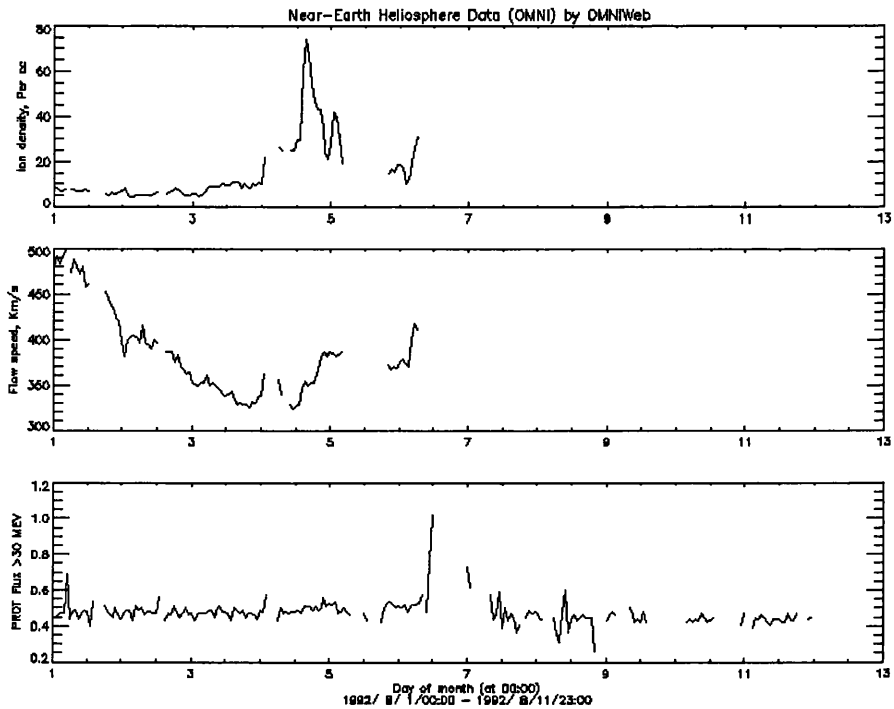

Figure 5.15: The IMP record for August 1992, showing solar wind density, velocity and high energy (>10 MeV) proton flux.

into the magnetopause.

The last plot in Figure 5.15 shows the proton flux over 10 MeV. This begins to rise on 4 August, then jumps to a maximum on 6 August, as IMP is entering the magnetopause, and at the same time that GOES and SAMPEX reach a maximum in high energy proton flux. It seems that all these different instruments are corroborating each other's high energy particle evidence.

Evidence that the disturbance was moving very fast is found in the Nagoya IPS velocity data. Figure 5.16 shows that on 4 August, the velocity of material east of the Sun was averaging at about 700 $\mathrm{km\,s^{-1}}$ for some sources. These high speeds are also seen on the next day, 5 August (Figure 5.17), but for sources farther out from the Sun, proving that this is fast-flowing material moving away from the Sun. On 6 August, more ambient speeds were recorded by the Nagoya telescope, showing that the disturbance had passed on by this time.

These observations suggest the following scenario. A coronal hole at longitude $\sim 80°$ was allowing the escape of fast flowing, low density material into the solar wind. This

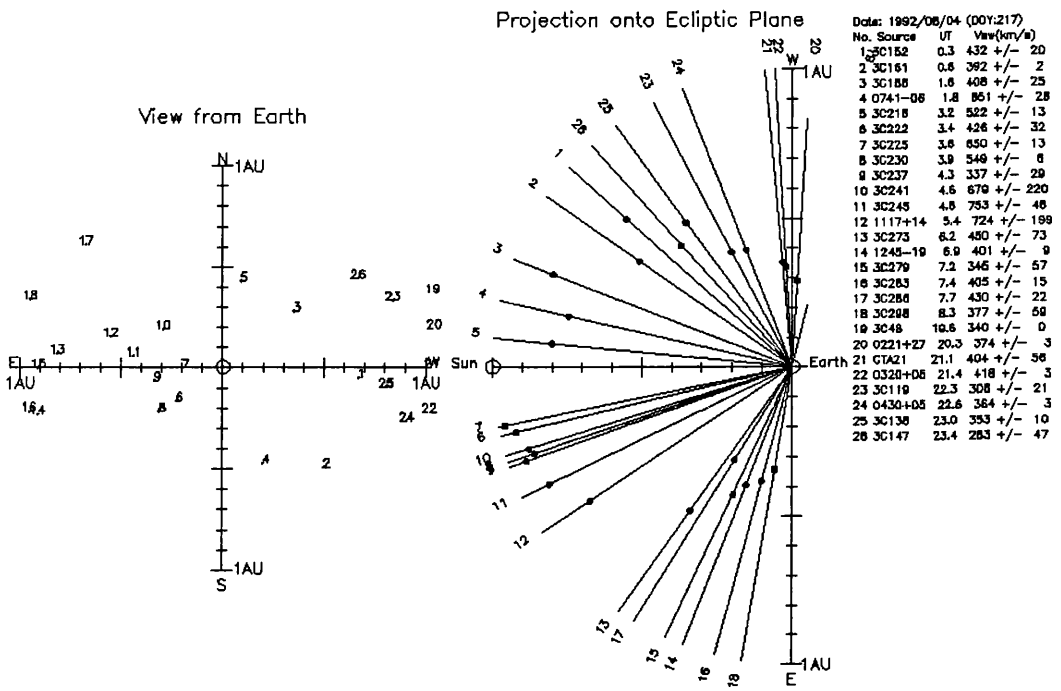

Figure 5.16: Map of Nagoya IPS velocity values for 4 August 1992. The typical wind speed to the east of the Sun is about 700 km s^{-1} for sources 10, 11 and 12. This corresponds to a fast moving disturbance, pushing out a shock front ahead of it. The high density shock can be seen clearly in Figure 5.44, the corresponding Cambridge IPS g map. This material is moving slower, at about 400 km s^{-1}, as can be seen for sources 13, 17 and 18.

hole appeared on the eastern limb of the visible solar disk in the middle of July 1992. The low density stream emerging from the hole was apparent as it moved westwards across the Sun, forcing the streamlines into an Archimedean spiral. A shock front was created by changes in the coronal hole structure which led to a huge increase in the velocity of the material emerging from it. This shock front swung into view for us at the Earth on 2 August, and totally engulfed the Earth from 4 to 5 August.

Also, this shock front created energetic particles by acceleration. Hewish *et al.* have explored this idea of particle acceleration by interplanetary shock fronts [34]. Using the α-particle flux in the range 9-70 MeV from the GMS/SEM satellites, they found that the largest particle events caused by shock passage can increase the flux by a factor of $\sim 10^3$.

There is the possibility that the energetic particles seen by GOES, SAMPEX and IMP

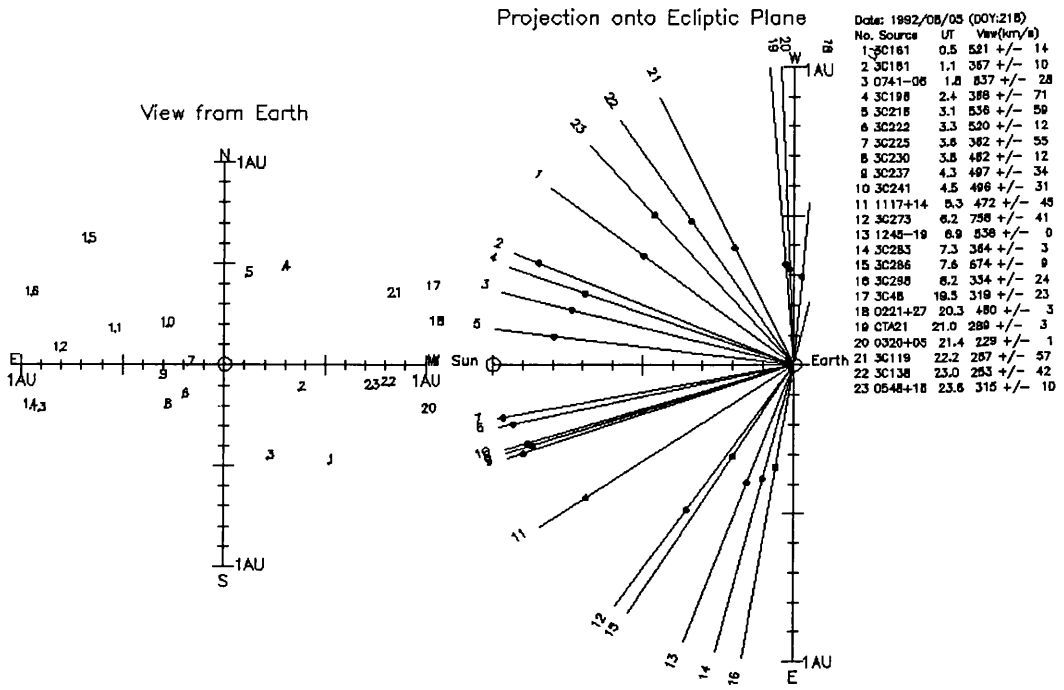

Figure 5.17: Map of Nagoya IPS velocity values for 5 August 1992. The very fast wind can still be seen for sources 12 and 15, which show a velocity of about 700 km s^{-1}. Sources closer to the Sun (9, 10 and 11) show slower speeds of almost 500 km s^{-1}, which show that the solar wind is returning to "normal" after the passage of this transient.

to maximize on 6 August could be caused by the flare of 3 August. But energetic particle fluxes from a flare are usually characterized by a short timescale [70], [26], only a few hours, rather than a few days, as was the case here. Also, the high density disturbance that arrived at the Earth on 4 August clearly indicates the arrival of a shock front that is capable of generating these particles. The evidence from IPS confirms that the shock front was most probably associated with a co-rotating stream emanating from Carrington longitude $\sim 80°$.

5.4.2 The March 1991 events

In late March 1991, there was a severe, well-studied geomagnetic storm. Figure 1.12 has shown that the Ap index rose to more than 150 on 24 March. Because of the severe

geomagnetic effects, this period has been extensively examined. A whole issue of *Geophysical Research Letters* was devoted to its study, e.g., Wenzel and Smith [95] and Phillips *et al.* [61].

There were extremely high fluxes of energetic particles measured by orbiting satellites during the storm. The measurements made by the GOES satellite are shown in **Figure 5.18**. They show a huge and sudden flux increase just before midday on 23 March. The IMP-8 satellite also observed a sharp increase in proton flux (> 10 MeV) just before midday on 23 March (**Figure 5.19**). Both of these satellites showed that the energetic particle flux had returned to near ambient conditions by 25 March 1991.

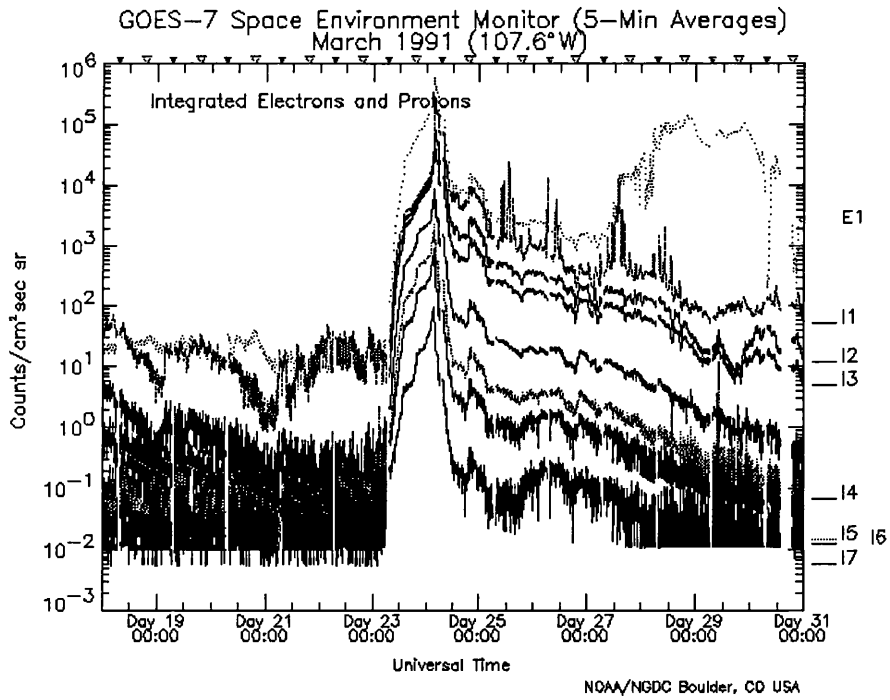

Figure 5.18: The GOES data for high energy electrons (E1) and protons (I1 to I7) in March 1991. The huge increase on 23 March heraalded the beginning for a severe geomagnetic storm.

Sanderson *et al.* [74] have explained the origin of these SEPs in terms of a series of intense solar flares, occurring in a very active region 20° south of the solar equator. These flares were also recorded as strong radio bursts at 37 GHz by the Metsähovi Radio Observatory, and are detailed in their flares catalogue.

Another possibility is that the energetic particles were created by a shock front travelling in the IPM. At this time, the Sun was extremely active, and many different phenomena

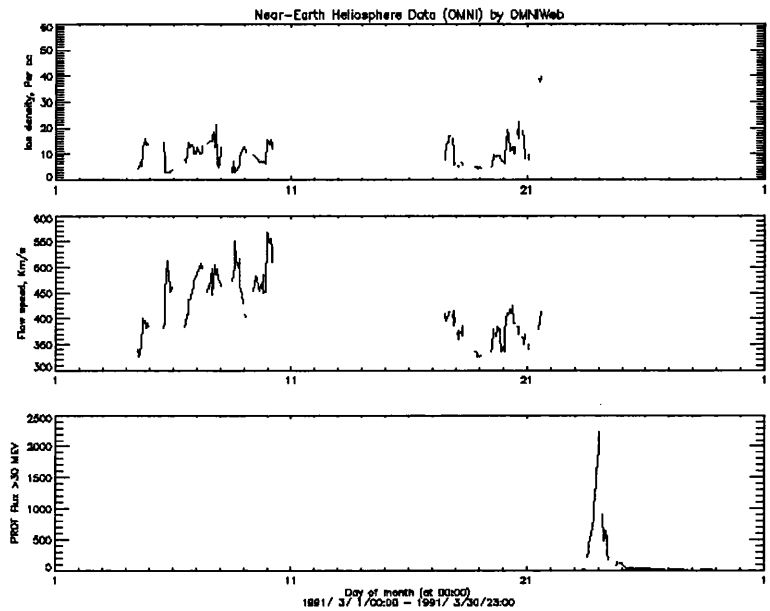

Figure 5.19: IMP-8 measurements of solar wind density and speed in March 1991, not including the period of interest, 22-25 March, when a geomagnetic storm occured. There are high energy proton flux recordings available in the third graph. These show an enormous increase in protons of energy >10 MeV on 23 March.

were happening at the same time, so it is very difficult to pick out exactly what occurrence on the Sun caused any particular geomagnetic effect. It appears however that there was one very fast and powerful shock which had a huge influence on the IPM. This shock front was observed by both the Cambridge IPS array, and by Ulysses which was ~2.5 AU from the Sun at this time.

First, we examine how the IPM was structured before this shock occurreded. On the IPS g-map for 17 March 1991, a relatively slow-moving, high density disturbance was observed to the east of the Sun (`Figure 5.46`). There is evidence to suggest that this is the co-rotating stream observed on the two previous months, see the IPS synoptic plots by Woan [97]. Moving slightly faster than the material preceding it, it compresses the material in front to form a high density, co-rotation interaction region (CIR). This is what we see as a density enhancement in the IPS g maps from 17 to 22 March.

On subsequent days, it moved slowly eastwards, dominating the IPM at 90° east on 20 March (`Figure 5.47`), and covering the whole sky on 21 March (`Figure 5.48`), before moving off to the west on 22 March. On 20 March, the density of the solar wind measured by IMP at 1 AU was about twice the average, peaking at 20 cm^{-3}, see `Figure 5.19`. The

velocity measured by IMP was nothing out of the ordinary, peaking at $\sim 425\,\mathrm{km\,s^{-1}}$ on 20 March.

Already on 21 March, another disturbance can be seen coming from the east of the Sun (Figure 5.48). This is the large, fast-moving shock noted earlier. It could have been caused by a sudden change in a coronal hole, resulting in the rapid outflow of low density plasma, or by a CME. Because it is moving in the rarefaction created by the CIR, there is not so much material in front of it to slow it down, as might occur normally. But it is still able to create a shock front, where the remaining material has been swept up. The leading edge of this shock front can be seen on 22 March at 90° east of the Sun (Figure 5.49).

On its Earth orbit, IMP would normally have entered the magnetopause on 21 March, and therefore, there is no solar wind data recorded on the OMNIWEB database. However, because this shock front was so powerful, the magnetopause was pushed in from its usual extent at 10 Earth radii to inside 6.6 Earth radii [49], making some solar wind measurements available. Through a private communication (A. Lazarus), it was learned that IMP recorded solar wind velocities over $1000\,\mathrm{km\,s^{-1}}$ on 24 March. At that speed, the shock front only took ~ 42 hours to reach the Earth from the Sun, i.e.

$$\text{travel time} = \frac{1\,\mathrm{AU}}{1000\,\mathrm{km\,s^{-1}}} = 41.7\,\mathrm{hrs}\,. \tag{5.3}$$

Of course, this is only a rough estimate, as the angular extent and direction of travel of the shock are not exactly known.

This very fast shock seems to have had a dramatic effect on the preceding CIR, driving it to even higher speeds. From $\sim 425\,\mathrm{km\,s^{-1}}$ at 1 AU, it arrived at Ulysses at a velocity of over $600\,\mathrm{km\,s^{-1}}$, in the form of a shock. Ulysses recorded this shock late on 23 March (Figure 5.20), where a large increase in velocity from $\sim 400\,\mathrm{km\,s^{-1}}$ to $\sim 600\,\mathrm{km\,s^{-1}}$ is followed by a decrease in plasma density. A travel time of four days (from 18 March to 23 March) is consistent with a disturbance travelling 1.5 AU at a speed of $\sim 600\,\mathrm{km\,s^{-1}}$.

Meanwhile, back at Earth, the IPS g map for 23 March (Figure 5.50) shows the leading edge of the big shock front to have moved beyond 90° eastern elongation. On 24 and 25 March, it totally dominates almost the whole sky as seen by the IPS array (Figure 5.51 and Figure 5.52). By the 28 March, this disturbance has left the near-Earth environment, and a low density rarefaction follows in its wake for at lease four days, see Figure 5.53.

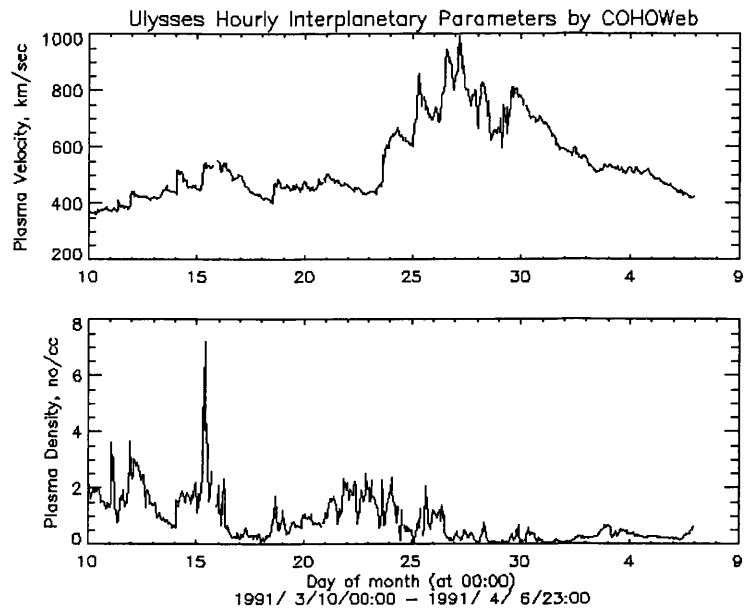

Figure 5.20: The solar wind velocity and density as measured by the Ulysses spacecraft at 2.5 AU in March 1991.

To further illustrate the shape and movement of the shock front from IPS g measurements, **Figure 5.21** plots out g as a function of eastern elongation, on 23 March. The shock front can be very clearly seen with its leading edge at 90°. **Figure 5.22** plots out the same graph for 24 March. The shock front has moved on by then, and the sharp leading edge is not so apparent.

Of course, we cannot dismiss the influence of the ionosphere on the IPS maps. During such a severe geomagnetic storm, the ionosphere is likely to be highly disturbed, leading to ionospheric scintillation and thus contamination of the g maps. This could account for some of the very high g values obtained from 24 to 25 March, especially at very large elongations. However, **Figure 5.21** clearly shows the shape of the leading edge of the shock front, leading to the belief that at least that day was free from ionospheric scintillation.

Ulysses detected the arrival of the big shock on 25 March, with an increase in speed from $\sim 600\,\mathrm{km\,s^{-1}}$ to $\sim 900\,\mathrm{km\,s^{-1}}$. This is to be as expected, as the leading edge of the shock was observed on a g map to be at 1 AU at about 1800 hrs on 22 March (**Figure 5.49**), and Ulysses was at 2.5 AU during this period. The travel time between these radii is 62.5 hrs at a speed of $1000\,\mathrm{km\,s^{-1}}$. 62.5 hrs after 1800 hrs on 22 March corresponds to

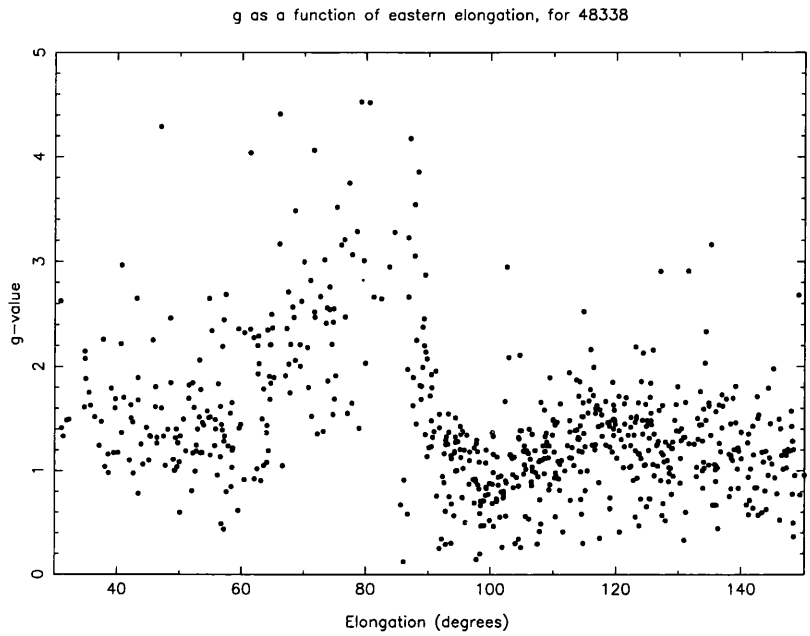

Figure 5.21: g versus elongation for all sources east of the Sun on 23 March 1991. The leading edge of the shock front is very apparent as the g value drops sharply at $\epsilon = 90°$.

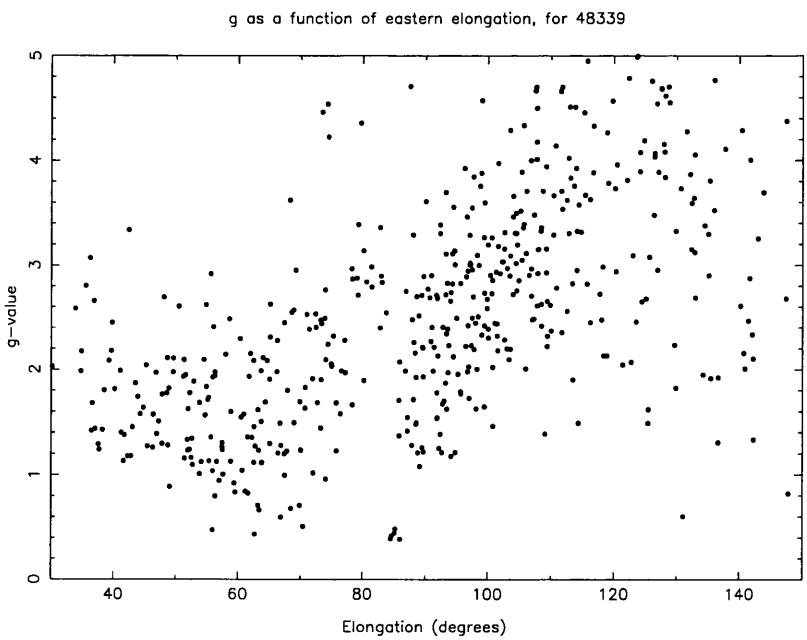

Figure 5.22: g versus eastern elongation on 24 March 1991. The wide spread in g for large elongations is suggestive of ionospheric interference.

early on 25 March, which is exactly when Ulysses observed this second, more powerful shock.

The body of evidence presented here suggest that the geomagnetic storm must have been caused by this huge, fast moving shock. At such a large velocity ($\sim$1000 km s^{-1}), the shock was able to accelerate a large number of particles to high energies, and thus generate the record-high fluxes that were recorded by GOES and IMP. Sanderson *et al.* [74] have noted the depletion in low energy particle flux at Ulysses during the shocks, suggesting that the high energy particles were indeed shock accelerated and not of direct flare origin.

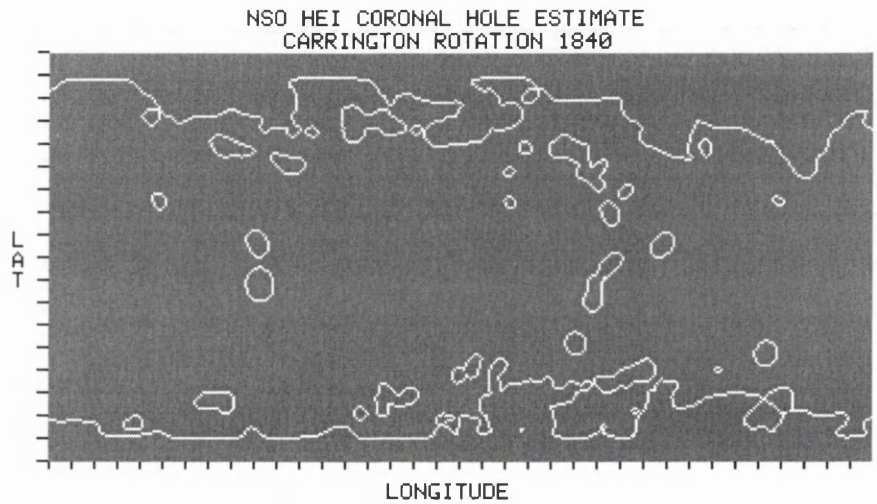

Figure 5.23: The Helium 10830 Å map for Carrington rotation 1840, from 11 March to 7 April 1991. Heliographic longitude runs from 0° at the left to 360° at the right. Heliographic latitude runs from −90° at the bottom (south pole) to +90° at the top (north pole). A lot of coronal holes are apparent. The central longitudes of this map correspond to the meridian passage on 24 March.

The powerful flaring going on at the Sun could be just another symptom of a very active period for the Sun, rather than the cause of the high fluxes of energetic particles. Perhaps the flaring was caused by large scale magnetic reconnection which also resulted in the ejection of a CME, and a sudden increase in velocity from a coronal hole. This type of velocity discontinuity would explain the big shock front. Looking at the Helium 10830 Å map for this rotation (`Figure 5.23`), there are indeed many coronal holes that could be the source of the high speed solar wind.

Considering all the relevant observations, it is clear that the event of March 1991 was a very complex and unusual affair, and perhaps the exact sequence of events will never be totally determined. Despite this complexity, the global IPS data have added significantly

to our understanding of the period, identifying the most likely trajectory of the powerful shock and the complex interplanetary environment through which it propagated.

5.4.3 The May 1992 events

Another major geomagnetic storm occurred in May 1992, when the Ap index rose to almost 200 on 10 May, see **Figure 5.24**. The GOES spacecraft recorded a sudden increase in energetic particles at about 12:00 UT on 9 May (**Figure 5.25**).

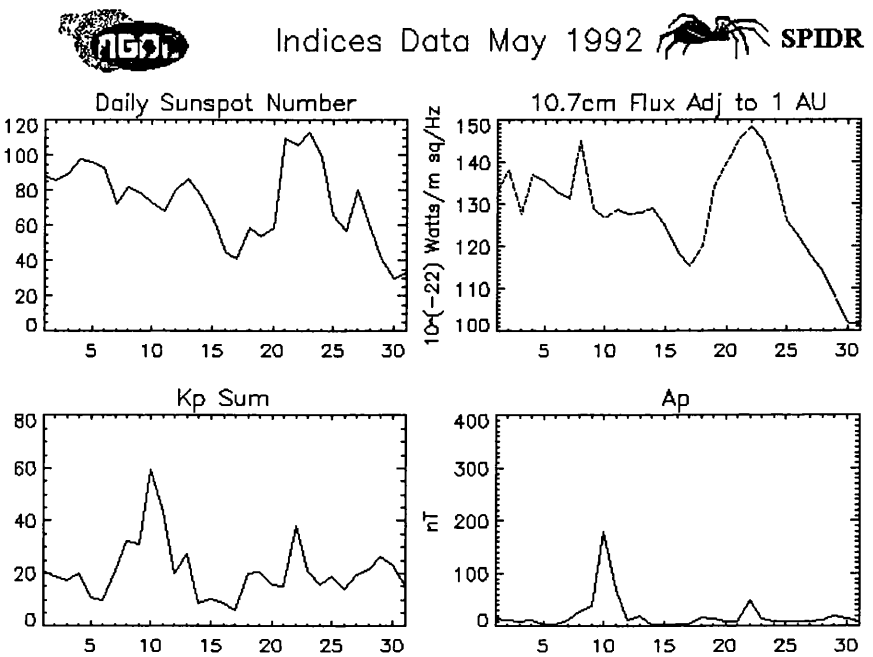

Figure 5.24: Data for May 1992 provided by NGDC, including the daily sunspot number, the 10.7 cm flux, the Kp sum index and the Ap index. Note the huge jump in Ap from 9 to 11 May.

According to Kozuka *et al.* [47], this geomagnetic storm was initiated by a shock wave associated with a disappearing filament on 7 May. They monitored the speed of this shock wave using the multi-station IPS array at Nagoya, and found that its initial speed was over $1000\,\mathrm{km\,s^{-1}}$, before deceleration nearer to the Earth.

The IMP measurements show a shock wave arriving at the Earth late on 9 May, at nearly $900\,\mathrm{km\,s^{-1}}$, while the density of the solar wind increases from $20\,\mathrm{cm^{-3}}$ to $30\,\mathrm{cm^{-3}}$ on the same day (**Figure 5.26**). The arrival of this shock wave was accompanied by a huge increase in proton flux of energy >10 MeV. These energetic particles were also observed by GOES.

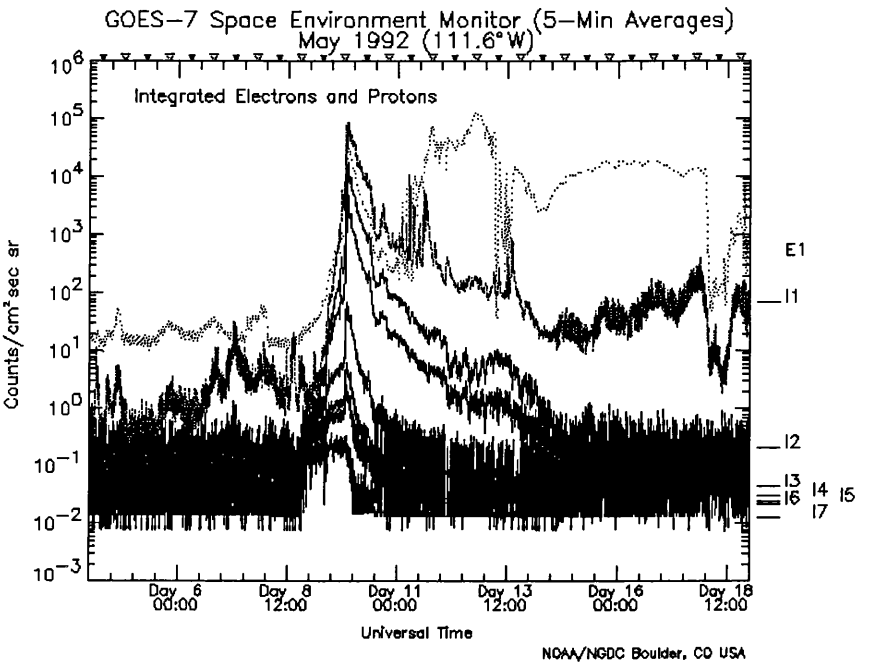

Figure 5.25: The GOES high energy particle flux in May 1992. Fluxes for all particles increase dramatically on 9 May.

By studying the Yohkoh soft X-ray images for this period, Kozuka *et al.* found a transient coronal hole appearing on 7 May in the same south-eastern quadrant as the disappearing filament, and lasting about 17 hours. They suggest that it was fast outflow from this coronal hole which was responsible for driving out the shock wave. The same magnetic reconfiguration that caused the filament to disappear could also have caused this coronal hole to appear. In the Yohkoh image for 7 May (**Figure 5.27**), we can just see this coronal hole to the east of the active arcade associated with the filament disappearance.

Looking carefully at the GOES plots for 9 May (**Figure 5.25**), we could split the data into two separate shock waves. In fact, there were two separate sudden commencements (SCs) on 9 May, the first at 15:41 UT and the second at 19:56 UT. And in the IMP density plot, there are two well-defined peaks late on 9 May (**Figure 5.26**). Kozuka *et al.* suggest that this second shock was related to a solar flare at S26E08 at 15:12 UT on 8 May. If this were the case, it would mean a shock velocity of about $2000\,\mathrm{km\,s^{-1}}$, which is uncomfortably high.

Next, the Cambridge IPS g maps will be investigated. As we saw in **section 4.4.1**, there was a long-lived CIR emanating from a coronal hole from September 1991 to May

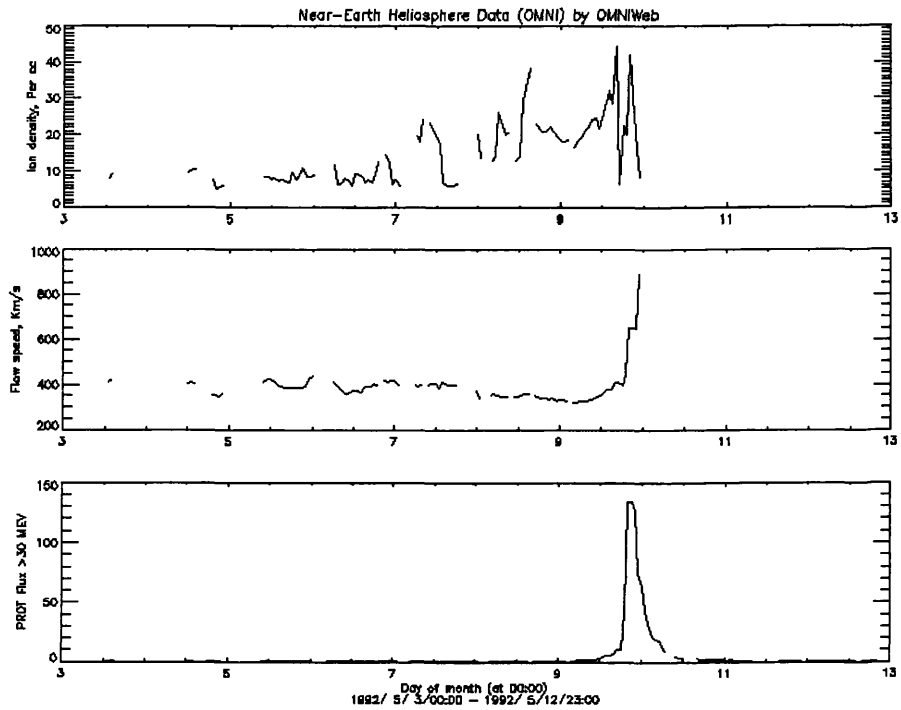

Figure 5.26: The IMP-8 recording in May 1992, of solar wind density and velocity, and high energy proton flux (>10 MeV).

1992, and evident in the g maps as it passed by the Earth every solar rotation. The coronal hole can be seen in the Helium 10830 Å spectroheliograph plot for this rotation, in Figure 5.28. It is at the centre of the diagram, reaching down to about 20° north of the equator, and the central longitude here corresponds to the meridian passage on 7 May.

On 7 May, the enhanced density interaction region at the leading edge of the CIR has reached 1 AU, and is obvious in the g map (Figure 5.54). This density enhancement was also recorded by IMP on 7 May (Figure 5.26). It totally dominates the eastern sky on 8 May (Figure 5.55). On 9 May (Figure 5.56), it is more intense at all eastern elongations, and western elongations are also showing density enhancements.

On 7 and 8 May, most of the τ_S values at the location of the density enhancement are quite low, suggesting a fast moving disturbance. On 9 May, there are even more τ_S values and they are lower again. It was late on 9 May that the previously mentioned shocks arrived at Earth, according to IMP and GOES. From the evidence, it is possible that these fast moving shocks collided into the CIR, and speeded it up, while at the same time accelerating many particles to give the huge fluxes of high energy particles that were

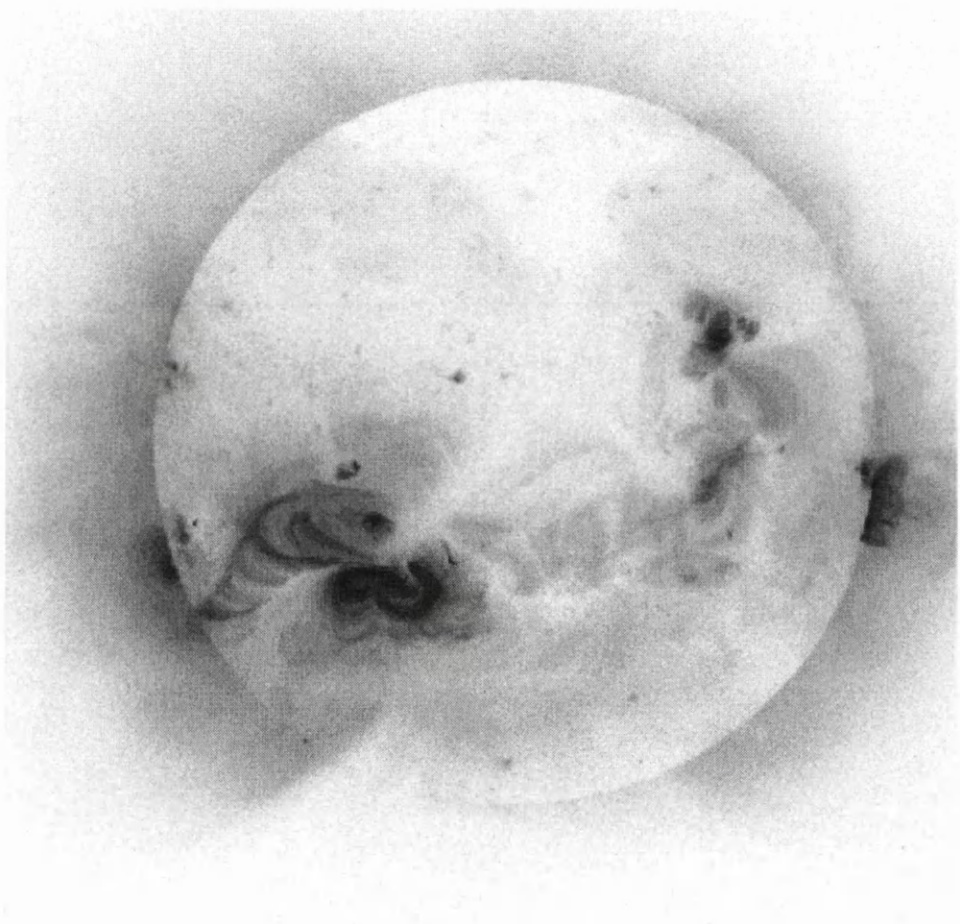

Figure 5.27: Yohkoh SXT image for 7 May 1992.

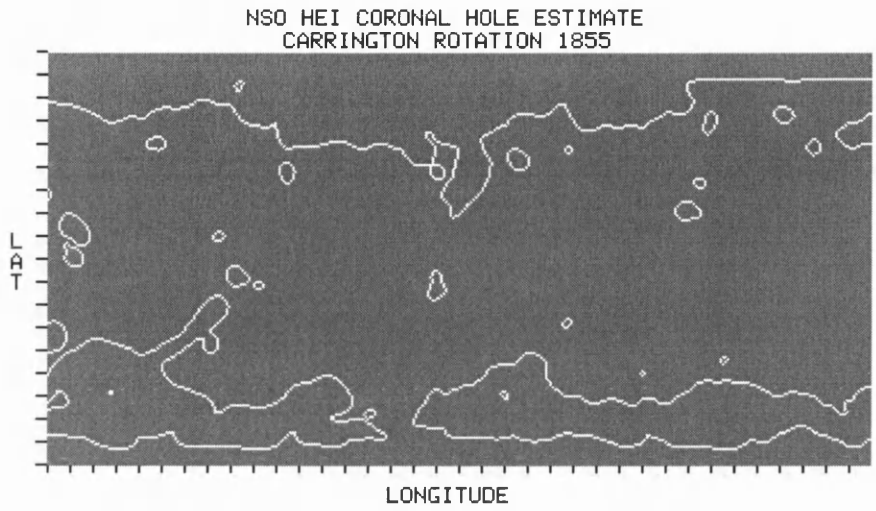

Figure 5.28: Helium 10830 Å spectroheliograph for Carrington rotation 1855. Heliographic longitude runs from 0° at the left to 360° at the right. Heliographic latitude runs from −90° at the bottom (south pole) to +90° at the top (north pole).

measured by GOES and IMP in the latter half of 9 May.

On 10 May, very high densities are seen almost all over the sky (Figure 5.57). This day was the peak in the geomagnetic storm, according to the Ap index. There is surely some ionospheric interference in this map as the ionosphere is bound to be disturbed by such a strong geomagnetic storm. Figure 5.29 shows the profile of g values as a function of eastern elongation for 9 May. The shock front can be seen as the decrease in g values at $\sim 110°$. Yet the profile for the next day, 10 May (Figure 5.30), has a wide spread of g values for elongations greater than $\sim 80°$. This lack of any structure could be caused by ionospheric scintillation.

On 11 May, the disturbance is seen moving off to the west (Figure 5.58). The g map for 12 May shows the low density rarefaction in the wake of the high density disturbances (Figure 5.59), which continues for four more days.

During April to May 1992, the Cambridge IPS array was used in a coordinated campaign with the Ooty radio telescope, located in southern India [57]. The Ooty telescope is a large, steerable, cylindrical paraboloid (530 m × 30 m), working at 327 MHz. For the coordinated campaign, the Ooty telescope observed about 150 scintillating sources between −45° and +45° in declination, and obtained a g value and a velocity estimate for each.

Figure 5.31 shows the g values recorded from 7 to 10 May 1992, by the Ooty telescope

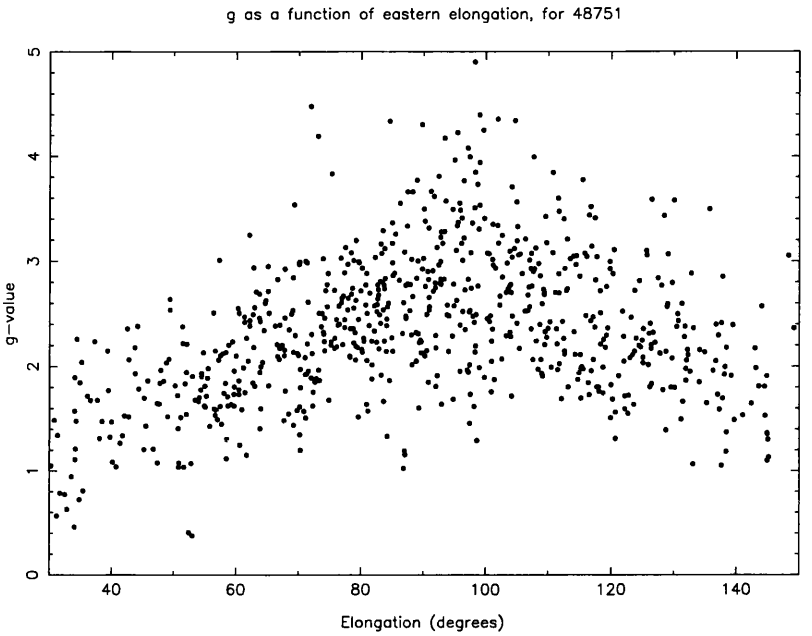

Figure 5.29: g versus elongation for all sources east of the Sun on 9 May 1992. The leading edge of the shock front is apparent as the g value drops at $\epsilon = 110°$.

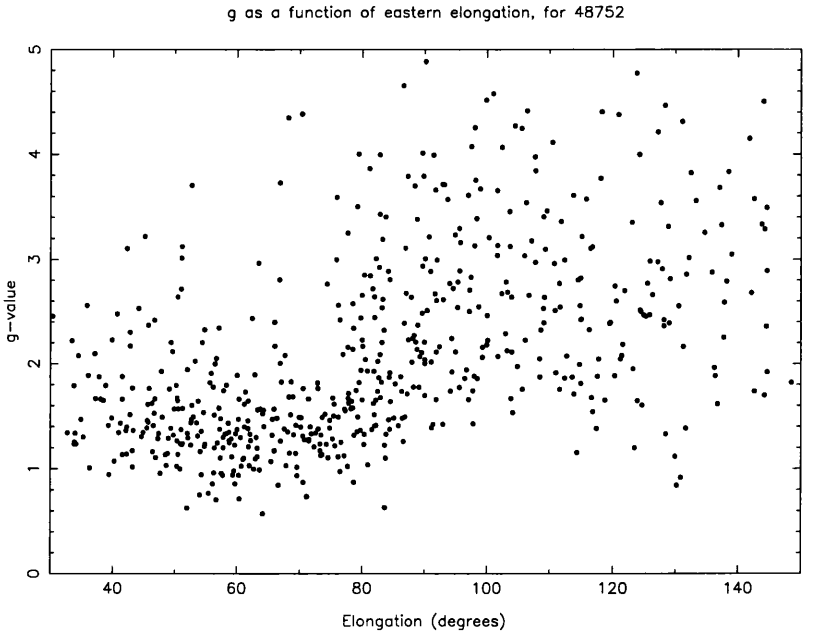

Figure 5.30: g versus elongation for all sources east of the Sun on 10 May 1992. At elongations greater than $\sim 80°$, there is no apparent structure in the g values. This confusion could be caused by ionospheric scintillation.

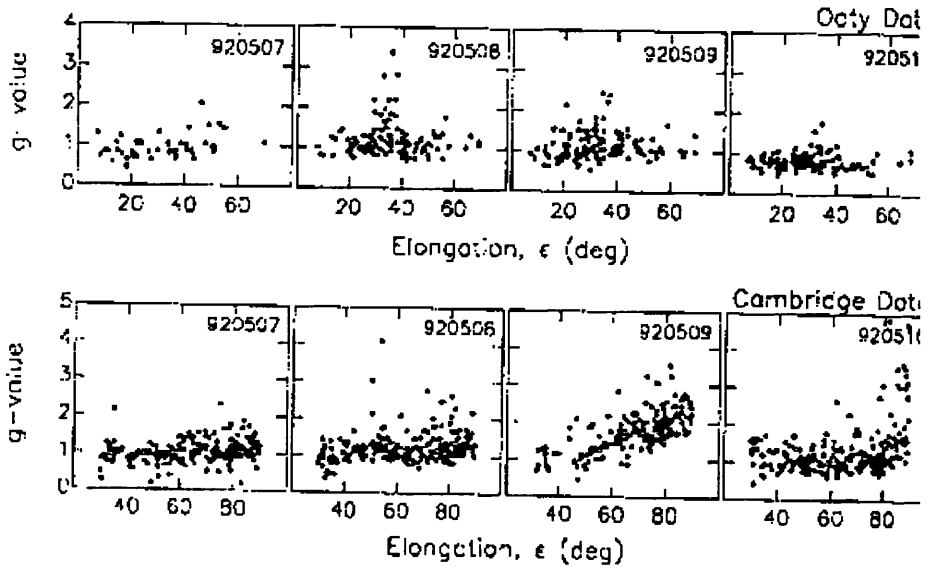

Figure 5.31: The g values measured by the Ooty telescope are on top, and those recorded by the Cambridge IPS array are on the bottom. The g values are plotted as a function of eastern elongation for four days, from 7 to 10 May 1992.

(on top) and the Cambridge array (on bottom), as a function of eastern elongation. This was taken from a paper by Manoharan *et al.* [57]. They were using the less accurate Cambridge g values that were computed at the time of the survey, rather than those calculated in this project. But comparison of the Cambridge g profiles in `Figure 5.31` for 9 and 10 May with the g profiles made during this project, `Figure 5.29` and `Figure 5.30`, shows that they are not too dissimilar.

It is clear from `Figure 5.31` that the g values obtained from the two different instruments are comparable, especially when considering the range of g obtained. On 7 May, for both instruments, $0.6 < g < 2$, though the Cambridge data show a general increase at higher elongations due to the passage of the CIR which, by then, was out of the observational range of the Ooty telescope. On 8 May, the range in g increases dramatically, where g rises to > 3 for both telescopes, indicating the passage of the large, high density shock wave. Enhanced scintillation is maintained on 9 May, before almost ambient conditions return for both telescopes on 10 May.

Of course, the Ooty and Cambridge telescopes observe the same sources, but at different times of the day, therefore making it difficult to do a direct comparison, and some spread of values is to be expected. It is satisfying that approximately the same results are obtained

by very different instruments at different sides of the world, confirming the validity of the IPS technique over the period of interest.

In this section, rather than attempt to fully explain the source of the shocks from the Cambridge IPS evidence alone, I have presented the evidence gathered by other investigators, together with that available from our g maps. The g maps help trace the evolution of interplanetary disturbances in the solar wind beyond 30°. Even with this new evidence, it is often difficult to determine the course of events, especially when the IPM is perturbed by more than one major disturbance. IPS can only give a 2-dimensional representation of the solar wind density structure. A complete understanding of complex events such as these will only be available once three-dimensional data (from spacecraft such as STEREO) are available.

Despite these issues, the g and τ_s maps have been useful in the investigation of certain events, by illuminating just how complex the chain of events is, and how it is not often as simple and clear-cut as might be first thought.

5.5 Pulsar planet detection

In 1967, the Cambridge IPS array was used in the discovery of pulsars [33]. Their trace is evident in IPS plots, as pulsars are intrinsically variable (or "pulsating"). The difference between pulsars and other "normal" scintillating sources is that pulsars will show a flatter $A(\epsilon)$ curve. The response of the scintillometer is NOT caused solely by diffraction in the solar wind, therefore their scintillation is less strongly affected by elongation from the Sun. This section will not deal with the detection of pulsars themselves, but with the planets that have recently been discovered to be in orbit around a pulsar, and how IPS can contribute to the verification of the existance of these planets.

In 1992, Wolszczan [99] announced the presence of two Earth-mass planets in orbit around the pulsar PSR B1257+12. This deduction came from highly sensitive timing observations of the pulse TOAs (Time Of Arrival of pulses) with the 350 m Arecibo radio telescope. The proposed planetary masses around the pulsar lead to reflex motion of the pulsar itself, which means that the light-travel times for the pulses arriving from the pulsar are disturbed. The timing residuals between the predicted and actual TOAs, reveal periodicities corresponding to planetary orbits. Two planets were observed to have highly

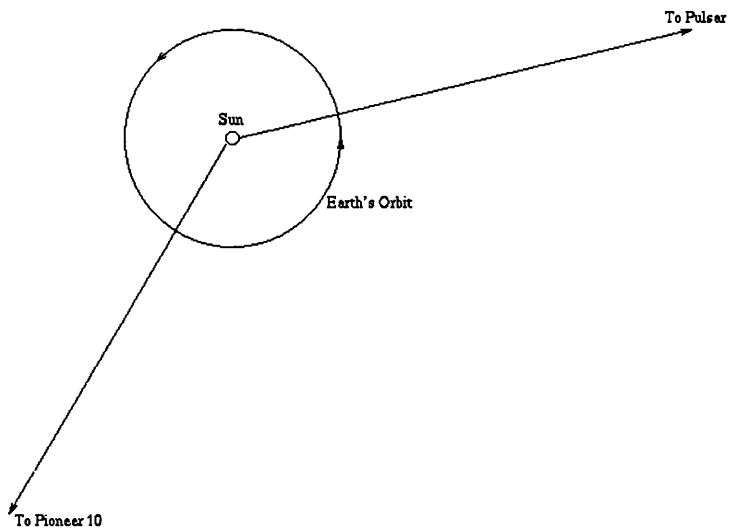

Figure 5.32: The positions of the Pioneer 10 spacecraft and the pulsar PSR B1257+12 in relation to the Earth and its orbit around the Sun.

stable, nearly sinusoidal periodicities at 66.6 and 98.7 days.

It is important to note that no other millisecond pulsars routinely observed at Arecibo with the same data acquisition equipment showed a similar affect in their timing residuals. Also, it appears that the periodicities are independent of radio frequency, implying that they are really caused at the source of the radio waves, and not by dispersive propagation effects along the line of sight to Earth.

In 1994, further TOA observations of PSR B1257+12 revealed a third planet with a 25.34 day orbit [98], referred to as planet A. The perturbations caused by this Moon-sized planet were weaker and had been more difficult to detect.

But later, in 1997, Scherer *et al.* [76] revealed evidence that the 25.34 day periodicity in the pulsar's TOA data was not caused by a planet in orbit around it. They suggested that the radio pulses from the pulsar were affected by their passage through the IPM, and hence showed a periodicity similar to the Sun's rotation. This same effect was observed with the Pioneer 10 spacecraft, whose radio carrier wave for Doppler data showed a 25.3 day periodicity over a long time span (nine months). They concluded that the 25.34 day periodicity seen in the TOA pulsar data was not caused by a planet A, but instead by electron density variations in the IPM.

It could be a mere co-incidence that the two periodicities are the same. The fact that

they are so similar actually raises suspicion. The IPM is a very turbulent place, with different phenomena dominating at different times, and structures being "swallowed up" by faster moving streams catching up with them. The pulsar PSR B1257+12 and Pioneer 10 are at very different longitudes (see Figure 5.32), and so the line of sight to each goes through different parts of the IPM. Therefore it is very unlikely that the same phenomenon (electron density variations in the solar wind) will affect the radio waves coming from both in exactly the same way, and leading to the exact same periodicity, to the precision of a few hours (a tenth of a day).

Scherer *et al.* claim that the periodicity in the Pioneer 10 Doppler data is caused by density variations in the IPM. IPS is another method which can observe density variations in the IPM, and the Pioneer 10 measurements occurred within our survey period. IPS should therefore be able to reveal the same periodicities seen by Scherer *et al.* We shall see that the IPM data do not confirm Scherer's claim, but rather undermine it.

When Pioneer 10 is in conjunction with the Sun, as viewed from Earth, it is impossible to carry out these Doppler experiments, due to solar noise. But there is a nine month window of opportunity, centred on solar opposition, when the Doppler observations can be carried out (see Figure 5.32). In 1993, solar opposition occurred around Dec. 4th, so, Scherer *et al.* analyzed the Pioneer 10 Doppler data from July 1993 to April 1994.

To obtain the Doppler data, a signal is sent from Earth at a frequency of 2.1 GHz. It is transponded by Pioneer 10, and then received back at Earth hours later. To determine the Doppler shift, the Doppler data are coherently referenced to hydrogen-maser frequency standards at Deep Space Network (DSN) stations in California, Australia and Spain.

Because they travel only in the IPM, the radio waves are affected by the plasma density variations along the ray path there. Changes in refractive index along the line of sight cause variations in optical path length that appear in the Doppler data.

One of the best ways to search for periodicities in a data set is to produce a periodogram. The periodogram, discussed in chapter 13 of Numerical Recipes [64], estimates the power spectrum of a time series. It can search through the Doppler data and find any periodicities in the data set.

Systematic effects were removed by Scherer *et al.* from the Doppler data taken during these nine months, and the resulting periodogram is in Figure 5.33. The strongest periods appeared at 25.3 and 13.3 days, both sharp peaks at a confidence level $> 95\%$.

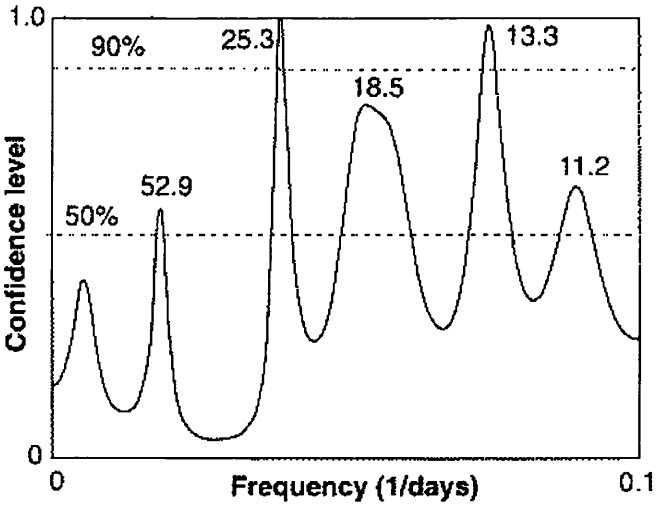

Figure 5.33: Scherer's periodogram for Pioneer 10 Doppler data, covering the nine month interval centred on solar opposition. The confidence level for each particular frequency is plotted. The strongest period is at 25.3 days.

There were three other periods with confidence levels > 50%. These were at 18.5, 11.2 and 52.9 days, in decreasing strength of confidence. Only the strongest period at 25.3 days is explained by Scherer *et al.*, and is interpreted as being due to solar rotation.

Periodicity searches in in-situ data

Pioneer 10 itself took in-situ density measurements, which should display the same proposed periodicities if the argument holds and, more importantly, if the same structure is "frozen in" to the IPM. If the structure is not "frozen in", then it would be highly unlikely that the same periodicities would be observed for lines of sight that were almost 180° away from each other, as are the lines of sight to Pioneer and the pulsar, see `Figure 5.32`.

From NSSDC (National Space Science Data Centre), I have downloaded the Pioneer 10 density measurements for the same nine month period that was dominated by the 25.3 day period, according to the Doppler data. `Figure 5.34` shows a Lomb-Scargle periodogram made from these data.

Spectral analysis on unevenly sampled data can be difficult. The Lomb-Scargle method for finding periods is a variant of the classical periodogram, i.e. the discrete Fourier periodogram (see `chapter 13` in Numerical Recipes [64]). It is particularly good with data sets with many missing data because it is invariable to a shift in the origin of time.

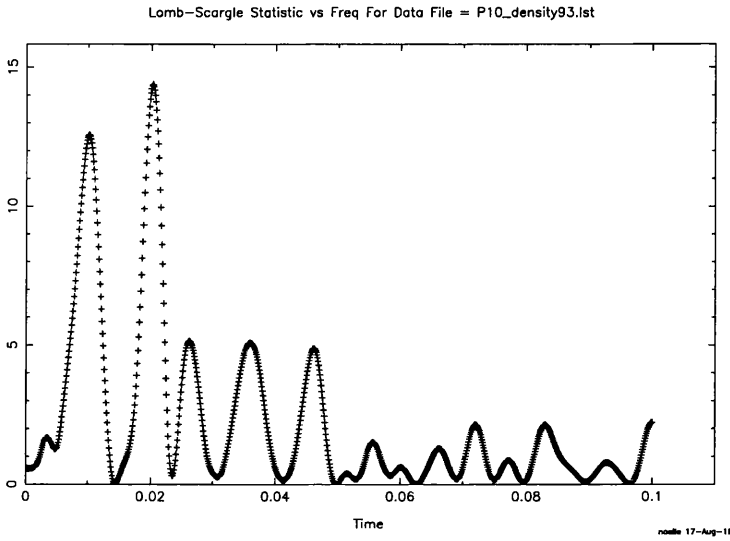

Figure 5.34: The Lomb-Scargle periodogram for Pioneer 10 in-situ density measurements, covering the nine month interval centred on solar opposition. The confidence level (vertical axis) is plotted for each particular frequency, given as $\frac{1}{\text{days}}$ on the horizontal axis .

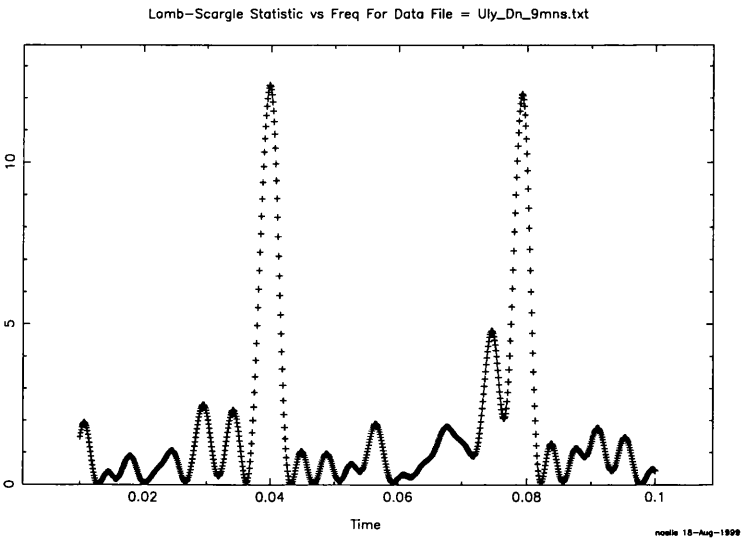

Figure 5.35: The Lomb-Scargle periodogram for Ulysses in-situ density measurements, covering the nine month interval centred on solar opposition.

It is described by Scargle [75] and applied by Black and Scargle [10] for detecting periodic signals in astrometric data. Because of the many gaps in the present data set, it is quite suitable for our purposes. It is available in a Starlink package called `Period`.

The strongest frequency in `Figure 5.34` is at $0.0202\ \frac{1}{\text{days}}$, corresponding to a period of 49.5 days. The closest peak to a period of 25.3 days is at 27.5 days (frequency $= 0.036\ \frac{1}{\text{days}}$), but this peak is much weaker than that for the 49.5 day period. So this evidence does not support the Doppler data for an exact 25.34 day period. This is probably explained by the fact that Pioneer 10 is measuring the density very far from the Sun, at the far reaches of the solar system (at 58 AU in 1993), while the Doppler carrier wave is travelling all the way through the IPM from Pioneer 10 to Earth and back again, thus sampling quite a different portion of the solar wind.

Scherer *et al.* also saw an electron density variation with solar rotation for the measurements made by Ulysses during these nine months. I have analyzed the Ulysses density data, and have found a strong peak at 25.13 days, and another at 12.63 days (see `Figure 5.35`). This first period is very close to the 25.3 days required, but the difference here is that Ulysses was measuring the IPM at a far removed location from what either the pulsar or Pioneer 10 measured. The pulsar and Pioneer 10 were at low heliographic latitudes ($17°$ and $-3°$ respectively). At the beginning of this interval, Ulysses was at a heliographic latitude of $-35°$, and at the end it was was $-60°$. The solar rotation at these latitudes is far longer than for the latitudes of the pulsar or Pioneer 10, so a 25.13 day periodicity might not be directly linked to solar rotation.

According to Phillips [62], the sidereal rotation period of the Sun (using large regular sunspots) at $0°$ latitude is 25.1 days. At $10°$ it is 25.2 days, at $20°$ it is 25.6 days, at $30°$ it is 26.4 days and at $40°$ it is 27.3 days So, Pioneer 10 (at $-3°$) should "see" a period of about 25.1 days. The pulsar (at $17°$) should "see" a period of about 25.6 days. And Ulysses will experience a periodic fluctuation in density measurements with a period of greater than 27.6 days. This does not match with the 25.1 day period seen in `Figure 5.35`. But it does highlight the fact that it is very difficult to predict what solar rotation period will be "felt" by radio waves in a certain direction. Also, it makes it difficult to say for certain that if two different lines of sight reveal the same periodicities, that they are reacting to the same IPM.

Periodicity searches in IPS data

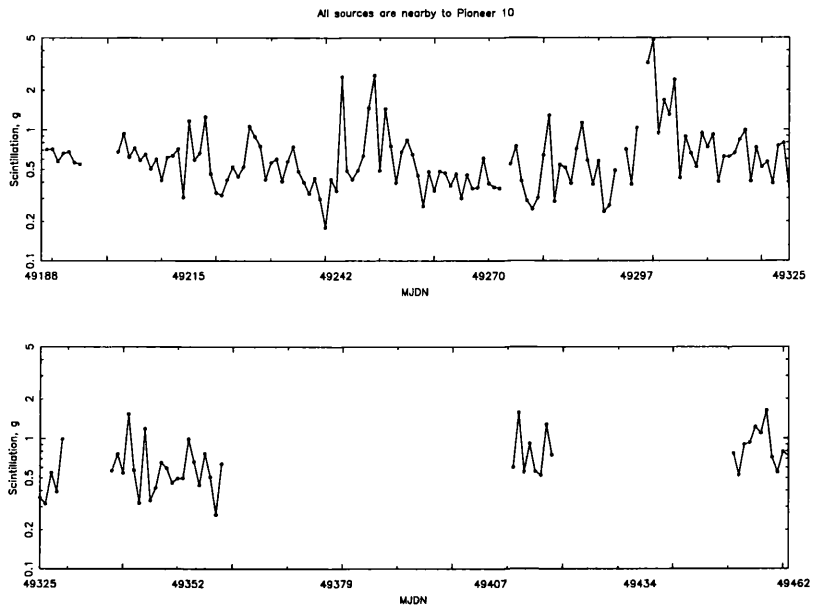

Figure 5.36: The graph of average g against time measured in Mean Julian days, over the same nine month interval as in `Figure 5.34`. All of the sources chosen to get the average g are near the position in the sky of Pioneer 10. Unfortunately, there are large gaps in the second half of the data (in 1994), due to the IPS array being out of action.

IPS g values are determined by the electron density variations along a line of sight to a radio source. Therefore, they should contain the same periodicities as seen by Scherer *et al.*, if they are real and indeed caused by solar rotation.

To analyse the IPS g values, a program `plotper.c` was written. A number of strong sources (16) were chosen near to the direction of interest, i.e. close to the pulsar, or to Pioneer 10. The g values were extracted from each source over a number of days. The geometric average was taken for each day, and plotted out over time, as in `Figure 5.36`.

The data for sources near to Pioneer 10 are then used to make a periodogram, `Figure 5.37`. The strongest peak here is for a period of 52.63 days. Perhaps the 52 day period is caused by a large gap in the data set, of about 50 days. The Lomb-Scargle method might not be able to deal with such a large amount of the data being missing (a gap of 50 days out of 274). Two other significant periods are at 17.21 and 26.11 days. The 26.11 period is quite close to the 25.3 day period seen in the Pioneer 10 Doppler data taken during this interval. As for the other peaks, there will always be some rogue periodicities in a periodogram of any time series that is not a perfect sine wave.

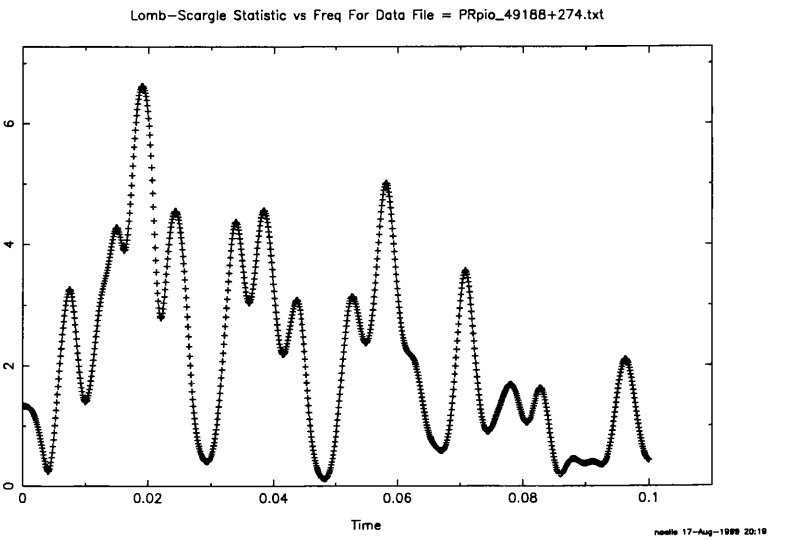

Figure 5.37: The Lomb-Scargle periodogram for IPS g values, for sources in the same direction as Pioneer 10, over the nine month interval.

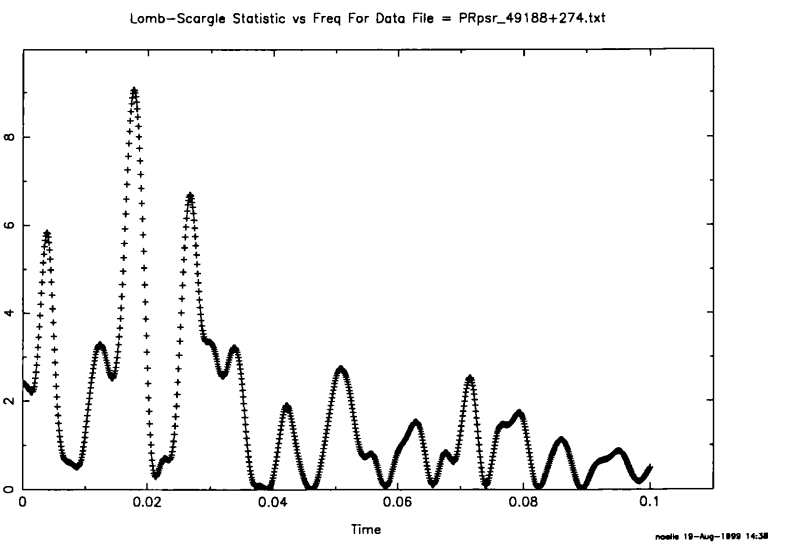

Figure 5.38: The Lomb-Scargle periodogram for IPS g values, for sources in the same direction as the pulsar PSR B1257+12, over the nine month interval.

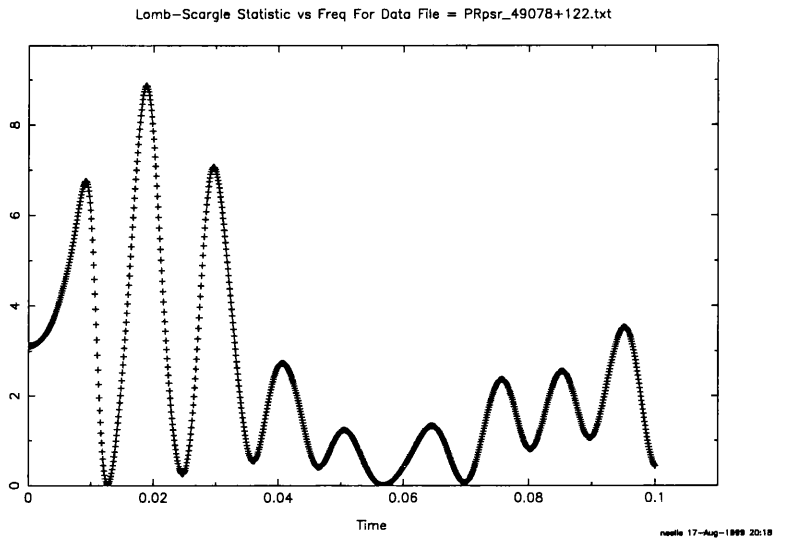

Figure 5.39: The Lomb-Scargle periodogram for IPS g values, for sources in the same direction as the pulsar PSR B1257+12, over the three months (April, July and August 1993) that the TOA data show a 25.34 day periodicity.

It is not possible to do similar analysis for the Ulysses spacecraft for this interval, because it was too far south of the ecliptic where the Cambridge IPS array cannot observe.

The periodogram for the same time interval for the sources nearby the pulsar is shown in `Figure 5.38`. Here, the strongest period is at 56.50 days, and there is only a weak peak at 23.70 days (frequency = $0.042\ \frac{1}{\text{days}}$). This $\sim$ 50 day period might also be caused by the large data gap, which is the same as for the sources near Pioneer 10.

`Figure 5.39` shows again the periodogram for the sources near the pulsar, but over a shorter time interval of just three months, April, July and August 1993. It was during this time that Wolszczan directly measured the 25.34 day period in the TOA data. The periodogram here looks slightly different to that in `Figure 5.38`. The strongest period is still around 50 days (53.19 to be precise), but the nearest peak to 23.70 is at 24.63 days. So over this shorter timescale, the shape of the periodogram has changed, and Wolszczan's periodicity of 25.34 days has not been found, at least not to the precision and certainty of Scherer's claim.

If the pulsar's TOA data have continuously been giving a period of exactly 25.34 days for a long observational time, then this must be a good argument that it is really caused by a planet in a stable orbit. The IPM on the other hand, is far from stable, and the IPS evidence confirms that it is unreasonable to associate the Pioneer data with Wolszczan's

observations as they do not correspond to the same line of sight. It has not been possible to totally disprove Scherer's argument, but it is clear how difficult it is to find exact periodicities in the parameters of the IPM.

5.6 Conclusions

In this chapter, the Cambridge IPS data set has been exploited to gain insights into the structure of the IPM. By providing an overall view of a large part of the solar wind, disturbances have been tracked by IPS, leading to a better understanding of the types of structures in the solar wind, such as interplanetary shocks, co-rotation interaction regions, CMEs and other transients. The effects of these disturbances on the near Earth space environment has been evaluated by monitoring the output from different spacecraft and satellites.

The statistical analysis of trends in the solar cycle, and the search for periodicities in the solar wind parameters has shown how variable the IPS measurements can be, but yet the underlying characteristics are still to be seen, if they are indeed real.

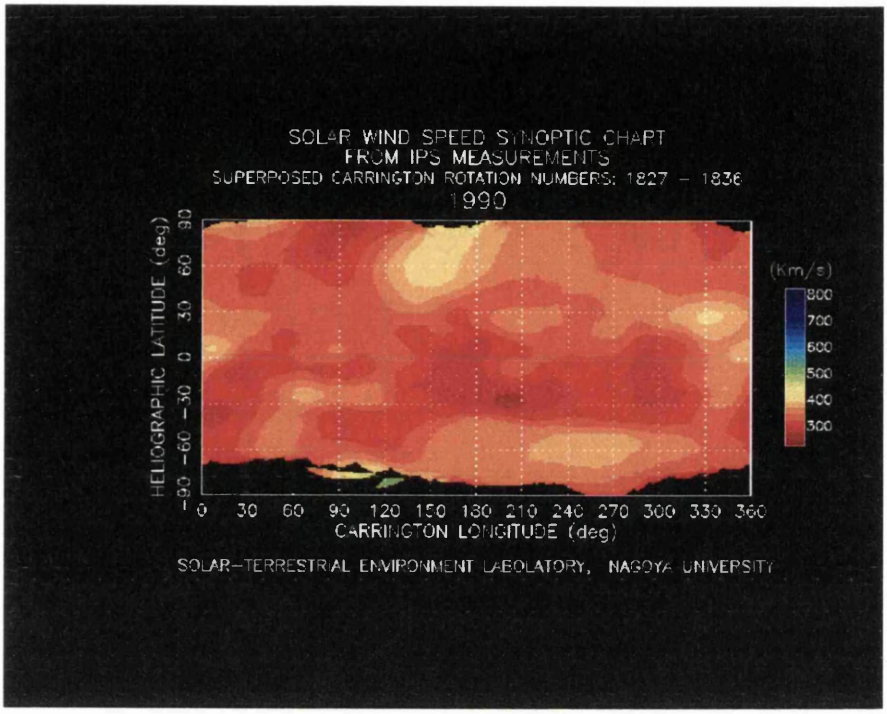

Figure 5.40: Nagoya synoptic map for 1990. At solar maximum, slow wind dominates all over the Sun.

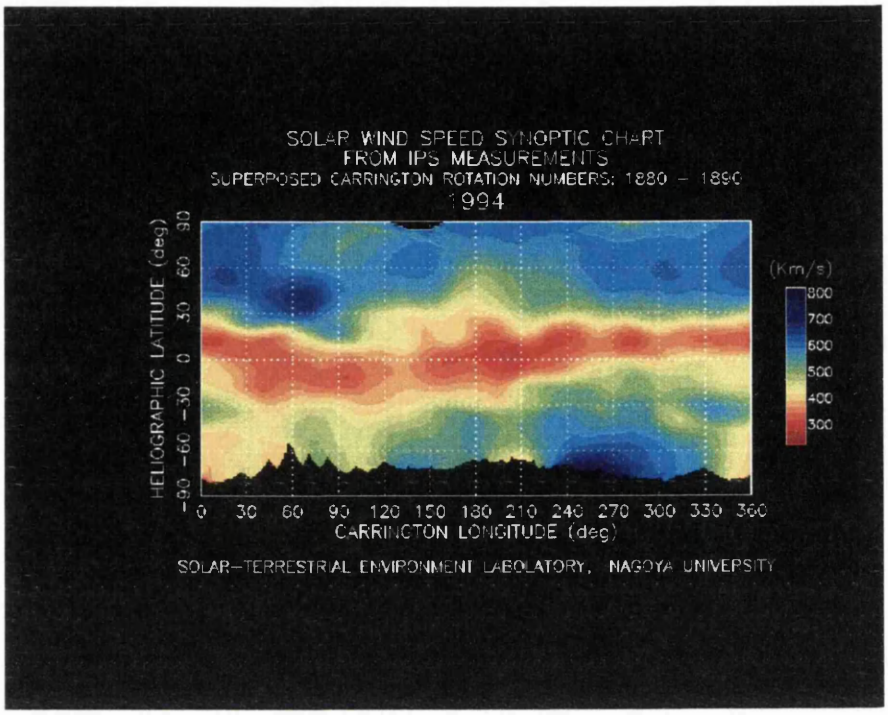

Figure 5.41: Nagoya synoptic map for 1994. The slow wind is only found in a narrow band near the equator, in the declining phase of the solar cycle.

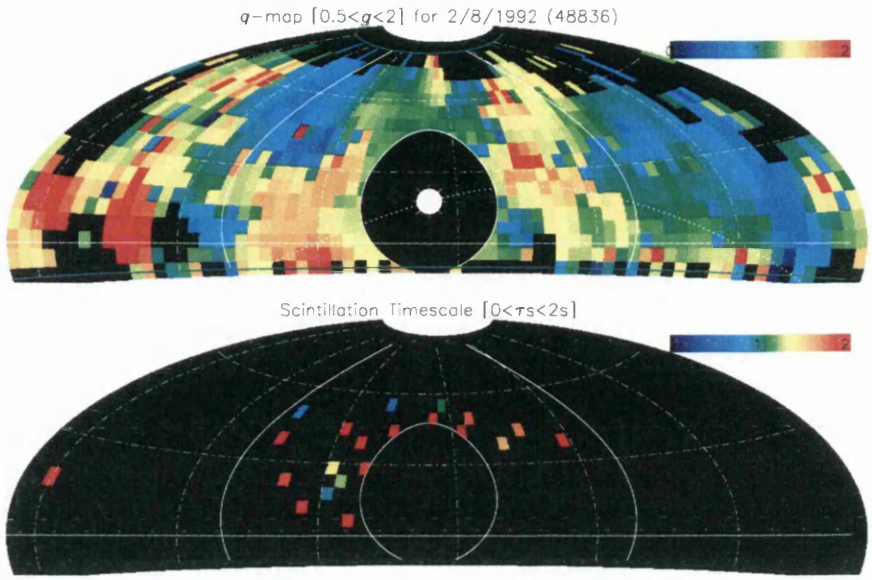

Figure 5.42: The g and τ_s maps for 2 August 1992. Of interest here is the area of enhanced material to the east of the Sun, at low latitudes, and at an elongation of about 60° on this day.

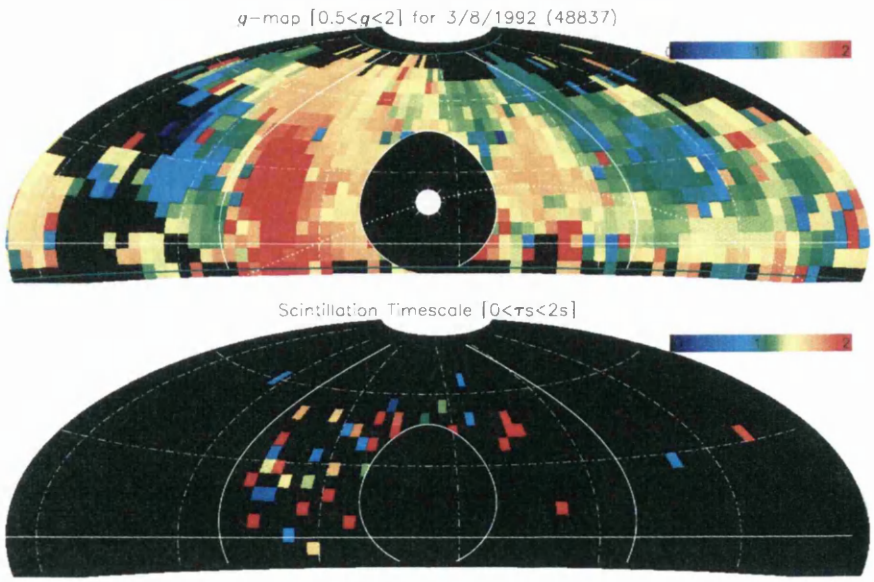

Figure 5.43: The g and τ_s maps for 3 August 1992. The density enhancement seen on the previous day has moved further east, and is now showing as at least double the ambient density (red means a g of 2 or more).

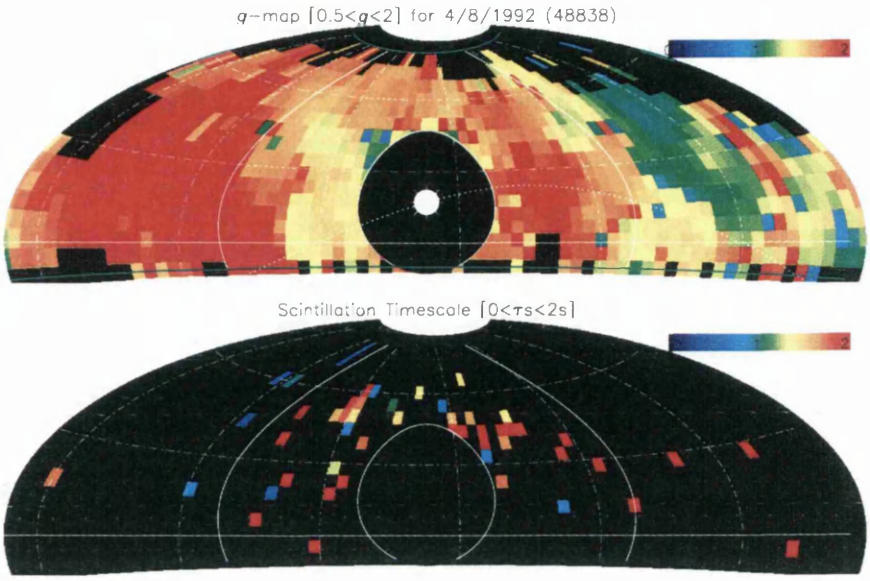

Figure 5.44: The g and τ_s maps for 4 August 1992. The disturbance has reached Earth (at elongations of $> 90°$) and can be seen both east and west of the Sun.

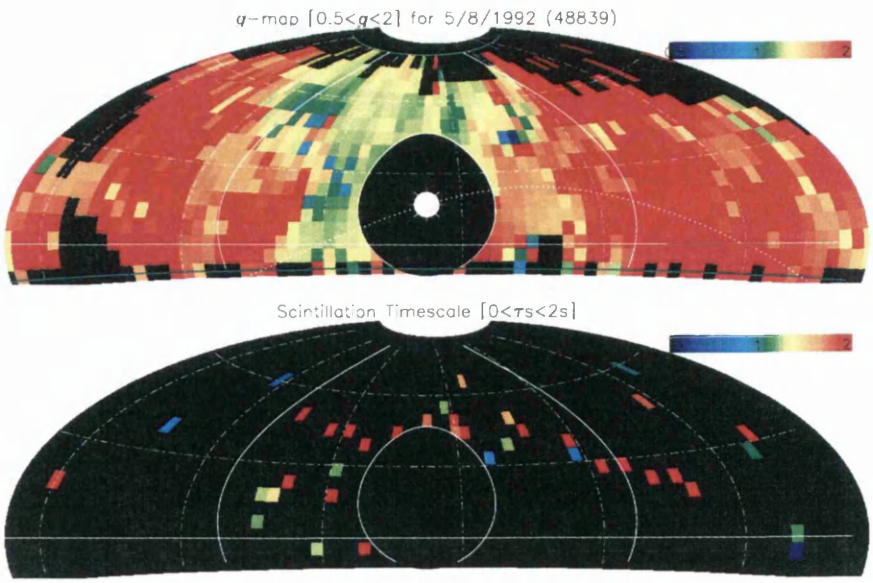

Figure 5.45: The g and τ_s maps for 5 August 1992. The high density disturbance is still dominating the local IPM at Earth.

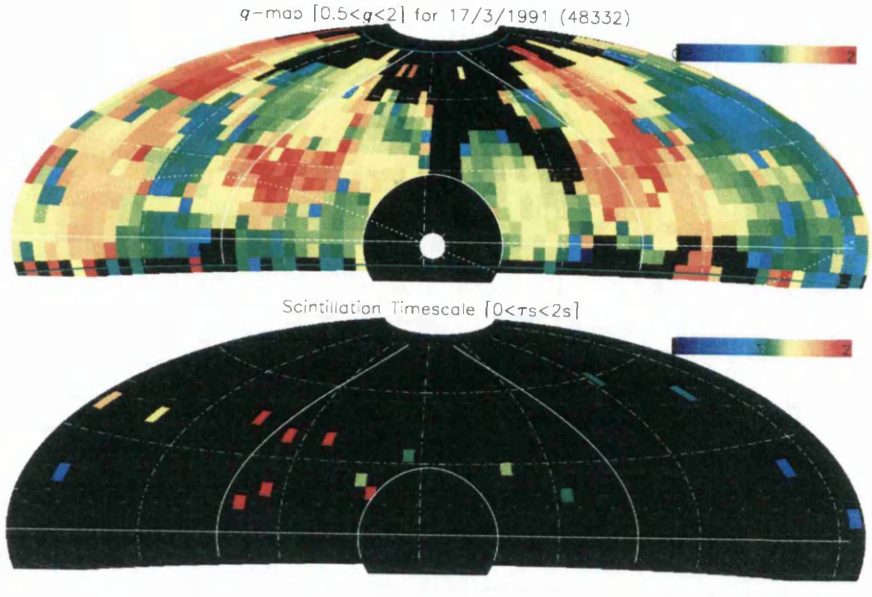

Figure 5.46: The g and τ_s maps for 17 March 1991.

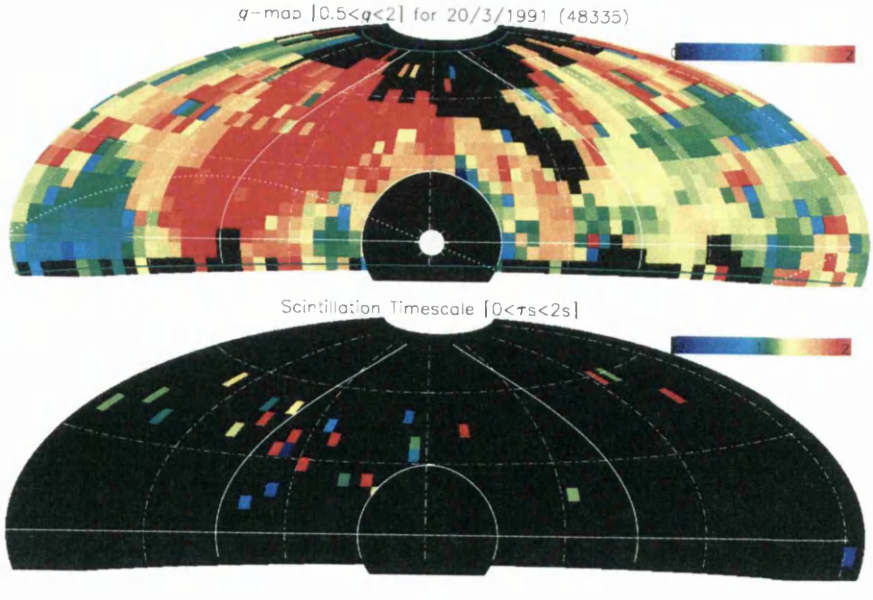

Figure 5.47: The g and τ_s maps for 20 March 1991.

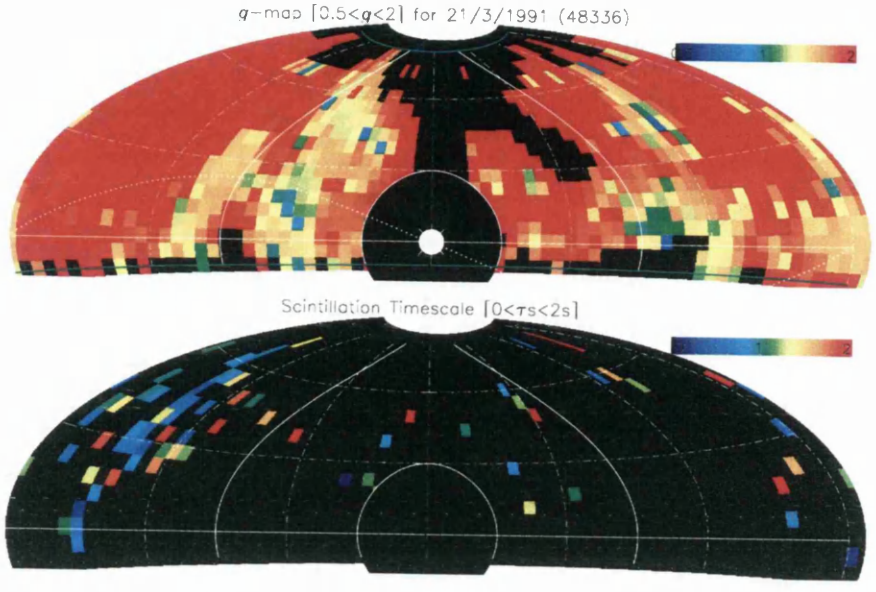

Figure 5.48: The g and τ_s maps for 21 March 1991.

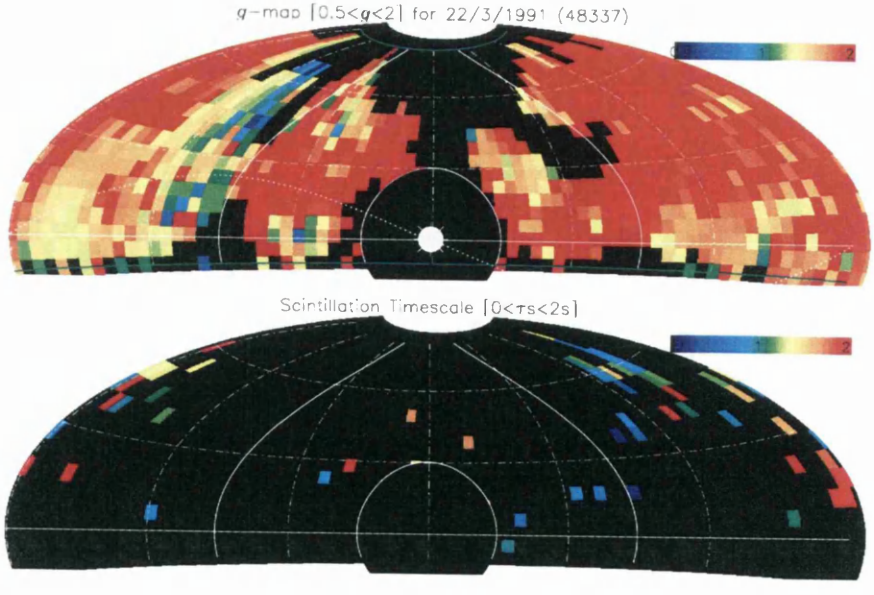

Figure 5.49: The g and τ_s maps for 22 March 1991.

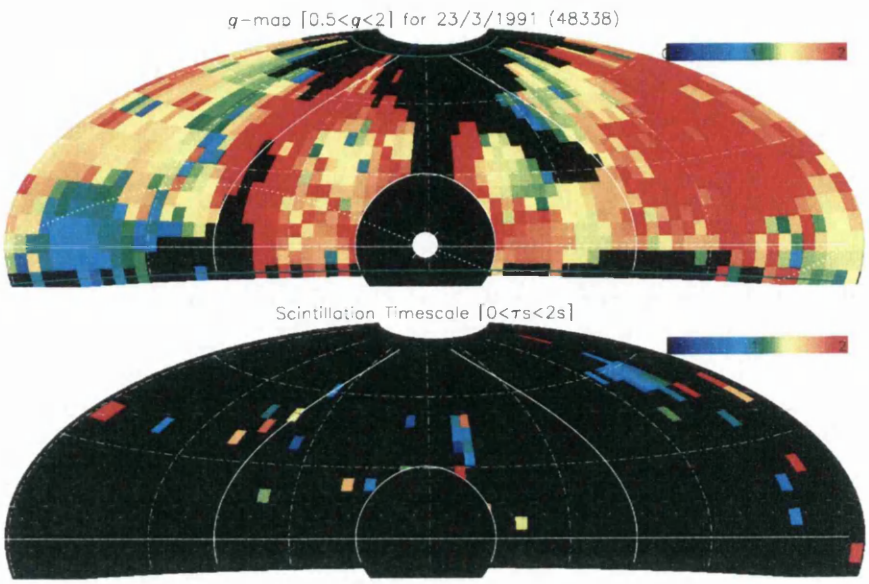

Figure 5.50: The g and τ_s maps for 23 March 1991.

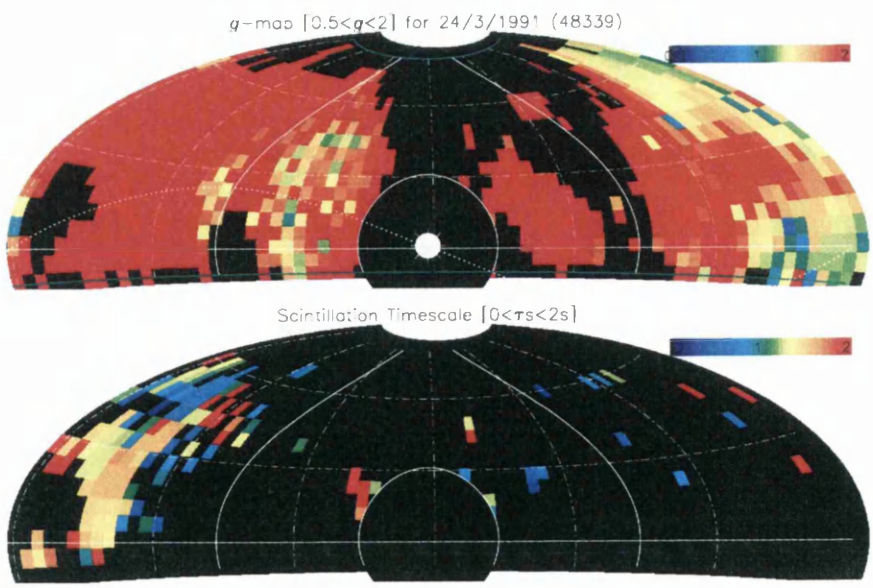

Figure 5.51: The g and τ_s maps for 24 March 1991.

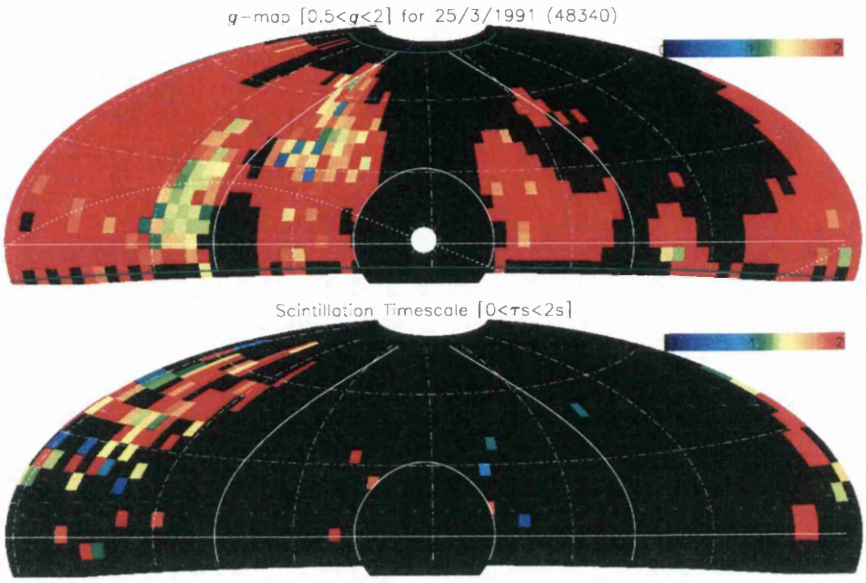

Figure 5.52: The g and τ_s maps for 25 March 1991.

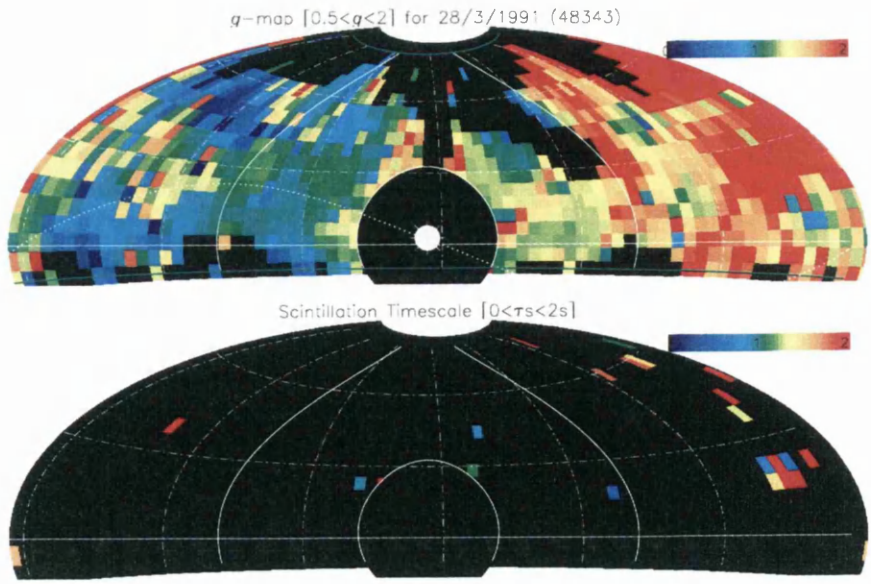

Figure 5.53: The g and τ_s maps for 28 March 1991.

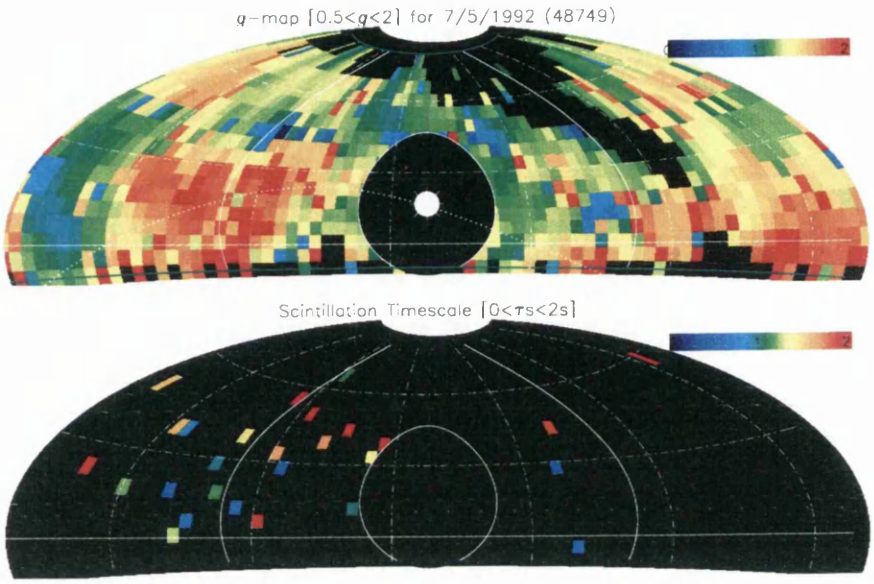

Figure 5.54: The g and τ_s maps for 7 May 1992.

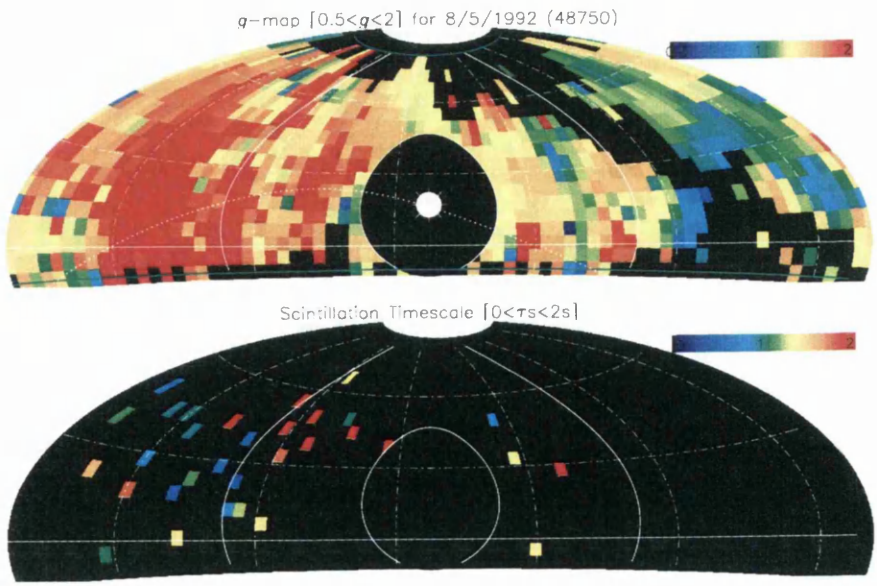

Figure 5.55: The g and τ_s maps for 8 May 1992.

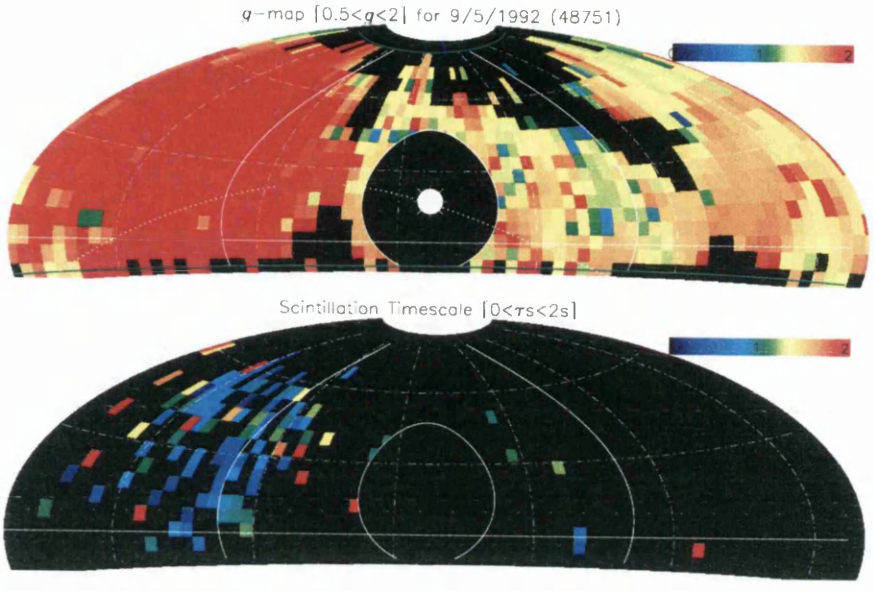

Figure 5.56: The g and τ_s maps for 9 May 1992.

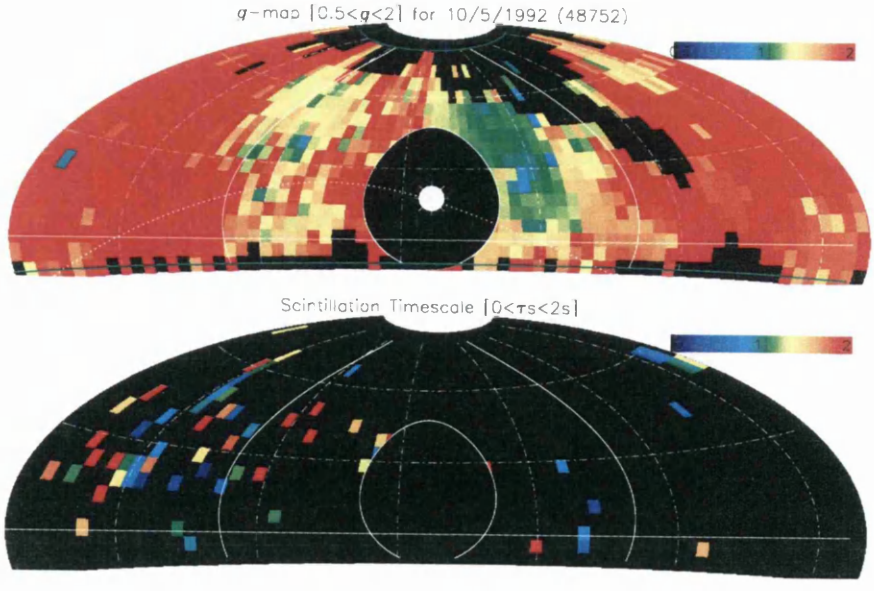

Figure 5.57: The g and τ_s maps for 10 May 1992.

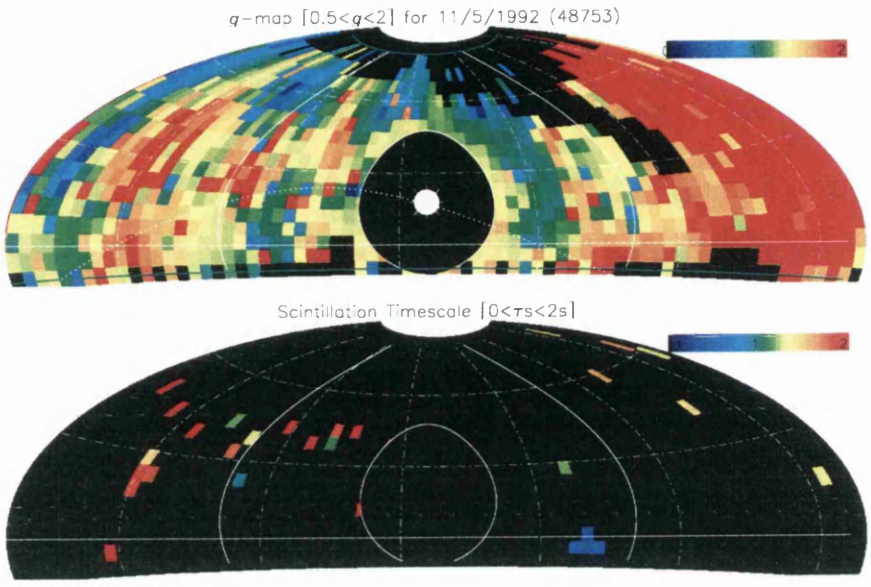

Figure 5.58: The g and τ_s maps for 11 May 1992.

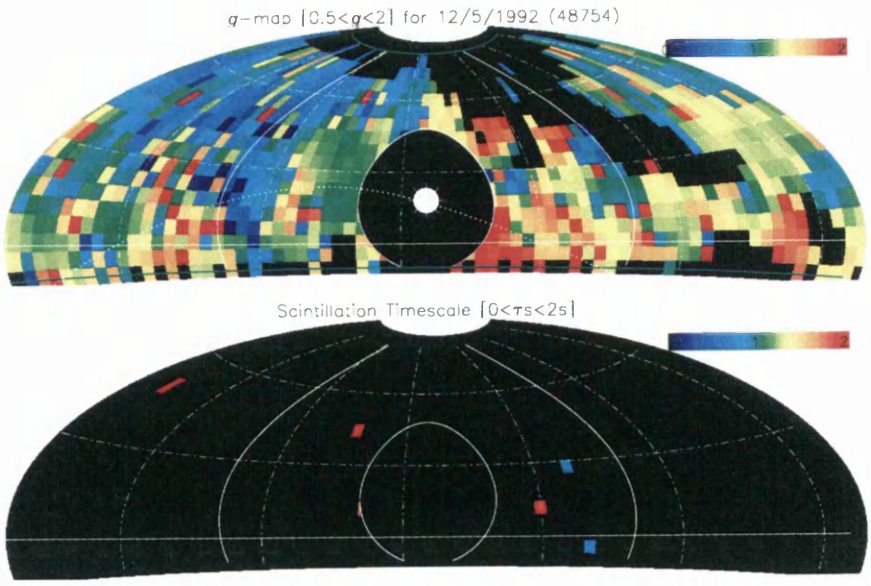

Figure 5.59: The g and τ_s maps for 12 May 1992.

Chapter 6

Conclusions and future work

"I found I was all out of exit lines, so said nothing.
...I also found a zinc bucket by kicking it. The symbolism didn't appeal to me."

A.E. Roy - Deadlight

6.1 Overview

The aims of this project have been to extract as much information as possible from the 1990-95 Cambridge IPS survey, and thus to investigate the ability of IPS techniques to probe the solar wind. This has been done by a careful analysis of the data set. When the survey was in progress, it wasn't possible to process the data as an ensemble and derive the five year averages needed for different computations. Therefore, this present analysis has been more thorough than previous attempts.

The more powerful computing power available during the course of this project has meant that for the first time, the whole data set can be stored together, and manipulated all at once. This has made a huge difference to the quality of the analysis possible. The maps that result are much more detailed than the early maps made during the course of the survey, and directly afterwards [97].

It was a rather big task to process over 1 Gb of raw data to a stage where it could be easily accessed and worked with. This was an essential undertaking which dictated the quality of the rest of the project. The resulting analysis would have been worthless if the data processing before it had been flawed, or done using unsound assumptions.

The subsequent work verified the integrity of the data set and provided a valuable diagnostic tool in the form of grey-scale synoptic plots for each beam. This also proved that the raw data files had been read correctly, with the timing of each observation computed in the right manner.

Probably the most vital stage of the project was the writing of the algorithms which determined the g and τ_s parameters in the presence of noise. It was difficult at the time to say that they were working as they should, but when the all sky maps were made, the overall structure showed the coherent density enhancements and reductions as expected. Monte Carlo simulations and statistical analysis of the computed g and τ_s values gave further proof of their credibility.

By comparisons with other data sources, the IPS maps displayed the same general conditions in the IPM as observed by other instruments. Furthermore, the Ooty radio telescope in southern India, was shown to observe comparable g values in a co-ordinated campaign in 1992 [57] and the present analysis has confirmed this correlation. It was not an easy task to compare IPS with IMP observations, because IMP was taking a localized, in-situ measurement, while the IPS array was observing thousands of sources during the course of a day. Only a few of those sources would be in the correct relative position so that the dominant scintillation along the line of sight occurred close to where IMP was situated. Nevertheless, some good correlation was found between the two data sources.

6.2 Outcome

The objective of this thesis has been to demonstrate the usefulness of IPS, and to search for new limits to its interpretative abilities. Has this been achieved? Certainly, the IPS maps are an improvement on the original ones and they have been successfully used to investigate particular events and disturbances in the solar wind. The all sky view afforded by these maps is invaluable for tracking transients and other disturbances in the IPM. When they arrive in the near Earth space environment, this is very obvious, as huge areas of scintillation enhancement cover the sky at 1 AU.

The root causes of disturbances in the IPM have been explored, with the help of other instruments, both ground-based and in space. Interplanetary shock fronts seem to be responsible for many of the geomagnetic effects. These shock fronts might be driven by

a sudden increase in velocity of the flow from a coronal hole [12]. It is only through collaboration with other instruments that all the secrets of solar activity and its influence on the solar wind will be revealed. IPS certainly has its part to play here.

In the search for trends in the solar cycle, it was found that the typical velocity of the solar wind had a much stronger dependency on heliographic latitude at the declining phase of the solar cycle, rather than at the maximum of solar activity. This trend had been observed before, e.g. by the Nagoya telescope.

In the pulsar planet question, the Cambridge IPS data were able to provide evidence to refute the argument of Scherer *et al.* [76] who claimed that the planet A (orbiting around pulsar PSR B1257+12) did not exist.

On the question of solar wind velocity, a novel technique was introduced to obtain the velocity with a single IPS station previously only able to make density measurements. This was done by measuring the timescale over which the scintillation typically occurs. This was successful only to a certain degree. There were large errors involved, but overall, statistically, the method showed good results. It was only when a lot of nearby sources were giving consistent velocity measurements that they could be considered valid.

6.3 Future work

One of the main problems with the new velocity determination technique was that the time of observation was much too short for the algorithm to work effectively on the IPS recording. It was noted that sources at higher declinations, and thus with a longer transit time, were giving more reliable estimations, thereby proving that a longer observation time allows the algorithm to produce better results. Therefore, to investigate this further, a different type of telescope needs to be used. A steerable telescope that can track any source would be ideal. Siting a new telescope at a more southerly latitude would mean that more of the sky could be observed.

When tracking disturbances in the IPM, one major difficulty was the fact that only one IPS image was produced per day. This long time resolution meant that some fast transients were not observed at all. To specifically study the dynamic structures in the solar wind, an IPS instrument would have to be steerable, and able to make all sky maps more quickly. This would mean that it has to be more sensitive and therefore able to obtain

a measurable scintillating signal even from weak sources. With this kind of telescope, IPS would be practically useful for real-time space weather predictions.

Ionospheric scintillation is a problem for IPS observations, but there are ways to deal with it. These two different types of scintillation have different characteristic timescales, which helps in eliminating ionospheric interference.

Travelling ionospheric disturbances (TIDs) sometimes cause refractive distortions, making the position of a source to appear to move about. This "wobbling" was allowed for in the fitting algorithm, in that the fit was tried for slightly offset positions. The shift that gave the best fit was chosen and recorded. An analysis of these shifts could provide some insight into the nature of TIDs.

For a more complete diagnostic of the solar wind, data from IPS, spacecraft and other experiments can be used together. This sort of international collaboration has already gotten underway with initiatives such as the International Solar Terrestrial Physics (ISTP) program, a joint project involving the United States, ESA and Japan. ISTP brings together a variety of spacecraft that are studying the Sun-Earth system, including SOHO, Geotail, Wind, Polar and ground-based observatories. For example, Peredo *et al.* [60] describe the events of 6-11 January 1997 as being the first observed by many of the instruments of the ISTP "Observatory" from "cradle to grave", i.e. from the origins of the disturbance (a CME) at the Sun, until it was past the Earth.

The proposed STEREO mission should give a valuable stereoscopic view of the propagation of CMEs and other disturbances as they travel from the Sun to the Earth. If it goes ahead, STEREO will consist of two identical spacecraft orbiting the Sun at 1 AU, one leading the Earth by 20°, and the other lagging the Earth by 30°. It will be able to measure the type II radio bursts (very low frequency) from interplanetary shocks, and thus, by triangulation, the position of the shock can be determined. These sort of data would be invaluable to an IPS station that was also tracking the interplanetary disturbance, and in the pursuit of a viable space weather forecast.

6.4 Final words

The 3.6 hectare Cambridge IPS array was not built specifically to study the solar wind, but despite its shortcomings in this department, it has made significant contributions to

the study of IPS and the IPM. The analysis contained in this thesis has helped to prove this. Now, in 1999, the Cambridge array has been switched off, and it is slowly decaying, leaving IPS in the new millennium to the next generation of radio telescopes!

Bibliography

[1] V.D. Albertson, J.M. Thorson, and S.A. Miske. The effects of geomagnetic storms on electrical power systems. In *IEEE PES Summer meeting*, 1973.

[2] C.W. Allen. *Astrophysical quantities.* The Athlone Press, 3rd edition, 1973.

[3] D. N. Baker. Solar wind-magnetosphere drivers of space weather. *Journal of Atmospheric and Terrestrial Physics*, 58:1509–1526, October 1996.

[4] D.N. Baker, G.M. Mason, O. Figueroa, G. Colon, R.M. Watzin, and R.M. Aleman. An overview of the solar, anomalous, and magnetospheric particle explorer (SAMPEX) mission. *IEEE transactions on Geoscience and Remote Sensing*, 31(3):531–541, May 1993.

[5] S. J. Bame, J. R. Asbridge, W. C. Feldman, and J. T. Gosling. Solar cycle evolution of high-speed solar wind streams. *Astrophysical Journal*, 207:977–980, August 1976.

[6] D. G. Banhatti and S. Ananthakrishnan. Interplanetary scintillation observations of an unbiased sample of 90 Ooty occultation radio sources at 326.5 MHz. *Monthly Notices of the Royal Astronomical Society*, 240:117–127, September 1989.

[7] P.R. Barnes and J.W. Van Dyke. Geomagnetic storm effects. *IEEE Power Engineering Review*, 1990.

[8] S.J. Bell Burnell. Results of an initial survey of fine structure in radio sources at 81.5 MHz. *Astronomy and Astrophysics*, 16:379, 1972.

[9] D. E. Billings, S. Hirsch, and C. Vaesavsky. Coronal temperature determination from emission lines. *Astrophysical Journal*, 123:532+, May 1956.

[10] D.C. Black and J.D. Scargle. On the detection of other planetary systems by astrometric techniques. *Astrophysical Journal*, 263:854–869, December 1982.

[11] S. Bravo. A solar scenario for the associated occurrence of flares, eruptive prominences, coronal mass ejections, coronal holes, and interplanetary shocks. *Solar Physics*, 161:57–65, 1995.

[12] S. Bravo and R. Perez-Enriquez. Coronal mass ejections associated with interplanetary shocks and their relation to coronal holes. *Revista Mexicana de Astronomia y Astrofisica*, 28:17+, April 1994.

[13] A. R. Breen, W. A. Coles, R. Grall, U. Løvhaug, J. Markkanen, H. Misawa, and P. J. S. Williams. EISCAT measurements of interplanetary scintillation. *Journal of Atmospheric and Terrestrial Physics*, 58:507–519, January 1996.

[14] A. R. Breen, P. J. Moran, C. A. Varley, W.P. Wilkinson, P. J. S. Williams, W. A. Coles, A. Lecinski, and J. Markkanen. Interplanetary scintillation observations of interaction regions in the solar wind. *Annales Geophysicae*, 16:1265–1282, 1998.

[15] J.L. Butler. *Microwave scanning antennas*, volume 3. Academic Press, New York, 1966.

[16] S. Chapman. *Smithsonian Contrib. Astrophys.*, 2(1-11), 1957.

[17] M.E. Clarke. The determination of the positions of 88 radio sources. *Monthly Notices of the Royal Astronomical Society*, 127:405, 1964.

[18] J. L. Codona. The scintillation theory of eclipse shadow bands. *Astronomy and Astrophysics*, 164:415–427, August 1986.

[19] W. A. Coles. The structure of the solar wind: As viewed using radio propagation methods (invited review). In *ASP Conf. Ser. 26: Seventh Cambridge Workshop on Cool Stars, Stellar Systems, and the Sun*, volume 7, pages 375+, 1992.

[20] C. J. Crannell, K. J. Frost, J. L. Saba, C. Maetzler, and K. Ohki. Impulsive solar x-ray bursts. *Astrophysical Journal*, 223:620–627, July 1978.

[21] B.R. Dennis. Results from the solar maximum mission. In *Solar Flares and Coronal Physics using P/OF as a Research Tool*, pages 67–97, April 1986.

[22] P.A. Dennison and A. Hewish. The solar wind outside the plane of the ecliptic. *Nature*, 213:343, 1967.

[23] V. Domingo, B. Fleck, and A. I. Poland. The SOHO mission: An overview. *Solar Physics*, 162:1–37, 1995.

[24] P.J. Duffett-Smith. The measurement of interplanetary scintillations in conditions of strong radio interference. *Monthly Notices of the Royal Astronomical Society*, 190:139–141, January 1980.

[25] G. R. Gapper, A. Hewish, A. Purvis, and P. J. Duffet-Smith. Observing interplanetary disturbances from the ground. *Nature*, 296:633–636, 1982.

[26] J.T. Gosling. The solar flare myth. *Journal of Geophysical Research*, 98(A11):18937–18949, November 1993.

[27] Pradeep Gothoskar and Shyam Khobragade. Detection of interplanetary activity using artificial neural networks. *Monthly Notices of the Royal Astronomical Society*, 277:1274–1278, December 1995.

[28] M.A. Hapgood. A double solar cycle in the 27-day recurrance of geomagnetic activity. *Annales Geophysicae*, 11:248–253, 1993.

[29] R. A. Harrison. Coronal transients and their relation to solar flares. *Advances in Space Research*, 11:25–, 1991.

[30] R. A. Harrison and D. G. Sime. Comments on coronal mass ejection onset studies. *Astronomy and Astrophysics*, 208:274–278, January 1989.

[31] A. Hewish. The solar origin of geomagnetic storms. *Solar Physics*, 116:195–198, 1988.

[32] A. Hewish. A user's guide to scintillation. *Journal of Atmospheric and Terrestrial Physics*, 51(9/10):743–750, 1989.

[33] A. Hewish, S.J. Bell, J.D. Pilkington, P.F. Scott, and R.A. Collins. Observations of a rapidly pulsating radio source. *Nature*, 217(709), 1968.

[34] A. Hewish and S. Bravo. Distribution of energetic particles near interplanetary shocks. *Nature*, 324:44–46, November 1986.

[35] A. Hewish and S. Bravo. The sources of large-scale heliospheric disturbances. *Solar Physics*, 106:185–200, 1986.

[36] A. Hewish and S.J. Burnell. Fine structure in radio sources at metre wavelengths-I. *Monthly Notices of the Royal Astronomical Society*, 150:141–147, 1970.

[37] A. Hewish, P.F. Scott, and D. Wills. Interplanetary scintillation of small diameter radio sources. *Nature*, 203:1214, 1964.

[38] E. Hildner, J. T. Gosling, R. M. Macqueen, R. H. Munro, A. I. Poland, and C. L. Ross. Frequency of coronal transients and solar activity. *Solar Physics*, 48:127–135, May 1976.

[39] Z. Houminer and A. Hewish. The solar origin of the 2-9 August 1972 events. *Planetary and Space Science*, 36:301–306, March 1988.

[40] R. A. Howard, N. R. Sheeley, D. J. Michels, and M. J. Koomen. Coronal mass ejections - 1979-1981. *Journal of Geophysical Research*, 90:8173–8191, September 1985.

[41] J.A. Joselyn and R.N. Grubb. The space environment monitors onboard GOES. *American Institute of Aeornautics and Astronomy, Aerospace Sciences Meeting, 23rd, Reno, NV*, January 1985.

[42] S. Kahler. Coronal mass ejections. *Reviews of Geophysics*, 25:663–675, April 1987.

[43] S. W. Kahler. Solar flares and coronal mass ejections. *Annual review of Astronomy and Astrophysics*, 30:113–141, 1992.

[44] G. Kanbach, D. L. Bertsch, C. E. Fichtel, R. C. Hartman, S. D. Hunter, D. A. Kniffen, P. W. Kwok, Y. C. Lin, J. R. Mattox, and H. A. Mayer-Hasselwander. Detection of a long-duration solar gamma-ray flare on June 11, 1991 with EGRET on COMPTON-GRO. *Astronomy and Astrophysics supplement series*, 97:349–353, January 1993.

[45] M. Kojima and T. Kakinuma. Solar cycle evolution of solar wind speed structure between 1973 and 1985 observed by the interplanetary scintillation method. *Journal of Geophysical Research*, 92:7269–7279, July 1987.

[46] M. Kojima and T. Kakinuma. Solar cycle dependence of global distribution of solar wind speed. *Space Science Reviews*, 53:173–222, 1990.

[47] Y. Kozuka, T. Watanabe, M. Kojima, M. Ohyama, S. Tsuneta, J. I. Khan, and S. Watari. The dynamical characteristics of a disappearing-filament associated interplanetary disturbance observed in 1992 early May. *Publications of the Astronomical Society of Japan*, 47:377–381, June 1995.

[48] A.S. Krieger, A.F. Timothy, and E.C. Roelof. *Solar Physics*, 29:505, 1973.

[49] M. Lauriente and A.L. Vampola. Spacecraft anomalies due to radiation in space. In *NASDA/JAERI 2nd international workshop on radiation effects of semiconductor devices for space applications*, 1996.

[50] A.J. Lazarus and K.I. Paularena. A comparison of solar wind parameters from experiments on the IMP-8 and WIND spacecraft. In Borovsky, Pfaff, and Young, editors, *Measurement techniques in Space plasmas*, AGU Geophysical Monograph Series, 1997.

[51] L.D. Lewis and R.N. Grubb. The IPS data acquisition and communication system : Noaa technical memorandum ERL SEL-81. Technical report, Space Environment Laboratory, September 1990.

[52] L.T. Little and A. Hewish. Interplanetary scintillation and its relation to the angular structure of radio sources. *Monthly Notices of the Royal Astronomical Society*, 134:221, 1966.

[53] L.T. Little and A. Hewish. Radio source structure derived from interplanetary scintillation. *Monthly Notices of the Royal Astronomical Society*, 138:393, 1968.

[54] R. MacQueen. The high altitude observatory coronagraph/polarimeter on the solar maximum mission. *Solar Physics*, 65:91, 1980.

[55] P. K. Manoharan. Study of solar wind using single-station interplanetary scintillation. *Bulletin of the Astronomical Society of India*, 21:383–384, September 1993.

[56] P. K. Manoharan and S. Ananthakrishnan. Determination of solar-wind velocities using single-station measurements of interplanetary scintillation. *Monthly Notices of the Royal Astronomical Society*, 244:691–695, June 1990.

[57] P. K. Manoharan, S. Ananthakrishnan, M. Dryer, T. R. Detman, H. Leinbach, M. Kojima, T. Watanabe, and J. Kahn. Solar wind velocity and normalized scintillation index from single-station IPS observations. *Solar Physics*, 156:377–393, February 1995.

[58] E. N. Parker. Dynamics of the interplanetary gas and magnetic fields. *Astrophysical Journal*, 128:664, November 1958.

[59] K.I. Paularena, G.N. Zastenker, A.J. Lazarus, and P.A. Dalin. Solar wind plasma correlations between IMP 8, INTERBALL-1 and WIND. *Journal of Geophysical Research*, 103(A7):14,601, 1998.

[60] M. Peredo, N. Fox, and B. Thompson. The ISTP Sun-Earth connection event of Jan. 6-7, 1997: First ever tracking of a solar event from "cradle to grave". *ISTP newsletter*, 7(1), 1997.

[61] J. L. Phillips, S. J. Bame, J. T. Gosling, D. J. McComas, B. E. Goldstein, E. J. Smith, A. Balogh, and R. J. Forsyth. Ulysses plasma observations of coronal mass ejections near 2.5 AU. *Geophysical Research Letters*, 19:1239–1242, June 1992.

[62] K.J.H. Phillips. *Guide to the Sun*, chapter 3, pages 78–79. Cambridge University Press, 2nd edition, 1992.

[63] S. Pohjolainen, E. Valtaoja, and S. Urpo. Solar microwave burst classification and correlation with soft x-rays. *Astronomy and Astrophysics*, 306:973+, February 1996.

[64] W. Press, S.A. Teukolsky, W.T. Vetterling, and B.P. Flannery. *Numerical Recipes in C*. Cambridge University Press, 2nd edition, 1992.

[65] A. Purvis, S.J. Tappin, W.G. Rees, A. Hewish, and P.J. Duffet-Smith. The Cambridge IPS survey at 81.5 MHz. *Monthly Notices of the Royal Astronomical Society*, 229:589–619, December 1987.

[66] A.C.S. Readhead and A. Hewish. Fine structure in radio sources at 81.5 MHz - III. the survey. *Memoirs of the Royal Astronomical Society*, 78:1–49, 1974.

[67] A.C.S. Readhead and A. Hewish. Compact features in a complete sample of radio sources. *Monthly Notices of the Royal Astronomical Society*, 176:571–588, 1976.

[68] A.C.S. Readhead, M.C. Kemp, and A. Hewish. The spectrum of small-scale density fluctuations in the solar wind. *Monthly Notices of the Royal Astronomical Society*, 185:207–225, 1978.

[69] A.C.S. Readhead and M.S. Longair. The spatial distribution and cosmological evolution of scintillating radio sources. *Monthly Notices of the Royal Astronomical Society*, 170:393–404, 1975.

[70] D. V. Reames, L. M. Barbier, and C. K. Ng. The spatial distribution of particles accelerated by coronal mass ejection–driven shocks. *Astrophysical Journal*, 466:473+, July 1996.

[71] J.D. Richardson, J.W. Bekcher, A.J. Lazarus, and K.I. Paularena. Statistical properties of the solar wind. In D. Winterhalter, editor, *Proceedings of the Eight International Solar Wind Conference, Dana Point, CA*, pages 483–486. AIP conference Proceedings, 1996.

[72] B.J. Rickett and W.A. Coles. Evolution of the solar wind structure over a solar cycle: Interplanetary scintillation velocity measurements compared with coronal observartions. *Journal of Geophysical Research*, 96(A2):1717–1736, February 1991.

[73] H. Rosenbauer, H. Gruenwaldt, M. D. Montgomery, G. Paschmann, and N. Sckopke. Helios 2 plasma observations in the distant polar magnetosphere - the plasma mantle. *Journal of Geophysical Research*, 80:2723–2737, July 1975.

[74] T. R. Sanderson, R. G. Marsden, A. M. Heras, K.-P. Wenzel, J. D. Anglin, A. Balogh, and R. Forsyth. Ulysses particle observations of the March 1991 solar flare events. *Geophysical Research Letters*, 19:1263–1266, June 1992.

[75] J.D. Scargle. Studies in astronomical time series analysis. II. statistical aspects of spectral analysis of unevenly spaced data. *Astrophysical Journal*, 263:835–853, December 1982.

[76] K. Scherer, H. Fichter, J.D. Anderson, and E.U. Lau. A pulsar, the heliosphere, and Pioneer 10: probable mimicking of a planet of PSR B1257+12 by solar rotation. *Science*, 278, November 1997.

[77] R. Schwenn and E. Marsch, editors. *Physics of the inner heliosphere*, volume I. Springer-Verlag, 1990.

[78] R. Schwenn, T. Watanabe, T. Kakinuma, and M. Kojima. Large-scale propagation properties of an interplanetary disturbance in association with a 'halo' coronal mass ejection on 27 November 1979. In *Nagoya University, Research Institute of Atmospherics, Proceedings (ISSN 0077-264X)*, volume 36, pages 11–28, March 1989.

[79] S. L. Scott, W. A. Coles, and G. Bourgois. Solar wind observations near the sun using interplanetary scintillation. *Astronomy and Astrophysics*, 123:207–215, July 1983.

[80] N. R. Sheeley, R. A. Howard, M. J. Koomen, D. J. Michels, R. Schwenn, K. H. Muhlhauser, and H. Rosenbauer. Associations between coronal mass ejections and interplanetary shocks. In *Solar Wind Conference*, pages 693–702, November 1983.

[81] N. R. Sheeley, D. J. Michels, R. A. Howard, and M. J. Koomen. Initial observations with the solwind coronagraph. *Astrophysical Journal Letters*, 237:L99–L101, May 1980.

[82] Shrauner, Taylor, and Woan. The second Cambridge pulsar search at 81.5 MHz. *Astrophysical Journal*, 509(2):785–792, December 1998.

[83] J. Shrauner. *Phase coherent observations and millisecond pulsar searches.* PhD thesis, University of Princeton, 1997.

[84] E. J. Smith, D. E. Page, and K. P. Wenzel. Ulysses - a journey above the sun's poles. *Earth and Space*, 4:10–14, September 1991.

[85] G.L. Squires. *Practical physics*, chapter 3, pages 12–21. Cambridge university Press, third edition, 1985.

[86] Z. Svestka. Solar flares. *Dordrecht, D. Reidel Publishing Co. (Geophysics and Astrophysics Monographs.)*, 8, 1976.

[87] E. Tandberg-Hanssen and A. G. Emslie. *The physics of solar flares.* Cambridge and New York, Cambridge University Press, 1988, 286 p., 1988.

[88] S. J. Tappin. *Solar wind transient disturbances.* PhD thesis, University of Cambridge, 1984.

[89] S. J. Tappin. Interplanetary scintillation and plasma density. *Planetary and Space Sciences*, 34, January 1986.

[90] S. J. Tappin. Expected IPS variations due to a disturbance described by a 3-d MHD model. *Planetary and Space Sciences*, 36(11):1155–1163, 1988.

[91] J.E. Titheridge. The characteristics of large ionospheric irregularities. *Journal of Atmospheric and Terrestrial Physics*, 30:73–84, 1968.

[92] R. Tousey. *The solar corona: Space research XIII*, page 713. Akademie-Verlag, 1973.

[93] N. Vilmer. Solar activity: flares; CMEs; SEPs; solar wind. In *ESA Workshop on Space Weather*, 1998.

[94] V.V. Vitkevich and V.I. Vlasov. Radioastronomical investigations of the drift of the inhomogeneous interplanetary plasma. *Soviet Astronomy A.J.*, 13(4):669, 1970.

[95] K.-P. Wenzel and E.J. Smith. The Ulysses mission: in-ecliptic phase. *Geophysical Research Letters*, 19:1235, June 1992.

[96] G. Woan. Robust estimation of interplanetary scintillation. *Monthly Notices of the Royal Astronomical Society*, 254:273–276, 1992.

[97] G. Woan. Observations of long-lived solar wind streams during 1990-1993. *Annales Geophysicae*, 13:227–236, 1995.

[98] A. Wolszczan. Confirmation of Earth-mass planets orbiting the millisecond pulsar PSR B1257+12. *Science*, 264, April 1994.

[99] A. Wolszczan and D.A. Frail. A planetary system around the millisecond pulsar PSR B1257+12. *Nature*, 355(145), 1992.

[100] H Zirin. *Astrophysics of the Sun*, pages 255–259. Cambridge University Press, 1988.